

Steps towards simultaneous atomic-force and fluorescence spectroscopy of single DNA

Thesis

Department of Mathematics and Natural Sciences
Heinrich-Heine-University Düsseldorf

Alexander Gaiduk

from Minsk

June 2006

Institute of Physical Chemistry,
Heirich-Heine University Düsseldorf

Printed with the permission of
Department of Mathematics and Natural Sciences
Heinrich-Heine-University Düsseldorf

1. Referee: Prof. Dr. C.A.M. Seidel
2. Referee: Prof. Dr. K. Kleinermanns
3. Referee: Prof. Dr. Th. Basche

Date of the oral examination: 29 November 2006

Посвящается моим родителям,
Анатолию Ивановичу и
Валентине Васильевне Гайдук

Acknowledgments

First of all I would like to thank my supervisor Prof. Dr. C.A.M. Seidel for giving me the opportunity to work on interesting interdisciplinary projects, to study and improve my knowledge in various fields of physics and chemistry. I am grateful for your enthusiasm, for fruitful discussions and ideas, for your help in understanding the results as well as for your faith in me and your kind support in everyday life outside lab.

I am truly grateful to...

Dr. Suren Felekyan for his help in various aspects of single molecules fluorescence detection and analysis. I would like to thank you for always showing interest in my work and for your critical remarks. Thank you for your patience, frankly conversations and a plenty of useful advice. I will always remember “training evenings”, “grilling on Rhein”, history of Armenia and many other things.

Dr. Matthew Antonik, for introducing and guiding me in exciting worlds of AFM, LabView tricks and biology as well as for being a nice roommate. I will really miss your extravagant jokes and our talks about science, history, languages, games, culture, and politics.

Dr. Ralf Kühnemuth for teaching fluorescence methods, as well as for his useful comments and valuable suggestions. It was a pleasure for me to work together with a tactful person and an experienced scientist like you. I hope we will have another chance to canoe with your nice family and to drink coffee in the middle of the lake again.

My progress would not have been possible without previous hard work of Dr. Matthew Antonik and Dr. Ralf Kühnemuth, who had started the complicated task of the equipment combination. I want to thank both of you for sharing your knowledge and experience. Thank you a lot for your help and support.

Volodymyr Kudryavtsev for his programming work and explanations. I have been enjoying discussions on the art of photography and visual perception. I will not forget our “just five kilometres” bicycle trips and “even sunburn”.

Carl Sandhagen, Martin Schramm and Marcel Merkwitz for their help with useful electronic devices and computers.

Alessandro Valeri for his help with the fluorescence spectrometer and bulk fluorescence spectra measurements, for being a nice company on whatever places and situations, for being positive and humorous.

Denis Dörr and Dr. Stanislav Kalinin for the exchange of ideas as well as for pleasant chats and joint activities.

Dr. Marcelle König, Dr. Enno Schweinberger, Dr. Anna Wozniak and Dr. Filipp Oesterhelt for useful tips as well as for the organization of most of the parties and social activities at the department.

I would like to thank many times to Bärbel Hoffman and Veronika Mendorf for your optimism and taking care of all the paper work.

Ralf Müller for being a good fellow and for his kind help during the move.

Opas Tojira for useful comments on my presentation in Berlin.

Harekrushna Sahoo for a real Indian food.

My uncle, Dr. Peter Gaiduk for his advices and support.

Prof.Dr. Sergey Gaponenko for initiating my interest in single molecules research.

I would like to express my gratitude once again to Ralf Kühnemuth, Suren Felekyan, Stefan Marawske, Matthew Antonik, Elena and Bernd Potthoff – people, who have carefully read my thesis. Dear Elena, thank your for your lessons.

Also I would like to thank everyone at the department of Physical Chemistry in Düsseldorf for their warm opened relationship and readiness to help. Special thanks to the dancing community of HHU Düsseldorf for the great time on a dance floor.

I thank my parents Anatoli Gaiduk and Valentina Gaiduk, my sister Olga and my friends, for their support and encouragement.

Finally, I would like to express my love and thank to my wife Ala Valetava, a wonderful woman. I thank you for your patience, understanding, support and making my life much more beautiful and full of tenderness.

Summary

The development of single molecule fluorescence detection allows studying the properties of molecules without ensemble averaging. The detailed information about the fluorescence lifetime, the fluorescence quantum yield, the quenching mechanisms and the motion parameters of individual fluorophores and fluorophore mixtures can be delivered by Multiparameter Fluorescence Detection (MFD). The structure, dynamics and functionality of complex biological molecules can also be probed with MFD.

An additional dimension can be added to the MFD for studies of complex biological molecules by applying an external force. A precise mechanical manipulation of the sample providing the information about the force would enhance the control of the experiments and the analytical power of the analysis.

Goals and objectives

This thesis is devoted to the combination of fluorescence microscopy and spectroscopy with atomic force microscopy (AFM) and spectroscopy techniques. The aim of the combination is simultaneous force and fluorescence studies of single biological molecules (in particular DNA).

This complex problem requires consecutive realization of several steps:

- preparation of transparent surfaces for a stable attachment of biomolecules,
- investigation of the atomic force cantilevers optical properties,
- development of fluorescence analysis techniques capable of resolving subnanometer distance changes between fluorophores,
- establishment of the atomic force spectroscopy method in the lab,
- development of simultaneous atomic-force and fluorescence spectroscopy experiment.

Surface preparation

Since there are two microscopy techniques with different spatial resolutions to be combined, there are two possible approaches to identify a DNA molecule on the surface. The first one implies finding a molecule with atomic force microscope, while the second one uses optical microscopy for the localization of DNA. Each approach has different requirements to the transparency, roughness and cleanness of glass substrates as well as glass modification procedures.

Glass cleaning and silanization provide surfaces for stable DNA molecule binding. The fluorescence of the surface after cleaning and silanization is very low and the optical signal detected after laser illumination consist mainly of Raman scattered light. Thus optical

microscopy allows finding a single DNA molecules labelled with the dye on the surface. A relatively rough glass surface (up to 3.4 nm RMS) does not promote the identification of single DNA by means of AFM.

Fluorescence from the cantilevers

Knowledge of the optical properties of AFM tips is relevant for the combination of optical and force spectroscopy. Detailed studies show whether the amount of scattered and luminescence light from an AFM tip would overwhelm the signal of a single fluorophore. The problem of the cantilever tips fluorescence is studied by means of the newly developed Multiparameter Fluorescence Imaging (MFI) technique. This technique is used for 3-dimensional optical imaging and characterization of the AFM tip. Cantilevers of two types of material (Si and Si₃N₄) were tested.

The Si tips have the lowest signal intensity and they are preferred for the combination of MFD and force spectroscopy. However, commercial Si cantilevers do not have mechanical properties (low stiffness) required for the sensitive force measurements. The Si₃N₄ tips have higher relative brightness which drops quickly with the distance from the tip. Since the sharp edges are typically the brightest scattering sources on a tip, unsharpened and blunt tips should be used when possible for combined applications. Alternatively, tips could be modified or replaced with materials which are more suitable for optical experiments, effectively substituting the native tip properties.

A time gating or a molecule separation from the tip by a linker can be employed to eliminate the additional signal from the tip.

In addition, modelling of the background in a multi-component fit of the data with fixed pre-determined background constants can be used for taking into account the optical signal from a cantilever in the data analysis.

Fluorescence detection and high precision distance measurements

The combination of fluorescence and force spectroscopy techniques can provide complementary data in studies of the structure and dynamics of complex biomolecules. Förster (fluorescence) resonance energy transfer (FRET) is used to measure distances in macromolecules. For FRET experiments a single molecule or molecular complex is labelled with two different dyes and the efficiency of energy transfer from one dye to the other is monitored. The main difficulty in extracting molecular information from fluorescence intensity distributions is the inability to unambiguously distinguish molecular fluctuations from either stochastic variations or background counts. A newly developed probability distribution analysis (PDA) is capable of predicting the shot noise limited shapes of

histograms generated from single photon counting data. The PDA takes into account the effects of background and stochastic processes for the high precision quantitative analysis.

The PDA can successfully extract the originating value behind shot noise limited FRET signal distributions and determine the underlying fluorescence signal ratio with a precision of better than 2%. This precision translates into a precision in the distance measurements better than 1 % of the Förster radius. A broadening of the distribution by 5Å due to mobility of the dyes on flexible linkers is easily revealed. However, detailed studies of the influence of background counts on PDA results are still required.

The PDA is also applied to study the spectral shifts of fluorescent molecules, which makes the method attractive for pH monitoring in a living cell or for probing a microenvironment of fluorescent molecules.

Force spectroscopy establishment

The custom-build setup for the force spectroscopy is based on a commercial AFM system and an additional acquisition board. Pulling experiments on single DNA molecules reveal structural transitions in the molecule upon the applied force.

The influence of the dye (SYBR Green I, groove binder) is studied. The results were found to be consistent with previous optical tweezers reports on dsDNA force spectroscopy using this dye, which indicate a hysteresis between the retraction and approach force curves. The dsDNA B-S transition force is increased up to 8.9% upon SYBR Green binding at an average concentration of 0.28–0.55 dyes/bp and 15% upon SYBR Green binding at an average concentration of 1-2 dyes/bp (comparing to the literature value of the B-S transition force of 65 pN).

Combined fluorescence and force spectroscopy

The piezo hysteresis in the sample plane is quantified and the way to eliminate it without a closed loop control is proposed. The position uncertainty of molecules binding on the AFM tip is discussed.

Several experimental approaches to realize the simultaneous force spectroscopy and multiparameter fluorescence detection have been demonstrated. Successful experiments are performed depositing DNA molecules on the tip or on the surface. Consecutive pulling on a single DNA and the simultaneous optical signal registration (more than 10 pulls) were achieved. As observed in the simultaneous experiments, the structural changes of a DNA molecule correlate with the intensity and the lifetime change of the fluorescence of the DNA binding dye.

Perspectives

Confocal scanning adds spatial resolution to the analysis available in MFD. Simultaneous 3D-mapping of all fluorescence parameters with MFI technique can be implemented for studies in cells and membranes. Additionally, image correlation analysis is capable of analysing temporal and spatial fluctuations in the raster scan images and extends the fluorescence correlation analysis to time scales of seconds or minutes.

Long Si or carbon cantilever tips have the best optical properties for combined experiments in order to minimize the influence of the tip's fluorescence signal. Sharp AFM probes and their proper chemical treatment will limit the attachment area of molecules on the tip.

The method of the fluorescence-directed force spectroscopy can be implemented to study different biological molecules and cells. Simultaneous MFD and force spectroscopy proposes a way to study the structure of macromolecules and fast dynamic processes. A molecule can be driven into a certain conformation and its behaviour can be monitored based on the fluorescence signal. Differently, unstable intermediate states can be probed by force spectroscopy and detailed temporal information about the fluorescence can be obtained in a single run experiment. The data analysis of the combined experiment then includes the correlation on the time scale of force events and changes in fluorescence parameters. Thus, an additional dimension (force values) is added to the standard two-dimensional MFD histograms.

The combination of force spectroscopy and FRET probability distribution analysis propose high spatial resolution in both mechanical and fluorescence measurements of the combined experiment.

Abbreviations

# of t.w.	number of time windows
a.u.	arbitrary units
A	acceptor
Abs	absorption
ADC	analogue to digital converter
AFM	atomic force microscopy
APD	avalanche photodiode
APDES	3-Aminopropyldimethylethoxysilane
APTES	3-Aminopropylthriethylethoxysilane
bp	base pair
BFP	back focal plane
conc.	concentration
CCD	charge coupled device
CFD	constant fraction discriminator
D	donor
DA	donor-acceptor
DAC	digital to analogue converter
DB	dichroic beam splitter
DM	dichroic mirror
DNA	deoxyribonucleic acid
DSP	digital signal processor
EBFP	equivalent back focal plane
FCS	fluorescence correlation spectroscopy
FDP	field diaphragm plane
FFT	fast Fourier transformations
FIFO	first-in-first-out memory buffer
Fluor	fluorescence
FP	focal plane
FRET	fluorescence resonance energy transfer
FS	focus-surface separation
FJC	freely joint chain
GOPDES	3-Glycidoxypropyldimethylethoxysilane
GOPTS	3-Glycidoxypropylthrimethoxysilane
HDC	high density carbon
HV	high voltage
IC	internal conversion
IF	interference filter
InvOLS	inverse optical lever sensitivity
IRF	instrument response function
ISC	intersystem crossing

k_B	Boltzmann constant (gas constant) $1.38 \cdot 10^{-23}$ J/K
MFD	multiparameter fluorescence detection
MFI	multiparameter fluorescence imaging
N_A	Avogadro's constant $6.022 \cdot 10^{23}$ mol ⁻¹
N.A.	numerical aperture
N/A	not available
NIM	nuclear instrument modules
o.D.	optical density
PC	personal computer
PCR	polymer chain reaction
PB	polarizing beam splitter
PBS	phosphate buffered saline
PD	photodiode
PDA	probability distribution analysis
PEG	poly(ethylene glycol)
Phosph	phosphorescence
PMT	photomultiplier tube
PSF	point spread function
Rh	rhodamine
RMS	root-mean-square
sm	single molecule
SCA	single channel analyzer
SFFS	simultaneous force and fluorescence spectroscopy
SFM	scanning force microscopy (=AFM)
SHO	simple harmonic oscillator
SPC	single photon counting
SPM	scanning probe microscopy
STM	scanning tunnelling microscopy
TAC	time-to-analogue converter
TCSPC	time-correlated single photon counting
TIR	total internal reflection
TIRF	total internal reflection fluorescence
TF	tip-focus separation
TGI	time-gated imaging
TS	tip-surface separation
TTL	transistor-transistor logic
vs.	versus
WLC	worm like chain

Contents:

INTRODUCTION	10
1 THEORETICAL BACKGROUND	14
1.1 Optical microscopy and fluorescence spectroscopy methods	14
1.1.1 Description of light	14
1.1.2 Fluorescence characterization	15
1.1.3 Fluorescence resonance energy transfer (FRET).....	19
1.1.4 Fluorescence correlation spectroscopy (FCS).....	21
1.1.5 Optical microscopy	24
1.1.6 Total internal reflection fluorescence (TIRF).....	25
1.1.7 Single molecule multiparameter fluorescence detection (smMFD)	29
1.2 Atomic-force microscopy	32
1.2.1 The atomic-force microscope.....	32
1.2.2 Forces (Van der Waals force, capillary force, adhesive forces, double layer forces).....	33
1.2.3 Imaging and imaging modes (contact dc mode, non-contact ac mode).....	35
1.2.4 Cantilevers (geometry, tip shape, mechanical properties).....	38
1.2.5 Piezo scanner (materials, construction, creep, drift, sensors).....	42
1.2.6 Coarse approach system.....	44
1.2.7 Sample holder, liquid cell.....	44
1.2.8 Detection methods, optical lever technique.....	44
1.2.9 Mechanical and thermal vibrations	46
1.3 Force spectroscopy	46
1.3.1 Atomic force microscope in force spectroscopy mode	47
1.3.2 Cantilever force constant calibration.....	49
1.3.2.1 Added mass method.....	49
1.3.2.2 Static loading methods.....	50
1.3.2.3 Reference spring method	50
1.3.2.4 Thermal motion method.....	51
1.3.2.5 Dynamic method.....	52
1.3.3 Polymer elasticity.....	53
1.3.3.1 Ideal chain models	54
2 EXPERIMENTAL SECTIONS	58
2.1 Experimental Setup	58
2.1.1 Optical microscopy and spectroscopy	59
2.1.1.1 Optical setup settings for Section 2.3.....	61
2.1.1.2 Optical setup settings for Section 2.4.....	62
2.1.1.3 Optical setup settings for Section 2.5.....	62
2.1.1.4 Optical setup settings for Section 2.7.....	63
2.1.1.5 Fluorescence data analysis software	63
2.1.2 Bulk optical spectroscopy	64
2.1.3 Atomic force microscopy and force spectroscopy	65
2.1.4 Combined AFM and optics: Simultaneous force and fluorescence spectroscopy (SFFS)	67
2.2 Materials and chemicals	69
2.3 Transparent surface substrates preparation and characterization	74
2.3.1 Silicon oxide (SiO ₂) surface.....	75
2.3.2 Surface cleaning procedures.....	76
2.3.3 Silanization of silicon oxide surface	79
2.3.4 Surface PEGylation.....	81
2.3.5 Immobilization of biomolecules (DNA)	84

2.3.6	Fluorescence studies of surface modification steps	85
2.3.7	Conclusions	88
2.4	Multiparameter fluorescence imaging development and application to cantilever tip fluorescence characterization	89
2.4.1	Cantilever in evanescent field.....	89
2.4.2	Fluorescence imaging development: time-gated imaging and multiparameter fluorescence imaging	91
2.4.3	Imaging application: cantilever tips optical signal characterization.....	93
2.4.3.1	Veeco Microlever.....	98
2.4.3.2	Veeco NPG	100
2.4.3.3	Olympus Biolever	101
2.4.3.4	Nanosensor.....	102
2.4.3.5	Nanotools HDC.....	103
2.4.4	Conclusions	107
2.5	High precision distance measurement via fluorescence detection.....	109
2.5.1	FRET and PDA formalism	110
2.5.1.1	Fluorescence Signals.....	110
2.5.1.2	Probability Distribution Analysis.....	111
2.5.1.3	PDA distributions properties.....	115
2.5.2	PDA application: Single dye FRET studies.....	118
2.5.2.1	Atto590 dye: a fixed FRET efficiency	118
2.5.2.2	Atto590 dye: a comparison of bulk fluorescence and single molecule FRET measurements.....	119
2.5.2.3	Goodness of PDA fit and dependence on number of bins and threshold	121
2.5.2.4	Shot Noise Limited Fluorescence Distributions.....	122
2.5.3	PDA application: FRET measurement on DNA molecules.....	124
2.5.3.1	Single Dye-DNA construct: fixed FRET efficiency	124
2.5.3.2	DNA-dye FRET pair construct: FRET broadening description via distance fluctuations.....	126
2.5.3.3	DNA-dye FRET pair construct: other FRET broadening mechanisms	127
2.5.4	Fluorescence-based ruler: DNA length estimation	133
2.5.5	Conclusions	137
2.6	Force spectroscopy of single DNA molecules	138
2.6.1	DNA molecules	138
2.6.2	Force spectroscopy: experimental procedure and protocol	139
2.6.2.1	Sample preparation approaches.....	140
2.6.2.2	Cantilever cleaning and modification	141
2.6.2.3	Force spectroscopy measurements	142
2.6.2.4	Calibration of AFM cantilevers.....	142
2.6.3	Pulling on DNA molecules.....	145
2.6.3.1	DNA on gold surfaces	146
2.6.3.2	DNA on APTES glass. Influence of the dye	146
2.6.4	Conclusion.....	154
2.7	Simultaneous force spectroscopy and fluorescence measurements.....	155
2.7.1	Fluorescence-directed localization of molecules.....	155
2.7.1.1	Mechanical manipulation of DNA molecules	157
2.7.1.2	AFM hysteresis influence on manipulations	158
2.7.2	Simultaneous force and fluorescence spectroscopy experiments on single DNA molecules	159
2.7.2.1	Pulling on many molecules: sample misalignment	160
2.7.2.2	Consecutive dsDNA pulls and fluorescence detection.....	163
2.7.2.3	DNA rupture. Fluorescence intensity and lifetime change.....	166
2.7.3	Conclusions and outlook	168
LITERATURE:		170
APPENDIX A: SOLID SUBSTRATES AFM IMAGING STATISTICS		186
APPENDIX B: APPARENT FLUORESCENCE EFFICIENCY PROBABILITY DENSITY		187

APPENDIX C: FLUORESCENCE RATIO PROBABILITY DENSITY.....	189
APPENDIX D: FRET RATIO HISTOGRAMS BACKGROUND CORRECTING PROCEDURE FOR PDA	191
APPENDIX E: DESCRIPTION OF CUSTOM-WRITTEN SOFTWARE.....	192
ControlPI.....	192
Imaging control with AFM scripting.....	194
Treat AFM data.....	196
WinSpec movies	197
PicoPull	198
ReadFFTs.....	199
PicoPeek	200
ViewPicoPeek (FoCuS)	201
LIST OF PUBLICATIONS.....	202
DECLARATION	203

Introduction

For thousands of years people were looking to the sky and dreaming about travelling to the stars. For hundreds of years mankind has known what the atom is, can prove its existence and even control and manipulate it. The micro-nano world of complex biological molecules is also as ‘big’ as the universe and the complicated laws acting in this world are exciting in the same way as exploration of the space.

Richard Feynman’s talk in 1959 at the annual meeting of the American Physical Society ‘There’s Plenty of Rooms at the Bottom’ has outlined many of the problems to be solved on the way of understanding the world that is below, the nano-world [1]. This talk was a milestone on the way of nanotechnology development. Among the discussions of the talk was the question about the amount of information that can be stored and retrieved on the small scale. The problem of manipulating and controlling things on a small scale was another topic of interest for scientific investigations. Nowadays, with the development of technology, computers, and microscopes these questions can be understood better and some answers can be given. Looking at the images of ordinary musical CD and DNA molecule obtained by a modern instrument one can compare the amount of information contained there (Figure i-1). Many lines on the left image are CD pits shown on the area of $25 \times 25 \mu\text{m}^2$. The right image has only $1.9 \times 1.9 \mu\text{m}^2$ area and depicts single DNA molecules. One pit of CD is one bit. A DNA molecule of a comparable size of $1 \mu\text{m}$ has about 3000 base pairs, carrying the information. A base pair, one bit of DNA molecule, which is about 50 atoms, is not visible in this case.

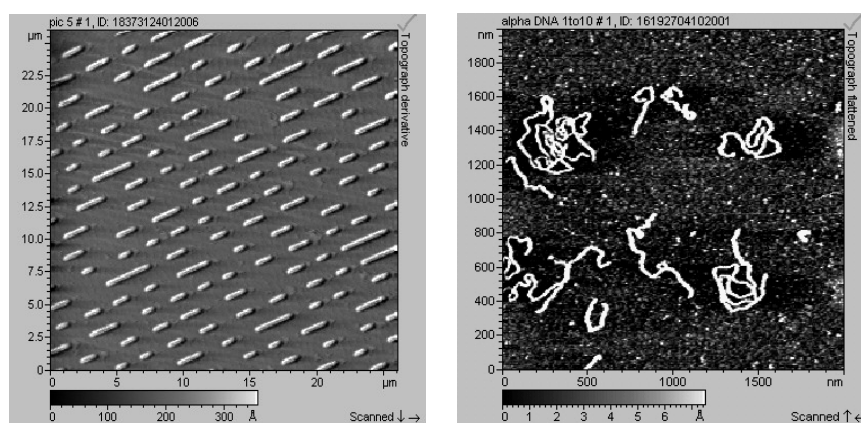


Figure i-1. Left: $25 \times 25 \mu\text{m}^2$ an image of a computer compact disk (CD), obtained on an atomic force microscope. One bit of information written on CD, a single pit is clearly visible. Right: $1.9 \times 1.9 \mu\text{m}^2$ atomic force microscope image of λ -DNA molecules. One bit of information about DNA structure, a single DNA base pair, is hard to resolve. A DNA molecule would easily fit inside one of the CD pit in size, but contains much more information.

Accessing the information on a DNA molecule for a living organism is as easy as listening to the music on a CD. Nevertheless, understanding how the information on DNA is transferred, used and what meaning this information has – are challenging problems. Solving any of these questions one can open ‘more doors at the bottom’ [1]: new materials and material properties, new medicine may be discovered and diseases may be cured. These aims usually require apparatus and techniques capable of studying the structure and functions of individual biomolecules.

Combined fluorescence spectroscopy and nanomanipulation

Advances in single-molecule fluorescence detection techniques [2,3] as well as developments in nanomanipulation and probe microscopy [4,5] allow one not only to illustrate the potential of these techniques, but to focus on detailed studies of specific problems in physics, chemistry and biology as well. Single molecules can be manipulated, and different phenomena can be studied without ensemble averaging.

A significant experimental enhancement is the combination of single molecule manipulation and optical measurements [6]. This combination allows molecules being placed under a controlled tension and probed with fluorescence techniques in order to determine molecular orientation, photo-physical activity, or sub-nanometer intra-molecular displacements using fluorescence resonance energy transfer (FRET) between two fluorophores. A variety of combined experimental advantages were discussed in reviews [7]. The combination of fluorescence detection and nanomechanical manipulation is the combination of two complementary techniques which is aimed to produce novel detailed information about molecular structure and functions. When combining them, particular experimental requirements should be considered. Various manipulation techniques are presented in the table (Table i-1).

Table i-1. Comparison of techniques used for the mechanical characterization of bio-molecules, adopted from [4].

Method	Force range (pN)	Temporal range
Magnetic beads	0.01–100	≥ 1 s
Optical tweezers	0.1–150	≥ 10 ms
Microneedles	>0.1	≥ 100 ms
Biomembrane force probe	0.5–1000	≥ 1 ms
AFM	>1	≥ 10 ms

In particular, combinations of two imaging techniques, different in complexity and precision allow correlating of topography and optical images [8,9], and at the same time provide fluorescence detection sensitivity down to a single molecule level [10]. New tools for multi chromophore polymer characterization, lipid domains formation monitoring, particle interactions with cell membranes and for a precisely targeted living-cell injection and manipulation employing the combination of techniques were suggested by several researches [11-14]. The interaction of a single actin-myosin system has been visualized and mechanisms of a chemical energy transfer into mechanical work were studied in detail [15]. Photo-excited change between the trans- and cis- conformations of an azobenzene molecule was demonstrated and an optomechanical single molecule based device was proposed in the work of Hugel et al. [16]. A technique for spatially selecting and grafting of a DNA-tethered bead to an AFM cantilever with subsequent pulling on the DNA molecule was demonstrated [17].

The combination of manipulation with AFM and fluorescence detection methods is greatly influenced by tip-induced effects. The evidence of fluorescence quenching, fluorescence rate and lifetime change near metal tips has been experimentally proved [18,19]. These effects limit the compatibility of AFM-based force spectroscopy and optical spectroscopy; however several approaches were recently suggested to overcome them. AFM cantilever-sample separation was calibrated either by means of a wave scattering intensity produced by a bead attached to the cantilever [20] or fluorescence intensity from beads [21] in an evanescent field. Indirect atomic force spectroscopy, performed via horizontal stretching of a DNA molecule non-specifically bound to the surface, and simultaneous far field fluorescence microscopy imaging experiments were conducted to study binding dynamics of dyes to DNA molecules [22]. Optical tweezers were used to perform a non-reversible mechanical transition on a DNA molecule and fluorescence signal from a single dye molecule attached was simultaneously monitored by Block and co-workers [23,24].

Thus increasing number of publications on fluorescence detection methods and mechanical manipulations indicates the strong scientific interest in the area.

Structure of the thesis

Literature overview and theoretical background on the research topics of the thesis is given in Section 1. Advances in technology and demands of new experiments drive technology development. The complicated task of combining atomic-force microscopy and fluorescence microscopy requires a detailed introduction into each experimental technique. Fluorescence spectroscopy formalism and advanced methods are presented in Section 1.1. Atomic force microscopy and atomic force spectroscopy techniques are considered in Sections 1.2 and 1.3.

Experimental setup description and experimental conditions are given in Section 2.1. Materials and chemicals are listed in Section 2.2.

Results of the preparation of transparent substrate suitable for single molecule fluorescence spectroscopy measurements on surfaces are presented in Section 2.3.

Section 2.4 is devoted to the scanning fluorescence imaging development and atomic force cantilever tips fluorescence characterization for combined atomic force and fluorescence spectroscopy experiments.

Section 2.5 presents the formalism for fluorescence resonance energy transfer (FRET) measurements. It introduces new FRET signal distribution analysis and proposes a high precision method for two fluorophores distance measurements.

Establishment of the force spectroscopy technique and its application to single DNA molecules mechanical properties studies are illustrated in Section 2.6.

Finally, combined simultaneous force and fluorescence spectroscopy (SFFS) experiments on DNA molecules are given in Section 2.7 of the thesis. Present experimental protocols and perspectives to macromolecules studies are also discussed in this Section.

1 Theoretical background

1.1 Optical microscopy and fluorescence spectroscopy methods

The aim of this Section is the consideration of general principles of light absorption and emission and in particular luminescence light. Here the basis of fluorescence detection techniques and fluorescence analysis will be introduced with special emphasis on fluorescence resonance energy transfer (FRET), fluorescence correlation spectroscopy (FCS) and multiparameter fluorescence detection (MFD). Two advanced optical microscopy techniques, confocal microscopy and total internal reflection (TIR) microscopy, are described. Some detailed considerations will be done in further experimental Sections.

1.1.1 Description of light

Light and phenomena and effects associated with its propagation and interaction with the matter can be described within two approaches:

According to the classical description of light, it is an electromagnetic wave [25]. The electric field vector at a point is given by the equation $\vec{E}(t) = \vec{E}_0 \cdot \cos(\omega t + \varphi)$, where \vec{E}_0 is the electric field amplitude at time zero, and ω and φ are the angular frequency and the phase of electromagnetic wave. Light propagation and interactions are described by a special case of Maxwell's equations. The exact state of the electromagnetic wave, due to the deterministic nature of the description, can be obtained for any point at any moment, leaving no space for statistical variations.

The quantum mechanical approach describes light as a flux of quanta (photons), with a photon energy defined by Plank's formula as $E_{ph} = \hbar\omega$, where \hbar is the Plank's constant. The Heisenberg uncertainty principle puts limitations on simultaneous photon impulse and position determination, and leads to statistical variations in photon detection. The Hamiltonian, based on the photon creation and annihilation operators describe the interactions of light with matter [26].

The intensity of light is defined accordingly as $F = |\vec{E}|^2$ or $F = n E_{ph}$, where n is the number of photons. The light intensity is the value usually measured in an experiment.

A special type of light, carrying rich information about the structure and properties of the emitters, is luminescence.

1.1.2 Fluorescence characterization

For more than three centuries the phenomenon of luminescence has attracted scientists. Detailed theories and plenty of careful experiments were developed to understand the origins of luminescence, and to exploit this phenomena for scientific and commercial purposes.

Luminescence is the emission of photons which exceeds the thermal radiation at a given temperature and possesses the finite time length, significantly larger than the light wave period. The term luminescence was first introduced by Eilhard Wiedemann in 1888 [27] with the time dependency first mentioned by F. Perrin [28] and defined by S.I. Vavilov [29].

Depending on the source of excitation, luminescence can be divided into various types [28,30]. The particular case of photoluminescence (excitation by absorption of light) can be divided into fluorescence, phosphorescence and delayed fluorescence. This distinction is based on the time scale of photoluminescence emission.

Jablonski diagrams can be used as a simple way to visualize the processes possible for the molecule luminescence emission (Figure 1-1).

Absorption of light by a fluorophore is accompanied by a molecular transition into an excited electronic state followed by vibration relaxation. From the excited state a molecule can undergo transition to the ground state, emitting a photon. This process is called fluorescence. A molecule can also perform nonradiative internal conversion back to the ground singlet state or inter-system crossing to the triplet state. A molecule in the triplet state can relax to the ground singlet state either via nonradiative inter-system crossing or emitting phosphorescence photon. Different timescales are characteristic for different processes, as can be seen below:

Absorption (Abs)	10^{-15} s	
Vibrational relaxation	10^{-12} - 10^{-10} s	
Singlet state lifetime (Fluor)	10^{-10} - 10^{-7} s	(fluorescence)
Inter-system crossing (ISC)	10^{-10} - 10^{-8} s	
Internal conversion (IC)	10^{-11} - 10^{-9} s	
Triplet state lifetime (Phosph)	10^{-5} - 1 s	(phosphorescence)

Fluorescence can be characterized by several parameters: absorption spectrum, emission spectrum, quantum yield, lifetime and anisotropy. These parameters are particularly interesting because they provide information about the molecule and will be considered separately.

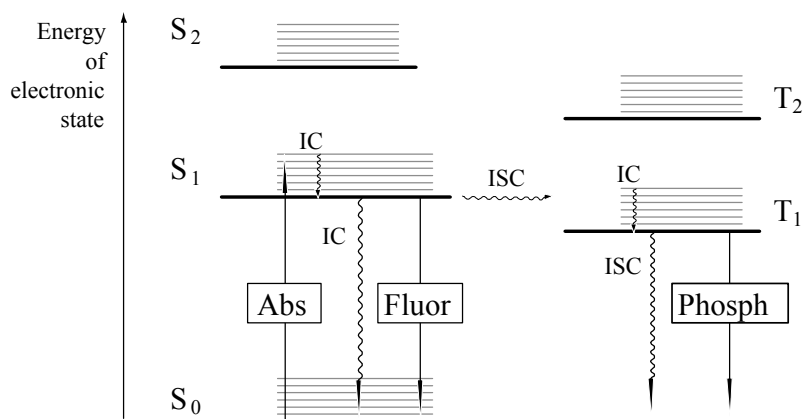


Figure 1-1. Jablonski diagram. S₀, S₁, S₂ – singlet states; T₁, T₂ – triplet states; Abs – absorption of photons; Fluor – fluorescence emission; Phosph – phosphorescence emission; ISC – intersystem crossing; IC – internal conversion (thermal non-radiative transitions).

Absorption of light

A dye molecule can be excited from the ground electronic state (S₀) to any of the excited electronic states (S_n) as a result of interaction with electromagnetic waves. The excitation probability is defined by the Franck-Condon principle which states that all electronic transitions occur without nuclei position and its environment change, and therefore are vertical on the potential energy – nuclear configuration diagrams [30]. The Lambert-Beer law gives the relationship between the incident and transmitted light, describing the absorption efficiency:

$$A(\lambda) = -\log_{10} T(\lambda) = \log_{10} \left(\frac{F_0}{F} \right) = \varepsilon(\lambda) \cdot c \cdot d = \text{o.D.}(\lambda) \cdot d \quad (1-1)$$

where $A(\lambda)$ is the absorbance, $T(\lambda)$ is the transmittance, F_0 is the incident light intensity, F is the transmitted light intensity, c is the fluorophores molar concentration, d is the thickness of the sample, $\varepsilon(\lambda)$ is the molar extinction coefficient, $\text{o.D.}(\lambda)$ is the optical density or absorbance of the sample for a given wavelength per unit distance.

The absorption of chromatic light is characterized by the absorption spectrum, which defines the dependence of absorption coefficient on the incident light wavelength.

The molecular absorption cross-section $\sigma(\lambda)$ characterizes the effective area around a molecule where light can be captured. It can be presented as follows:

$$\sigma(\lambda) = \frac{2.303}{N_A} \cdot \varepsilon(\lambda) = 3.825 \cdot 10^{-19} \cdot \varepsilon(\lambda), \quad (1-2)$$

where N_A is Avogadro's number.

Fluorescence emission

The excited molecule can relax from the excited state by emitting a fluorescence photon. According to Kasha's rule the shape of fluorescence emission spectrum is

independent of the excitation wavelength [30]. As follows from of Franck-Condon principle, electron transitions in a molecule take place without nuclei position changes [30]. Therefore the fluorescence spectrum has a mirror shape of the absorption spectrum. Figure 1-2 presents the absorption spectrum and shifted fluorescence emission spectrum. The shift between the maximum of the fluorescence emission spectra and the maximum of the first electronic transition in adsorption spectrum is called the Stokes shift. It is expressed by $\Delta\lambda = \lambda_{\text{Abs}} - \lambda_{\text{Fluor}}$ or in terms of wavenumbers $\bar{\nu} = 1/\lambda$ as follows $\Delta\bar{\nu} = \bar{\nu}_{\text{Abs}} - \bar{\nu}_{\text{Fluor}}$. The symmetry of spectra can be broken in some special cases: given a long-lived excited state, photoreactions in excited state and molecular complex formation.

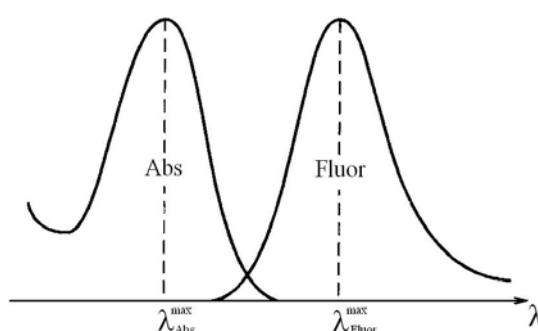


Figure 1-2. Illustration of absorption and fluorescence spectra of a molecule.

It is important to distinguish between the fluorescence emission spectrum and the fluorescence excitation spectrum. The fluorescence emission spectrum is obtained, measuring the fluorescence signal at different wavelength with excitation at a fixed wavelength, whereas the fluorescence excitation spectra is obtained measuring the fluorescence signal at a fixed wavelength and exciting at different wavelengths.

Fluorescence lifetime and quantum yield

According to Vavilov's law, the fluorescence lifetime is independent of the excitation wavelength [29]. The fluorescence lifetime is defined as the average time the molecule spends in the excited state, before it returns to the ground electronic state. Generally fluorophore lifetime is given by the equation:

$$\tau = \frac{1}{\Gamma + k_{nr}}, \quad (1-3)$$

where Γ is the radiative decay rate and k_{nr} is the non-radiative decay rate, influenced by various phenomena (internal conversion, intersystem crossing, fluorescence quenching). If $k_{nr} = 0$ then $\tau = \tau_n$ is the natural or intrinsic lifetime. On one the one hand it can be expressed via radiative decay rate and on the other hand via a measured lifetime and a fluorescence quantum yield (Φ):

$$\tau_n = 1 / \Gamma \text{ and } \tau_n = \tau / \Phi \quad (1-4)$$

The fluorescence quantum yield is the ratio of the number of emitted photons to the number of adsorbed photons. Obeying the energy conservation law it is less than or equal to 1, and can be given by equation:

$$\Phi = \frac{\Gamma}{\Gamma + k_{nr}} \quad (1-5)$$

Fluorescence quantum yield can be calculated from the emission spectrum, when the fluorescence emission spectrum is as follows:

$$\Phi = \int_0^{\infty} F_{\lambda_{EX}}(\lambda_{Fluor}) \cdot d\lambda_{Fluor} \quad (1-6)$$

where λ_{ex} is the excitation wavelength, λ_{Fluor} is the fluorescence wavelength and $F_{\lambda_{EX}}(\lambda_{Fluor})$ is the fluorescence spectrum or emission spectrum (in m^{-1} or in nm^{-1}).

Fluorescence quenching

The fluorescence intensity can be considerably reduced when the fluorescence light passing through the media. The phenomena of fluorescence intensity decrease are called quenching. Different quenching mechanisms such as collision, electron transfer, intersystem crossing, spin coupling are known [31]. Quenching reactions provide valuable information about the location of fluorescent groups in the macromolecular structure. It allows probing of topographical features of macromolecular assembly, and sensing the structural changes in conformational fluctuations.

Considering dynamic quenching, the steady state fluorescence intensity can be expressed as follows:

$$\frac{F}{F_0} = \exp\left(-\frac{t}{\tau_0}\right) \quad (1-7)$$

where τ_0 is the fluorescence lifetime in the absence of quencher.

Fluorescence polarization and anisotropy

Fluorescent molecules effectively adsorb excitation light if electric vector is parallel to a dipole moment of a molecule. In isotropic solution molecule dipoles are randomly oriented. The polarized light excitation will excite molecules which have dipoles parallel to the excitation electric vector. The light emitted by a molecule also has electric vector parallel to the fluorophore dipole moment. During the time between adsorption and emission a molecule moves changing the dipole moment direction. Thus, the selective excitation results in a partially polarized fluorescence emission.

The fluorescence polarization (P) and anisotropy (r) are defined as follows [28,30]:

$$P = \frac{F_{\parallel} - F_{\perp}}{F_{\parallel} + F_{\perp}} \text{ and } r = \frac{F_{\parallel} - F_{\perp}}{F_{\parallel} + 2F_{\perp}}, \quad (1-8)$$

where F_{\parallel} and F_{\perp} are fluorescence intensities of the vertically and horizontally polarized emission for the sample which is excited with vertically polarized light.

Total fluorescence signal $F = F_{\parallel} + 2 F_{\perp}$ can be measured with a fluorescence detection polarizer installed at the angle of $\alpha_0 = 54.7^\circ$ with the excitation polarizer. The angle is also known as “magic angle” [28,30].

The fluorescence anisotropy (see equation 1-8) can be affected by several mechanisms. Fast rotational movements of the fluorophore can easily change the mutual orientation of dipole positions. The angle between the absorption and emission dipole determines the maximum measured anisotropy, fundamental anisotropy value r_0 . Fundamental anisotropy is the intrinsic property of a fluorophore in the absence of any fluorescence depolarization effects.

The effect of fluorophore rotation is described by Perrin equation:

$$r = \frac{r_0}{1 + \tau/\rho}, \quad (1-9)$$

where ρ is the rotation correlation time connected with macroscopic parameters of the sample and depends on the medium viscosity (η), temperature (T), volume of the rotating unit (V) and universal gas constant (R) as $\rho = \eta V / RT$.

For the ensemble of randomly oriented fluorophores having the equal probability for dipole orientation, the anisotropy value is determined by the formula [30]:

$$r_0 = \frac{3 \cos^2 \theta - 1}{5} \quad (1-10)$$

Here θ is the angle of the emission dipole relative to the absorption dipole. As the θ changes from 0 to $\pi/4$, the fundamental anisotropy value changes from 0.4 to -0.2.

1.1.3 Fluorescence resonance energy transfer (FRET)

Resonance energy transfer (RET) is an important phenomena, observed when one molecule (called the donor, D) has the emission spectra which overlaps the absorption spectra of another molecule (called the acceptor, A). Energy transfer from the excited state of the donor to the ground state of the acceptor can happen, and is not the result of the fluorescence emission from the donor molecule and photon absorption of the acceptor, rather the result of the radiationless dipole-dipole coupling of the two fluorophores. This process is known as fluorescence or Förster energy transfer (FRET).

Factors such as the extent of the spectral overlap of the emission spectrum of the donor and the absorption spectrum of the acceptor, the quantum yield (lifetime) of the donor, the relative orientation of the transition dipoles of molecules, and the donor-acceptor distance influence the rate of the energy transfer. Any effect which causes one of these parameters to change can be quantified via FRET measurements. The energy transfer rate is expressed as follows:

$$k_T(R_{DA}) = \frac{1}{\tau_D} \left(\frac{R_0}{R_{DA}} \right)^6, \quad (1-11)$$

where R_{DA} is the distance between donor and acceptor; τ_D is donor lifetime in the absence of acceptor; R_0 is Förster radius, is the distance at which the energy transfer and spontaneous decay are equally probable and $k_T = 1/\tau_D$.

Modern theory of FRET is based on the classical and the quantum-mechanical consideration [32, 33]. It gives the expression for the Förster radius:

$$R_0 = 0.211 \cdot [\kappa^2 n^{-4} \Phi_D J(\lambda)]^{1/6}, \quad (1-12)$$

where dimension R_0 is in Å and λ is in nm; Φ_D is the fluorescence quantum yield of the donor in absence of the energy transfer; κ^2 is the orientation factor, describing the dipoles mutual orientation; τ_D is the fluorescence lifetime of the donor in absence of the energy transfer; $J(\lambda)$ is the spectral overlap integral, defined as follows:

$$J(\lambda) = \int_0^{\infty} f_D(\lambda) \cdot \varepsilon_A(\lambda) \cdot \lambda^4 \cdot d\lambda \quad (1-13)$$

where $f_D(\lambda)$ is the corrected fluorescence emission spectrum intensity of the donor with the total intensity normalized to unity, $\int_0^{\infty} f_D(\lambda) \cdot d\lambda = 1$; $\varepsilon_A(\lambda)$ is the extinction coefficient of the acceptor at λ in $M^{-1}nm^{-1}$ units.

The efficiency of the energy transfer for a single DA pair at a fixed distance is given by the following equation:

$$E = \frac{1}{1 + \left(\frac{R_{DA}}{R_0} \right)^6} \quad (1-14)$$

The transfer efficiency is most typically measured using the relative fluorescence intensity of the donor in the absence (F_D) and presence (F_{DA}) of the acceptor, but can also be calculated from the lifetimes under the same conditions:

$$E = 1 - \frac{F_{DA}}{F_D} \text{ or } E = 1 - \frac{\tau_{DA}}{\tau_D} \quad (1-15)$$

These equations are valid if the DA pair which has a fixed distance. A more complex expression derived for the transfer rate averaging over an assumed spatial R_{DA} distribution is used frequently [28,34].

The last parameter in FRET characterization is the orientation factor κ^2 . It is given by the equation:

$$\kappa^2 = (\cos \theta_T - 3 \cdot \cos \theta_D \cdot \cos \theta_A)^2 = (\sin \theta_D \cdot \sin \theta_A \cdot \cos \phi - 2 \cdot \cos \theta_D \cdot \cos \theta_A)^2 \quad (1-16)$$

where θ_T is the angle between the donor emission dipole and the acceptor absorption dipole, θ_D and θ_A are angles between dipoles and the vector \vec{R}_{DA} , connecting the donor and acceptor; ϕ is the angle between the donor- \vec{R}_{DA} and acceptor- \vec{R}_{DA} planes.

The FRET energy transfer rate, accounting for the orientation, factor will be:

$$k_T(R_{DA}) = \frac{2}{3} \frac{\kappa^2}{\tau_D} \left(\frac{\bar{R}_0}{R_{DA}} \right)^6, \quad (1-17)$$

where \bar{R}_0 is the Förster radius for isotropic dynamic average (freely rotating donor and acceptor at a rate much higher than the transfer rate) κ^2 factor equal to 2/3.

The value of κ^2 can range from 0 to 4. For parallel dipoles $\kappa^2 = 4$, for antiparallel dipoles $\kappa^2 = 1$ and for perpendicular $\kappa^2 = 0$. It is usually assumed $\kappa^2 = 2/3$ which is valid for the random equally probable orientations of donor and acceptor dipoles. Different models of dipole orientations at a timescale of fluorescence lifetime are described in literature [30] and usually resulting in distance estimation errors in the range of 10-35% for $2/3 < \kappa^2 < 4$ and up to 200% for $0 < \kappa^2 < 2/3$.

1.1.4 Fluorescence correlation spectroscopy (FCS)

Fluorescence correlation spectroscopy (FCS) is a technique which allows studying temporal fluctuations in the fluorescence intensity measurements from either several or single fluorophores. A correlation curve analysis reveals information about the processes inducing fluctuations in the intensity of the fluorescence signal [35-37]. Translational and rotational diffusion coefficients, chemical kinetic rate constants, flow rates, molecular weights as well as photophysical and spectral properties of fluorophores can be estimated [31,38-42].

When fluorescent molecules move through a small detection volume, they produce a fluctuating fluorescent signal $F(t)$, with an average value $\langle F(t) \rangle$. The intensity correlation function $G^{(2)}(t_c)$ can be defined as follows:

$$G^{(2)}(t_c) = \frac{\langle F(t+t_c) \cdot F(t) \rangle}{F^2(t)} \quad (1-18)$$

For independent and uncorrelated processes their contributions in the complete correlation curve are additive. The processes with different characteristic timescales can be observed on the correlation curve. The example given in Figure 1-3 depicts a fluorescence intensity signal correlation curve for a system with a translational diffusion, a triplet formation, a rotational diffusion and a photon antibunching.

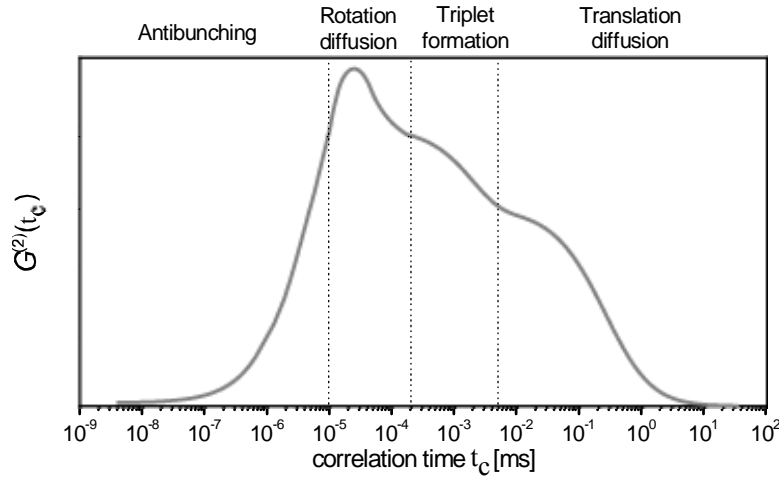


Figure 1-3. Schematic representation of the correlation curve.

Theoretical description of the correlation function shape is based on fluorescence signal represented as $F(t) = kQ \int W(\vec{r}) \cdot C(\vec{r}, t) \cdot dV = kQ \int E(\vec{r}) \cdot CEF(\vec{r}) \cdot C(\vec{r}, t) \cdot dV$, where $C(\vec{r}, t)$ is the concentration of fluorescent particles at a given position and time, k describes the detection quantum efficiency of the detectors and attenuation of fluorescence signal prior to detection, Q is a product of absorption cross section of fluorescent molecules and their fluorescence quantum yield, $W(\vec{r})$ is the function describing detection volume [38]. It depends on experimental conditions and expressed via the spatial excitation intensity profile $E(\vec{r})$ (excitation volume) and the collection efficiency function $CEF(\vec{r})$ (collection volume), which describes the fraction of light emitted by a point source, that passes through the pinhole. The function $CEF(\vec{r})$ depends on the location and the size of the image of the point source with respect to the pinhole. A three dimensional Gaussian shape volume is usually assumed for confocal optical microscopy and is described as follows: $W(x, y, z) = \exp(-2(x^2 + y^2)/\omega_0^2) \cdot \exp(-2z^2/z_0^2)$, where ω_0 and z_0 are distances from the center of the detection volume in radial and axial dimensions respectively, where detected fluorescence has dropped by a factor e^2 [31,37,38].

Experimental correlation curve obtained from fluctuations in fluorescence from freely diffusing particles can be described with the equation [38]:

$$G^{(2)}(t_c) = 1 + \frac{1}{N} \left(1 + \frac{t_c}{t_d}\right)^{-1} \left[1 + \frac{t_c}{t_d} \left(\frac{\omega_0}{z_0}\right)^2\right]^{-1/2}, \quad (1-19)$$

where N is the average number of fluorescent particles, τ_D is the characteristic translation diffusion time, connected with the particles diffusion coefficient D : $\tau_D = \omega_0^2 / 4D$.

For the more complicated case of fluorophore photophysics, in particular the presence of triplet formation, the correlation function would be [40]:

$$G^{(2)}(t_c) = 1 + \frac{1}{N} \left(1 + \frac{t_c}{t_d}\right)^{-1} \left[1 + \frac{t_c}{t_d} \left(\frac{\omega_0}{z_0}\right)^2\right]^{-1/2} \left[1 - T + T \exp\left(-\frac{t_c}{t_T}\right)\right], \quad (1-20)$$

where τ_T is the characteristic triplet correlation time given as $1/t_T = k_T + k_{0I} \cdot k_{ISC} / (k_{0I} + k_0)$; T is the average fraction of molecules in the first excited triplet state $T = k_{0I} \cdot k_{ISC} / [k_{0I} (k_{ISC} + k_T) + k_0 \cdot k_T]$. Here k_{0I} is a ground singlet to the first excited singlet level transition rate, k_0 is the excited singlet to ground singlet level transition rate; k_{ISC} excited singlet to the triplet level transition rate and k_T triplet to ground singlet level transition rate. Triplet decay and intersystem crossing rates can be described in such a manner.

When the timescales of all the effects are at least an order of magnitude different, the correlation curve can be modelled by the product of their respective correlation functions. Translational diffusion, triplet formation, rotational diffusion and fluorescence antibunching effects are included in the correlation function equation as given by [43,44]:

$$G^{(2)}(t_c) = 1 + \underbrace{\frac{1}{N} \left(1 + \frac{t_c}{t_d}\right)^{-1} \left[1 + \frac{t_c}{t_d} \left(\frac{\omega_0}{z_0}\right)^2\right]^{-1/2}}_{\text{translational diffusion term}} \underbrace{\left[1 - T + T \cdot \exp\left(-\frac{t_c}{t_T}\right)\right]}_{\text{triplet term}} \cdot \underbrace{\left[1 + R \cdot \exp\left(-\frac{t_c}{t_R}\right)\right]}_{\text{rotational diffusion term}} \cdot \underbrace{\left[1 - A \cdot \exp\left(-\frac{t_c}{t_A}\right)\right]}_{\text{antibunching term}} \quad (1-21)$$

where R is the rotational fraction of the correlation function amplitude, t_R is a characteristic rotational diffusion time, A is the antibunching fraction of the correlation function amplitude, t_A is the characteristic photon antibunching which reflects the quantum nature of light emission and is defined by the excitation and fluorescence decay rates.

A high signal-to-noise ratio requirement puts some restrictions on experimental conditions, the detection volume assumption and the number of fluorophores in the detection volume [45-49]. No-optimized parameters may result in experimental artefacts and falsify the results [50].

1.1.5 Optical microscopy

The conventional microscope, invented more than four hundred years ago, is a useful tool for a variety of scientific applications. The main function of a microscope is to provide an angular magnification of a selected close object [25,51]. The simplest design is a combination of two thin lenses (objective and eyepiece). A microscope is characterized by the objective lens numerical aperture and the microscope magnification M . The numerical aperture $N.A. = n \cdot \sin\alpha$. It is the product of n , the refractive index of the object medium, and $\sin\alpha$, where α is the half aperture of the imaging optics/objective. The microscope magnification is the product of objective and eyepiece magnifications. New optical microscopy techniques have appeared with the development of lens corrections and coatings, artificial light sources, optical filters and sensitive light detectors [31,52-55].

Optical microscopy resolution

The milestones of optical microscopy were grounded more than a century ago: the diffraction theory of microscopy developed by Ernst Abbe [56,57] helps to define the resolving power of a system of lenses. According to the wave theory of light, a point light source image is never a point, but rather a diffraction pattern, which appears as a bright spot (Airy disk) surrounded with dark and light (or colour) rings. Soon the first criteria (Rayleigh criterion) for the observation of two separate point sources in the image was formulated [25,54,58]: two incoherently radiating points can be separately observed if the distance in the image space between them is equal or larger than the radius (δr) of the first dark ring around the central disk of the Airy diffraction pattern:

$$\delta r = 0.61 \frac{\lambda}{N.A.}, \quad (1-22)$$

where λ is the wavelength of the observed light; $N.A.$ is the numerical aperture of an optical microscope objective lens. Accordingly, the axial resolution (δz) is given by:

$$\delta z = 2n \frac{\lambda}{(N.A.)^2} \quad (1-23)$$

The Rayleigh criterion defines the diffraction limited resolution of conventional optical microscopy in lateral and axial dimensions, and can be expressed by a point spread function (PSF). A point spread function (PSF) is a response of a conventional optical system to a point-size light source.

However, in conventional fluorescence microscopy, excitation light produces a significant intensity within a solid cone angle and results in unwanted fluorescence light

collected by the objective, which lowers signal-to-noise ratio and increases the depth of field, which is ideally equal to the axial resolution of conventional light microscopy.

Confocal microscopy

The optical microscopy depth of field is improved in the confocal optical scheme which was first described by Nipkow and patented by Minsky [59,60]. For confocal microscopy (confocal is defined as “having the same focus”) a microscope condenser is replaced with a lens identical to the objective lens, or the microscope is used in epi-illumination configuration. The next important feature is a use of two pinholes, for the excitation and detection of light, which removes undesired light from solid cone and improves the contrast, depth of field and fluorescence detection signal-to-noise ratio (Figure 1-4).

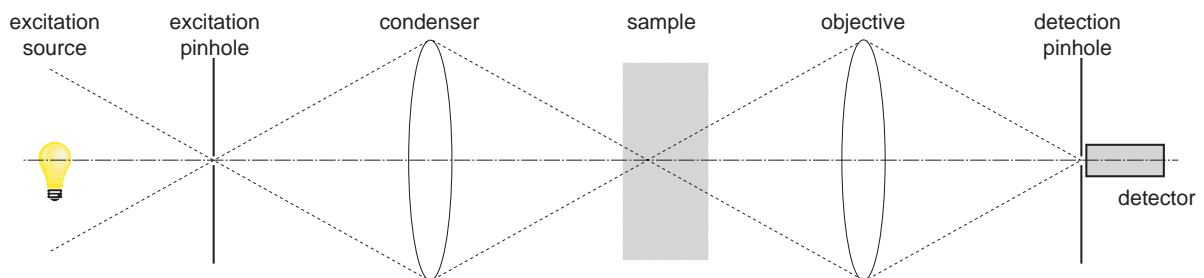


Figure 1-4. Schematic optical path of a simple confocal microscope. Condenser lens forms an image of excitation pinhole in the sample. Objective lens forms the image of excitation spot in a sample on the detection pinhole. The detection pinhole is confocal with this spot in a sample and the excitation pinhole. The optical signal from other points in the sample volume, which are not confocal with the detection pinhole, is attenuated. In the epi-illumination confocal microscope, the condenser and objective lenses are substituted with one lens.

Confocal optical microscopy due to its spatial sectioning capabilities has found a wide range of applications, also in combination with various fluorescence spectroscopy techniques (FCS, single molecule detection). Different questions of instrumentation and performance optimization were studied in details in the past decades [55], and resulted in a number of commercial systems based on the confocal microscope.

1.1.6 Total internal reflection fluorescence (TIRF)

The phenomenon of the total internal reflection of a plane wave at the interface of two media with different refractive indices reveals the field in the vicinity of the interface. The field near the interface might have very high amplitude. TIRF proposes an experimentally simple technique for selective excitation of fluorophores near the surface and has the depth of optical sectioning $\sim 0.1 \mu\text{m}$.

Evanescent field

The term evanescent suggests the idea of something which disappears and fades away. This term is applied to phenomena if something has been generated but nevertheless escapes direct measurement. Newton, who proved the existence of evanescent waves, started evanescent light investigations [61]. First quantitative measurements of these waves were done in 19th century. Some distinctive properties were discovered in the early 20th century. It was discovered that the phenomenon of total internal reflection of light on the border of two media is accompanied by two distinct shifts, lateral and longitudinal. Newton had already predicted the existence of a longitudinal shift and in 1947 F.Goos and H.Hänchen carried out their first experiments demonstrating the existence of this shift [62-64]. This shift corresponds to linearly polarized waves, either in p or s polarization, or any combination of these two polarizations. The existence of a lateral shift and the physics underlying this phenomenon were foreseen by Fedorov [65] in 1955 and experimentally proven by Imbert [66].

Let us consider two media with refractive indices n_1 and n_2 and a plane wave striking the interface between two media at an angle of incidence θ_1 . Axis Z is to be directed from the more refractive medium towards the less refractive medium, while X and Y lie on the interface between the two media (Figure 1-5). The light beam is partially reflected and partially transmitted. Directions for transmitted and reflected beams depend on refractive indices of two media, the incidence angle and they are given by Snell's law [25,67]:

$$n_1 \sin \theta_1 = n_2 \sin \theta_2, \quad (1-24)$$

where θ_2 is the angle of the direction of propagation formed by the refracted beam with the normal to the surface.

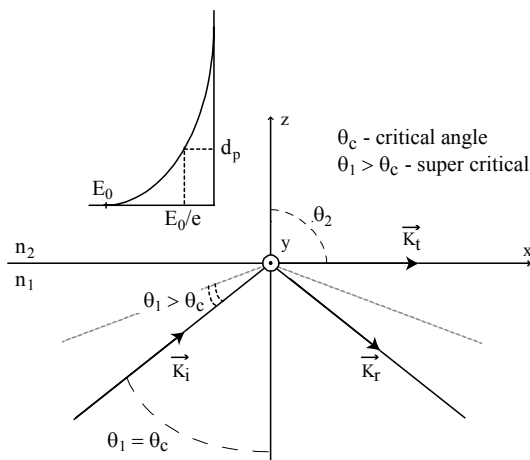


Figure 1-5. A schematic representation of the light propagation at the interface between two surfaces with different refraction indices. The $z = 0$ plane is the plane of incidence. The incident, reflected and transmitted wave vectors are referred to as \vec{k}_i , \vec{k}_r and \vec{k}_t respectively. Insert: variation of the evanescent field amplitude in the second medium. The penetration depth d_p goes from infinity to $\lambda/2\pi\sqrt{n_1^2 - n_2^2}$ as the incidence angle extends from θ_c to $\pi/2$ ("super critical" incidence angles). A few values for the penetration depth angles are presented in Table 1-1.

Depending on the refractive indices ratio, transmitted and reflected light can behave differently. If the value of incidence angle is smaller than $\theta_1 = \theta_c = \arcsin(n_2/n_1)$, the angle

of the refracted ray can be determined by Snell's law. The value θ_c of the incidence angle is referred to as either the "boundary angle of refraction" or as the "critical angle". If the incidence angle exceeds the value of the critical angle, the light can no longer propagate within the second medium, and is therefore totally reflected. However, light waves can still be detected in the second media close to the interface. Considering the case of total internal reflection, the incidence angle θ is greater θ_c .

Detailed analysis of TIR could be performed using the Maxwell's formalism for electromagnetic waves, which reached the interface between these media. Relationships between amplitudes of incident, reflected and transmitted waves at the boundary of two transparent isotropic media are given by Fresnel formulas [25,31].

The intensity of the electric field at $z = 0$ depends on the value of the incidence angle. The maximal value for the intensity at a glass/water interface is reached at a value of incidence angle equal to the critical angle θ_c and almost equal for two light polarizations. A different effect occurs if an intermediate layer of thin metal film (≈ 20 nm and almost opaque to the eye) exists between two dielectric media. The s – polarization intensity becomes negligibly small. However, the p – polarization of evanescent intensity at a certain angle θ_p becomes an order of magnitude brighter than the incident light at the peak. This resonance-like effect is due to excitation of a surface plasmon mode at the metal/water interface. The peak is at the "surface plasmon angle", due to resonant excitation of electron oscillations at the metal/water interface [31].

The amplitude of the electric field (E) decreases exponentially as the distance (z) from the interface increases (Figure 1-5). The confinement of the evanescent field in the vicinity of the interface is expressed by the parameter d_p . The value of the parameter d_p reflects the decrease of the evanescent field amplitude when the distance to the interface increases and defined as the distance required for electric field amplitude to fall to e^{-1} of its value at the surface.

$$E = E_0 \cdot e^{-z/d_p}, \quad d_p = \frac{\lambda}{2\pi\sqrt{n_1^2 \sin^2 \theta - n_2^2}} \quad (1-25)$$

Table 1-1. Values of the penetration depth of the evanescent field in different configurations.

Wavelength (nm)	First medium refractive index	Second medium refractive index	θ_c (degrees)	θ (degrees)	d_p (nm)
496	glass: 1.458	air: 1	43.30	45	315
496	glass: 1.458	water: 1.33	65.81	85	135
496	oil: 1.515	air: 1	41.30	85	70
496	oil: 1.515	glass: 1.458	74.23	85	202

TIR realization

TIR could be realized in various ways, which can basically be divided into two classes: 1) TIR with prism and 2) prismless TIR [31,68].

The key element for the first type is an optical element, a prism that permits the incident laser light beam to strike the TIR interface. The prism is usually placed in contact with glass via a drop of immersion oil and excitation light is directed through the prism onto the glass/water interface (Figure 1-6 a,b).

For the second class of TIR realization an objective with a high numerical aperture is used. A supercritical angle incident light can be cast upon the sample by epi-illumination through such the objective (Figure 1-6 c,d). The critical angle for TIR for a glass/water ($n_2 = n_g = 1.5$ and $n_1 = n_w = 1.33$) is $\theta_c = 61.4^\circ$. The maximal angle θ_m that light rays (emerging from the objective) can form with the normal to the sample depends on the numerical aperture N.A. of the objective: $N.A. = n_g \sin\theta_m$. Only those rays that propagate at angles greater than the critical angle will produce an evanescent field at the TIR interface. Since the condition for TIR is $\sin\theta_m > \sin\theta_c$, that means $N.A. > n_w$. For N.A. = 1.4 objective $\theta_m = 67.5^\circ$. Therefore the light in the range of angles between 61.4° and 67.5° will create an evanescent field.

The angle with which a ray emerges from the objective into the immersion oil and glass coverslip depends on its radial position from the optical axis as the ray passes the back focal plane (BFP) inside the objective. One way to create TIR via microscope objective is based on the radial laser beam shifting from the axis to a super critical angle range $\theta > \theta_c$ (Figure 1-6 c). Selective exclusion of subcritical angle ($\theta < \theta_c$) illumination light could be accomplished by placing an opaque disk of appropriate radius at the BFP. Since this plane is practically inaccessible, the opaque disk could be located in the excitation path outside the microscope at the unique fixed plane equivalent to the BFP. This plane is equivalent in terms of rays intersecting and is known as the equivalent BFP (=EBFP). The available super critical angles values of a microscope objective are usually limited by the numerical aperture.

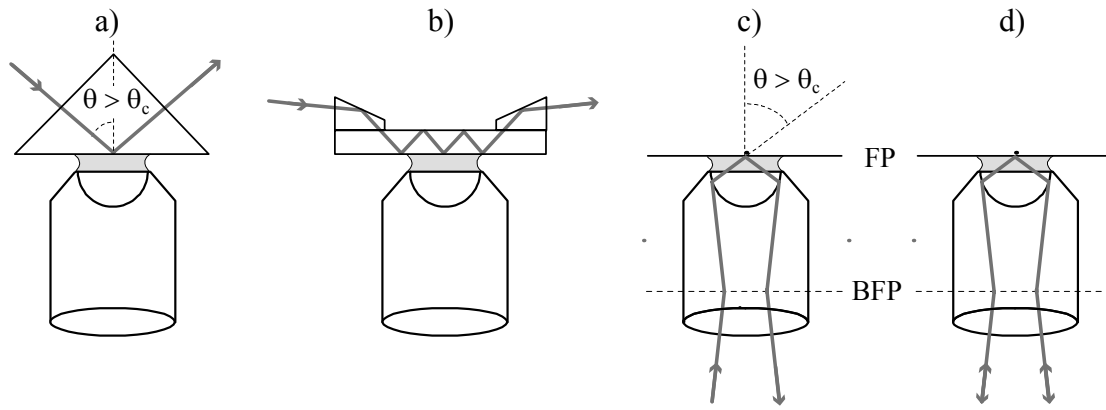


Figure 1-6. Optical arrangement for several TIR configurations: a,b – prism based and c,d – prismless. BFP is a back focal plane of the objective which has equivalent back focal plane (EBFP) outside the microscope. FP is a field diaphragm plane. Any sharp feature in EBFP will form sharp image in BFP and in FP accordingly.

1.1.7 Single molecule multiparameter fluorescence detection (smMFD)

Advances in photon detector manufacture make it possible to register single photons. Such sensitivity permits a single molecule fluorescence observation. Spatial separation of fluorescence molecules is one of common methods used in single molecules fluorescence detection [2,3]. Sufficient spatial separation can be obtained for optical microscopy detection by diluting the sample to \sim nM concentration. Here, individual photon detection is done by a time correlated single photon counting (TCSPC) technique [69,70].

Time correlated single photon counting (TCSPC).

TCSPC is a well established technique based on time measurements of detected single photons with respect to the excitation pulse. A reverse TCSPC mode is usually used for the fluorescence detection where a detector is connected to the start input and excitation light source synchronization pulses to the stop input of analysis electronics. Providing a negligible dead time of the electronics this mode allows counting of all fluorescence photons which are much less frequent than excitation pulses.

TCSPC electronics consists of several discrete or integrated modules as presented in Figure 1-7. A constant fraction discriminator (CFD) is necessary for the arrival times of the input pulses to be independent of their height and shape. A time-to-amplitude converter (TAC) measures the time interval between pulses to its start and stop inputs and generates an analog output pulse proportional to the measured time. It serves as a fast clock which starts with the photon arrival and stops with the next laser pulse arrival. An analogue to digital converter (ADC) determines the time between start and stop pulses and defines the measurement quantization. These data as well as the information about the number of pulses

are stored in first-in-first-out (FIFO) memory buffer and then on a hard drive of a personal computer (Figure 1-8).

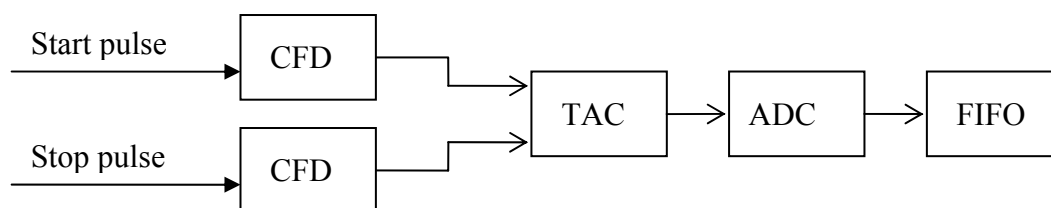


Figure 1-7. TCSPC signal proceedings diagram.

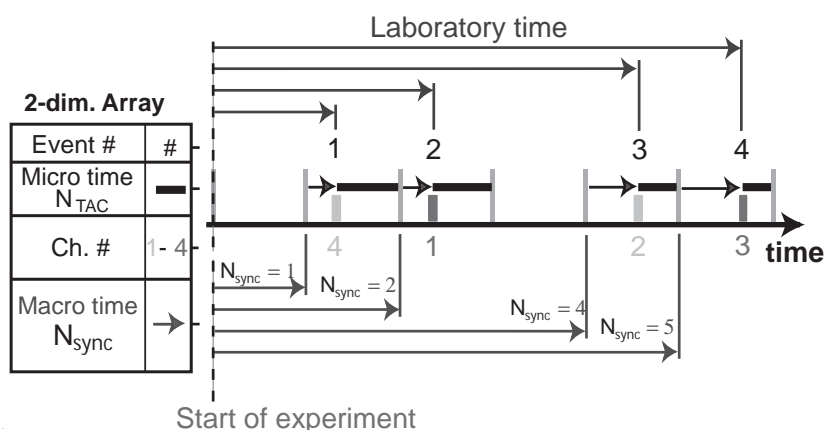


Figure 1-8. TCSPC data structure. For each detected pulse (event #) a micro time (TAC channels number N_{TAC}), a macro time (Stop pulses number N_{SYNC}) and a detection channel number are recorded.

Multiparameter Fluorescence Detection

The approach of Multiparameter Fluorescence Detection (MFD) is based on TCSPC technique and provides the information about the properties of a fluorophore that can be accessed in a fluorescence experiment: absorption and fluorescence spectral properties, fluorescence quantum yield, fluorescence lifetime and anisotropy [71].

Each detected photon is characterized by four parameters: (1) spectral range, λ_F , of the detected fluorescence (green or red); (2) the polarization of the light (parallel or perpendicular) with respect to the linear polarization of the excitation laser; (3) the arrival time of the signal photon relative to the incident laser pulse; and (4) the interphoton time Δt . Different detection channels represent different spectral ranges and polarizations.

The selection of single molecule fluorescence events (bursts) is realized in subsequent analysis of fluorescence intensity traces (Figure 1-9). In single molecule MFD, single molecule diffusing through the detection volume is characterized by a small interphoton time. Fluorescence intensity with a drop of Δt below a chosen threshold value is classified as a

fluorescence burst and is used for a further data analysis. For each burst, the average green and red count rates, S_G and S_R , are calculated by dividing the number of registered photons by the duration of the burst. The photon arrival time is used to generate a fluorescence decay histogram for each of the four detectors (green parallel, $g_{||}$, green perpendicular, g_{\perp} , red parallel, $r_{||}$, red perpendicular, r_{\perp}) in each spectral range. Decay histograms of parallel and perpendicular polarized signal are used to calculate the anisotropy r and to characterize the decay properties. A maximum likelihood estimator based fit routines [72,73] is used for fluorescence lifetime and anisotropy estimation by a fit to a single exponential convoluted with the instrument response function. At the same time each fluorescence burst can be subdivided into time windows and similar analysis can be performed within a time window [41,74-76]. Fluorescence parameters can be displayed on two-dimensional histograms, which provide a flexible tool for the data selection and analysis. The application of MFD to FRET analysis will be discussed in details in experimental section (Section 2.5)

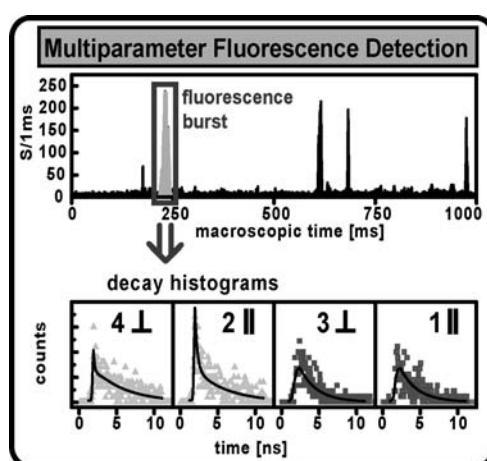


Figure 1-9. Illustration of MFD technique. Fluorescence traces are obtained reconstructing the photon arrival time information recorded via TCSPC. Fluorescence bursts are selected from fluorescence signal traces for further burstwise or burst time window analysis. Decay histograms can be calculated for different detection channels and fitted to obtain fluorescence lifetime and anisotropy values.

1.2 Atomic-force microscopy

This Section is an introduction to a relatively new scanning probe microscopy technique: the atomic force microscopy (AFM). It describes the principles of atomic force microscopy and gives detailed description of AFM technical realizations and AFM imaging modes.

1.2.1 The atomic-force microscope

Scanning probe microscopy

Scanning probe microscopy (SPM) began in the early 1980s with Binnig's and Rohrer's invention of the scanning tunnelling microscope (STM) [77,78]. This discovery led to them receiving the Nobel Prize in Physics in 1986. The STM was the first probe microscope, which senses the structure of a surface by scanning it with a sub micron size probe and measuring some form of interaction between it and the surface.

SPM allows acquiring 3-dimensional images of surface topography and surface properties with high precision and subatomic spatial resolution [79,80]. SPM is relatively simple to realize and it has enormous applications. It is effectively used for surface investigations in various scientific disciplines from physics and chemistry to biology and medicine. Probe microscopy techniques are implemented in two configurations: scanning the sample relative to the probe or probe relative to the sample. While scanning, forces acting between atoms as well as electrostatic forces, magnetic interactions, temperature gradients and optical signal intensity can be detected [81-85]. These signals are also used for a feedback.

Atomic-force microscopy

Atomic-force microscopy (AFM), or scanning force microscope (SFM), is one type of SPM. In 1986 Binnig and colleagues announced the atomic-force microscope [86] based on the detection of local forces acting between the tip of the probe and the sample surface (Figure 1-11). Forces of different types (see Section 1.2.2) dominate at different probe-surface distances (Figure 1-12).

A schematic representation of the AFM is given in Figure 1-10. In general an AFM consists of a force sensing probe or a cantilever (1), a coarse approach system (2) which brings the sample (6) and the probe closer, a fine positioning system (3), a cantilever deflection sensor (4) and controlling electronics (5).

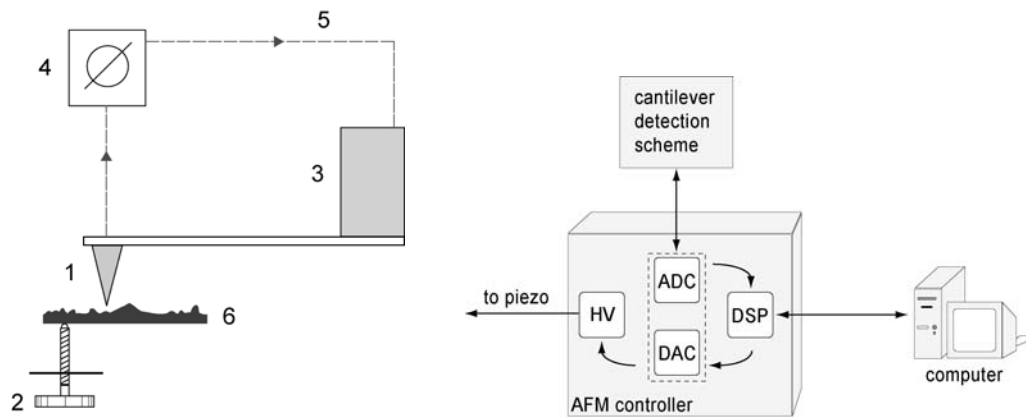


Figure 1-10. Left: Schematic representation of a scanning probe microscope; 1 – a cantilever tip, 2 – system of rough approach, 3 – fine positioning system (AFM piezo), 4 – a cantilever position sensor, 5 – a feedback loop, controller and computer, 6 – sample. Right: principle scheme of AFM electronics. DSP - digital signal processor, DAC – digital to analogue converter, ADC – analogue to digital converter, HV – high voltage amplifier.

The AFM works in the following way: using the system of coarse approach (2) the cantilever (1) is brought close to a sample (6). As the cantilever “senses” the desired interaction force with the surface or jumps into contact with the surface the feedback loop (5) passes the position control to the piezoscanner (3). The probe position is monitored during the coarse approach by the position sensor (4). The deflection detection scheme is described in details in Section 1.2.8. An analogue to digital converter (ADC) quantizes the signal provided by the deflection detection part and transfers it to a digital signal processor (DSP). The DSP is responsible for a signal processing and calculations during the real-time AFM operation. A digital to analogue converter (DAC) transfers a control signal from the DSP to a high voltage (HV) amplifier, which amplifies the control signal and drives the piezoelectric scanner. In such a manner the control loop or the feedback (5) is provided.

When the tip and the surface are in operation regime, the piezoscanner can perform two dimensional sample scans and cantilever translations perpendicular to the sample (see Section 1.2.3). The control loop keeps the predefined scanning conditions by adjusting the cantilever Z position.

1.2.2 Forces (Van der Waals force, capillary force, adhesive forces, double layer forces)

The force acting between the AFM cantilever and the surface is defined by the interaction potentials between atoms of the tip and atoms of the surface (Figure 1-11). Different interactions dominate at various distances from the sample and influence the interaction potential. The theoretical treatment of interaction forces assumes the tip consists of one to a few rigid atoms. Nearest neighbour atoms on the surface influence the tip. The total

potential is assumed to be the sum of two-body potentials. The interaction potential for a single atom tip is given by the following equation:

$$U(\vec{r}_1 \dots \vec{r}_N) = \sum_i V(\vec{r} - \vec{r}_i) + \bar{V}(\vec{r}_1 \dots \vec{r}_N), \quad (1-26)$$

where $V(\vec{r} - \vec{r}_i)$ is the interaction potential between the tip atom and the i -th atom of the surface and $\bar{V}(\vec{r}_1 \dots \vec{r}_N)$ is the many-body potential in the absence of the tip. The vectors \vec{r}_i and \vec{r} denote the position of the i -th atom in the sample and the position of the tip respectively.

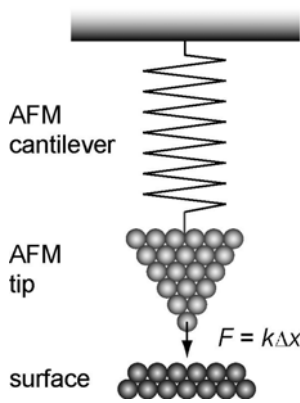


Figure 1-11. The AFM cantilever can be modelled as a force sensitive spring.

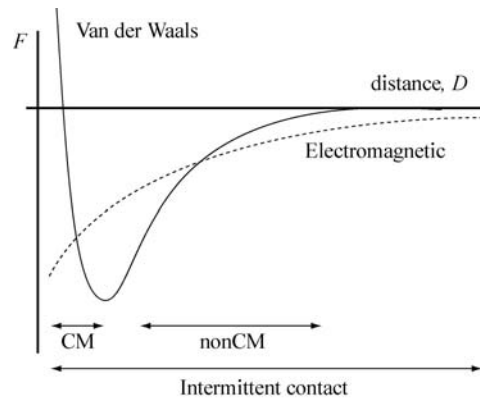


Figure 1-12. The qualitative curve for the interaction potential between two atoms. This curve has been calculated using a Lennard-Jones potential. Different imaging modes (contact, non contact and intermittent contact modes) are accessible at different distances.

The interaction is attractive at large distances and repulsive at small distances. *Van der Waals interactions* have main influence at small distances and it is described semi-quantitatively by the Derjaguin, Landau, Verwey and Overbeek (DLVO) theory [87]. According to this theory the asymmetry of the electronic charge distribution around the atom, fluctuates on small timescale and leads to subtle charge imbalances known as ‘dipoles’ and ‘multipoles’. The charge distribution causes forces to be attractive or repulsive. The potential energy $E(r)$ can be described mathematically by a “Lenard-Jones” function:

$$E(r) = 4\varepsilon \left[\left(\frac{\sigma}{r} \right)^{12} - \left(\frac{\sigma}{r} \right)^6 \right], \quad (1-27)$$

where ε is the dielectric constant of the surrounding medium and σ is approximately equal to the diameter of the interacting atoms and is known as a “hard sphere diameter”. Van der Waals forces present for all, even for electrically neutral, materials. At the distances $r < \sigma$ atoms strongly repel each other. At distances $r > \sigma$ attractive forces dominate, and at much

larger distances $\sigma \gg r$, Van der Waals forces are completely masked by much stronger electrostatic forces (Figure 1-12). A detailed description of interactions can be found in the book of Israelachvili [87].

Electrostatic interactions are present in ionic bonds and have the largest physical influence of any intermolecular forces. Two charges at a distance r in vacuum will interact with the Coulomb force. Two oppositely charged ions brought close show an attractive interaction force.

Double layer forces usually arise when imaging in solution. Charged surfaces can attract oppositely charged ions from solution and cause them to cluster at the interface, creating charged layers or “ionic atmospheres”. The characteristic distance is known as “Debye length” (λ) indicates the distance from the surface where the potential (ϕ) is e times smaller than the potential at the surface (ϕ_0). The double layer effect for the tip can be reduced by adding a small quantity of divalent metal salt (mM) to the imaging liquid.

Capillary and adhesive forces become apparent in tip-surface interaction. The water present in air condenses on a small radius of curvature tip (typical AFM tip radius of curvature is around 10-30 nm). In addition to water condensation on the tip, water will condense on the surface even at normal relative humidity. As a result the tip will be pulled towards the surface by a strong liquid meniscus giving rise to “capillary force”. This force is independent of the instrument settings and cannot be easily compensated and hence can destroy or move the sample on the surface.

With time the tip can be contaminated with small amounts of the sample or become blunted. These effects lead to a greater contact area between the tip and the surface and thus an adhesive force can appear. This is especially critical when studying small objects and molecules which can be damaged by high forces.

1.2.3 Imaging and imaging modes (contact dc mode, non-contact ac mode)

AFM imaging is realized via scanning the sample surface with the tip. The piezo scanner changes the position of the tip relative to the sample in the XY-plane (sample plane) in one of the following ways:

- the tip moves along the first scan line in X direction and back, then it shifts one step in the perpendicular Y direction, moves along a new scanning line and back, and finally it shifts one more step in Y direction (Figure 1-13, A).

- the tip moves along the first scan line in X direction, then it shifts one step in perpendicular direction (Y direction), moves along a new scanning line back, shifts one more step in Y direction (Figure 1-13, B)
- the tip moves along the scan line in X direction, at the same time moving much slower in perpendicular Y direction. At the end of the line it moves back in X direction continuing slow movements in Y (Figure 1-13, C).

The trajectory of the raster scan can also be different and for some systems programmed according to the requirements of the particular experiment.

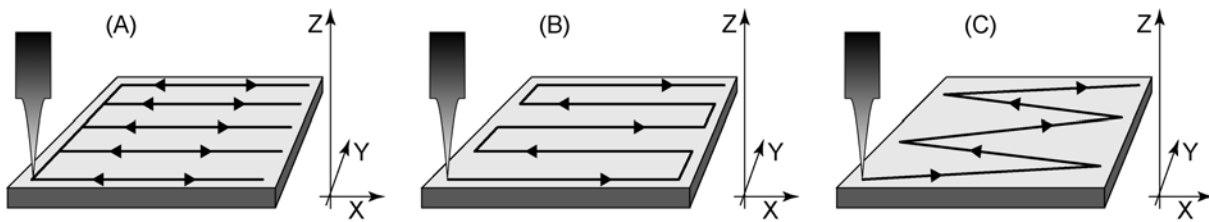


Figure 1-13. Raster scans of the tip over the sample surface using a piezoscanner.

During the scanner movement along the scanning line data are digitized at equidistant intervals. The interval between two points is called a *scanning step size*. The step size is defined by the full scan range and the number of digitalization points per scan line. The digitized signal is used to reconstruct the topography of the sample and as an input in a feedback circuit.

Depending on the scanning conditions (tip distance to the surface and thus main acting forces) different AFM modes are distinguished (Figure 1-12). AFM scanning can be divided into contact, non-contact and intermittent contact modes.

Contact imaging mode

The contact imaging mode is realized in the repulsive force regime (Figure 1-12). In contact mode the tip is brought into physical contact with the sample. Two imaging modes may be distinguished by the selected feedback loop, *constant height* mode and *constant force* mode (Figure 1-14).

In *constant height* mode, the feedback is disabled and the scanner height in Z direction is constant. As a result, the deflection of the cantilever depends on the surface roughness. This limits the variety of samples suitable for studies in this mode and puts requirements for the mechanical properties of the cantilevers. In case of rough surfaces stiff cantilever (with big spring constant) can be damaged. The scanning speed depends on the resonance frequency of the cantilever. This mode is usually used for atomic-scale imaging of flat surfaces.

In *constant force* mode, the deflection of the cantilever is input into a feedback loop. The scanner moves in the vertical direction responding to topography changes in a way which keeps the cantilever deflection (and therefore the tip-surface interaction force) constant. Typical tip-surface interaction forces for contact mode range from 10 pN – 10 nN. The scanning speed is limited by the response of the feedback loop and piezo resonance.

In contact mode, the cantilever can also be twisted along its long axis (lateral deflection). Twisting is caused by surface friction properties or by extensive slopes on the surface.

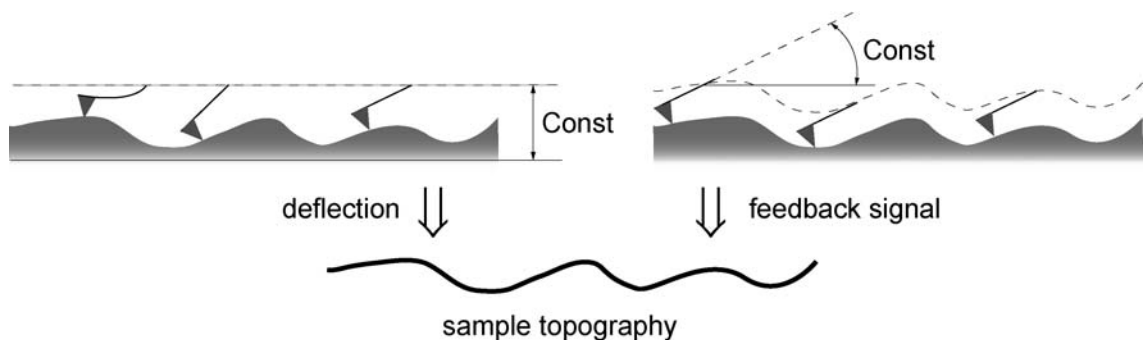


Figure 1-14. Schematic illustration of constant height (left) and constant force (right) AFM imaging modes. Deflection of the cantilever or feedback signal is used for sample topography reconstruction correspondingly.

Non-contact imaging mode

The non-contact imaging mode is realized in the attractive force regime (Figure 1-12). In this imaging mode the cantilever is positioned above the surface and long range interaction between the tip and the surface are determinant. Constant height (feedback loop is active) and constant force/deflection (feedback loop is not active) modes are also available in non-contact imaging. Usually, in non-contact mode the cantilever is forced to oscillate close to its resonance frequency. Then the raster scanning is performed slowly enough that in each pixel in the image the cantilever performs many oscillations. Long range interactions between the tip and the surface change the oscillation amplitude, the resonance frequency or the phase of the cantilever oscillations. A feedback loop is used to keep the chosen parameter constant and to control the scanner movement in vertical direction.

Intermittent contact (tapping) imaging mode

Intermittent contact mode is used to eliminate lateral forces (drag and friction) between the tip and the surface and to minimize the sample damage. In this mode the cantilever oscillates above the surface and periodically comes into contact with it for a short time (tapping on the surface). The image is reconstructed from the changes in the cantilever's oscillating amplitude. Forces from the cantilever acting on the surface are usually of the order of 10 pN.

1.2.4 Cantilevers (geometry, tip shape, mechanical properties)

The part of the AFM which actually probes the surface is the tip (Figure 1-15, Figure 1-16). The tip is mounted on the cantilever.

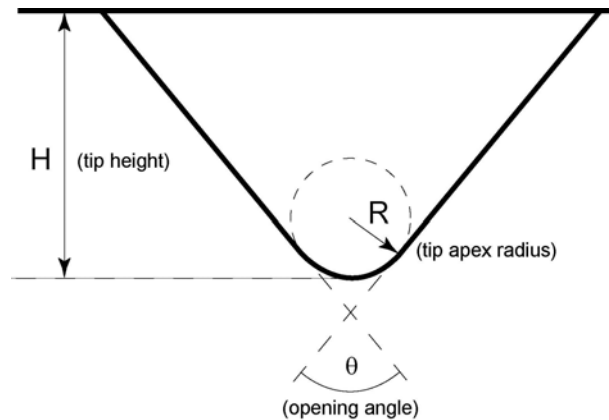
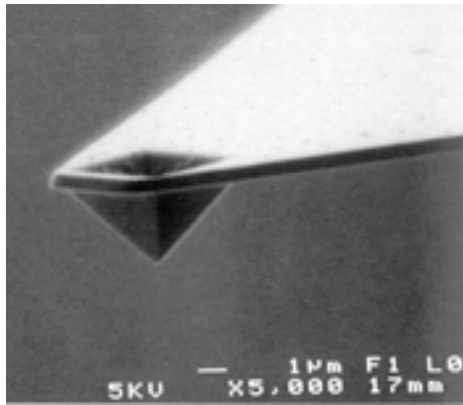


Figure 1-15. Electron microscopy image of an AFM cantilever and the tip. (Picture from www.di.com)

Figure 1-16. Schematic representation of a cantilever tip, showing the main parameters of pyramidal shape tips.

First AFM sensors were platinum foil cantilevers with a sapphire needle glued to it. Till the first commercial AFM appeared in 1990 there was no mass production of cantilevers. Nowadays cantilevers are produced by various companies using the selective anisotropic etching technology. The most commonly used materials are silicon (Si), silicon oxide (SiO_2), and silicon nitride (Si_3N_4) [88,89]. For the reflectivity enhancement and for better surface mechanical properties cantilevers can be covered with the thin metal film of gold (Au), silver (Ag) or chromium (Cr) on one or on both sides [90]. Such metal films can also be made to have magnetic properties, which is used in some AFM modes.

The shape of the cantilever tip is important for particular applications and influences the quality of the AFM images. The *aspect ratio* is defined by the ratio of the tip height to the tip base and usually characterized by the opening angle of the apex of the tip (Figure 1-16). A high aspect ratio tips have small opening angles. The tip aspect ratio defines the depth of field in atomic-force microscopy (see Figure 1-17). Larger depths of field can be obtained with high aspect ratio tips. A large depth of field is usually required for imaging rough samples. Another parameters of the cantilever tip which influences the resolution ability is a *tip sharpness* (R) (Figure 1-16). The sharpness of the tip is defined by the tip apex radius and varies from 2 to 10 nm.

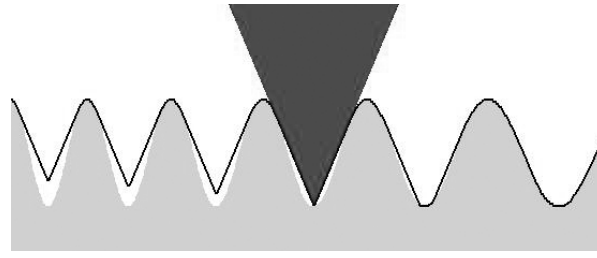


Figure 1-17. Schematic representation of depth of field in force microscopy. The black line represents the reconstructed surface topology. A given tip aspect ratio does not allow probing features placed close to each other. The picture is generated with the free ProbeSimulator. (www.nanoscience.com/education/software.html).

There are various methods for tip fabrication and tip parameters control such as oxidation and ozone sharpening. A sharp cantilever tip can be fabricated connecting a thin and long needle to a normal tip. Such a long needle can be a carbon nanotube or a tip, grown from carbon or other organic materials.

The image obtained by AFM is a convolution of real surface topography with the shape of the cantilever. Reconstruction of the real surface topography from the obtained image is a mathematically complicated inverse problem, even with the known shape of the tip [91,92]. Ultimate resolution can be obtained with a sharp tip and proper imaging conditions.

Cantilevers usually are of two types, rectangular and triangular (V-shape). The mechanical properties of the cantilevers are defined by the fabrication material, geometry and size of the cantilever. These parameters define *stiffness coefficient* or *spring constant* (k) and *resonance frequency* (ω_0) of the cantilever as illustrated in Table 1-2 [93].

Table 1-2. Mechanical parameters of AFM cantilevers of different shape

	Rectangular	V-shaped
<i>Spring constant</i> (k)	$k = \frac{E w \cdot t^3}{4 l^3}$	$k = \frac{E w \cdot t^3}{2 l^3}$
<i>resonance frequency</i> (ω_0)	$\omega_0 = 0.162 \sqrt{\frac{E}{\rho}} \frac{t}{l^2}$	$\omega_0 = a \sqrt{\frac{E}{\rho}} \frac{t}{l^2}$

where E is the Young modulus, ρ is the density, w , t , l are the width, thickness and length of the cantilever respectively, h is the height of the cantilever tip and a is a parameter, dependent on the shape of the cantilever and is usually varying between 0.194 and 0.284.

The choice of a cantilever with particular mechanical properties depends on experimental requirements and the operation mode. Spring constant, resonance frequency, cantilever material and coating, the size and the shape of the tip should be optimized to provide reasonably quick, stable and non-destructive imaging.

The response time of the cantilever in non-contact mode during the scan is limited by its *resonance frequency* (ω_0). If the resonance frequency is too low in comparison to the scanning speed then the cantilever will not be able to respond to changes and image artefacts would appear. The description of the cantilever oscillations is based on the simple harmonic oscillator (SHO) model. Hence, the cantilever's resonant frequency for SHO is defined as follows:

$$\omega_0 = \sqrt{\frac{k}{m}}, \quad (1-28)$$

where k is the cantilever spring constant, m is the mass of the cantilever.

The *spring constant* (k) defines the stiffness of the cantilever. A stiffer cantilever is a cantilever with a high spring constant. A stiff cantilever pushes into a sample with a high force.

The higher the resonance frequency of the cantilever the better the time resolution of the processes being probed. Stiff cantilevers are useful for scribing the surface and for moving particles on the surface. Most biological samples cannot survive the high forces, hence soft cantilevers, with small spring constants are required. However, as we see from the equation 1-28, low spring constants result in low resonance frequencies, and correspondingly in lower imaging speeds. Low speed places a practical limit on the types of experiments that can be performed - the dynamics of a sample, usually relevant for biological samples could not be revealed.

The operation environment, the cantilever's internal friction and mechanical hysteresis lead to a cantilever damping. The damping which is caused by external forces acting on the cantilever can be characterized by a *damping constant* (γ) and a cantilever *quality factor* (Q) as follows:

$$\gamma = f / 2m \quad (1-29)$$

$$Q = \frac{\sqrt{\omega_0^2 - 2\gamma^2}}{2\gamma} \quad (1-30)$$

Here f is the velocity coefficient entering the equation for the frictional force $F_{friction} = -f \cdot \dot{x}$ and m is the cantilever mass¹. The motion of the cantilever can be described analogously to the Brownian particle motion leading to the classical solution [94,95]. The position of the cantilever is described by the Langevin equation 1-31:

¹ \dot{x} stands for first the time derivative of the value x whereas \ddot{x} stands for the second time derivative.

$$m\ddot{x} + f \cdot \dot{x} = F_{th} \quad (1-31)$$

The spectral density $F_{th}^2(\omega)$ of a random force F_{th} is given by the following equation:

$$F_{th}^2(\omega) = 4k_B T \cdot f \cdot \Delta\omega, \quad (1-32)$$

where k_B is the gas constant, T is the temperature and $\Delta\omega$ is the bandwidth.

A damped SHO can be described by adding an additional term representing a Hook's law force ($F_{spring} = -kx$) into the Langevin equation:

$$m\ddot{x} + f \cdot \dot{x} + kx = F_{th} \quad (1-33)$$

Replacing $x(t)$ with $x(\omega) \cdot e^{i\omega t}$, the Langevin equation 1-33 can be solved in the frequency domain and provides the solution for the probability distribution density of the cantilever deflection:

$$x^2(\omega) = \frac{4k_B T \cdot f \cdot \Delta\omega}{(k - m\omega^2)^2 + f^2 \omega^2} \quad (1-34)$$

In the approximation of a small velocity damping ($\gamma \ll \omega_0$) the quality factor (equation 1-30) becomes $Q = m\omega_0 / f$. Equation 1-34 can be rearranged substituting f with Q and taking into account equation 1-28:

$$x^2(\omega) = \frac{4k_B T \cdot \Delta\omega}{k \cdot Q \cdot \omega_0 \left[\left(1 - \frac{\omega^2}{\omega_0^2}\right)^2 + \frac{\omega^2}{Q^2 \omega_0^2} \right]} \quad (1-35)$$

A high quality factor is wanted in AFM imaging, because the damping broadens and diminishes the resonance frequency peak and causes a reduction the resolution. Operation in a fluid immediately damps a high-Q cantilever. There are currently two approaches to compensate for this. The first approach is to use tiny cantilevers. The small cantilever size results in a lower profile, and therefore less damping in fluid. Furthermore, the smaller size cantilevers have spring constants similar to the standard cantilevers, but much lower mass, resulting in high resonance frequencies (see equation in Table 1-2). Small cantilevers are, however, more difficult to use experimentally. The second approach is to use an active control (Q-control) [96]. This approach is valid when the cantilever is driven into higher amplitude resonant oscillations. Under this condition the motion of the cantilever and the effects of viscous damping are predictable. A second driving frequency is applied with the help of additional piezo to the cantilever. The frequency is exactly designed to cancel the effect of damping, in such a way simulating an undamped cantilever.

Cantilevers available on the market have spring constants varying in the range of 0,005 - 200 N/m and have resonance frequencies between 1 - 400 kHz. In practice, however, values

specified by a manufacturer can be significantly different from calculated values due to difficulties in cantilever thickness estimation and the average density of the cantilever. For the accurate estimation of the spring constant of the cantilever one has to perform a spring constant calibration, which will be described below in details (see Section 1.3.2).

1.2.5 Piezo scanner (materials, construction, creep, drift, sensors)

The AFM piezoscanner is the main part of an AFM. It provides a rigid assembly and a displacement control down to picometers. Scanners usually are made of polycrystalline piezoelectric materials. Polycrystalline piezoelectric is a solid matter, which has crystals of ferroelectric. An important property of such ceramics is a piezoelectric effect: a crystal changes the shape if the opposite faces of the piezoelectric crystal are subjected to a difference in the electric potential.

Fabrication of ferroceramic materials includes agglomeration of pressed powder of the ferroelectric polycrystal material, machining, electrodes attachment and material polarization. Polarization is achieved by applying strong electric fields to electrodes on the ferroelectric material for a time long enough to reorient most of the ferroelectric domains and to create a stable domain structure in the material. To enhance domain mobility and to decrease the polarization process time a temperature rise can be used.

A piezoscanner consists of hollow piezotubes, providing three independent scanning directions over the sample surface (Figure 1-18). Scanning is controlled by applying voltages to the electrodes mounted to internal and external faces of the tubes. The external tube face is split into quarters parallel to the axis in order to make the tube bending more pronounced and improve the scanning range. Known problems with a piezoscanner are: (a) scanning speed limitation due to piezoceramics microstructure and resonance frequency; (b) the unmounted scanner side is moved in a sphere-like manner rather than in a plane. That can either be corrected by the AFM software or a more complicated scanner design can be used. Piezoscanners can also exhibit undesired effects resulting in scanning artefacts such as hysteresis, creep, aging and non-orthogonally of the scanner.

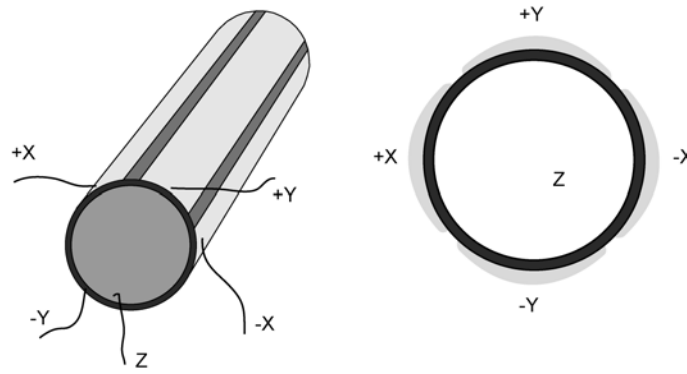


Figure 1-18. AFM piezoscanner assembly. A voltage applied to control electrodes on the piezotubes causes the piezo to move.

Hysteresis is a property of piezomaterials which is observed when the piezo extension does not instantly follow the applied voltage, but reacts slowly, or does not return completely into the initial position as the voltage is released. The hysteresis is almost negligible for small displacements and depends on the voltage change rate.

Also *creep* can affect positioning and displacement of the piezo. It usually reveals as piezo position displacement under constant stress and on longer timescales.

Non-linearity can be observed for any geometry of the piezo movements and appears as non-linear relation between the applied voltage and the actual piezo displacement.

Nonorthogonality of the scanner means applying the voltage on Z electrodes of the scanner will not only extend and compress the scanner, but may also lead to deflection in X-Y plane and vice versa. Nonorthogonality can be caused by either piezotubes geometry defects and polarization heterogeneity of the piezotubes or electrodes defects.

Modern AFM piezoscanner is usually equipped with a closed-loop feedback system which is based on additional position sensors to monitor the true displacement of the piezo. Its primary goal is to provide the correction of the piezo motion.

Finally, the characteristics of piezoelectric materials change with time due to thermal movements of ferroelectric domains in the domain structure. Constant use of the piezoscanner helps to prevent this process which is also known as *aging*.

Using AFM and studying the surface structure one need to extract quantitative information about surface topography. This generally requires calibration of the instrument. Structures with well-known dimensions of the surface features are usually used as calibration standards. These could be diffraction grids, specifically fabricated three dimensional structures, crystals, etc. Well defined test structure allows calculating correction coefficients from actual measurements. A piezoscanner calibration has to be done regularly to eliminate aging effects.

1.2.6 Coarse approach system

The main requirements for coarse approach system are stability and a big enough lag, that a feedback loop and piezo are able to stop the coarse approach when the piezo is in its working regime. Many mechanical devices can fulfil these requirements such as automatic motor and micrometer screw.

1.2.7 Sample holder, liquid cell

The AFM has found a wide range of applications due to its ability to operate under various conditions and in particular under liquid. Sample holder requirements depend on both AFM design (whether cantilever or sample is scanned) and experimental conditions. For operations in liquid the sample holder should be able to contain a sample and a liquid, should provide a stable optical path and should be capable of stable control of the environment inside the liquid cell. The liquid cell should be made of inert materials with respect to the planned experiment, and possible sources of sample contamination should be minimized.

1.2.8 Detection methods, optical lever technique

Several methods have been used to measure the cantilever deflection: e.g. the optical lever technique, electron tunnelling, optical interferometry, capacitance measurements and piezoresistance and piezovoltage measurements.

The *optical lever technique* is the most commonly employed technique in commercial AFMs (Figure 1-19). Here light is focused onto the reflective back side of the cantilever and the reflected beam is detected by a position-sensitive photodiode. This could be a two or four segment photodiode or a charge-coupled device (CCD) matrix. As the cantilever is deflected, the cantilever tilt changes the light reflection angle, which results in a laser spot motion over the detector. The signal from the detector is used by the AFM electronics to provide a feedback signal and to reconstruct the AFM image. This detection scheme is easy to realize and it has high sensitivity to small longitudinal and lateral cantilever motion.

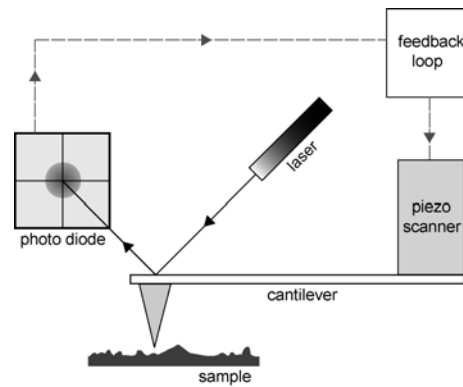


Figure 1-19. Schematic representation of the optical lever detection technique in AFM measurements.

Some applications require different cantilever deflection measurement techniques, since optical detection is not advisable due to the laser light excitation. Several such methods are available. Electron tunnelling was historically the first cantilever deflection measurement method (Figure 1-20, left). An additional STM tip is used to monitor the motion of the cantilever. The cantilever surface should be conductive and then the tunnelling current varies with the STM tip – AFM cantilever separation. It has, however, drawbacks: first it requires good vibration isolation. Second, while scanning with the AFM tip over the sample surface, the STM tip will probe the profile of the cantilever surface. Thus sample roughness, reconstructed from the cantilever position measurements will be the convolution of sample surface structure and the cantilever surface structure. These existing drawbacks make it hard to use this detection method in commercial AFM systems.

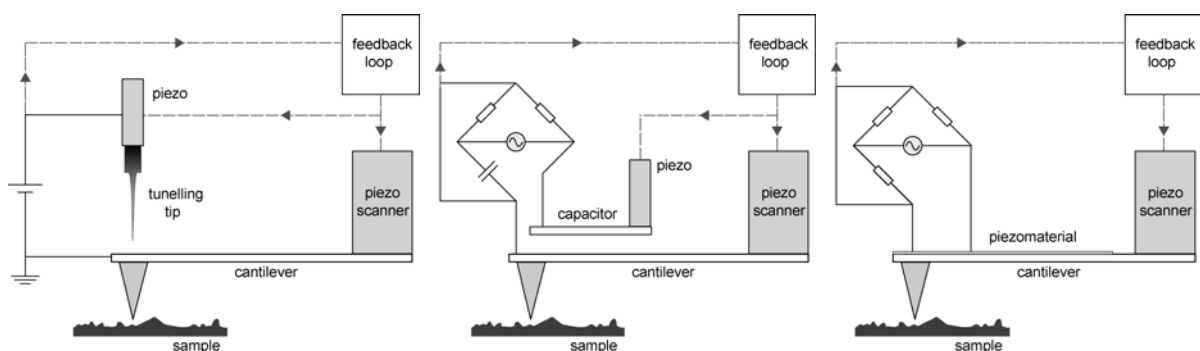


Figure 1-20. Schematic representation of cantilever deflection measurements techniques in AFM. Left: electron tunnelling. Middle: capacitance detection. Right: piezoelectric resistance.

Electrical methods are used for cantilever deflection measurements too. A capacitance measurement method is based on a small metal plate positioned above the conducting cantilever (Figure 1-20, middle). Two separated metal surfaces form a capacitor, whose capacitance depends on the surfaces separation and therefore is sensitive to the cantilever deflection. This method provides a compact, easy-to-handle system. A disadvantage is the

sensitivity to thermal drift of the reference capacitor in the capacitance bridge. This method is commonly used to detect the piezoelectric scanner position in a closed-loop feedback.

Electrical methods include also piezoelectric resistance and piezoelectric voltage detection (Figure 1-20, right). A piezoelectric material on the top of the cantilever is able to generate a voltage or shows change in its resistance upon the deformation of the cantilever. However such cantilevers are expensive and piezoelectric materials are suffering of known artefacts such as hysteresis, aging, etc.

1.2.9 Mechanical and thermal vibrations

Since AFM cantilever displacement detection schemes are capable of small cantilever displacement detection, AFM operation requires a stable environment. Stable temperature and controlled vibration isolation are the most important factors. To reduce undesired effects, which may be introduced by temperature gradients, careful selection of materials with similar coefficients of thermal expansion are used in AFM designs. For high resolution measurements the AFM is usually left for thermal equilibration.

Another type of noise which can be minimized via proper AFM design is mechanical vibration. Making the microscope construction compact and rigid mechanical vibrations transmission and amplification by the instrument itself may be reduced. In addition to optimized design, the AFM unit is usually placed on a vibrationally isolated table with a passive or active vibration damping system or a heavy platform hanging from bungee cords.

1.3 Force spectroscopy

This Section is devoted to the force spectroscopy description and considers particular aspects of this experimental technique on the basis of an AFM. A detailed overview of force sensors calibration relevant for quantitative characterization of the pulling force is presented. A short introduction into the polymer physics is given in the section.

Force spectroscopy is a powerful technique that provides much of the progress in various fields of fundamental and applied research in physics, chemistry, biology, and medicine. Force spectroscopy has been used to explore the molecular mechanics of biological motors, of receptor-ligand binding, as well as elastic/nonelastic properties of polymer and biopolymer. It can directly compare mechanical properties of a single probed molecule in a single run to theoretical simulations as well as to explore complex biological systems energy landscapes.

1.3.1 Atomic force microscope in force spectroscopy mode

The AFM is not only capable of 3D surface topology mapping – it can also be used as a high sensitivity force probe between a tip and a sample. This AFM mode is called a force-distance curve mode or a force spectroscopy. In this mode the cantilever deflection is measured as a function of distances from the sample. After the deflection and cantilever spring constant calibration the force vs. piezo extension or force vs. tip-surface separation curves can be obtained. These curves are known as force-distance curves or force-spectroscopy curves. Force spectroscopy curves provide information about specific mechanical properties of a sample and usually reveal features which can be used as ‘fingerprints’ of the studied sample. Force spectroscopy is employed to study fundamental inter- and intramolecular interactions directly at the molecular level. Present instrumentation can measure forces directly at the level of single molecules or their complexes. It is applied to a wide range of molecules: from simple polymers to complex biological macromolecules.

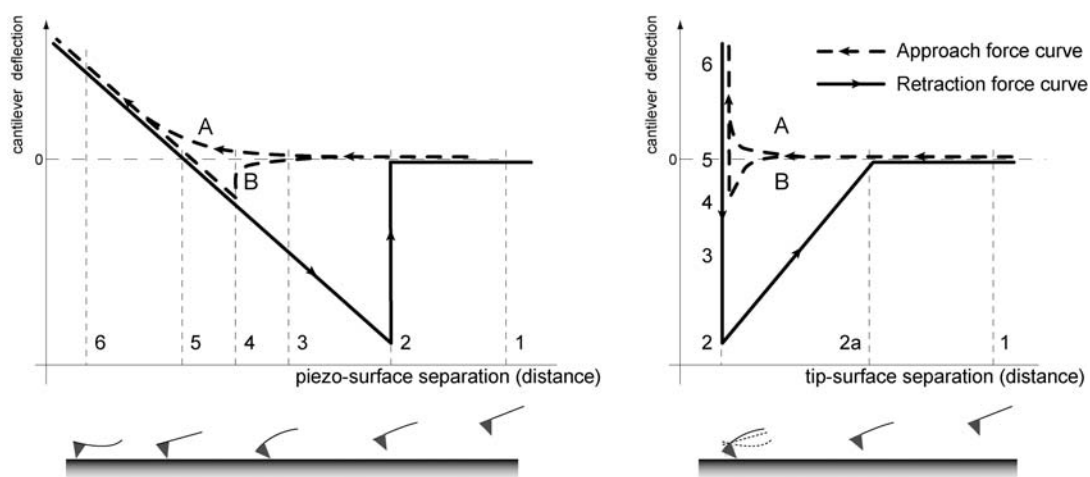


Figure 1-21. Schematic cantilever deflection via distance curves illustrating the force spectroscopy technique.

An illustration of the force spectroscopy mode is the following (Figure 1-21, left): the AFM tip approaches a sample surface (dashed curve) and then retracts (solid curve). At the start point (1) away from the surface there is no interaction between the tip and the surface. The cantilever deflection is zero. As the cantilever approaches the surface attractive van der Waals forces (B) or repulsive electrostatic forces (A) tilt the cantilever towards the surface or away from the surface (3-5). At a certain force value the cantilever may snap into contact with the surface under attractive force (4). During further piezo approach the cantilever stays in contact with the sample (4-5). Due to the van der Waals repulsive forces the cantilever deflects away from the surface (6). In this region (5-6) elastic or plastic sample/probe deformation may happen. On the retraction curve the cantilever may stay in contact with the

surface due to attractive electrostatic interactions or binding chemically to the surface. At position 2 it jumps out of contact.

The flexibility of the cantilever or the sample softness results in a substantial difference in shape between the piezo-surface separation curve (Figure 1-21, left) and the tip-surface separation curve (Figure 1-21, right). Once in contact with the surface, the cantilever tip stays in contact and the flexible lever bends, whereas the piezo is moving (Figure 1-21, right, bottom, position 2 – 6). Tip-surface separation is obtained from piezo-surface separation by a cantilever deflection correction:

$$d_{tip-surface} = d_{piezo-surface} - (\text{cantilever deflection}) \quad (1-36)$$

The deflection of the cantilever measured by the photodiode has the dimension of Volts. The photodiode sensitivity has to be calibrated to obtain the deflection in metric units (m or nm). The sensitivity calibration is usually done by pressing the cantilever against a hard surface as in the case described above (region 4-6, Figure 1-21, left). Here the piezo-surface separation is linear with the cantilever deflection measured by the photodiode. The voltage response of the photodiode is measured for a known distance change of the piezo. The inverse optical lever sensitivity (InvOLS) has the dimension of V/m and is defined as follows:

$$\text{InvOLS} = \frac{\Delta(\text{cantilever deflection})}{\Delta(\text{piezo - surface separation})} \quad (1-37)$$

The measurement of the InvOLS is critical for accurate cantilever spring constant calibration (see the next section). An error of 10% in InvOLS results in an error of 20% for the spring constant [97].

After the deflection calibration procedure the actual interaction force can be calculated using Hooke's law:

$$F = -k \cdot d, \quad (1-38)$$

where F is the interaction force, k is the cantilever spring constant and d is the cantilever deflection.

The force sensitivity of the technique is defined by the AFM cantilever stiffness (k) and the detection system stability and resolution (in case of optical lever detection scheme mainly by the laser power stability). Ultimately the force sensitivity is limited by the cantilever thermal motion [81,95,98], as well as by the laser shot noise and the detection bandwidth. Based on just thermal motion consideration it can be calculated as follows:

$$F = \sqrt{\frac{4k_B T \cdot \Delta\omega \cdot k}{\omega_0 \cdot Q}}, \quad (1-39)$$

where F is the force noise, k_B is the Boltzmann's constant, T is the temperature, $\Delta\omega$ is the measurements bandwidth, k is the cantilever spring constant, ω_0 is the resonance frequency, and Q is the quality factor.

1.3.2 Cantilever force constant calibration

Quantitative analysis of force curves requires the knowledge of the spring constant of the cantilever. Cantilevers available on the market may have different spring constants than specified by the manufactures. Thus the spring constant should be determined experimentally. The spring constant calculation method to be used depends on the experiment. There are several different methods available [97,99-101]. Generally accepted methods and most popular are: 1) the added mass (Cleveland's) method, 2) the static loading methods, 3) the reference spring method, 4) the thermal motion method and 5) the dynamic (Sader's) method.

1.3.2.1 Added mass method

This method was proposed by Cleveland et. al [102] for rectangular or V-shaped cantilevers. The cantilever is approximated as a spring with stiffness k and effective mass m^* , dependent on the cantilever geometry. Loading the cantilever with additional mass M changes the cantilevers resonant frequency ω , which can be estimated as follows:

$$\omega = \sqrt{\frac{k}{m^* + M}} \quad (1-40)$$

This equation can be rearranged as follows:

$$M = k(\omega)^{-2} - m^* \quad (1-41)$$

Adding of several known masses to the cantilever leads to a linear plot of added masses versus resonance frequencies, where the slope is proportional to the cantilever spring constant. Spheres of a defined mass and a size of 5-10 μm can be mounted close to the tip of the cantilever, thus increasing the cantilevers effective mass. A measurement of unloaded and loaded cantilever resonance frequencies is usually enough to determine the cantilevers effective mass and spring constant. The main source of error is the cantilever spring constant estimation arises from the perfect positioning of the sphere at the end of the cantilever. The estimated values possess about 10% accuracy [103].

1.3.2.2 Static loading methods

An elegant method proposed by Senden and Ducker [104] is based on the gravitation forces. Tungsten spheres 10–50 μm in diameter were attached to a cantilever similar to the added mass method. Then the cantilever static deflection is measured in both the normal AFM position and the AFM placed upside down. The differences between the two deflections correspond to twice the gravity force acting on the mass. The cantilever spring constant is given by:

$$k = \frac{8\pi R^3 \cdot \rho \cdot g}{3 \cdot X}, \quad (1-42)$$

where ρ and R are the density and radius of the sphere, g is the acceleration due to gravity, X is the measured deflection difference (in metric units). The accuracy of this method depends on the measurement of the sphere radius and deflection measurements errors. The cantilever spring constant values vary about 10%.

There are other static bending methods which are based on hydrodynamic drag effects. The cantilever spring constant can be determined measuring the cantilever deflection which is caused by the force acting on the cantilever approaching a flat surface [105,106].

1.3.2.3 Reference spring method

This method is based on the calibration accuracy of another spring (or a cantilever) as a reference. This reference should have comparable stiffness. The required calibration can be determined from the cantilever deflection dependence when it is pressed against the reference spring. A slice from a polymer film with known geometric parameters and mass can be used as the reference spring. The unknown spring (k) constant is that defined by the following equation:

$$k = k_{ref} \left(\frac{\text{InvOLS}_{ref}}{\text{InvOLS}} - 1 \right), \quad (1-43)$$

where InvOLS_{ref} and InvOLS are the inverse optical lever sensitivity for reference spring and unknown spring constant cantilever respectively, k_{ref} is the reference spring constant. Typical spring constant uncertainties of this method are about 20%. Error sources include proper cantilever and reference spring positioning as well as surface contaminations [107,108].

1.3.2.4 Thermal motion method

A simple harmonic oscillator (SHO) model describes a cantilever in equilibrium with the environment. In such a case thermal motion causes small cantilever deflections. The Hamiltonian of a simple harmonic oscillator with one degree of freedom is the following:

$$H = \frac{p^2}{2m} + \frac{1}{2}m\omega_0^2q^2, \quad (1-44)$$

where q is the displacement of the cantilever, p is its momentum, m is the mass and ω_0 is the resonance angular frequency. According to the equipartition theorem, the average value for every independent quadratic term in the Hamiltonian (total energy) of a system is given by $\frac{1}{2}k_B T$, where k_B is Boltzmann's constant and T is the temperature. Since $\omega_0^2 = k/m$, the spring constant k can be obtained as follows:

$$k = \frac{k_B T}{\langle q^2 \rangle} \quad (1-45)$$

According to Parseval's theorem, the sum (or integral) of the square of a function is equal to the sum (or integral) of the square of its Fourier transformation.

$$\int_{-\infty}^{\infty} |q(t)|^2 dt = \int_{-\infty}^{\infty} |Q(\omega)|^2 d\omega \quad (1-46)$$

The cantilever deflection is measured as a function of time. Using fast Fourier transformations (FFT) [109] it can be transformed into a power spectral density function in the frequency domain. Analysis of the power spectral density function proposes direct cantilever oscillations monitoring and deflection signal filtering. In the limit of a small cantilever damping the power spectral density of cantilever displacement fluctuations can be described with a Lorentzian shaped function [98, Section 1.2.4] and the noise (white noise and $1/f$ noise [110,111]) can be subtracted from the power spectrum. Thus, the area below the power spectrum (P) is a measure of the cantilever fluctuations. Hutter and Benchofer [112] suggest estimation of the cantilever spring constant (a free cantilever case) as follows:

$$k = k_B T / P \quad (1-47)$$

However, the optical lever technique measures the inclination at the end of the cantilever rather than the deflection itself. Hence the correction of inclination measurements has to be done to obtain the deflection. In addition, more than one cantilever vibration mode can be excited by thermal motion. Butt and Jaschke [113] have proposed the thermal noise calculation of a free and supported rectangular cantilever by assuming a Boltzmann distribution of the thermal energy between all possible vibrational modes. The authors also

have pointed out the importance of exact cantilever shape knowledge for the spring constant estimation which may cause a 10-25% error in spring constant calculations. They estimated the spring constant of the free rectangular cantilever as:

$$k = \frac{3}{4} \frac{k_B T}{P} \quad (1-48)$$

The proposed correction for the energy distribution between the various cantilever eigenmodes is developed further in the work of Stark et al. [114]. A V-shaped cantilever is treated as a SHO with the average potential energy $\frac{1}{2}k_B T$. Finite element analysis has been carried out to calculate shapes and potential energy fractions of ten transversal eigenmodes. For the considered V-shaped cantilever the spring constant at 22°C can be calculated as follows:

$$k = 0.764 \frac{k_B T}{P} \quad (1-49)$$

Expanding the Butt and Jaschke work the correction factor (see Eq.1-51) accounting for different sensitivities of a freely vibrating and end loaded cantilever is introduced by Proksch and by Schäffer [115,116].

$$\chi = \frac{\text{InvOLS}_{\text{free}}}{\text{InvOLS}_{\text{end}}} \quad (1-50)$$

The optical lever sensitivity of loaded cantilevers is estimated as described in Section 1.3.1 and is used for the force presentation, while the optical lever sensitivity of free cantilevers is calculated using the correction factor χ and is used for the cantilever spring constant calibration procedure calculations. The correction factor value depends on the size and the position of the laser spot on the cantilever. Correction factors for a various Gaussian shaped laser spot profiles on a cantilever are presented by Proksch et al. and by Schäffer [115,116].

A variation of the thermal motion method is based on the kinematical description of the cantilever motion (Section 1.2.4). The power spectral density function characterizing cantilever oscillations can be estimated. An analytical description for the free cantilever can be approximated by equation 1–35. Consideration of the contribution of white noise (constant background) and $1/f$ noise [110,111] leads to the cantilever spring constant estimation. The method is described by Colton et al. [84] and Burnham et al. [99].

1.3.2.5 Dynamic method

This method proposed by Sader [103,117] is based on the knowledge of the plain view cantilever dimensions, its density, thickness, resonance frequency and the quality factor.

Common problems of this method are the cantilever thickness and precise density determination. Dimensions of the cantilever are specified by the manufacturer or can be measured by optical microscopy. Dynamic parameters can be obtained from the thermal noise spectra of the unloaded cantilever. The spring constant of a rectangular cantilever whose length to width ratio (L/b) is within the range 3.3 – 13.7 can be determined according to Sader et al. [118]:

$$k = 0.1906\rho_f \cdot b^2 \cdot L \cdot Q \cdot \omega_0^2 \cdot \Gamma_i^f(\omega_0), \quad (1-51)$$

where ρ_f is the density of the fluid; b , L are width and length of the cantilever; Q is the quality factor in fluid, ω_0 is the resonance frequency (radial) and Γ_i^f is the imaginary part of the hydrodynamic function [119] which depends on the fluid density and viscosity as well as cantilever width and resonance frequency but not on the cantilever mass. The calculation software and the online calibration are available on the author's webpage [120].

Cantilever chips may also have cantilevers with the shape differing from rectangular. Performing the calibration of the rectangular cantilevers and assuming that the thickness and material properties are the same for all cantilevers on a single cantilever chip, spring constants for other cantilevers can also be calculated.

1.3.3 Polymer elasticity

Single molecule force spectroscopy experiments on polymer molecules provide a unique access to mechanical properties of a single molecule. A number of models can be applied to describe the experimental data and understand the polymer molecules properties and behaviour. Polymer molecules are large molecules made up of many smaller chemical units joined together by chemical bonds. They play a central role in chemical technology, providing new properties of materials. The structure and behaviour of native polymers - biological molecules, such as DNA and proteins is also promising for research.

A polymer can be described by various ideal chain models [121,122]. An ideal chain is the chain with no interactions between parts (monomers) of the chain far from each other along the chain. Consider a flexible polymer with $n+1$ structural elements S_i and n bonds between them which have length r (Figure 1-22). The bond vector \vec{r}_i goes from S_i to S_{i+1} . A polymer can be described by the *end-to-end vector* \vec{R} defined as:

$$\vec{R} = \sum_{i=1}^n \vec{r}_i \quad (1-52)$$

The polymer can be in different states which differ by spatial configurations of structural elements. The average end-to-end vector over all possible states of an isotropic system is zero [122]. The largest end-to-end distance among the polymer configurations is called *contour length* L . The *mean-square end-to-end distance* $\langle R^2 \rangle$ is the following:

$$\langle R^2 \rangle = \langle \bar{R} \cdot \bar{R} \rangle = \sum_{i=1}^n \sum_{j=1}^n \langle \bar{r}_i \cdot \bar{r}_j \rangle = r^2 \sum_{i=1}^n \sum_{j=1}^n \langle \cos \theta_{ij} \rangle = C_n n r^2 \quad (1-53)$$

where θ_{ij} is the angle between bond vectors \bar{r}_i and \bar{r}_j .

The term $\langle \cos \theta_{ij} \rangle$ describes the correlation between different bond directions averaged over all possible states of the polymer. In an ideal chain this term is equal zero. In typical polymer chains there are correlations between the directions of the bonds which are described by *Flory's characteristic ratio*:

$$C_n = \frac{1}{n} \sum_{i=1}^n \sum_{j=1}^n \langle \cos \theta_{ij} \rangle \quad (1-54)$$

An infinite chain has the ratio C_∞ and a real chain Flory's ratio C_n approaches it.

Depending on the polymer chemical structure different assumptions about the allowed bond angles can be made. Each ideal chain model assumes a certain range of values for angles between the chain bonds and describes universal properties of the polymer which are independent on the local chemical structure.

1.3.3.1 Ideal chain models

Besides the mean-square end-to-end distance describing the average polymer conformation, it can also be characterized by the statistical distribution of the end-to-end vectors. The statistics of ideal chain conformations is similar to random walk statistics. Given the Gaussian distributions of each Cartesian component of the end-to-end vector \bar{R} in an ideal chain (Gaussian chain) model is introduced. This model is valid if the extension $\langle R \rangle$ is smaller than the contour length L of the chain.

A polymer can be modelled with N equivalent freely joined effective bonds (Kuhn monomers) of length b (*Kuhn length*) and no correlations between the directions of different bond vectors (Figure 1-22, left). This model is known as a *freely joined chain* model (FJC).

The Kuhn length can be estimated from the equation: $b = \frac{C_\infty n r^2}{L}$.

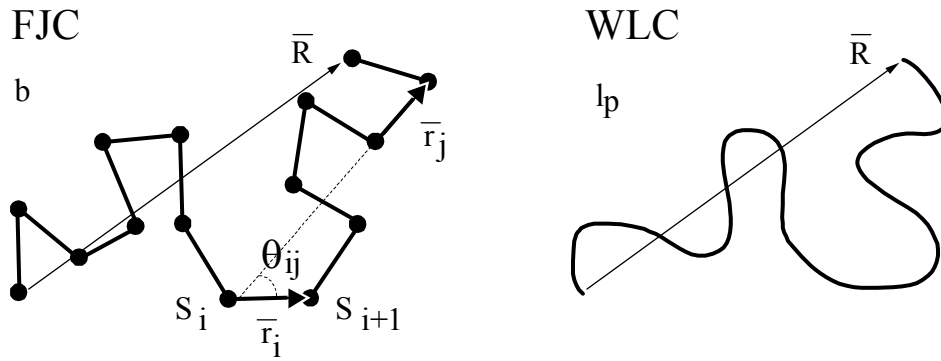


Figure 1-22. Schematic representation of different polymer models and model parameters. A polymer can be represented as a set of N bonds with bond vectors \bar{R}_i joined together. The end-to-end distance vector \bar{R} is the sum of bond vectors \bar{R}_i and characterizes the state of a polymer. The freely-joint chain (FJC) consists of freely coupled rigid Kuhn segments with the Kuhn length b (left). The worm-like chain (WLC) consists of structural parts linear on the scale of persistence length l_p (right). Persistence length measures the ability of a flexible polymer to point in the same direction.

A special case of the FJC model for small values of angle between neighbouring bonds is called *worm-like chain* model (WLC). This model is usually valid for very stiff polymer chains (for example double stranded DNA molecules). The bonds in the WLC model are characterized by a *persistence length* l_p which is the half of the Kuhn length (Figure 1-22, right) [122]. The WLC model is defined as the limit $l \rightarrow 0$ and $\theta \rightarrow 0$ at a constant persistence length and constant chain contour length $L \cong nl$.

The difference between FJC and WLC models is that each bond of Kuhn length b of the FJC model is assumed to be completely rigid. Bonds in the WLC model are rigid on the scale of the persistence length l_p .

A polymer chain consists of many monomers and can be treated by means of statistical physics. The free energy of the chain (H) becomes [122]:

$$H(N, \bar{R}) = \frac{3}{2} k_B T \frac{\bar{R}^2}{Nb^2} + H(N, 0) \quad (1-55)$$

where N is the number of monomers in FJC model, \bar{R} is the end-to-end distance vector and $H(N, 0)$ is the free energy of the chain with both ends at the same point.

To hold the chain at a fixed end-to-end vector \bar{R} would require forces acting on the chain ends. To separate the chain ends by a distance (R_x) in X direction, requires force (F):

$$F = \frac{\partial H(N, \bar{R})}{\partial x} = \frac{3k_B T}{Nb^2} R_x \quad (1-56)$$

where $3k_B T/(Nb^2) = k_{ent}$ is the entropic spring constant of an ideal chain polymer. The ideal chain obeys Hooke's law. A smaller force is required to stretch a polymer with a larger

number of longer segments at lower temperature. The result of the entropic spring is valid for small chain extensions (Gaussian approximation), where $|\bar{R}| \ll L = Nb$.

If a large force is applied between the chain ends and the end-to-end vector length approaches the maximum chain extension, the extension upon the force becomes non-linear and is described by Langevin function:

$$\mathbf{L}(\beta) = \coth(\beta) - \frac{1}{\beta} \quad (1-57)$$

where $\beta = Fb/k_B T$ is the normalized extension force.

For a given constant force F the ensemble of the chain segments can be modelled as isothermal-isobaric ensemble at constant pressure. The the average end-to-end distance $\langle R \rangle$ at a constant force can be calculated using the Langevin function from the Gibbs energy G according to the following equation [122]:

$$\langle R \rangle = - \frac{\partial G}{\partial F} = Nb \mathbf{L} \quad (1-58)$$

The Langevin function relates the average chain extension $\langle R \rangle / L$ and the normalized extension force. For small relative extensions $|\bar{R}| \ll L = Nb$, the Langevin function $\mathbf{L}(\beta) \cong \beta/3$, ($\beta \ll 1$) and converts into Hooke's law. For large extensions, as the Langevin function approaches unity, the extension force becomes:

$$\text{for FJC model and } \frac{Fb}{k_B T} \gg 1 \text{ it is } \frac{Fb}{k_B T} = \frac{L}{L - \langle R \rangle}, \quad (1-59)$$

$$\text{for WLC model and } \frac{F \cdot 2l_p}{k_B T} \gg 1 \text{ it is } \frac{Fl_p}{k_B T} = \frac{1}{2} \left(\frac{L}{L - \langle R \rangle} \right)^2 \quad (1-60)$$

The force difference between FJC and WLC models is illustrated in Figure 1-23. The real measurements data from the force-extension measurements on a single polymer molecule can be fitted by the analytical equation for the extensional force. The simple analytical solution for the WLC model extension force at all extensions is given by Marko et al. [123]:

$$\text{FJC: } \frac{Fb}{k_B T} = L \cdot \mathbf{L}^{-1} \left(\frac{\langle R \rangle}{L} \right) \text{ or } \langle R \rangle = L \cdot \mathbf{L} \left(\frac{Fb}{k_B T} \right) = L \left[\coth \left(\frac{Fb}{k_B T} \right) - \frac{k_B T}{Fb} \right] \quad (1-61)$$

where \mathbf{L}^{-1} is the inverse Langevin function.

$$\text{WLC: } \frac{Fl_p}{k_B T} = \frac{1}{4} \left(\frac{L}{L - \langle R \rangle} \right)^2 + \frac{\langle R \rangle}{L} - \frac{1}{4} \quad (1-62)$$

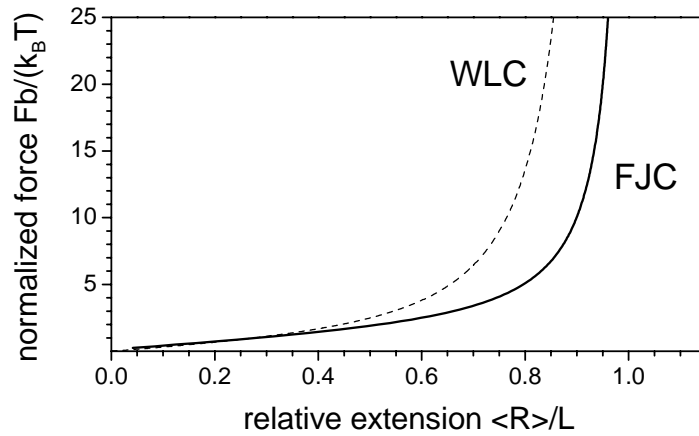


Figure 1-23. Comparison of the normalized force applied to a chain for different ideal chain models at various relative extensions. Here the applied force is F ; k_B is the Boltzmann constant; T is the temperature; b is the Kuhn length (in FJC model) and it is equal to $2l_p$ (persistence length in WLC model); $\langle R \rangle$ is the extension and L is the polymer contour length.

An improvement of the FJC and WLC models for large extensions of polymers takes into account deformation of bonds and bond angles. Each bond of the molecule is modelled as an elastic spring. The extension and force for the so called extended FJC and WLC models [124] become:

$$\text{FJC:} \quad \langle R \rangle = L \cdot \mathbf{L} \left(\frac{Fb}{k_B T} \right) \left(1 + \frac{F}{\kappa L} \right) = L \left[\coth \left(\frac{Fb}{k_B T} \right) - \frac{k_B T}{Fb} \right] \left(1 + \frac{F}{\kappa L} \right) \quad (1-63)$$

$$\text{WLC:} \quad \frac{Fl_p}{k_B T} = \frac{1}{4} \left(\frac{L}{L - \langle R \rangle} + \frac{F}{\kappa} \right)^2 + \frac{\langle R \rangle}{L} - \frac{1}{4} - \frac{F}{\kappa}, \quad (1-64)$$

where κ is the elastic modulus of an individual bond of the chain.

2 Experimental Sections

2.1 Experimental Setup

The experimental setup is based on two microscope systems: optical and atomic-force. The optical microscopy system includes lamp and laser excitation and allows single molecule fluorescence detection, optical imaging and multiparameter fluorescence detection (MFD) [Section 1.3, 125,126]. AFM can operate in various imaging modes including a custom-developed high temporal resolution force spectroscopy mode. Both systems can be used independently and in combination, thus providing exceptional flexibility for a broad range of applications. The schematic diagram of the combined AFM/MFD experimental setup is shown in Figure 2-1.

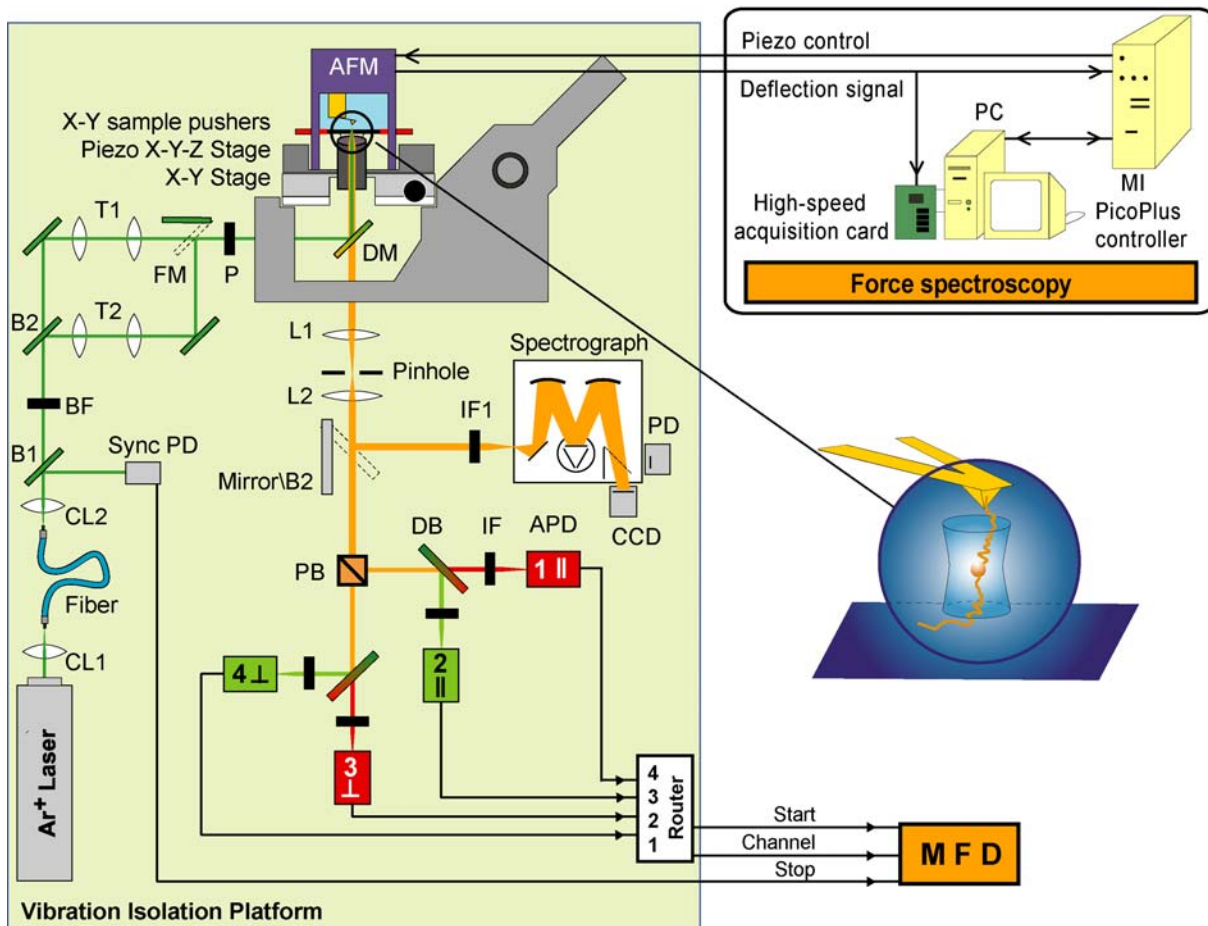


Figure 2-1. Experimental setup for combined MFD and AFM: CL1, CL2 - collimating lenses; B1, B2 - beam splitter; BF - interference filter; T1, T2 - telescopes; FM - flipping mirror; P - polarizer; DM - dichroic mirror; L1, L2 - lenses; Mirror/B2 - optional mirror or beam splitter; IF1 - interference filter; Sync PD - photodiode; PB - polarizing beam splitter; DB - dichroic beam splitter; IF - interference filter; APD - avalanche photodiode.

2.1.1 Optical microscopy and spectroscopy

The optical part of the setup is based on a confocal epi-illuminated (optional evanescent wave illuminated) inverted optical microscope IX70 (Olympus, Hamburg).

The illumination and fluorescence excitation light in optical microscope can be provided by various sources. A xenon light source LQX1800 (Spindler&Hoyer, Göttingen) and a halogen light source LQ1600 (Feiberoptic-Heim AG, Uetikon am See, Switzerland) are used for sample illumination and for optical microscope calibration. Together with a set of excitation filters these lamps can be used for fluorescence excitation. A mercury lamp and a calibrated halogen lamp² are used for spectral calibration. The linearly-polarized, argon-ion laser, Innova Sabre R (Coherent, Palo Alto, CA) is a source of laser excitation. Continuous and pulsed light at different wavelengths is available. The wavelength of 496.5 nm is usually used for this work. Pulsed excitation at a rate of 73.5 MHz with a 200 ps pulse time is obtained with an acoustooptic active modelocker (APE, Berlin).

The laser is coupled to the singlemode, polarization-maintaining optical fiber kineFLEX (Point Source, Hamble) and delivered to the optical table Breadbord Performance Plus (Melles Griot, Bensheim), hanging on bungee cords (Jumbo-Textil GmbH, Wuppertal). Here the laser light is splitted: (a) to a high speed photodiode module PHD400 (Becker&Hickl GmbH, Berlin) to provide a synchronization signal for time resolved experiments; (b) passing through an acousto-optic modulator AOM80 (APE, Berlin) for the fine laser power adjustment and then coupled to another, shorter, optical fiber³. Laser light from the second optical fiber is going through an excitation filter HQ480/40 (AHF, Tübingen). Afterwards the beam is divided for two different telescopes, aimed to provide an epi-fluorescence and an evanescent field excitation in the focal plane of the microscope's objective. The light coming via the first telescope is focused with a water or oil immersion objective into a spot of adjustable size. With the flipping mirror light from the second telescope via oil immersion objectives is focused to obtain total internal reflection (TIR) conditions i.e. the evanescent field excitation. A polarizer VISHT11 (Gsänger, Planegg) is mounted at the entrance of the microscope.

The information about the microscope objectives UPlanApo (Olympus, Hamburg) used in the optical setup is summarized in Table 2-1.

² Dr. Viktor Galievski (MPI für Biophysikalische Chemie, Göttingen) is gratefully acknowledged for the help with the calibrated light source.

³ Parts are not shown on the schematic representation (Figure 2-1) of experimental setup.

Table 2-1. Information about microscope objectives UPlanApo (Olympus)

	immersion	magnification	numerical aperture N.A.	application
1.	water	60	1.2	“in-solution”
2.	oil	60	1.45	“in-solution” and “on-surface”
3.	oil	100	1.4	“in-solution” and “on-surface”

The laser power is measured with the power meter FieldMaster GS (Coherent, Dieburg) equipped with the measuring head LM-2, designed for the spectral range 0.4-1.064 μm and the power range of 10 nW-50 mW.

A 2-axis mechanical positioning stage (OWIS, Staufen) and a 3-axis piezo-crosstable (Physik Instrumente, Karlsruhe) are mounted directly onto the optical microscope and allow coarse and fine positioning of a sample or a sample stage mounted devices. The piezo-crosstable fine positioning in three dimensions (3D) is provided by a piezo-controller (Physik Instrumente, Karlsruhe) and is controlled manually or via RS232 interface with the help of custom-written LabView base ControlPI program (see Appendix E). The software provides automated control for 3D optical imaging (Section 2.4) as well as the laser power adjustment.

Fluorescence detection is performed with the same objective. The fluorescence signal is separated from the laser light by a dichroic beamsplitter (specified for each experimental section separately), and focused on an optional pinhole (different sizes 50 to 200 μm are available). As estimated from fluorescence correlation spectroscopy (FCS) measurements, the confocal detection through a pinhole results in a detection volume of $\sim 0.6\text{-}2$ fl [126-131].

The optical signal can be diverted with a mirror/beamsplitter to an imaging spectrograph SP-308 (Acton Research Corporation, Acton, MA) with a liquid-nitrogen cooled charge-coupled devices (CCD) camera Spec-10:1340-400BI (Princeton Scientific Instruments, Trenton, NJ), where either images or spectra can be recorded. The CCD is controlled by the ST133 controller and is managed with the help of commercial WinSpec software (Roper Scientific GmbH, Ottobrunn). Optional interference filters can be installed here in the optical part before the spectrograph focusing lens. The spectrograph is equipped with two diffraction gratings with different grooves number (600 g/mm and 1200 g/mm) for spectral analysis, allowing a spectral resolution of 0.1 nm with a 10 μm slit and 1200 g/mm grating; and a mirror for the optical imaging.

The total/partial fluorescence signal can also be analyzed in the multiparameter fluorescence detection (MFD) part. There the fluorescence signal is divided into parallel and perpendicular components by a polarizing beamsplitter VISHT11 (Gsänger, Planegg) and

separated by a dichroic (Analysentechnik, Tübingen) into “green” and “red” channels. Channels are characterized by different wavelength ranges. The parameters of the dichroic beamsplitter and the bandpass filters are specified for each experimental section separately.

Single photons are detected by four avalanche photodiodes (APD) AQR-141 (EG&G, Vaudreuil, Quebec, Canada) coupled to a computer-based time correlated single photon counting (TCSPC) module SPC630 or to the modified SPC131 (Becker&Hickl, Berlin). For each photon, the arrival time after the laser pulse, the laboratory time and the polarization channel are recorded (Section 1.3.6) and saved with commercial SPC program (Becker&Hickl, Berlin). The APDs can also be coupled to a digital multi-tau hardware correlator module ALV6010/200 (ALV GmbH, Langen) with a fast mode option and real-time initial correlation down to 5 ns, which is controlled by commercial software.

Optical parts parameters were varied for a particular experiment as additionally specified.

2.1.1.1 Optical setup settings for Section 2.3

Excitation was performed using the active mode-locked Ar⁺ laser at a wavelength of 496.5 nm either in TIR or epi-illumination excitation mode. Fluorescence detection is performed with the CCD camera or in the conventional MFD confocal setup.

The laser beam was either focused with objectives 2 or 3 (Table 2-1) on the surface-solution interface, or with objective 1 (Table 2-1) into solution. Settings for the optical path in the experimental setup are given in Table 2-2.

The diameter of the focus in the epi-illumination mode was estimated to be $2\omega_{0E} = 1.17 \mu\text{m}$, based on the FCS diffusion time measurements of free Rh110 in water ($\tau_D = 0.293 \text{ ms}$). Different laser power at the objective was used and it is specified in the result Sections. Fluorescence detection for FCS measurements is performed through a confocal pinhole ($\varnothing = 100 \mu\text{m}$). If other pinholes were used it is specified later in the text.

The diameter of the illumination area in TIR mode varies with the optical path alignment and the objective used, since measurements presented in this chapter may considerably be separated in time. However, illumination parameters remain constant for the same type of experiments.

Table 2-2. Optical setup (Figure 2-1) settings for the experiments in Section 2.3

λ [nm]	DM, filter	pinhole [μm]	DB	IF _{Green}	IF _{Red}	IF1
496,5	498CCLP HQ580/140	100 (or more)	Q595LPXR	(optional) HQ535/50	–	–

2.1.1.2 Optical setup settings for Section 2.4

Excitation was performed using the active mode-locked Ar⁺ laser at 496.5 nm. The optical path settings are specified in the table (Table 2-3).

Prior to the imaging, the focus in epi-illumination mode was adjusted. The laser beam is focused into solution with objective 1 (Table 2-1). The excitation volume diameter is estimated by FCS. Based on free Rh110 diffusion time $\tau_D = 0.061$ ms in water the focal spot diameter is estimated to be $2\omega_{0E} = 0.54$ μm and the dimension ratio z_0/ω_0 is 6 (Figure 2-30). Fluorescence detection is performed through a confocal pinhole ($\varnothing = 50$ μm) that results in a detection volume of ~ 0.6 fl. The mean irradiance $I_0/2$ was either 3 kW/cm² (for Si₃N₄ cantilevers) or 14 kW/cm² (for Si cantilevers). The mean countrate per Rhodamine 110 molecule was measured by FCS to be 9.7 kHz at 3 kW/cm² and 48 kHz at 14 kW/cm².

For bulk fluorescence measurements with spectrograph and CCD camera various filters were additionally used (Table 2-3).

Alternatively, analogue electronics were used for the fluorescence signal detection. These were TTL to NIM module converters (Max-Plank-Institute for Biophysical Chemistry, Göttingen), time to pulse height converter (TAC) Ortec457, timing single channel analyzer (SCA) Ortec420A, Log/Ln ratemeter Ortec449 and the power supply with NIM bins Ortec4002 (Ortec, Oak Ridge, TN, USA).

Table 2-3. Optical setup (Figure 2-1) settings for the experiments in Section 2.4

λ [nm]	DM, filters	pinhole [μm]	DB	IF _{Green}	IF _{Red}	IF1
496,5	498CCLP	50	Q595LPXR	HQ580/140	–	HQ580/140 HQ645/75 HQ780/150

2.1.1.3 Optical setup settings for Section 2.5

Excitation was performed using either a cw He-Ne laser at 594 nm for the Atto590 experiments or an active mode-locked Ar⁺ laser at 496.5 nm for the DNA experiments.

The laser beam is focused into solution with objective 1 (Table 2-1). The diameter of the focus was estimated to be $2\omega_{0E} = 1.17$ μm in the xy-plane based on the diffusion time of free Rh110 in water ($\tau_D = 0.293$ ms) as measured by FCS. The laser power at the objective for FCS and DNA experiments was 439.2 μW , corresponding to a mean irradiance of $I_0/2 = 42.7$ kW/cm² in this focus; for the Atto590 it was 275 μW and 25.7 kW/cm² correspondingly. Fluorescence detection is performed through a confocal pinhole ($\varnothing = 100$ μm) that results in a

detection volume of ~ 2 fl. Settings for the optical path in the experimental setup are listed in Table 2-4.

Table 2-4. Optical setup (Figure 2-1) settings for the experiments in Section 2.5

λ [nm]	DM	pinhole [μm]	DB	IFGreen	IFRed	IF1
594	Q595LPXR, Q595LP	100	DCSBXP655	HQ630/60	HQ680/60	–
496,5	502/636PC	100	Q620DCXR	HQ535/50	HQ730/140	–

2.1.1.4 Optical setup settings for Section 2.7

Excitation was performed using the active mode-locked Ar^+ laser at 496.5 nm either in TIR or epi-illumination excitation mode. Fluorescence detection is performed with the CCD camera or in the conventional MFD confocal setup. Settings for the optical path in the experimental setup are listed in Table 2-5.

The laser beam was focused on the surface-solution interface with objective 2 (Table 2-1). The excitation volume diameter $2\omega_{0E} = 0.54 \mu\text{m}$ is estimated by FCS from free Rh110 diffusion time $\tau_D = 0.061$ ms in water. Fluorescence detection is performed through a confocal pinhole ($\varnothing = 50 \mu\text{m}$) that results in a detection volume of ~ 0.6 fl.

The diameter of the illumination area in TIR mode varies with the optical path alignment; however illumination parameters remain constant for the same type of experiments and will be specified in the result sections.

Table 2-5. Optical setup (Figure 2-1) settings for the experiments in Section 2.7

λ [nm]	DM	pinhole [μm]	DB	IF _{Green}	IF _{Red}	IF1
496,5	498CCLP	50	Q595LPXR	HQ535/50 IR800	HQ730/140 IR800	IR800

2.1.1.5 Fluorescence data analysis software

Several software packages developed previously in the group of Prof. Seidel were used for the fluorescence data analysis and visualization: “Fit machine”, “Jordi Girl”, “Elke”, “Kristine”, “Margarita” and “Tatiana”. The software was developed with LabView (version 5.1-7.0, National instruments) and Visual C++ (Microsoft Corporation) by Dr. J.Schaffer, Dr. C.Eggeling, Dr. E.Hausstein, Dr. M.Antonik, Dr. S.Felekyan and V.Kudrytsev.

2.1.2 Bulk optical spectroscopy

Absorption spectroscopy

The absorption spectrometer Cary-5Bio (Varian, Mulgrave, Australia) is used to obtain optical absorption spectra. Measurements are performed in quartz fluorescence cuvettes (Hellma, Müllheim). For all obtained spectra a cuvette with a clean buffer is used in the reference signal channel.

Bulk fluorescence spectra measurements.

The fluorescence spectrometer FluoroLog (Instruments SA, Edison, USA) is used for bulk fluorescence spectral measurements. A calibrated Xenon lamp (Osram, Frankfurt) is used as the excitation source. Fluorescence light is detected at a magic angle perpendicular to the excitation direction, passing through a double monochromator to a photon counting photomultiplier tube (PMT) R928P (Hamamatsu) with a combined water- and Peltier-cooling.

2.1.3 Atomic force microscopy and force spectroscopy

An AFM is placed on the 3-axis piezo-crosstable on top of the optical microscope. The AFM head PicoSPM I (Molecular Imaging, Phoenix, Arizona) is equipped either with a 30 μm scanner or a 5 μm scanner.

The AFM is connected to a break-out box, which is a signal access module that provides access to input and output channels of the PicoPlus system. The BNC connectors on the box allow monitoring of each channel, feeding a channel with a custom signal and user-defined operations as well as providing a signal for synchronization or custom operations.

A sample is placed onto the sample plate for the AFM, which hangs under the AFM scanner with the cantilever holder. Different sample plates are available with magnetic or mechanical sample holding option, depending on the properties of a sample. The sample is fixed mechanically either with a metal spring or with a teflon O-ring, which also works as a fluid cell. These sample plates have a reach-through hole, allowing approach with an immersion free and immersion microscope objective from the other side of the sample. Micrometer-replacement actuators (MRAs) with linear step size less than 100nm controlled manually or via a picomotor multi-axis driver M8801 (New Focus Inc., Santa Clara, USA) that allow fine positioning of the sample plate.

The functionality of the AFM is provided by the controller, which employs a hybrid feedback servo system with a 32-bit DSP to perform scans and image acquisition. Five 20-bit DACs provide high-precision X, Y, and Z positioning. However, the signal acquisition rate is not higher than 60 kHz, thus the number of data points available restricts the functionality of the AFM for force spectroscopy applications.

The AFM controller and the commercial PicoScan software (Molecular Imaging) communicate with each other via a USB connection. The PicoScan software provides a flexible imaging control, post-imaging processing and allows for advanced scripting features for imaging and spectroscopy as well as communication with LabView software via ActiveX protocol.

Beside the standard AFM contact mode, a MAC mode controller (Molecular Imaging) provides acoustically and magnetically driven non-contact and intermittent contact modes.

The AFM can operate in a stand-alone box. Vibration isolation, critical in AFM measurements, is realized by placing the microscope head on a block suspended by bungee cords.

The AFM scanners are calibrated in three axes, performing scans of NT-MDT (Tallinn, Estonia) calibration grids. A TGX01 grating (Figure 2-2, left) with a $3\mu\text{m} \pm 5\text{nm}$ pitch size is used for lateral calibration and a TGZ02 grating (Figure 2-2, right) with $100\text{nm} \pm 1.5\text{nm}$ step height is used for Z-axis calibration. This calibration, as suggested by AFM manufacturer, has to be repeated every six month for reliable standardized AFM scanner functionality.

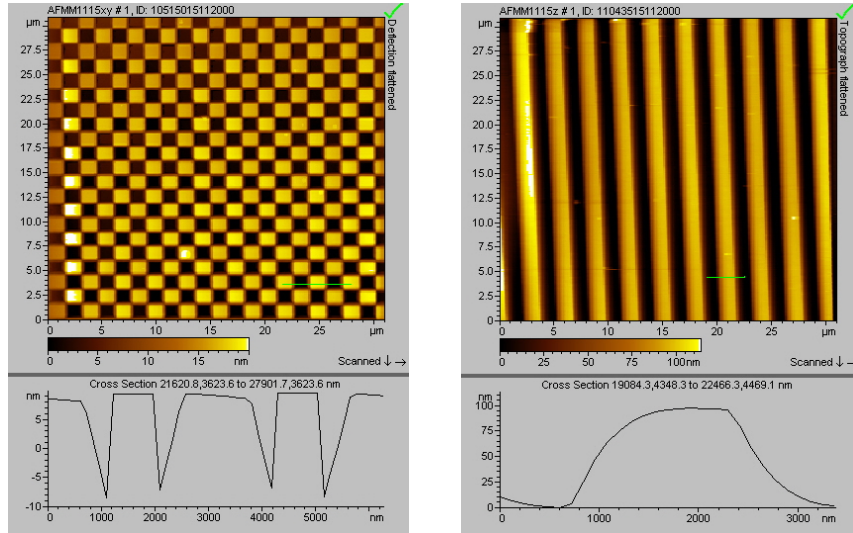


Figure 2-2. AFM images and cross sections of silicon calibration gratings TGX01 (left) and TGZ02 (right).

AFM surface characterization

The atomic-force microscope was mainly used in the tapping mode. Tapping mode eliminates continuous tip-sample contact thus minimizing lateral forces exposed to the sample surface. Some samples were also investigated in contact mode. Nanosensors cantilevers (Nanosensors GmbH, Wetzlar-Blankenfeld) with high aspect ratio (3:1) pyramidal shape Si tips with a nominal tip radii of 10 nm and a spring constant of 42 ± 5 N/m were used for imaging (see Section 2.2).

Each sample was imaged at several randomly selected positions. For all AFM images presented minor image manipulations were performed. First, a global slope was removed to account for the inclined tip orientation and the sample mount. Second, each line was flattened with a 4th order polynomial [84].

The roughness of the samples is characterized by the mean height, the maximum peak to valley (Rv-p) and the *RMS* within an image. The analysis is performed with standard functions in the commercial PicoScan software.

The mean height for all pixels in the image is defined as $R_a = \sum_{i=1}^N |z_i| / N$, where z_i is the difference in height from the mean plane for i -th point and N is the number of points in the image.

The maximum peak to valley value is defined as the sum of mean height of peaks and mean depth of valleys from the mean elevation plane, calculated from all pixels in the image.

The root-mean-square roughness (*RMS*) is defined as the root-mean-square average of height deviations from the mean elevation plane calculated from the relative heights of each

pixel in the image:
$$RMS = \sqrt{\sum_{i=1}^N z_i^2 / N} .$$

Force spectroscopy

The functionality of the microscope controller, in particular force spectroscopy capabilities, was greatly increased by custom-build modernization. A data acquisition computer board (Measurement Computing) allows sampling and averaging of the deflection signal at high rates. In our modification the deflection signal is not passing through AFM head electronic circuit. The computer board digitizes the deflection directly and provides the control voltage for AFM piezo via the microscope controller. The deflection signal is digitalized at a rate up to 10 MHz and is recorded for the time up to 20 seconds due to the present computer memory limitations. That suits to the most experimental needs in force spectroscopy experiments. The acquisition board is installed in the same computer, and communicates to the AFM controller via PicoScan commercial software and ActiveX protocol. A LabView based PicoPull program (see Appendix E) offers flexible control for the force spectroscopy acquisition: custom experimental steps like voltage ramp, pause and synchronization signal generation.

The analysis of force spectroscopy data is realized in a LabView-based PicoPeek program and/or in a MatLab-based FoCuS (**F**orce **C**urves **S**tatistics) package (see Appendix E for details).

The Veeco Microlever Si₃N₄ cantilevers (Veeco Instruments GmbH, Mannheim) with rectangular and triangular shaped levers and with pyramidally shaped tips were used for the force spectroscopy. The spring constants specified for different levers on a chip varied between 0.01 – 0.6 N/m.

2.1.4 Combined AFM and optics: Simultaneous force and fluorescence spectroscopy (SFFS)

Several additional changes are implemented in the AFM design to increase the compatibility of the combined setup for simultaneous fluorescence and force spectroscopy experiments.

A standard red-light diode laser is substituted by an infra-red (IR) 830nm single-mode fiber-coupled diode laser 48TE-FCC (Schäfter&Kirchhoff GmbH, Hamburg). This modification avoids the influence from the AFM head laser on an optical signal. A single mode laser is focused into a near-diffraction limited size spot which is smaller than cantilevers width. This helps to remove the interference pattern on force curves which is the result of the interference of the light reflected from the cantilever and the light reflected from the sample surface. A Find-R-Scope infrared viewer 84499A (FJW Optical Systems Inc., Palatine, IL) is used for the IR laser beam visualization and the cantilever alignment procedure.

The excitation light provided by the Ar⁺ laser is blocked by an optical filter mounted in front of the position-sensitive photodiode of the AFM.

An AFM sample plate equipped with a fluid cell is aligned so that the sample surface is parallel to the focal plane of the microscope objective.

The PicoPull software offers the control of the combined experiment: opening the laser beam and triggering the TCSPC acquisition card or the CCD camera controller with the synchronization signal taken from the AFM break-out box.

2.2 Materials and chemicals

Substrates

Mica sheets, V1 and V2 grates, were purchased from Science Services (München). Glass substrates (Table 2-7) were obtained from Gerhard Menzel Glasbearbeitungswerk GmbH&Co. KG (Braunschweig) and Olympus Deutschland GmbH (Hamburg).

Substrates cleaning chemicals

Solvents for the glass cleaning (Table 2-8) and modification were purchased from: H₂SO₄ (Fluka Chemicals, Seelze); H₂O₂ 38% (Fluka Chemicals, Seelze); propanol (C₃H₈O) GR for analysis (Merck KgaA, Darmstadt); ammonium hydroxide (NH₄OH) 25% (Baker analyzed, Deventer, Holland); acetone GR for spectroscopy (Uvasol, Merck KgaA, Darmstadt); methanol (a) GR for UV spectroscopy (Fluka Chemicals, Seelze) and (b) GR for analysis (Merck KgaA, Darmstadt); ethanol GR for spectroscopy (Merck KgaA, Darmstadt); Helmanex solution (Helmanex, Müllheim/Baden).

Silanes and Poly(ethylene glycol) (PEG)

Silanes (Table 2-9) were purchased from Sigma-Aldrich Chemie GmbH (Schnelldorf) and ABCR (Karlsruhe). PEG with molecular weight of 2000Dalton and different combination of active groups at the ends (NH₂-POE-NH₂ and CH₃O-POE-NH₂) was bought from RAPP Polymer GmbH (Tübingen).

Other substrates modification chemicals

Avidin, BSA-biotin and epoxies were purchased from Sigma-Aldrich Chemie GmbH (Schnelldorf).

Buffers

Buffers were prepared in the deionised water at Arium 611VF (Sartorius, Göttingen) and micro-filtered through 0.22µm filter (Millipore GmbH). High quality chemicals were used for the buffer preparation: Natriumchlorid or NaCl (Fluka Chemicals, Seelze), Tris-(hydroxymethyl)-methylamin or TRIS (Sigma-Aldrich, Seelze), Na₂HPO₄ (Fluka Chemicals, Seelze), NaH₂PO₄ (Fluka, Seelze), Magnesiumchloride or MgCl₂ (Fluka Chemicals, Seelze), EDTA (Serva, Heidelberg), Na-ascorbate (Sigma-Aldrich, Seelze).

TRIS buffer: 150mM NaCl, 10mM TRIS, 1mM EDTA, pH 7.5 were used for biomolecules immobilization and pulling experiments (nonspecific DNA binding to the surface).

TRIS buffer: 50mM NaCl, 20mM TRIS, 0.2mM EDTA, 10mM MgCl₂, pH 9 was used for the studies of Atto590 dye.

Sodium Cacodylat buffer: 100mM NaCl, 10mM Na-Cacoylat, 10mM MgCl₂, pH 6 was used for the studies of Atto590 dye.

Sodium phosphate (PBS) buffer: 150mM NaCl, 10mM Na₂HPO₄/NaH₂PO₄, 1mM EDTA, pH 8.2 were used for biomolecules immobilization, pulling experiments (nonspecific and specific DNA binding to the surface), as well as for simultaneous force and fluorescence spectroscopy experiments.

Sodium phosphate (PBS) buffer with 180 mM NaCl, 10 mM NaH₂PO₄/Na₂HPO₄, and 400 μ M Na-ascorbate, pH 7.5 is used for all FRET experiments on DNA constructs.

DNA samples

Specifically modified dsDNA 6000bp long were obtained from IBA (Göttingen). Table 2-6 gives detailed information about the molecules. Digest λ -DNA and plasmid λ -DNA were from Sigma-Aldrich Chemie GmbH (Schnelldorf).

Table 2-6. IBA modified dsDNA molecules information.

description	abbreviation	PCR (IBA)	conc. [μ g/ml]	buffer	bp conc. / μ l
5'-amino and 5'-three biotin modification	NHdna3Bio	381/165/1	24	dH ₂ O	1.05 $\times 10^{21}$
5'-amino modification	NHdnaFree	396/188/1	10	PBS	
no modification	FreednaFree	397/188/1	12	PBS	
5'-amino and 5'-three biotin and Alexa594 dye modification	NHdna3BioA12	403/17	36	dH ₂ O	
5'-amino and 3'-three biotin and Alexa594 dye modification	NHdna3BioA11	402/15 Lig586	9.9	dH ₂ O	

For the FRET experiments the fluorescently labelled double stranded 27-mer DNA was used which has been previously described [129]. The DNA strands were synthesized by the standard aminophosphoramidite technology. In the (+)-strands, Cy5 was attached at a fixed site at the 5'-end via a C6-linker and a 5'-aminomodifier (C6). Unlabeled complementary DNA (-)-strands were produced for use in the donor only experiments, as well as (-)-strands with Alexa488, attached via a C6-linker, to a thymidine residue 13 bp from the end, designated here as the DA-13 DNA (Amino-Modifier C6 dT from Glenresearch). The FRET efficiency for the donor-acceptor labelled system was previously determined to be 0.4 [129].

Fluorescence beads

Fluorescent beads in PS-Spec microscope point source kit (P7220) were purchased from Molecular Probes (Leiden, The Netherlands).

Dyes

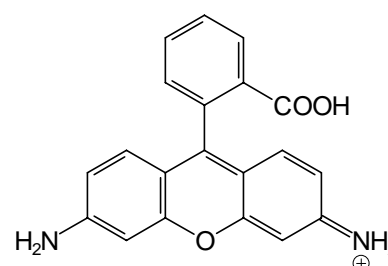
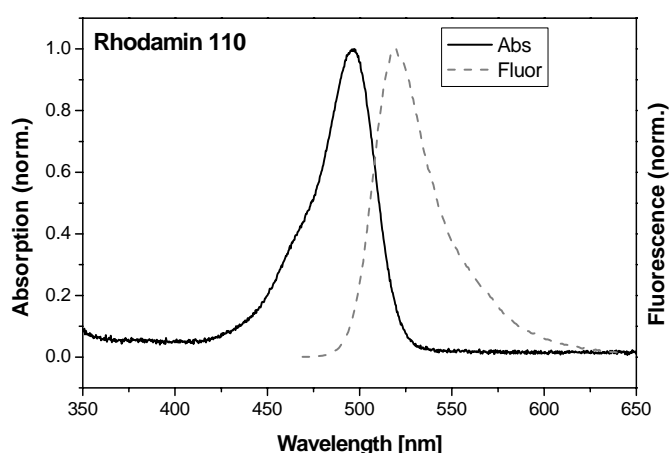
Rhodamine 110 and Rhodamine 101 (Molecular probes) were used for the optical setup fluorescence detection alignment and FCS measurements.

SYBR Green I (Molecular probes) was used as a DNA molecules binding agent.

An ultra-pure samples (HPLC purity >99%) of two isomers of Atto590 dye (Atto-Tec, Siegen) were used in Section 2.5. They were prepared in the TRIS buffer at pH 6 and 9.

Alexa488 (Molecular Probes) as a donor and Cy5 (Amersham-Pharmacia) as an acceptor, were used as the FRET pair, offering a large Förster radius of $R_0 = 51 \text{ \AA}$.

Rh 110



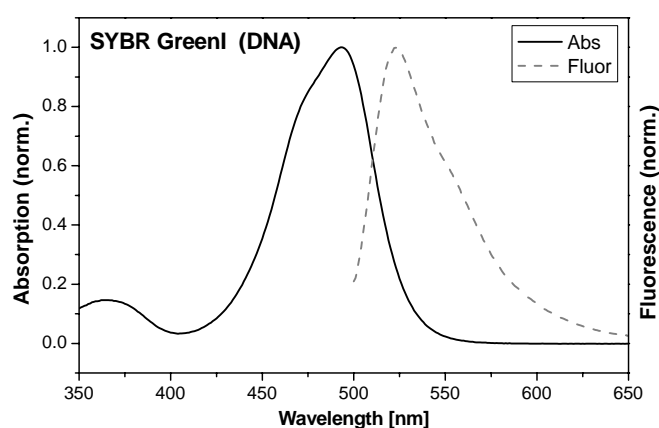
Absorption maximum: 496 nm

$\epsilon_{496 \text{ nm}}: 73\,000 \text{ M}^{-1}\text{cm}^{-1}$

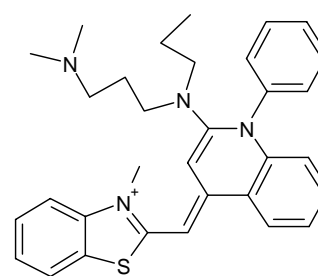
Fluorescence maximum: 527 nm

$\Phi_F: 0.95$ (PBS buffer)

SYBR Green I



References: [229,228]



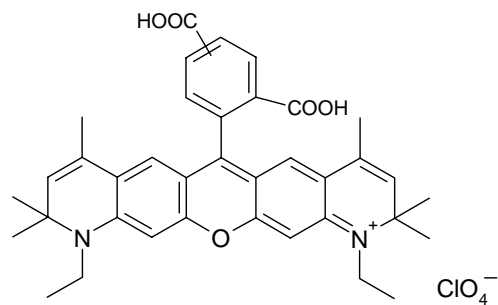
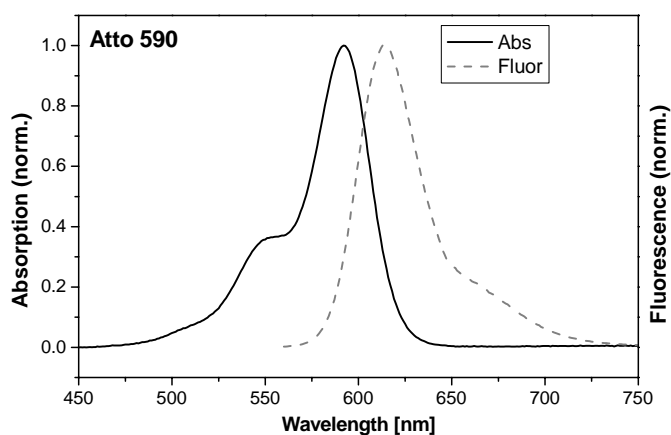
Absorption maximum: 494 nm

$\epsilon_{494 \text{ nm}}: 73\,000 \text{ M}^{-1}\text{cm}^{-1}$

Fluorescence maximum: 524 nm

(TRIS buffer, stained DNA 100dye/bp)

	free	dsDNA	ssDNA
Φ_F :	0.0004	0.69	0.39
τ :		4.78ns	2.26ns

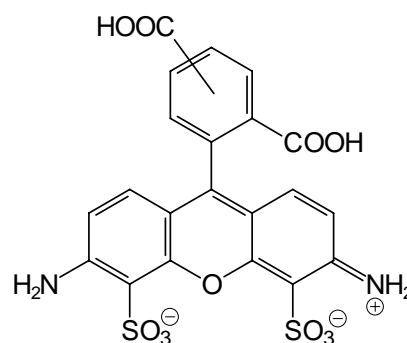
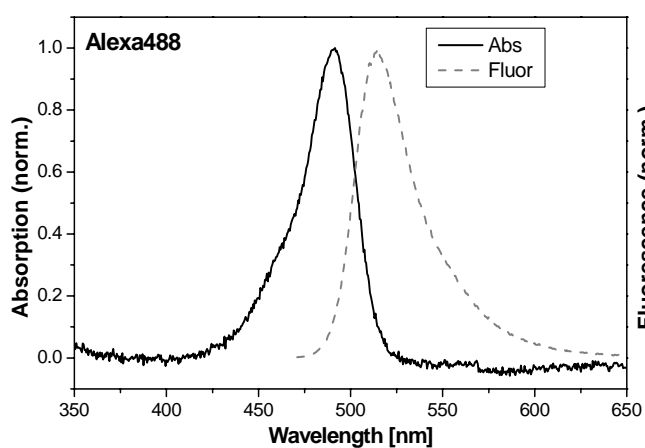
Atto 590

Absorption maximum: 592 nm

$\epsilon_{590 \text{ nm}}$: 120.000 M⁻¹cm⁻¹

Fluorescence maximum: 613 nm

Φ_F : 82% (TRIS buffer)

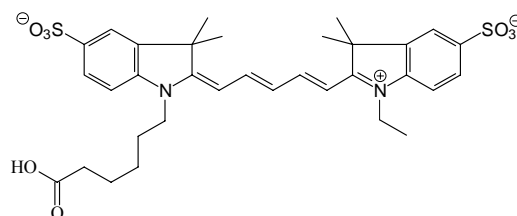
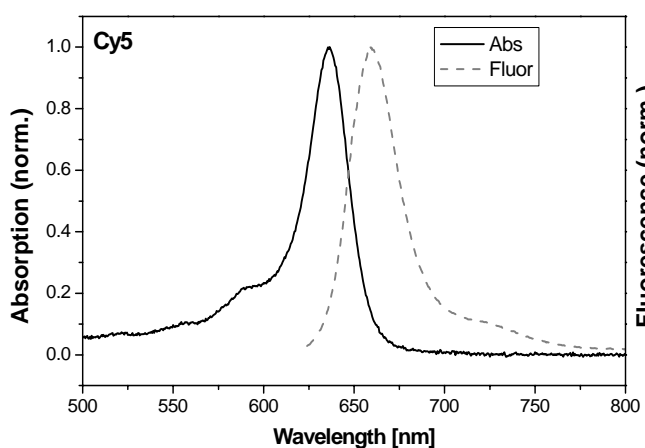
Alexa 488

Absorption maximum: 495 nm

$\epsilon_{495 \text{ nm}}$: 71 000 M⁻¹cm⁻¹

Fluorescence maximum: 519 nm

Φ_F : 0.90 (PBS buffer)

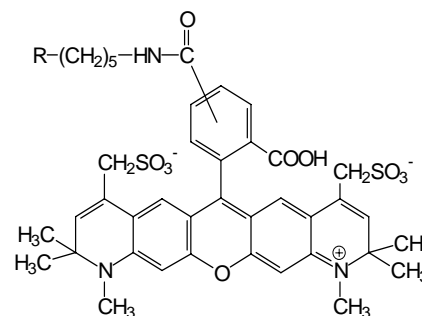
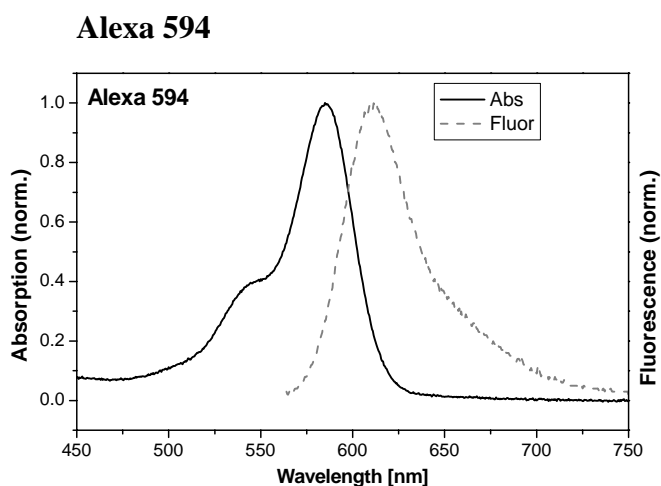
Cy5

Absorptions maximum: 649 nm

$\epsilon_{649 \text{ nm}}$: 250 000 M⁻¹cm⁻¹

Fluorescence maximum: 670 nm

Φ_F : 0.40 (PBS buffer)



Absorption maximum: 585 nm

$\epsilon_{585 \text{ nm}}$: 73 000 M⁻¹cm⁻¹

Fluorescence maximum: 610 nm

Φ_F : 0.86 (PBS buffer)

Cantilevers

Nanosensors cantilevers (Nanosensors GmbH, Wetzlar-Blankenfeld) with high aspect ratio (3:1), pyramidal shape, Si tips with a nominal tip radius of 10 nm and a spring constant of 42±5 N/m were used for AFM imaging.

Cantilevers examined in Section 2.4 for the tips fluorescence signal:

- 1) Olympus biolever, a soft Si₃N₄ cantilever gold coated on both sides (# BL-RC150VB, Atomic Force F&E GmbH, Mannheim);
- 2) Veeco Si₃N₄ cantilever, gold coated on the tip side (NPG, Veeco Instruments GmbH, Mannheim);
- 3) Veeco Microlever Si₃N₄ cantilever (former Park microlever, # MLCT-AUHW, Veeco Instruments GmbH, Mannheim);
- 4) Nanosensors Si tapping tip (# FM-20, NanoAndMore GmbH, Darmstadt);
- 5) Nanotools Si cantilever with a high density carbon (HDC) tip of more than 0.6µm length grown at the apex (Type U2, Nanotools GmbH, Munich).

For the force spectroscopy of DNA molecules as well as for the combined optical and fluorescence experiment soft Veeco Si₃N₄ cantilevers (NPG, Veeco Instruments GmbH, Mannheim) were used.

2.3 Transparent surface substrates preparation and characterization

Reproducible preparation of surfaces for various applications is motivated by academic interests and also finds many technological applications. Clean, smooth and compositionally reproducible sample surfaces are desirable for a thin metal film deposition [132], express analysis and a stable spatially controlled immobilization of biomolecules [133-139]. The immobilization can be mechanical (on local structures in topography), electrostatic (uncompensated charge on the surface) or chemical (active chemical groups). Each method can be preferable for a particular combination of a biomolecule and experimental conditions. Existing methods propose high precision in spatial control of immobilization-active surface areas. A covalent immobilization procedure may be harmful for molecules due to particular reaction conditions of the covalent binding. It however provides stable attachment and adsorption selectivity due to the active layer functionalities. A modification of surfaces with silanes and poly(ethylene glycol) derivatives provides surfaces for a flexible surface chemistry and a stable biomolecules support.

The quality of a surface for adsorption and immobilization of biomolecules is known to dependent on each step of the surface pre-treatment and modification. The influence of preparation steps was investigated by the use of a combination of optical and atomic force microscopy. Several requirements have to be strictly fulfilled for the reproducible surface chemistry establishment and suitability of glass substrates for combined simultaneous fluorescence and force spectroscopy.

A single biomolecule (object) adsorbed on the surface can either be found via AFM or optical microscopy. A flat surface will facilitate finding of molecules with AFM. Transparent surfaces showing low scattering/fluorescence signals make it easy to locate the fluorescence light from molecules (or a labelled macromolecule). The fluid cell geometry of the experimental setup imposes limitations on size and thickness of the surface substrates as well as on its optical properties.

Substrates surface quality, cleaning procedures and chemically-active layer depositions are examined based on the experimental requirements to the sample.

Various glass types were investigated by the AFM and optical spectroscopy. Several different glass cleaning procedures have been tested and final substrate cleaning protocols are suggested for several applications.

2.3.1 Silicon oxide (SiO₂) surface

Silicon oxide surfaces are used for several reasons: relatively low topographical roughness which is important for AFM studies of single molecules; substrates transparency which is required for SFFS; flexible and well developed surface chemistry modification.

The surface of silicon consists of a large number of native silicon oxide SiO_x molecules. They form a layer resulting from the oxidation in air which has thickness around 1-2 nm and 5×10^{14} SiOH groups/cm² [140]. The SiO_x layer makes surface chemistry of silicon and silicon oxide (glass and quartz) similar. At normal conditions water molecules bind to the silicon oxide surface. Siloxane bonds between Si atoms and O atoms can react with water and generate silanol groups (SiOH), important for the chemical treatment. The amount of water depends on the relative humidity and is difficult to control. It is known to be 2.5-4 H₂O molecules/nm² and more than 3.1 OH groups/nm² at standard atmosphere conditions and temperatures between 22-150°C [141].

It is generally known that glass slides are prepared either by mechanical drawing malleable glass or by casting molten glass on liquid Sn [132,142]. Drawn glass slides are also named as “water white” glass, can vary in roughness from batch to batch. They can be distinguished from float glass by the colour observed viewing the slides along an edge. Drawn glass is clear whereas float glass is a light green. The float glass is usually flat, but the two sides can be very different in structure due to different conditions in fabrication. Various cleaning and chemical treatments result in different surface composition and surface roughness [143-147]. Glass substrates were found to be a critical issue for the further reproducible handling of substrates for metal film deposition applications [132]. Similar problem take place for chemical modification of glass surface.

Different glass substrates studied are listed in the table (Table 2-7).

Table 2-7. Information about studied glass/quartz substrates

	Sample	Geometrical parameters /thickness	Refraction index	Index/Source	Fabrication type
1.	Glass	24×24mm and 24×60mm /0,16-0,19mm	n = 1,523	(Mendel)	drawn
2.	Quartz	18×18mm /0,16-0,19mm	n = 1,553	test sample (Olympus)	unknown
3.	Glass	18×18mm /0,16-0,19mm	n = 1,521	test sample (Olympus)	unknown
4.	Quartz #1420	25mm (diameter) /0,16-0,19mm	unknown	test sample (Mendel)	unknown

AFM studies of different substrates reveal the maximal roughness to be up to 100 nm for non-cleaned surfaces. Particles and large contaminated areas can be observed (see Figure 2-3 to Figure 2-5).

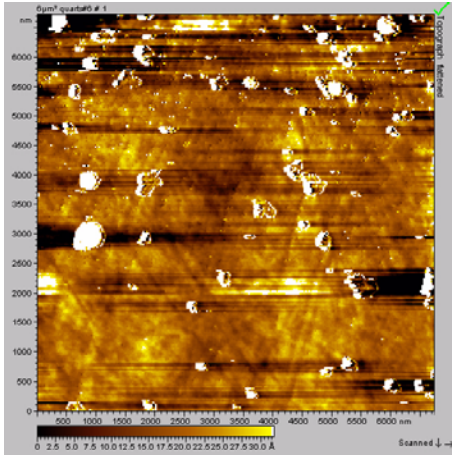


Figure 2-3. AFM image of a contaminated SiO₂ substrate (6×6 μm², quartz test sample from Olympus). Lines (polishing scratches) are visible.

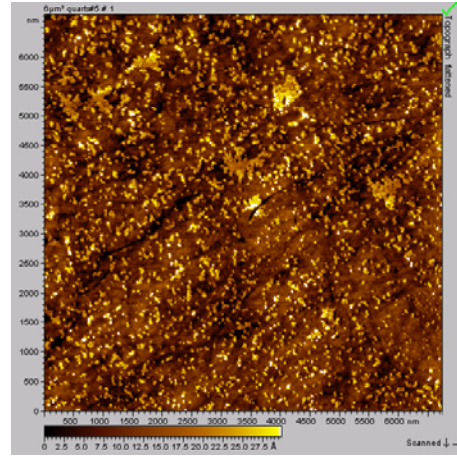


Figure 2-4. AFM image of another strongly contaminated SiO₂ substrate (6×6 μm², quartz test sample from Olympus). Polishing scratches could hardly be recognized.

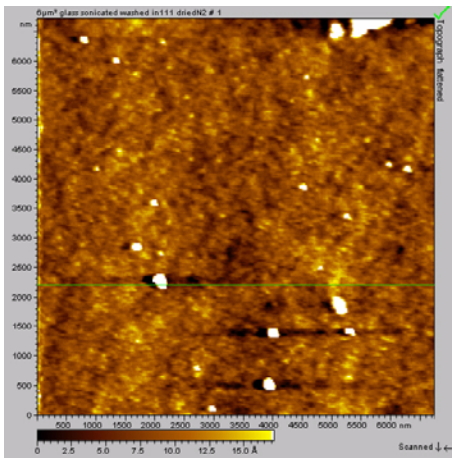


Figure 2-5. AFM image of a typically contaminated SiO₂ substrate (6×6 μm², glass from Mendel).

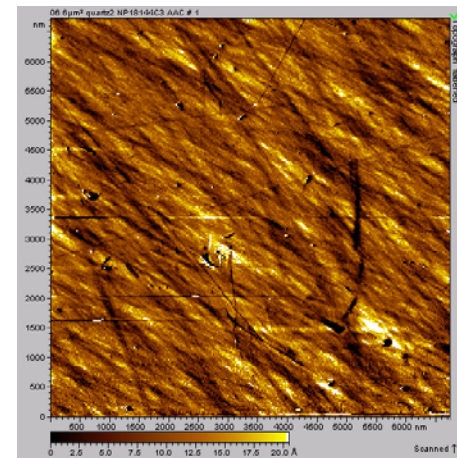


Figure 2-6. AFM image of contaminated quartz from Mendel (6×6 μm² area). The surface is less contaminated.

2.3.2 Surface cleaning procedures

A glass surface may be contaminated with water-soluble or water-non-soluble contaminants. Furthermore, micro- and nano-particles may stay on the surface after glass polishing procedures or appear in some of the surface cleaning steps. A surface cleaning protocol is important for a particular experiment and is normally aimed to remove contaminations.

Based on different cleaning approaches, developed for SiO₂ and Si surfaces in AFM and optical microscopy, several procedures were tested. All cleaning protocol steps are listed in

Table 2-8. Atomic force microscopy at high spatial resolution requests very clean surfaces. Among various possibilities surface can be cleaned with acetone or ethanol [144,148], different etchants [142,146], “piranha” solution [149], CO₂ ice cleaning [150], etc. Aggressive cleaning procedures also remove carbon contaminations, etch upper silicon layers and allow the subsequent regrowth of the silicon oxide. Glass post-treatments (modifications) of the surface tighten the requirements for the glass treatment. Usually, the increase of the number of reactive hydroxyl groups by breaking siloxane bonds is useful (see silanization and PEGylation sections).

In the case of fluorescence microscopy, luminescent properties of the surface are more important than surface topography since the spatial resolution is typically not good enough to detect small particles on the surface. All glass types listed in Table 2-7 can be used without additional cleaning for single molecule fluorescence measurements in solution. They do not show noticeable fluorescence signal [151]. However, for “on surface” fluorescence experiments crucial factors are the cleanness (non-fluorescence) of the glass surface and the subsequent chemical modification (see Section 2.3.6). Multiple step cleaning protocols were developed to remove loosely bound fluorescence impurities, debris and oil deposits [152,153].

Table 2-8. Cleaning protocols tested

A:	1. Washing in a “piranha” solution (H ₂ O ₂ / H ₂ SO ₄ , ratio 1:3)	15 min
	2. Sonication in a double distilled water (dH ₂ O)	30 min
	3. Drying with nitrogen	
B:	1. Sonication in dH ₂ O / propanol (C ₃ H ₈ O), ratio 1:1	30 min
	2. Washing on heat plate (90°C) in dH ₂ O / H ₂ O ₂ / ammonium hydroxide (NH ₄ OH), ratio 1:1:1	20min
	3. Sonication in dH ₂ O	30 min
	4. Drying with nitrogen	
C:	1. Sonication in acetone	30 min
	2. CO ₂ ice cleaning	
D:	1. Sonication in acetone	30 min
	2. Sonication in methanol	30 min
	3. Sonication in dH ₂ O	60 min
	4. Drying with nitrogen	
E:	1. Sonication in 2-4% detergent (Helmanex) solution in dH ₂ O	30 min
	2. Sonication in dH ₂ O	30 min
	3. Sonication in acetone	30 min
	4. Sonication in ethanol	30 min
	5. Sonication in dH ₂ O	15 min
	6. Drying with nitrogen	

Figure 2-8 to Figure 2-10 show the cleaning procedure capabilities to remove most of contaminations. However, chemical surface treatment does not result in reproducible surface flatness. It can hardly be improved and depends on a particular sample. Mean values for surface roughness do not exceed 3.5 nm (see Appendix A). It was also observed (not shown), that differently fabricated glasses have different topographical structure of the surface on different sides.

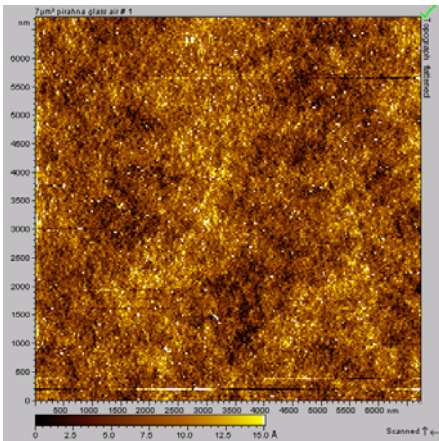


Figure 2-7. A typical AFM image of a glass surface ($7 \times 7 \mu\text{m}^2$), cleaned via A (Table 2-8).

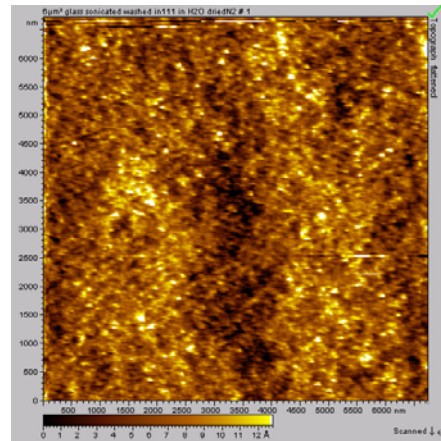


Figure 2-8. A typical AFM image of a glass surface ($6 \times 6 \mu\text{m}^2$), cleaned via B (Table 2-8).

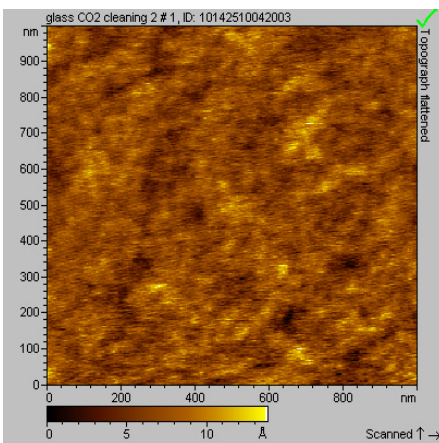


Figure 2-9. A typical AFM image of a glass surface ($1 \times 1 \mu\text{m}^2$), cleaned via C (Table 2-8).

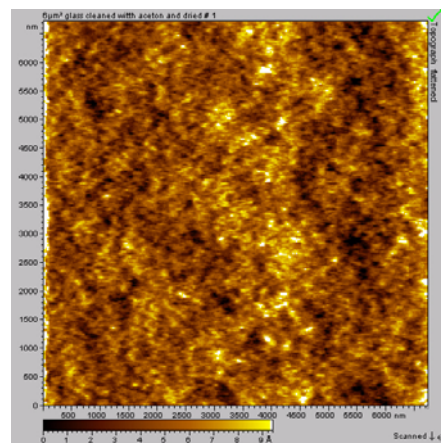


Figure 2-10. A typical AFM image of a quartz surface ($6 \times 6 \mu\text{m}^2$), cleaned via D

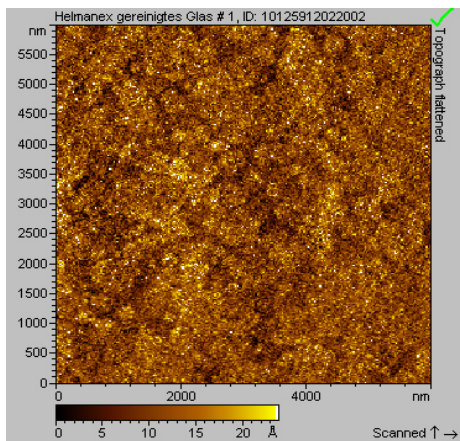


Figure 2-11. A typical AFM image of a glass surface ($6 \times 6 \mu\text{m}^2$), cleaned via E (Table 2-8). Glass substrates cleaned using this procedure are used for further sample preparation.

2.3.3 Silanization of silicon oxide surface

The silanization process involves the covalent binding of silane molecules to the surface and the formation of a durable bond between organic and inorganic materials. Silane general formula indicates two classes of functionality (Figure 2-12). At least one X is a hydrolysable reactive group ($-\text{OH}$, $-\text{OCH}_3$, $-\text{OCH}_2\text{CH}_3$, etc.), which is responsible for a reactive silanol group formation and a following siloxane bonding with a surface or other silane molecule. Otherwise these are nonreactive groups ($-\text{H}$, $-\text{CH}_3$). The R group is a nonhydrolysable organic radical possessing the functional characteristics of a silane surface layer. In this work different silanes are used, depending on the experiment. Further information about silanes and structure are given in Table 2-9 as well as in Figure 2-13.

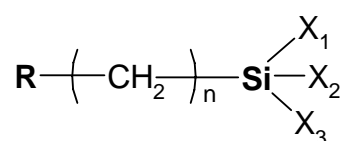


Figure 2-12. Schematic representation of a silane molecule structure. R stands for a functional organic radical (amino, epoxy). X is a hydrolysable reactive group ($-\text{OH}$, $-\text{OCH}_3$, $-\text{OCH}_2\text{CH}_3$, etc.) or a nonreactive group ($-\text{H}$, $-\text{CH}_3$).

Table 2-9. Information about silanes

Silane/Formula/ Abbreviation	Application
3-Aminopropyldimethylethoxysilane, $\text{C}_7\text{H}_{19}\text{NOSi}$ (APDES)	non covalent immobilization
3-Aminopropyltriethylethoxysilane, $\text{C}_9\text{H}_{23}\text{NO}_3\text{Si}$ (APTES)	non covalent immobilization
3-Glycidoxypropyldimethylethoxysilane, $\text{C}_{11}\text{H}_{24}\text{O}_4\text{Si}$ (GOPDES)	covalent immobilization, PEGylation
3-Glycidoxypropyltrimethoxysilane, $\text{C}_9\text{H}_{20}\text{O}_5\text{Si}$ (GOPTS)	covalent immobilization, PEGylation

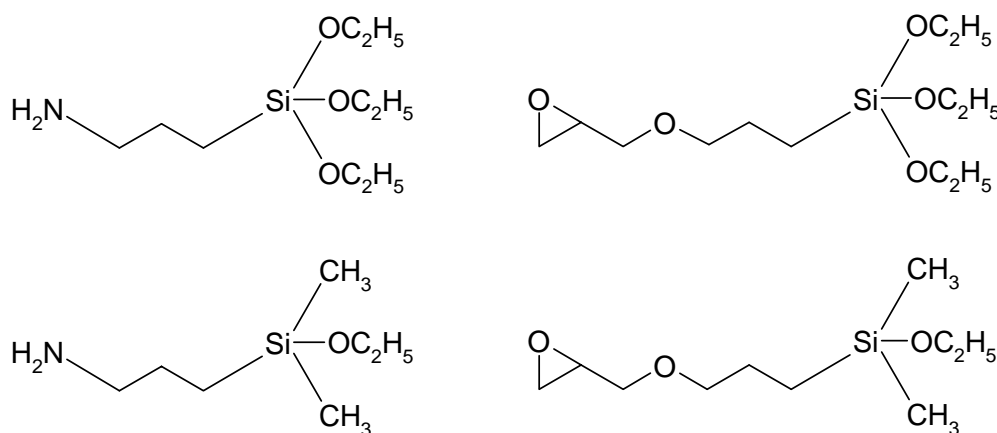


Figure 2-13. Schematic representation of different silane molecules (Table 2-9): a multireactive aminosilane APTES (left, top), a monoreactive aminosilane APDES (left, bottom), a multireactive epoxysilane GOPTS (right, top) and a monoreactive epoxysilane GOPDES (right, bottom).

The silanization process can be divided into two cases depending on the conditions: hydrolytic and anhydrous. At hydrolytic conditions [140] the surface modification consists of several steps and may be illustrated by the following scheme. First, a hydrolysis of reactive groups occurs. It is followed by the condensation of hydrolyzed silane molecules. Silane molecules containing more than one reactive group can polymerize. The degree of polymerization depends on the initial amount of water. The choice of the glass cleaning procedure, silanization pre-treatment and silane solvent defines the amount of water involved in the process. At high water concentration, silane molecules may collapse and cause the formation of heterogeneous structures in the following silanization steps. However, polymerized molecules with just one reactive site are excluded from the process in this step. A condensation is followed by hydrogen bonding with OH groups to the substrate. Finally, covalent bonds form during drying at high temperature (so called “curing”) process. Hydrolytic depositions usually result in the formation of multilayer. Multilayers are attached to the surface at many points; they are usually mixed and interconnected.

Anhydrous silanization occurs via direct reaction of silane reactive groups with hydroxyl groups present on the surface. A lack of water prevents silane polymerization and results in a silane monolayer formation.

Depending on the silanization conditions, liquid and gas phase silanization methods can also be distinguished. The silane solvent and the silanization time were varied for the liquid phase. Liquid phase silanization is performed in a glass beaker, according to the following protocol:

1. Clean silicon oxide surfaces up to step 5 as indicated in case cleaning procedure E (Table 2-8).
2. Sonicate in acetone for 30 min.
3. Immerse glass slides in 2% silane solution in acetone and leave overnight (~14h).
4. Wash in acetone for 5min.
5. Rinse with water.
6. Dry with nitrogen flow.

Gas phase silanization is performed in a nitrogen atmosphere in a polypropylene tube (a modification of the method of Pavlovich et al. [154]). Here after step E4 (Table 2-8) the surfaces were placed into the polypropylene tube on a teflon glass holder. The nitrogen enters the tube through a buffer filter at a flow of approximately 1 L/min. In 1h a droplet of a silane is placed into the tube with a syringe needle and left for surface silanization for 2h. Silanized surfaces are clean and can be used immediately.

Aminosilanized glass slides show high hydrophobicity. They can be stored under normal conditions at a dark place for a long time (up to 8 month tested) and used for the immobilization of biomolecules without further treatment. However, longer storing times or improper conditions can result in surface contaminations and an increase of fluorescence. Epoxysilanised glasses are hydrophilic and require a special storage atmosphere, since active epoxy groups can react with water. Epoxysilanised glasses can be stored up to three month (longest time tested).

A typical surface of amino and epoxy modified glass slides obtained with AFM is presented in Figure 2-14. The silanization results in homogeneous surface structures with low roughness and a lack of contaminations over large surface areas.

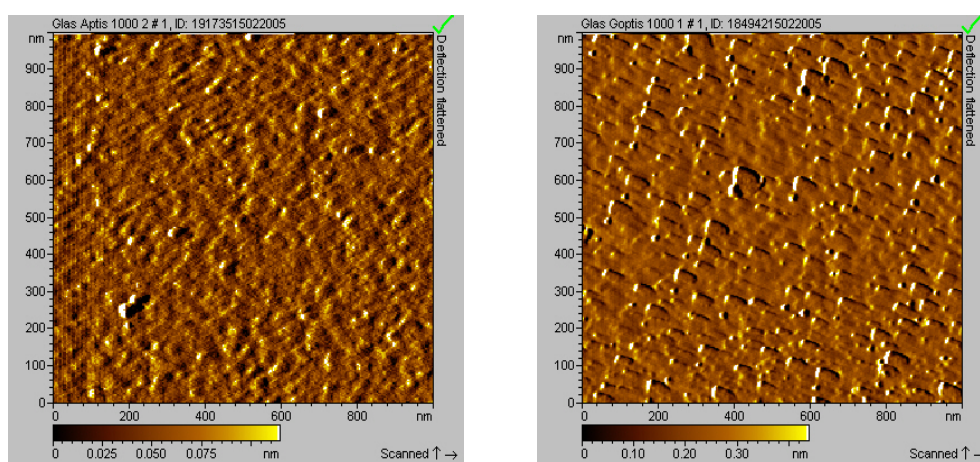


Figure 2-14. A typical AFM deflection image of APTES silanized glass surface $1 \times 1 \mu\text{m}^2$ (left); and AFM deflection image of GOPTS silanized glass surface $2.2 \times 2.2 \mu\text{m}^2$ (right).

2.3.4 Surface PEGylation

The variety of surface chemistry for further immobilization of biomolecules is enriched by silanized glass coverslide modification with poly(ethylene glycol) (PEG). PEG is a highly investigated polymer for the covalent modification of biological macromolecules and surfaces [155].

Samples with various surface modifications were obtained from the group of Prof. G.Gaugglitz⁴ (University of Tübingen). A preparation of microscope glass plates includes washing and activation with a mixture of $\text{H}_2\text{SO}_4/\text{H}_2\text{O}_2$, followed by silanization with GOPTS epoxy silane. Mono- and bi- functional PEG coverage produces substrates with different surface properties: Dicarboxy-PEG (highly negatively charged surface), Carboxy-Methoxy-PEG (slightly negatively to neutrally charged surface), Amino-Hydroxy-PEG (slightly

⁴ Dr. Oliver Birkert is gratefully acknowledged for the granted test samples.

negatively to neutrally charged surface), Amino-Methoxy-PEG (slightly negatively to neutrally charged surface) and Diamino-PEG (highly positively charged surface). PEG – GOPTS Langmuir-Blodgett coated microscope glass cover slides from Molecular Machines and Industries (Heidelberg) [156] were also tested.

Alternatively, epoxy silanized glass coverslips are covered with pure PEG derivatives according to modification of Piehler et. al protocol [157]. Slides are assembled face-to-face avoiding exposure to the atmosphere and allowing for PEG melting on the surface at 75°C for 24h. Afterwards the surfaces were thoroughly rinsed with water and dried at room temperature. Commercial slides were found to be microscopically rough (see Figure 2-15 to Figure 2-20). Various AFM scans over large areas reveal contaminated surfaces. However, small and relatively flat regions can be found on every sample. The contamination source may be the PEGylation procedure or improper sample handling.

The surface PEGylation process is less reproducible than the surface silanization and often results in crystal-like structure formation on surfaces (results not shown).

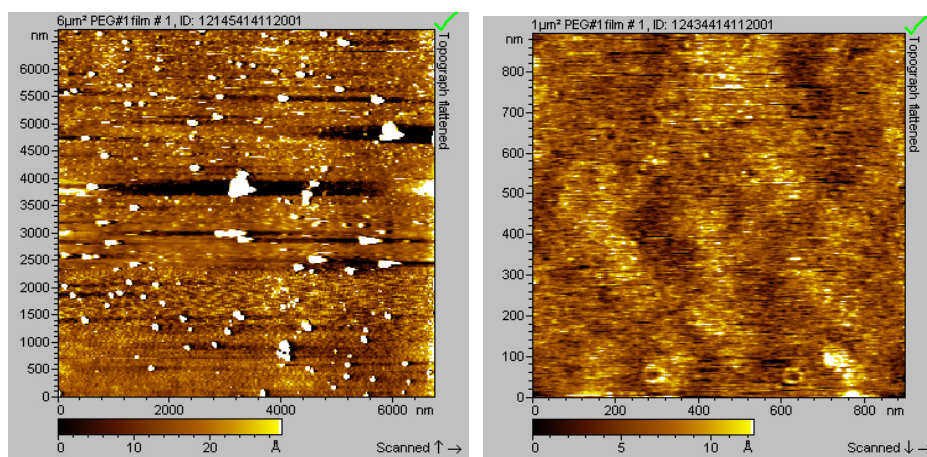


Figure 2-15. A typical AFM image of Dicarboxy-PEG modified glass surface ($7.5 \times 7.5 \mu\text{m}^2$, left) and the same glass surface ($0.9 \times 0.9 \mu\text{m}^2$, right).

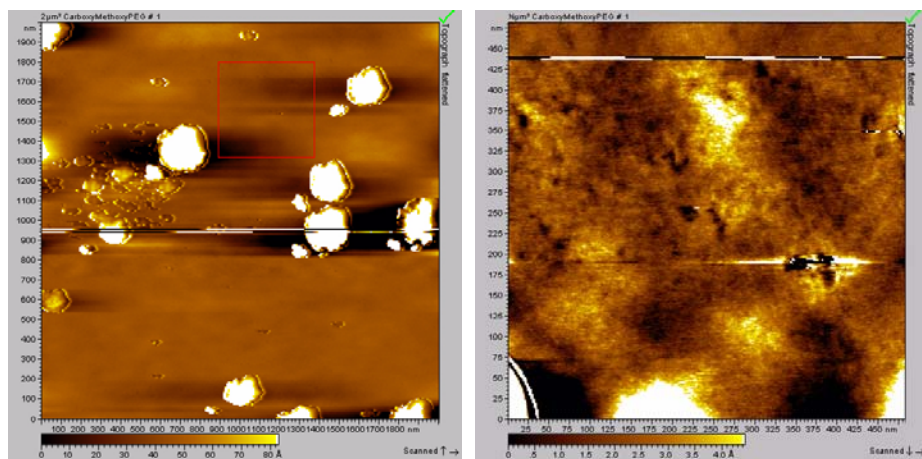


Figure 2-16. A typical AFM image of a Carboxy-Methoxy-PEG modified glass surface ($2 \times 2 \mu\text{m}^2$, left) and the same glass surface ($0.5 \times 0.5 \mu\text{m}^2$, right).

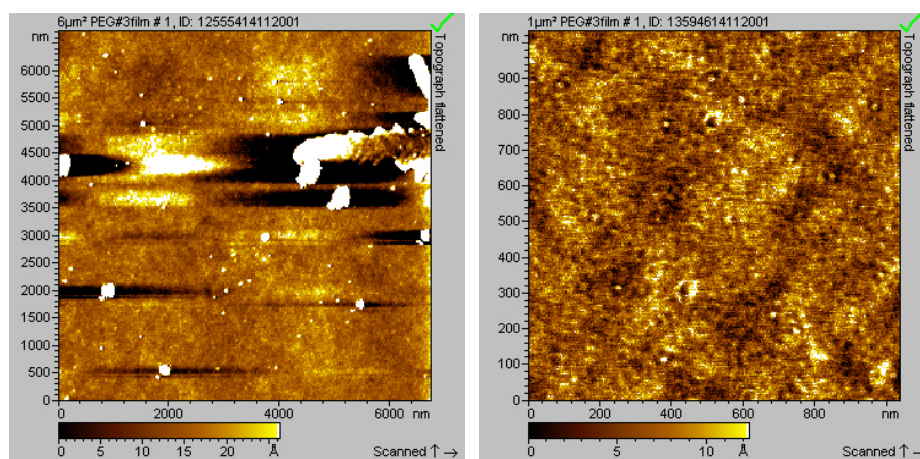


Figure 2-17. A typical AFM image of Amino-Hydroxy-PEG modified glass surface ($7.5 \times 7.5 \mu\text{m}^2$, left) and the same glass surface ($1 \times 1 \mu\text{m}^2$, right).

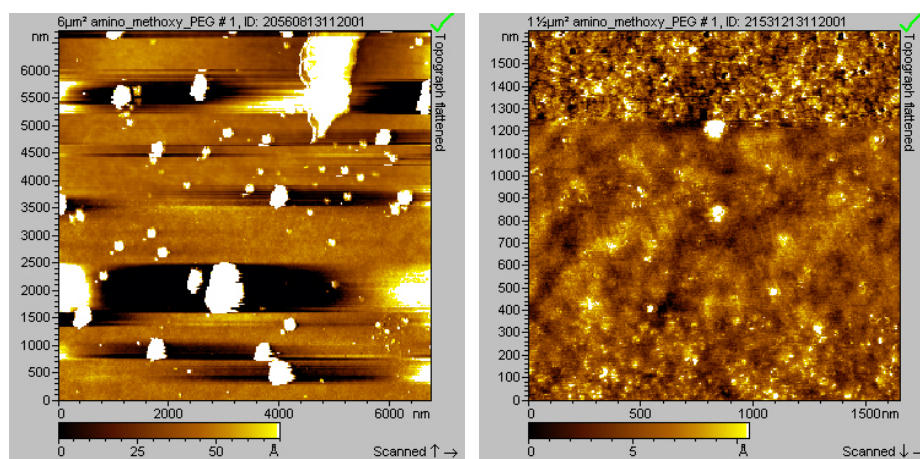


Figure 2-18. A typical AFM image of Amino-Methoxy-PEG modified glass surface ($7.5 \times 7.5 \mu\text{m}^2$, left) and the same glass surface ($1.75 \times 1.75 \mu\text{m}^2$ right).

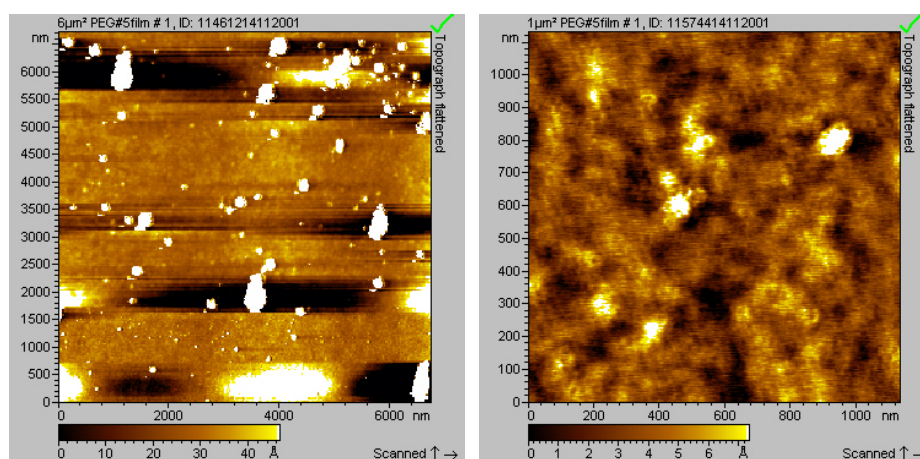


Figure 2-19. A typical AFM image of Diamino-PEG modified glass surface ($7.5 \times 7.5 \mu\text{m}^2$, left) and the same glass surface ($1.2 \times 1.2 \mu\text{m}^2$, right).

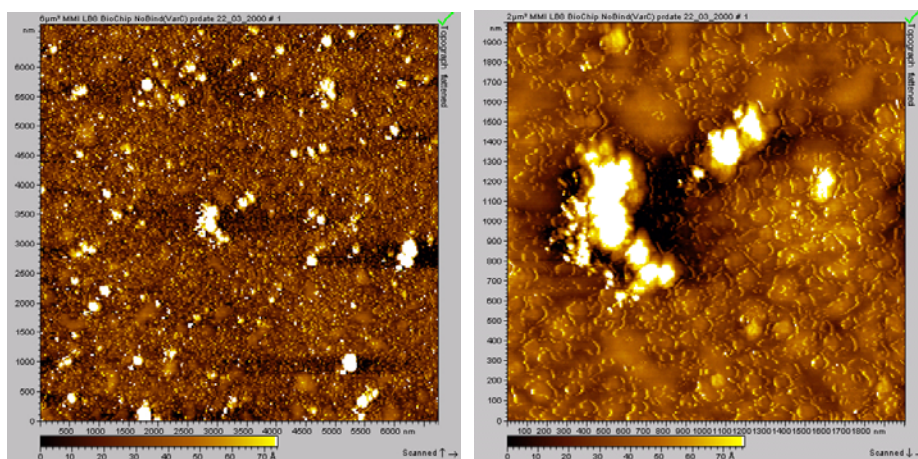


Figure 2-20. A typical AFM image of MMI LB8 BioChip - a PEG covered glass surface ($7.5 \times 7.5 \mu\text{m}^2$, left) and ($2 \times 2 \mu\text{m}^2$, right).

2.3.5 Immobilization of biomolecules (DNA)

Biomolecules can be either specifically or non-specifically immobilized on a surface. The electrostatic adsorption of DNA molecules to a mica surface where surface charges are compensated by divalent ions in the buffer [158,159] allows obtaining images of adsorbed DNA molecules (Figure 2-21).

Electrostatic interactions can also drive the molecular adsorption process for the negatively charged molecules and uncompensated charges of silane or PEG amino functional groups on the surface in liquid [160]. The adsorption efficiency of DNA molecules depends strongly on adsorption conditions e.g. a buffer's ionic strength and its pH values [161,162].

A surface modified with properly selected functional groups offers a specific immobilization of biomolecules via covalent bonds formation [137,163,164].

An AFM investigation of amino-silanized glass slides with DNA molecules adsorbed show how difficult it is to find the area with a clear picture of a single DNA molecule (Figure 2-22). Experimental difficulties can be explained by high roughness and increased heterogeneity of a modified glass surface in comparison with a mica surface.

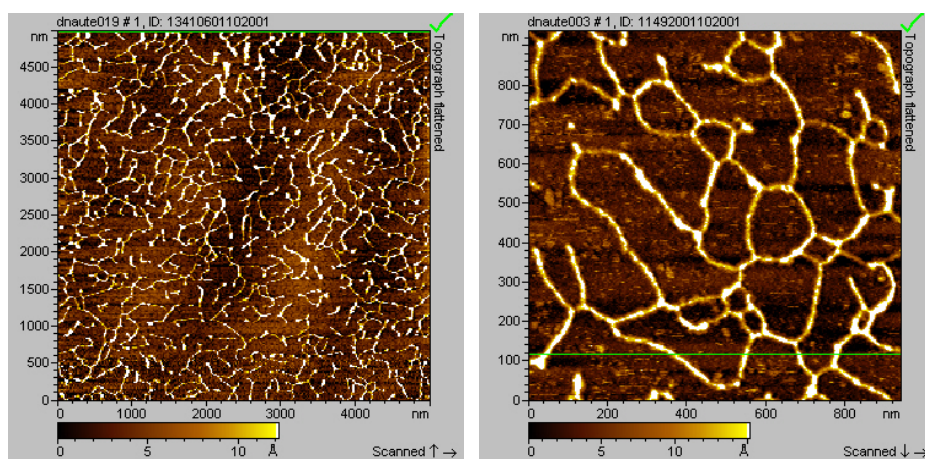


Figure 2-21. AFM topography images of λ -DNA molecules adsorbed on mica surface $5 \times 5 \mu\text{m}^2$ (left) and $0.95 \times 0.95 \mu\text{m}^2$ (right).

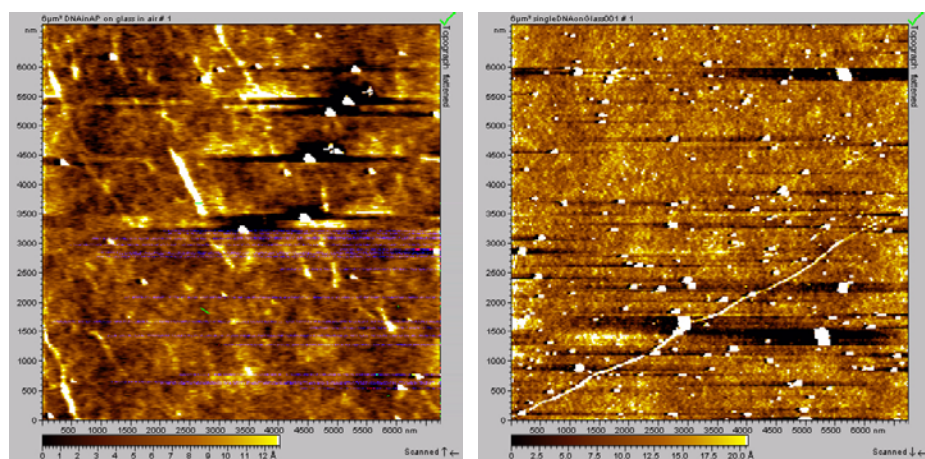


Figure 2-22. AFM topography images of λ -DNA molecules adsorbed on APTES modified glass cover slides. Images were obtained in liquid $7.5 \times 7.5 \mu\text{m}^2$ (left) and in air $7.5 \times 7.5 \mu\text{m}^2$ (right). Surface contamination with particles coming from buffer solution is observed. It increases when the sample is dried. The Si cantilever used for imaging has a spring constant of 42 N/nm. The radius of the pyramidal tip is 10 nm.

2.3.6 Fluorescence studies of surface modification steps

Complementary to AFM studies, the quality of glass modification steps and the immobilization of DNA molecules onto a modified glass surface are studied by TIRF.

Figure 2-23 presents the typical results of TIRF imaging of untreated Mendel glass and the same glass after cleaning (procedure E, Table 2-8). The untreated Mendel glass (left) is “dirty” in comparison with the cleaned one (right): bright spots are observed in the round-shaped illumination area. The cleaned glass is less fluorescent at the same illumination and imaging conditions. The evanescent field interference pattern is recognizable. The same result is observed for quartz surfaces. Glass cleaning procedure helps to obtain a low background and allows single dye molecules fluorescence detection on the surface (Figure 2-29, left).

The shapes of the luminescence spectra are quantitatively and qualitatively different for glass and quartz surfaces (Figure 2-24). Glass surfaces show smooth and in general a bit more intense spectra than quartz surfaces. In addition, different quartz samples reveal peaks at 520 nm to 580 nm due to the Raman scattering on polycrystalline quartz surfaces. The wide band in the range of 580-610 nm corresponds to the water Raman scattering. The Raman signal is increased when the laser light is focused 5 μm above the surface in water as shown in Figure 2-24b. The overall luminescence intensity of glass/quartz substrates is comparable to the Raman signal from water.

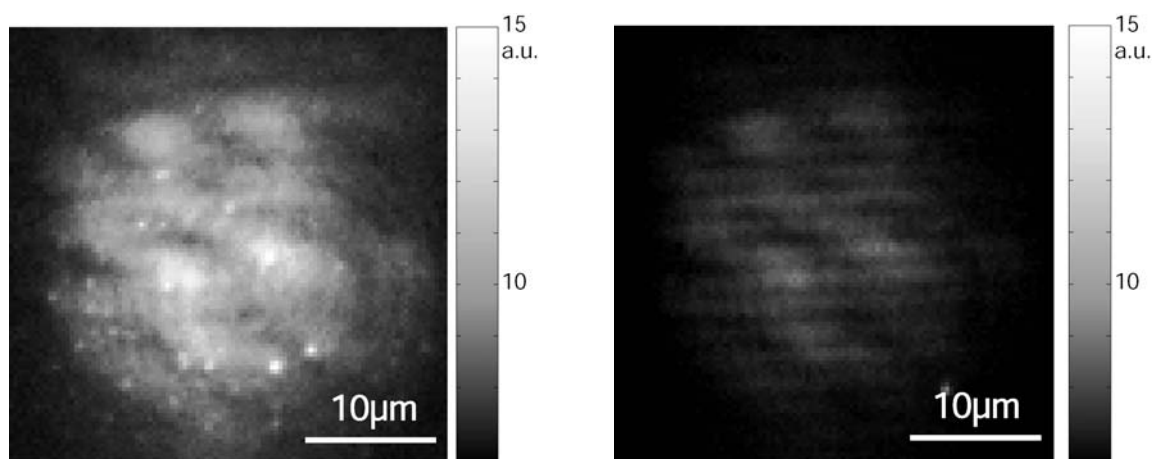


Figure 2-23. A typical TIR optical image of “dirty” glass surface (left) and cleaned one (procedure E, Table 2-8). The TIR illuminated area is visible as a bright spot of approx. 30 μm in diameter. The bright spots in the left image are due to the fluorescence contamination of the surface and they are not observed in the image on the right side. The excitation irradiance is $\sim 100 \text{ W/cm}^2$, the acquisition time is 1 sec.

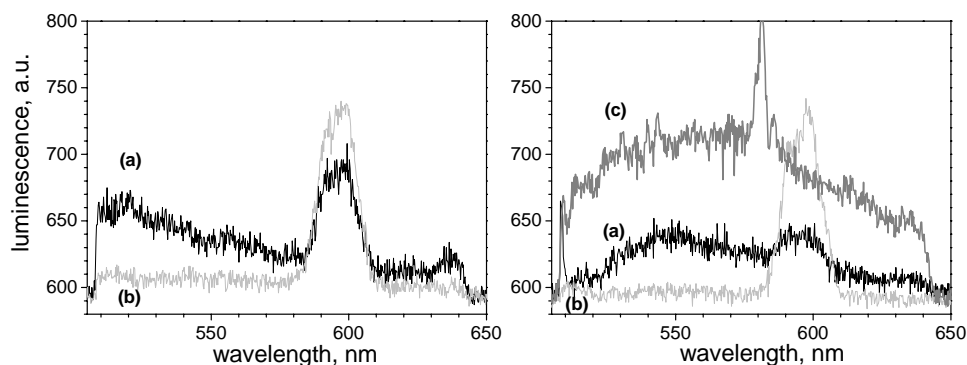


Figure 2-24. Typical luminescence spectra for differently cleaned (Table 2-8, E) glass and quartz substrates: a glass from Mendel (left, a), a quartz test samples from Olympus (right, a) and a quartz sample from Mendel (right, c). The laser light is focused on the glass surface which is covered with clean water. The Raman scattering spectrum of water, obtained 5 μm above the surface, is shown in both cases (b). The laser is focused into a 2 μm diameter spot by a 100 times magnification oil-immersion objective lens. The laser power at the objective plane is 35 μW . A confocal pinhole of a 200 μm diameter is used for the luminescence signal detection.

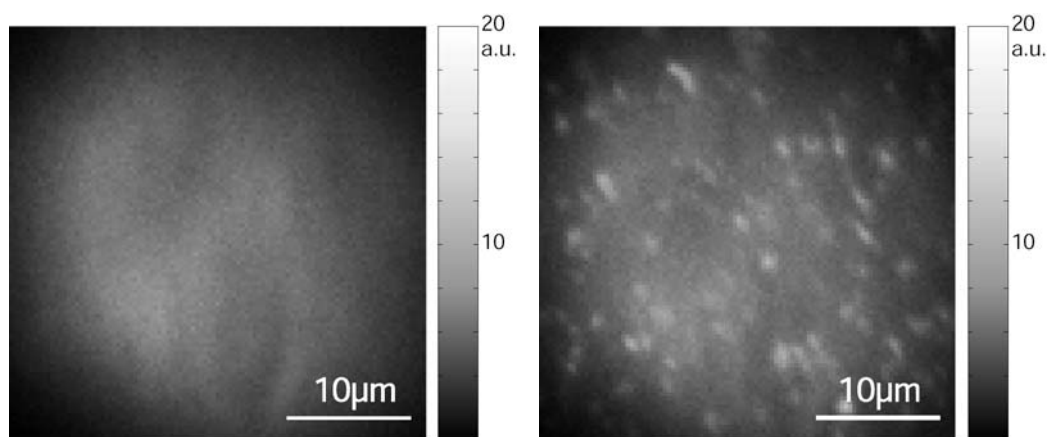


Figure 2-25. A typical optical TIR image of a glass surface modified with amino-functional silane (APTES). Left: SYBR Green I fluorescence dyes in buffer solution. Right: SYBR Green I fluorescence dyes in buffer solution and DNA molecules electrostatically adsorbed on the surface. Excitation irradiance is $\sim 25 \text{ W/cm}^2$, acquisition time 0.25 sec., 1-10 μM SYBR Green I dye concentration.

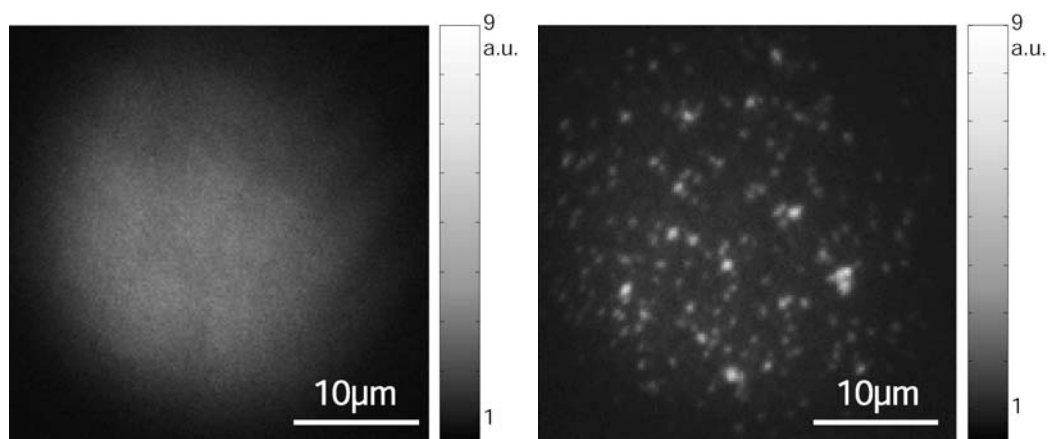


Figure 2-26. A typical optical TIR image of a glass surface modified with epoxy-functional silane (GOPTS). Left: SYBR Green I fluorescence dyes in buffer solution. Right: SYBR Green I fluorescence dyes in buffer solution and DNA molecules electrostatically adsorbed on the surface. Excitation irradiance is $\sim 25 \text{ W/cm}^2$, acquisition time 0.25 sec., 1-10 μM SYBR Green I dye concentration.

A surface cleaning is sufficient for further surface modification. Clean chemicals (spectroscopy grade) are used for further surface modification steps in order to keep the luminescence signal from the cleaned surfaces low and homogeneous. The surface silanization does not result in poorer optical quality of the surface. Optical images of a clean APTES silanized glass surface and an APTES silanized surface with DNA molecules adsorbed are shown in Figure 2-25. DNA binding fluorescence dyes (SYBR Green I) are present in the buffer solution in both cases. The dye shows low fluorescence in the absence of DNA molecules (Figure 2-25, left). The fluorescence quantum yield of the dyes increases 1000-1500 times when the dyes binds to DNA molecules and thus helps to visualize DNA molecules adsorbed on the surface (Figure 2-25, right). Similar results for GOPTS silanized glass surfaces are presented in Figure 2-26. In the case of GOPTS functionalized surfaces,

DNA molecules bind to the surface specifically. Covalent bonds form after the reaction between the active epoxy groups on the surface and the amino groups of functionalized DNA molecules (Table 2-6).

The PEGylation procedure results in surface contamination: bright fluorescent spots appear on the surface and the optical images look like the optical images of not cleaned glass or even worse. The luminescence spectra obtained for silanized and PEGylated glass surfaces do not differ from the luminescence spectra of clean glass surfaces which may be explained by a low sensitivity of such measurements to several luminescent spots on the surface. Bulk luminescence spectra of PEG solution in ethanol reveal strong fluorescence, which indicates the contamination of PEG powder (results not shown).

2.3.7 Conclusions

The results of AFM surface topology studies of different SiO₂ substrates indicate that glass cleaning successfully removes contaminants (Figure 2-7 to Figure 2-11). The results are summarized in the table in Appendix A.

The surface modification (silanization) provides stable support for biological molecules. The identification of single biomolecules by means of AFM is difficult due to the relatively rough surface (up to 3.5 nm RMS) of the modified glass substrates (Figure 2-22). A single DNA molecule localization on a glass surface prior to mechanical manipulation experiments was found to be complicated. It is advisable that other Si-based substrates with less rough surface topology than glass or quartz should be used for these purposes.

The optical signal from a cleaned glass and a modified glass is very low and contains mainly the Raman scattered light. High purity chemicals are preferred for the surface cleaning as well as for the surface functionalization and the immobilization of the molecules. Optical microscopy allows detecting the fluorescence of a single DNA molecule labelled with fluorescent dye (Figure 2-25, right and Figure 2-26, right). That is required for the optical localization of the molecules prior to mechanical manipulations. The quality of the glass substrates (including the cleaning and modifications procedures) is also acceptable for the fluorescence detection of a single dye on a DNA molecule.

2.4 Multiparameter fluorescence imaging development and application to cantilever tip fluorescence characterization

Knowledge of the optical properties of AFM tips is relevant for the combination of optical and force spectroscopy. Detailed studies show whether the amount of scattered and luminescence light from an AFM tip would overwhelm the signal of a single fluorophore. Scanning techniques together with confocal MFD are used to measure all of the relevant parameters in a fluorescence signal (intensity, lifetime, anisotropy and spectral range) and also take into account scattered light in the signal. The multiparameter fluorescence imaging (MFI) technique evaluates the optical properties of different commercially available AFM cantilevers, quantifying the signal under epi-illuminated conditions and confocal fluorescence detection.

2.4.1 Cantilever in evanescent field

A number of researches have moved to an evanescent field excitation of molecular fluorescence. The evanescent field allows limiting the excitation volume (Section 1.3.5) and eliminating the possible effect of a high optical signal from an AFM cantilever tip [21,22]. The spatial heterogeneity of the evanescent field [165] (Figure 2-23, left) may still be a problem for the calibration of an optical signal from the cantilever as a function of tip-surface distance in various positions on the surface of the sample.

The fluorescence signals from a tip and different fluorescent objects are compared to estimate the “tip effects”. A cantilever tip (Veeco NPG) in contact with a surface and a fluorescent bead adsorbed on the surface are presented in a series of fluorescence images (Figure 2-27). The shape of the cantilever is clearly visible. The evanescent field illumination area is not clearly visible but has the same radially decreasing intensity profile for all pictures as in Figure 2-23. The intense signal at the lower edge of the cantilever is the unfiltered AFM IR laser light. The cantilever is moved in vertical direction and the maximum fluorescence signal from the tip and the bead are monitored as a function of the distance R between them. As the tip is moved towards the bead its maximum fluorescence signal decreases up to 37% of the initial signal (Figure 2-28). The bead shows a constant signal for large distances ($R = 9-5.5 \mu\text{m}$) and then a sudden signal increase up to 22% at $R = 3.7-2.5 \mu\text{m}$ distances is observed. The tip signal decrease and the simultaneous bead signal increase can be explained by local field effects (evanescent field perturbations) induced by the gold coated cantilever tip. However, the distances are too big for near field effects to take place [19,166-168].

The signal from the unmodified SiN₄ cantilever in an evanescent field is smaller than the signal from a fluorescent bead containing many molecules ($7,4 \cdot 10^3 - 1,1 \cdot 10^5$) [169] but it is still bigger than the signal from a single molecule.

Another experiment demonstrates that an optical signal of a Si cantilever in a water solution of freely diffusing dye molecules is comparable to what is observed from a single molecule (Figure 2-29). CCD imaging does not provide good temporal resolution and does not allow for time-resolved measurements. Exact characterization of tip's optical signal leads to multiparameter fluorescence imaging development, described below.

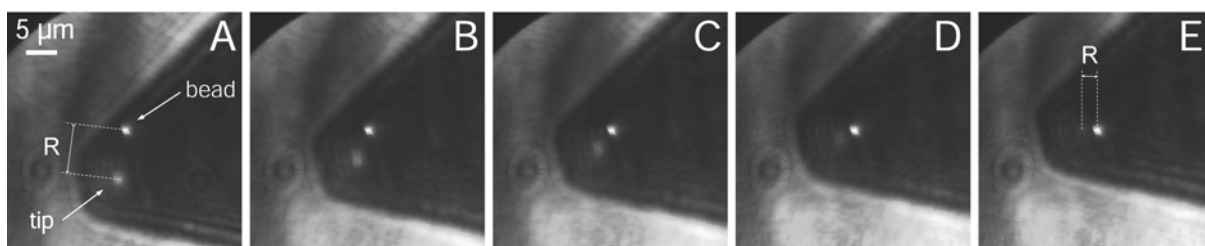


Figure 2-27. Optical microscopy images of a fluorescence bead and a Veeco NPG cantilever under evanescent field excitation conditions. The fluorescence signal from the bead is stronger than the signal from the tip. A decrease of the tip fluorescence is observed as the tip is moved towards the bead.

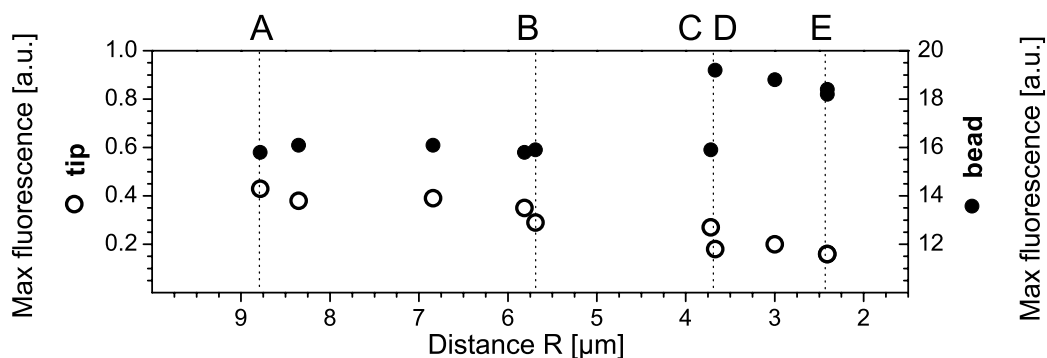


Figure 2-28. Maximum tip and bead fluorescence signals as a function of the distance between the tip and the bead. The signal from the tip decreases, when it moves towards the bead. The signal from the bead stays constant at distance 5.5–9 μm and increases at 2.5–3.5 μm. The maximum cantilever tip signal is much smaller than bead signal at all distances.

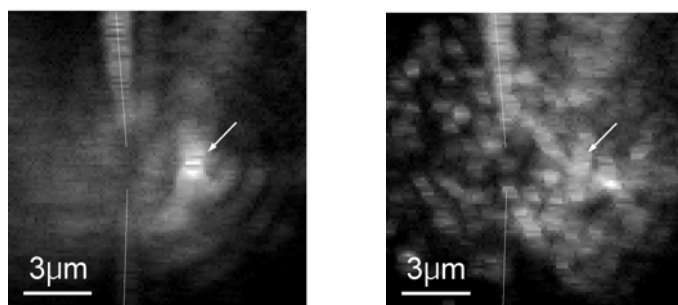


Figure 2-29. Evanescent field excitation optical microscopy images of a Si cantilever in water solution of fluorescent R110 dye molecules. An arrow points to the cantilever tip. Vertical lines indicate boundaries of the cantilever. (Left): the bright cantilever tip is in contact with a glass surface. (Right): the cantilever is moved away from the surface less than 1 μm. The optical signal from the cantilever is comparable to the signal from freely diffusing molecules in solution.

2.4.2 Fluorescence imaging development: time-gated imaging and multiparameter fluorescence imaging.

Stable excitation conditions and a small detection volume are obtained in confocal optical microscopy. Scanning techniques allow for spatial investigation of a cantilever's optical signal. The laser light is focused into a diffraction limited spot for detailed optical studies. For this purpose the laser beam is expanded with the telescope lenses to the size equal or slightly bigger than the entrance pupil of the microscope objective (typically 9-12mm). The optical setup parameters are specified in Section 2.1.1. The characteristic diffusion time of Rh110 through the detection volume was $t_D = 0.061$ ms corresponding to a detection volume of 0.6 fl and an excitation volume radius of 0.27 μm . FCS studies are applied to estimate the parameters of the detection volume (Figure 2-30).

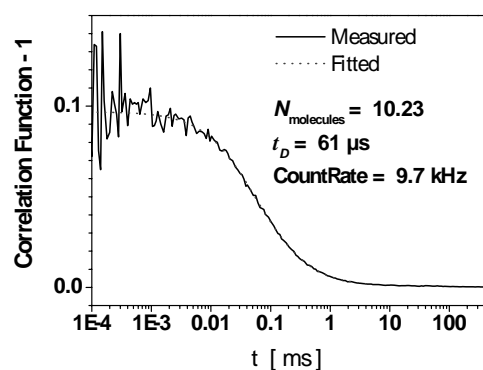


Figure 2-30. A normalized correlation function for the fluorescent signal of freely diffusing rhodamine 110 dye in water. Mean count rate per molecule is 9.7 kHz, characteristic diffusion time $t_D = 61 \mu\text{s}$. Excitation irradiance is 3 kW/cm².

Confocal scanning is realized in various ways, as shown in Figure 2-31. Raster sample scanning can be performed by one of the two piezo stages: AFM or PI, controlled by different computers.

In time-gated imaging (TGI), discrete electronic elements are used. The fluorescence signal is detected in a classical “reversed start-stop” configuration [170] with a time-to-amplitude-converter module (TAC). A photon arrival time interval between the laser pulses is selected for the analysis with a single-channel-analyzer (SCA); the signal is integrated with a ratemeter and directed to the analogue input of the AFM controller. The AFM controller and the commercial PicoScan software visualize the fluorescence signal and drive the AFM piezo. Standard software functions offer flexible control of a sample scanning procedure: real time operation, custom scanning area/volume shapes, fast screening and various image analysis features. After a scan a point of interest can be moved on the optical axis. Therefore SPC data and fluorescence spectra can be obtained for a time longer than a single pixel acquisition time in the scan.

Multiparameter fluorescence imaging (MFI) is realized via SPC card direct recording the arrival time of each detected photon in different scan positions. Either the ControlPI program on imaging PC can control the PI piezo scanning or the PicoScan program on AFM computer can control the AFM piezo or PI piezo stage (see Appendix E). Pixel identification is realized by shifting a detector channel in SPC data for each pixel neighbouring in a line (see Figure 2-32). The switching is driven by a synchronization box, triggered by the AFM controller or by the imaging PC, depending on the realization of the scanning control. Further fluorescence data analysis provides time axis identification marks for pixels and lines and includes SPC data macrotime reconstruction for the whole experiment. The analysis is performed using the TreatAFMdata program (see Appendix E).

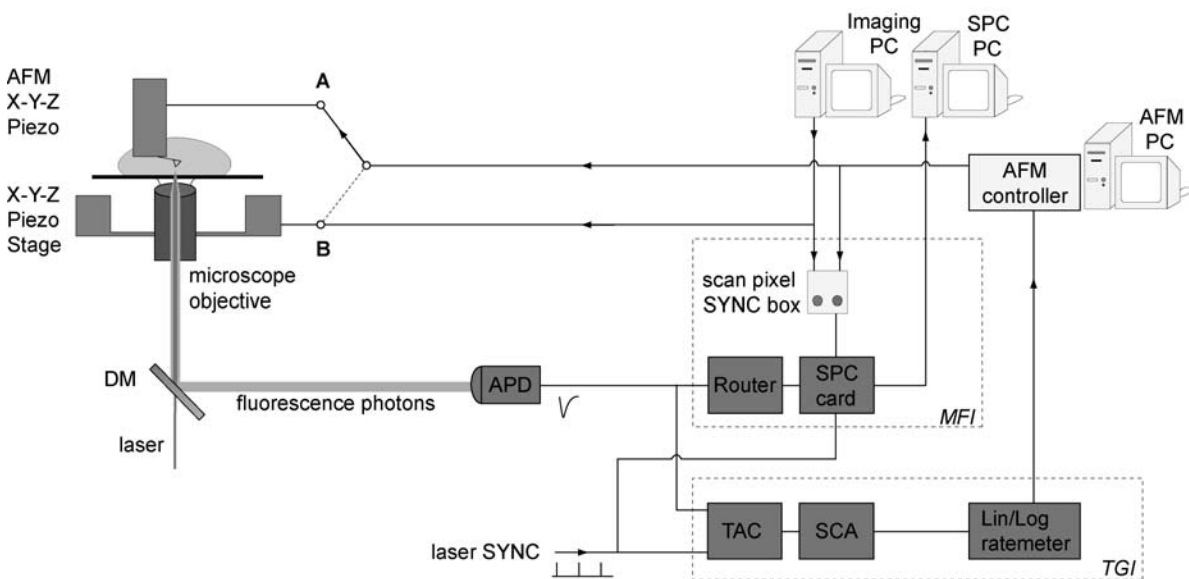


Figure 2-31. Schematic representation of the scanning and fluorescence confocal detection in combined AFM and optics setup. Either the AFM piezo (controlled via AFM PC) or the PI stage piezo (controlled via AFM PC or Imaging PC) perform the sample raster scanning. Fluorescence signal is taken to discrete modules in time-gating imaging (TGI): time-to-amplitude-converter module (TAC), single-channel-analyzer (SCA) and ratemeter. MFI data is recorded by a SPC card storing the arrival time of each detected photon in different image pixels.

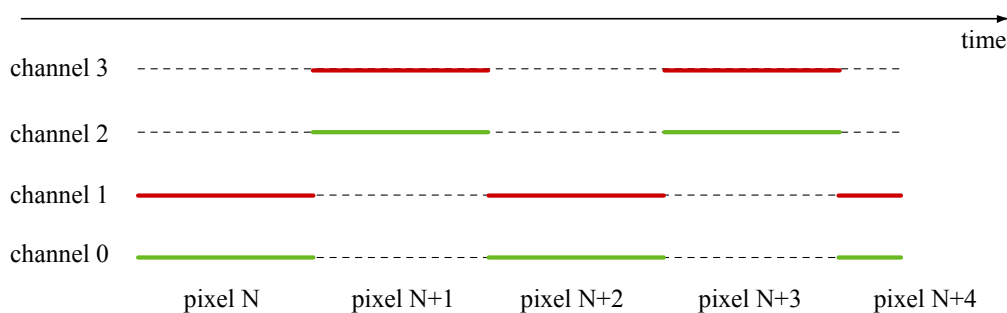


Figure 2-32. Schematic representation of the pixel identification in SPC data. Two fluorescence signals (green and red) are switched between channels 0, 1 and channels 2, 3 respectively, for each new pixel of the image. The signal for the channel switching is provided by the imaging software. Two fluorescence signals are considered for simplicity. The SPC card has 8 channels (from 0 to 7) and allows detecting of four signals.

2.4.3 Imaging application: cantilever tips optical signal characterization

After focusing the optics onto the top surface of the coverglass, the coverglass (and the entire AFM) is moved 3 μm closer to the lens via the piezo-crosstable. This procedure positions the image plane 3 μm above the glass surface where it remains during the experiment. Such definition of the image plane places the surface of the coverglass at $-3 \mu\text{m}$. The AFM scanner is subsequently used to position the tip on the optical axis and to bring the tip into contact with the surface ($-3 \mu\text{m}$). Then the tip is withdrawn from the surface by 0.84 μm , placing the apex at a height of $-2.16 \mu\text{m}$. Once the tip is withdrawn from the surface, an image can be performed. Subsequent scanning images are acquired at heights of $-1.32 \mu\text{m}$, $-0.48 \mu\text{m}$, $-0.06 \mu\text{m}$, $0.36 \mu\text{m}$, and $2.04 \mu\text{m}$. These values indicate the height of the tip after the AFM piezo was allowed to stabilize, and were calibrated by performing a z-scan approach to the surface for each image plane. The raster pattern was 52×52 pixels, covering an area of $13 \mu\text{m} \times 13 \mu\text{m}$ (250 nm per step). At each pixel, the tip is held stationary for 100 ms. Measurements are performed in deionised, doubly distilled water.

The fluorescence signal is divided into parallel and perpendicular components, and single photons in the range from 510 nm to 650 nm are detected by two avalanche photodiodes, as specified in Section 2.1.1. For TGI, signals from two APD are coupled together to a TAC input. For MFI, signals are directed to a counting board SPC 630.

TGI tips characterization

The application of TGI to cantilever optical signal studies is shown in Figure 2-33. The set of optical images at different cantilever-surface distances with a fixed focal plane-surface distance clearly demonstrates the geometry of the tip and the cantilever itself.

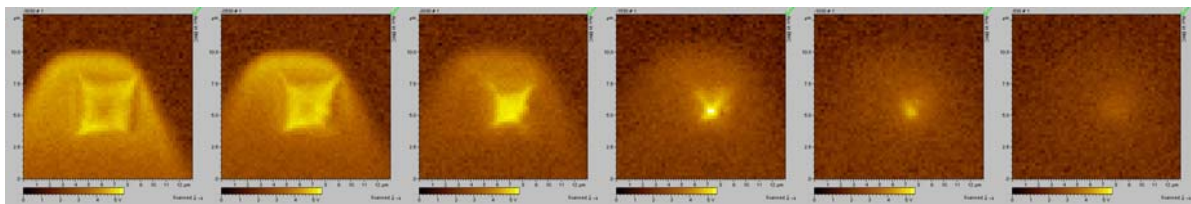


Figure 2-33. Optical images of Veeco NPG cantilever obtained using TGI configuration at different tip-surface distances, increasing from left to right. The tip is moved from the position at $1 \mu\text{m}$ above the surface $3 \mu\text{m}$ away from the surface in $0.5 \mu\text{m}$ steps. Focal plane is always kept at $3 \mu\text{m}$ above the surface. Optical signal intensity without time gating is presented in arbitrary units and equally normalized at all images.

The advantages of TGI are: (i) a real time visual control and (ii) a quick switching between optical intensity signal acquisition and a high-resolution time-resolved experiments or a fluorescence spectra acquisition.

Scanned cantilever can be positioned at any point on the optical axis and either time resolved data or fluorescence spectra can be acquired. Experimental data for four different

cantilevers are shown in the figures (Figure 2-34 to Figure 2-37). Optical images are acquired close to the cantilever tip apexes. Decay and spectral measurements indicate that the high signal from the cantilever tips (position 2 at all images) is mostly light scattering, background and long-life luminescence. Long-life luminescence can not be distinguished from background in time resolved experiment at the present configuration of experimental setup. The drop at the long wavelength side of the optical spectra visible in subset (b) is due to optical filter (HQ 580/140) cutting.

Further detailed quantitative characterization of AFM cantilevers fluorescence is realized in MFI.

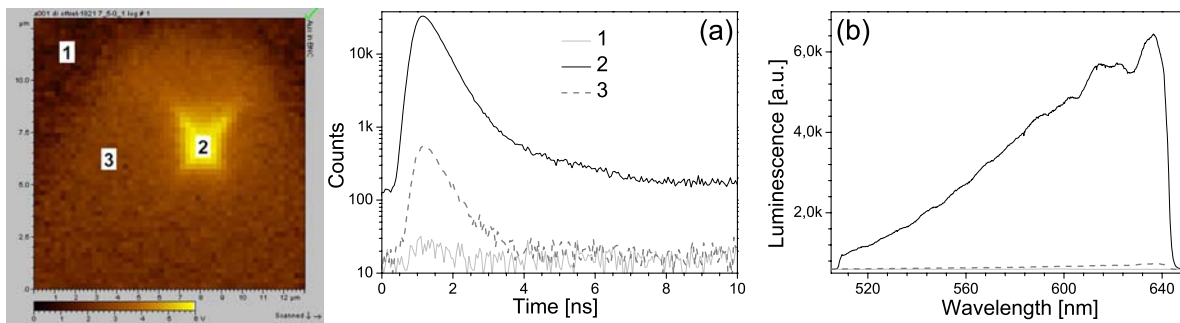


Figure 2-34. Optical signal observed from the Veeco NPG cantilever tip in TGI setup. Decay histograms (a) and luminescence spectra (b) are obtained in different points positioning the cantilever on optical axis. Decay histogram and optical spectra acquisition time was 30sec.

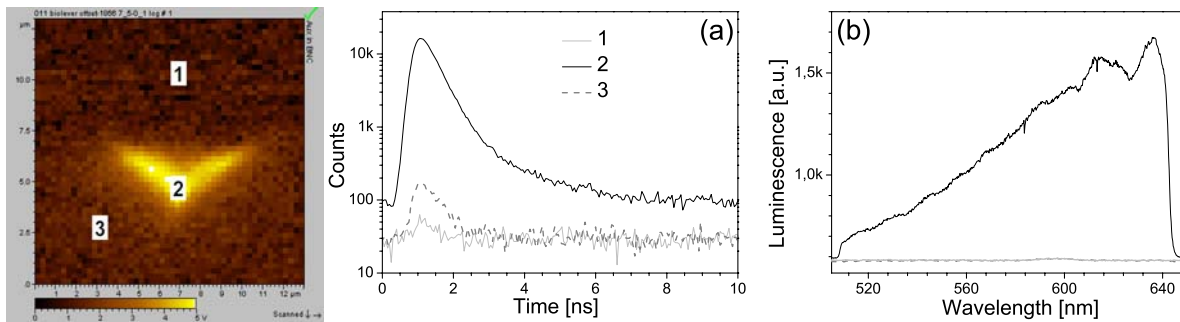


Figure 2-35. Optical signal observed from the Biolever cantilever tip in TGI setup. Decay histograms (a) and luminescence spectra (b) are obtained in different points positioning the cantilever on optical axis. Decay histogram and optical spectra acquisition time was 30sec.

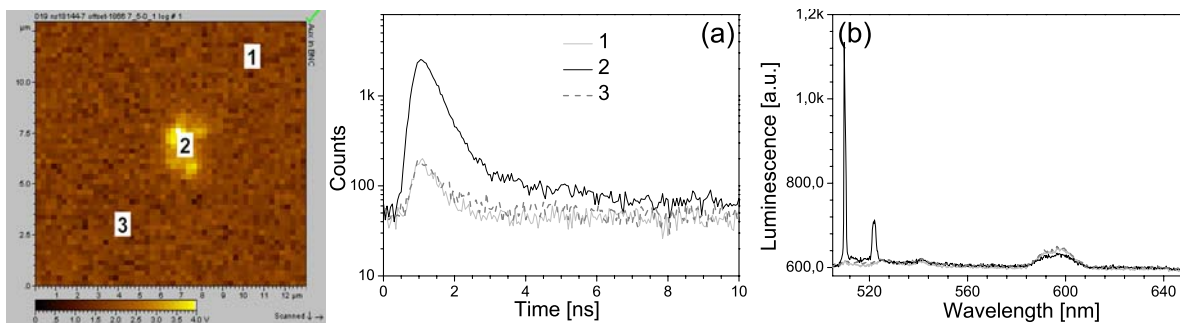


Figure 2-36. Optical signal observed from the Nanosensor cantilever tip in TGI setup. Decay histograms (a) and luminescence spectra (b) are obtained in different points positioning the cantilever on optical axis. Decay histogram and optical spectra acquisition time was 30sec.

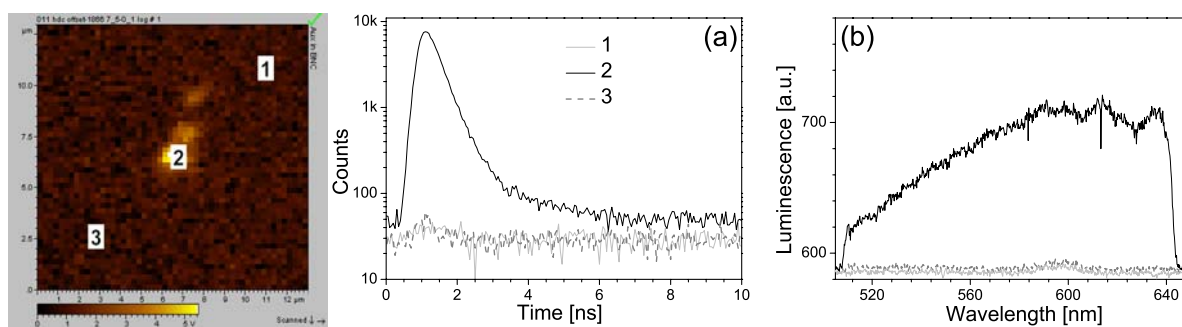


Figure 2-37. Optical signal observed from the Nanotools cantilever tip in TGI setup. Decay histograms (a) and luminescence spectra (b) are obtained in different points positioning the cantilever on optical axis. Decay histogram and optical spectra acquisition time was 30sec.

The optical signal spectra are measured with different sets of optical filters and are glued together for the detailed characterization of the luminescence properties of the AFM tips. The Si_3N_4 tips in general exhibited spectra with similar characteristics: i.e. a broad, featureless emission with the maximum around 610 nm. A representative spectrum of a Si_3N_4 tip, the Olympus Biolever, is shown in Figure 2-38. The spectra recorded for the Si and HDC tips (Figure 2-38) were dominated by a single peak corresponding to the well known Raman line of bulk crystalline Si at $\Delta\tilde{\nu} = 521 \text{ cm}^{-1}$ [171]. The spectra were otherwise featureless.

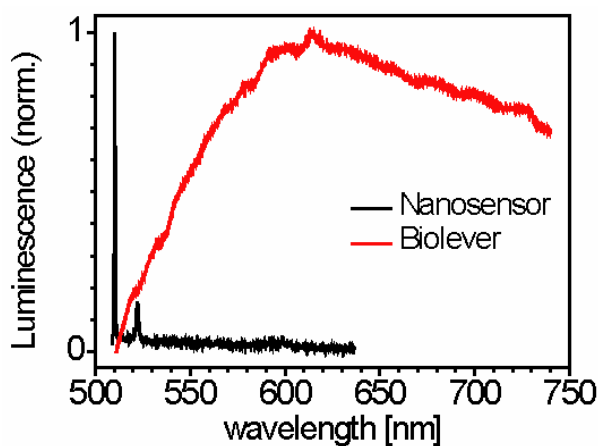


Figure 2-38. Signal spectrum for Olympus Si_3N_4 Biolever and Nanosensor Si cantilever. Parts of the Biolever spectrum were serially recorded through three different bandpass filters (HQ 580/140, HQ 645/75 and HQ 780/150).

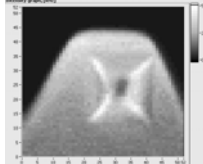
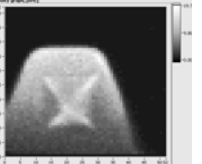
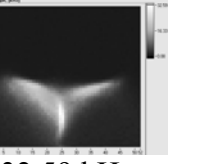
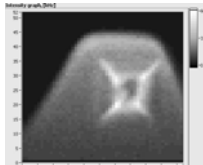
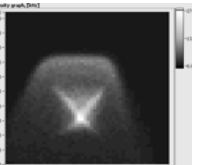
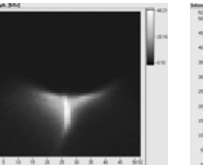
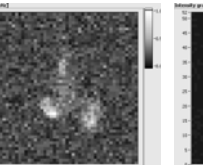
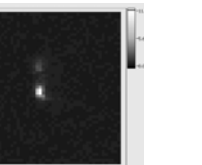
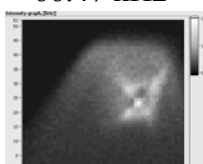
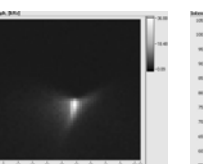
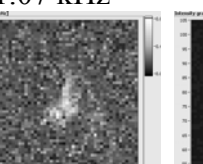
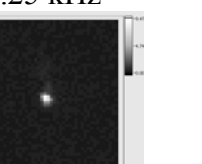
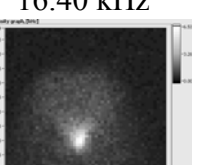
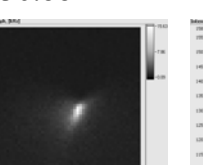
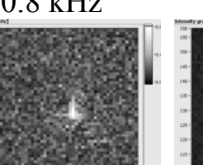
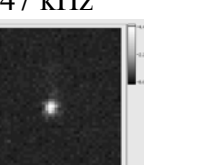
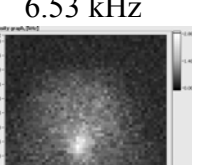
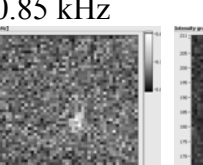
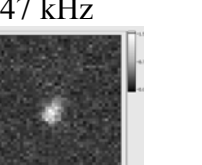
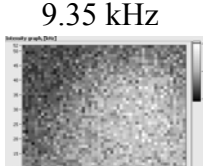
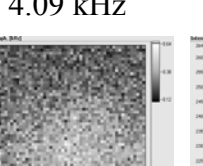
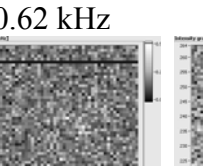
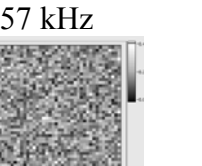
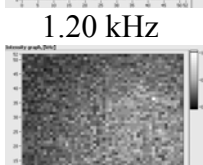
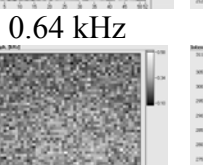
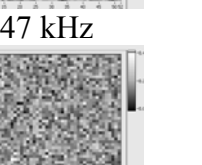
MFI tips characterization

Before each tip measurement, an instrument response function (IRF) is determined by recording a histogram of the arrival times of scattered photons from pure water. Due to the low signal intensity a significant fraction of the histogram consisted of dark counts of the detectors and, not being part of the instrumental function, needed to be subtracted. Average dark counts per bin are determined by measuring a signal without laser illumination. Since there is ideally no luminescence in the IRF measurements (the Raman scattering is prompt

within our experimental time resolution), the tail of the measured histogram should consist only of Poisson distributed dark counts. Therefore, subtracting an average dark counts per bin value from the measured bin values results in roughly half of the histogram bins in the tail of the IRF having negative values. These negative values cannot be shown on a log scale, and omitting the negative values while keeping the positive values would result in a visually misrepresentative figure. Therefore the IRF is plotted only as far as the first negative value.

The first 7 ms and the final 3 ms are excluded from the analysis in order to avoid photons captured as the tip is moved. MFD data analysis allows calculating the intensity, decay time, and anisotropy for either the complete or the time gated signal [73]. Optical images of different cantilevers studied are presented in the table (Table 2-10).

Table 2-10. Results of MFI for various commercial cantilevers at different scan planes distances from the glass. Focal plane is 3 μm above the glass surface. Maximum count rate is given below each image. Single molecule signal, obtained from FCS measurements of freely diffusing dye in water is 9.7 kHz for Si_3N_4 cantilevers and 48 kHz for Si cantilevers.

Plane distance	Veeco NPG Si_3N_4	Veeco Microlever Si_3N_4	Olympus Biolever Si_3N_4	Nanosensors Si	Nanotools NDC Si
0.84 μm	 58.85 kHz	 19.73 kHz	 32.59 kHz	N/A	N/A
1.68 μm	 66.47 kHz	 27.30 kHz	 40.21 kHz	 1.07 kHz	 11.25 kHz
2.52 μm	 39.45 kHz	 16.40 kHz	 36.88 kHz	 0.8 kHz	 9.47 kHz
2.94 μm	 18.95 kHz	 6.53 kHz	 15.63 kHz	 0.85 kHz	 4.47 kHz
3.36 μm	 9.35 kHz	 2.80 kHz	 4.09 kHz	 0.62 kHz	 1.57 kHz
5.04 μm	 1.20 kHz	 0.75 kHz	 0.64 kHz	 0.55 kHz	 0.47 kHz
6.3 μm	 1.40 kHz	N/A	 0.58 kHz	 0.45 kHz	 0.47 kHz

2.4.3.1 Veeco Microlever

These cantilevers are most commonly used for force spectroscopy, and therefore the results for this cantilever are analyzed in detail. Figure 2-39 shows a series of images which present the intensity data for the Microlever cantilever acquired at z-positions of $-2.16\ \mu\text{m}$, $-1.32\ \mu\text{m}$, $-0.48\ \mu\text{m}$, $-0.06\ \mu\text{m}$, and $0.36\ \mu\text{m}$. In order to facilitate comparisons between cantilevers, the data are presented as ratios of the tip intensity to the intensity of a single Rhodamine 110 fluorophore excited at the same power. Tip signal intensities were calculated for each pixel from the number of photons counted and the integration time at each pixel (90 ms). In each image there is an inset which illustrates the geometry of the tip and the image plane. The red outline on each intensity ratio image indicates the portion of the tip which extends below the image plane, based on the company's specifications for the tip geometry. For all of the pixels within this outline, the optical detection volume would nominally be located within the body of the tip. Interpretation of the data within this volume is difficult due to the uncertainty of the exact shape and composition of the tip, as well as the shape of the confocal volume within a solid material. Imperfections in the tip geometry, the tilt of the cantilever and the incidental rotation of the cantilever in the tip holder cause the deviation between the tip cross-section and the red outline.

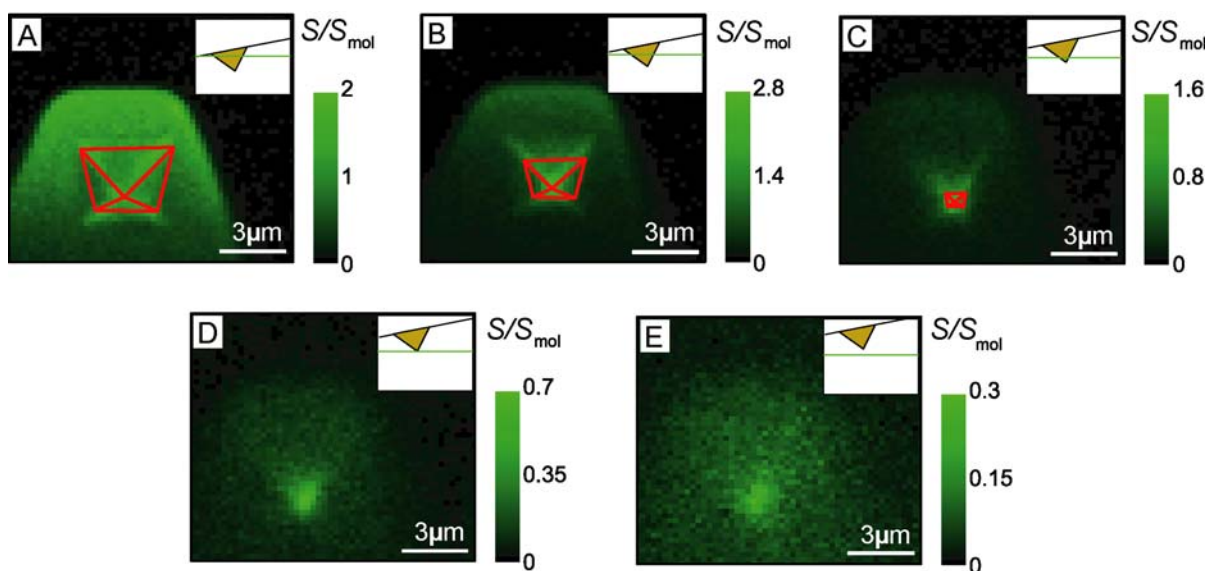


Figure 2-39. Veeco Microlever intensity ratio images at several z-positions: A) $-2.16\ \mu\text{m}$, B) $-1.32\ \mu\text{m}$, C) $-0.48\ \mu\text{m}$, D) $-0.06\ \mu\text{m}$, and E) $0.36\ \mu\text{m}$. The inset indicates the geometry of the image plane relative to the tip, and the red outline indicates the part of the tip below the image plane. The single molecule intensity S_{mol} used for normalization was $9.7\ \text{kHz}$.

At each z-position, the highest intensities occur at the edges and the apex of the tip. It is worth noting here that the maximum intensity ratio of 2.8 occurs when the focal volume is positioned within the volume of the tip, above the apex at a z-position of $-1.32\ \mu\text{m}$ (Figure

2-39B). If the tip is moved even closer to the surface, as seen in Figure 2-39A, the intensity ratio measured above the apex decreases. As the tip is moved away from the surface, the peak intensity ratio drops quickly to less than unity when the image plane is tangent to the apex of the tip (Figure 2-39D) and close to the background levels by the time the tip is 2 μm or more from the image plane (Table 2-10).

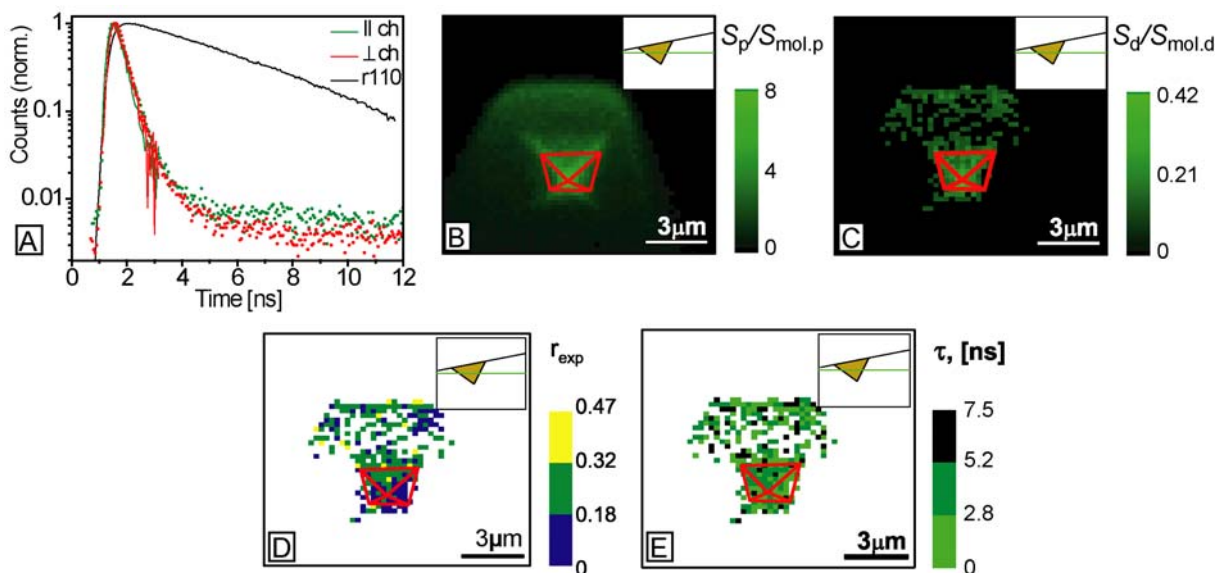


Figure 2-40. MFI analysis of Veeco Microlever tip image corresponding to the z-position $-1.32 \mu\text{m}$. A) The decay histogram of the tip signal (dots) corresponds mainly to the instrumental function (solid line), indicating a high portion of scatter. For comparison, a decay of Rh110 fluorescence is shown. B) Prompt intensity signal in the range of 0–2.4 ns, normalized to the single molecule signal. C) Delayed intensity signal in the range of 2.4–12 ns, normalized to the single molecule signal. D) The anisotropy values had a mean value of $r_{\text{exp}} = 0.21 \pm 0.07$. E) Lifetime image resulting from a single exponential lifetime fit of the delayed signal. The red outline indicates the portion of the tip that extends below the image plane. For D and E only those pixels are shown for which the delayed signal had at least 20 photons.

The advantages of MFI are illustrated in Figure 2-40. The information about each photon arrival time allows reconstructing decay histogram for each pixel and displaying time-gated intensity images with arbitrary time gating.

The time decay signal in Figure 2-40A (open diamonds) includes all of the photons from the portion of the image corresponding to the tip. The instrument response function (IRF, solid lines) and the Rhodamine 110 decay histogram (black line) are also plotted for comparison. The signal decay curve does not show any visible deviation from the IRF, suggesting that the measured signal is predominantly scattering.

The prompt (0-2.4ns) and the delayed (2.4-12ns) intensity images, normalized to the signal from single molecule in the same time interval are shown in Figure 2-40B and C). Time gating improves the signal-to-noise ratio in fluorescence detection. This can be used in a combined fluorescence and AFM experiment. The tip signal-to-molecule signal ratio for

delayed signal (Figure 2-40C) is 19 times better than for the total signal as illustrated in Figure 2-39B.

The anisotropy image (Figure 2-40D) with anisotropy values for each pixel with at least 20 photons was calculated using all of the photons in the pixel from the relation:

$$r_{\text{exp}} = \frac{GS_p - S_s}{(1 - 3l_2)GS_p + (2 - 3l_1)S_s} \quad (2-1)$$

where the factor G compensates for unequal detection efficiencies in the two channels and is calculated separately for each experiment from a measured fluorescence decay histogram of Rhodamine 110 solutions, which exhibits virtually no anisotropy in its tail. The correction factors $l_1 = 0.1419$, $l_2 = 0.0265$ take into account mixing of polarizations in the high N.A. objective [172]. S_p and S_s signify the parallel and perpendicular components of the intensity signal. In Figure 2-40D, r_{exp} has a mean value of 0.21 ± 0.07 and is observed to be sensitive to the local geometry of the tip.

The lifetime image of Veeco Microlever shows the result of a single exponential lifetime fit in those pixels of the image which have minimum number of 20 photons. It shows a homogeneous distribution and a slight dependence on the tip geometry.

2.4.3.2 Veeco NPG

Figure 2-41 summarizes the results for the Veeco NPG Si_3N_4 . The intensity ratio image for the plane at $-1.32 \mu\text{m}$ relative to the apex again clearly reveals the geometry of the cantilever (Figure 2-41A). The highest intensity ratio of 6.8 occurs along the leading edges of the tip at the points where the image plane intersects the pyramid. Time gating yields a highest intensity ratio of 1.4 (Figure 2-41C). That improves the signal-to-noise ratio of single molecule fluorescence detection up to 5 times.

The anisotropy image shown in Figure 2-41C has an average value of $r_{\text{exp}} = 0.23 \pm 0.06$, and reveals position dependent values, with the anisotropy of the signal from outside the tip being higher than the anisotropy of the signal nominally originating from the tip. The time decay signal does not correspond perfectly with the IRF, suggesting the possibility of either an increased background or a weak luminescence signal (Figure 2-41B). The image with a single exponential lifetime fit (Figure 2-41E) of the delayed signal shows homogeneously distributed values.

The intensity ratio image of the plane tangent to the apex is shown in Figure 2-41F. The maximum intensity ratio is 2, with three local intensity maxima and a broad region of several

square microns where the intensity ratio remains above 1 (Figure 2-41F). The outline of the cantilever remains visible.

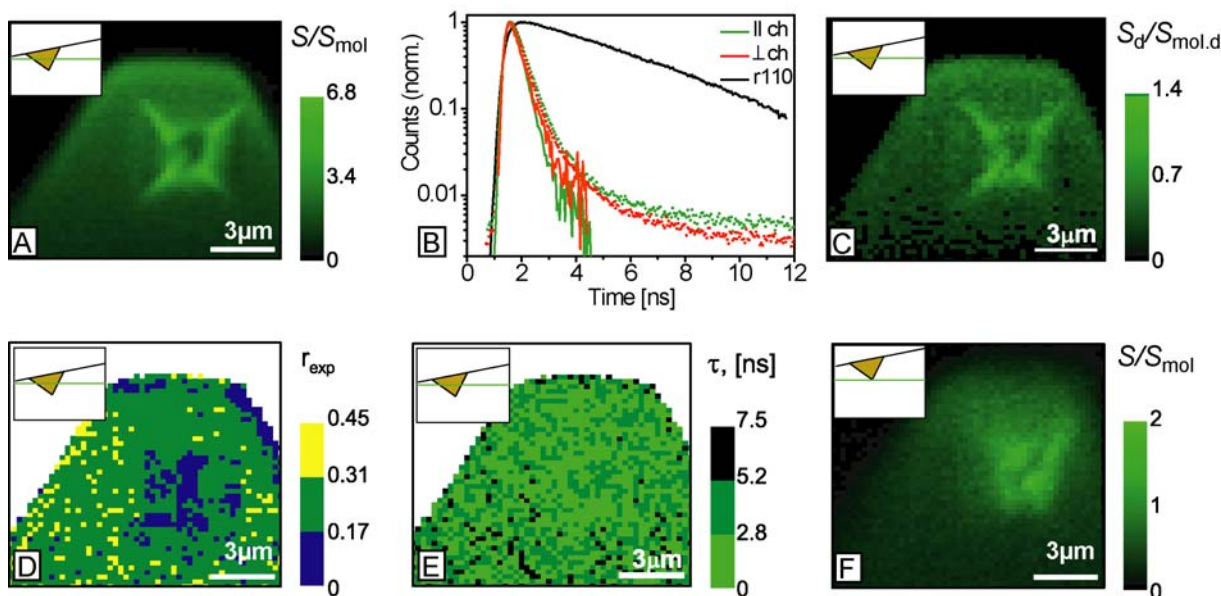


Figure 2-41. MFI analysis of Veeco NPG tip image corresponding to the z-position $-1.32 \mu\text{m}$ (A) and z-position $0.06 \mu\text{m}$ (F). B) The decay histogram of the tip signal (dots) corresponds mainly to the instrumental function (solid line), indicating a high portion of scattering. For comparison, a decay of Rh110 fluorescence is shown. C) Delayed intensity signal in the range of 2.4–12 ns, normalized to the single molecule signal. D) The anisotropy values had a mean value of $r_{\text{exp}} = 0.23 \pm 0.06$. E) The lifetime image resulting from a single exponential lifetime fit of the delayed signal. For D and E only those pixels are shown for which the delayed signal have at least 20 photons.

2.4.3.3 Olympus Biolever

The results for the Si_3N_4 Olympus Biolever for a plane at $-1.32 \mu\text{m}$ are shown in Figure 2-42. The geometry of the cantilever is again clearly visible in (A), with the highest intensity ratio of 4.1 occurring along the leading edge of the tip. Time gating yields a highest intensity ratio 0.75 (Figure 2-42C). That improves the signal-to-noise ratio up to 6.5 times and allows single molecule fluorescence to be detected.

The mean anisotropy value is calculated to be 0.13 ± 0.06 , differing from the previous tips. However as for the previous Si_3N_4 cantilevers, Figure 2-42D clearly indicates that the local geometry influences the anisotropy. The Biolever does not have a pyramidal shape, but rather a hollow half-pyramidal shape. Therefore the band of low anisotropy values observed along the top edge of the Biolever does not correspond to the detection volume being focused inside the tip, but into a hollow cavity.

The time decay signal indicates an optical signal whose waveform deviates only slightly from the IRF (Figure 2-42B). The image with a single exponential lifetime fit (Figure 2-42E) of delayed signal shows homogenous values, not influenced by the tip geometry.

In the plane tangent to the apex, the Biolever still generates a comparatively high intensity ratio of 1.6, but over a smaller lateral area than other Si_3N_4 tips (Figure 2-42F).

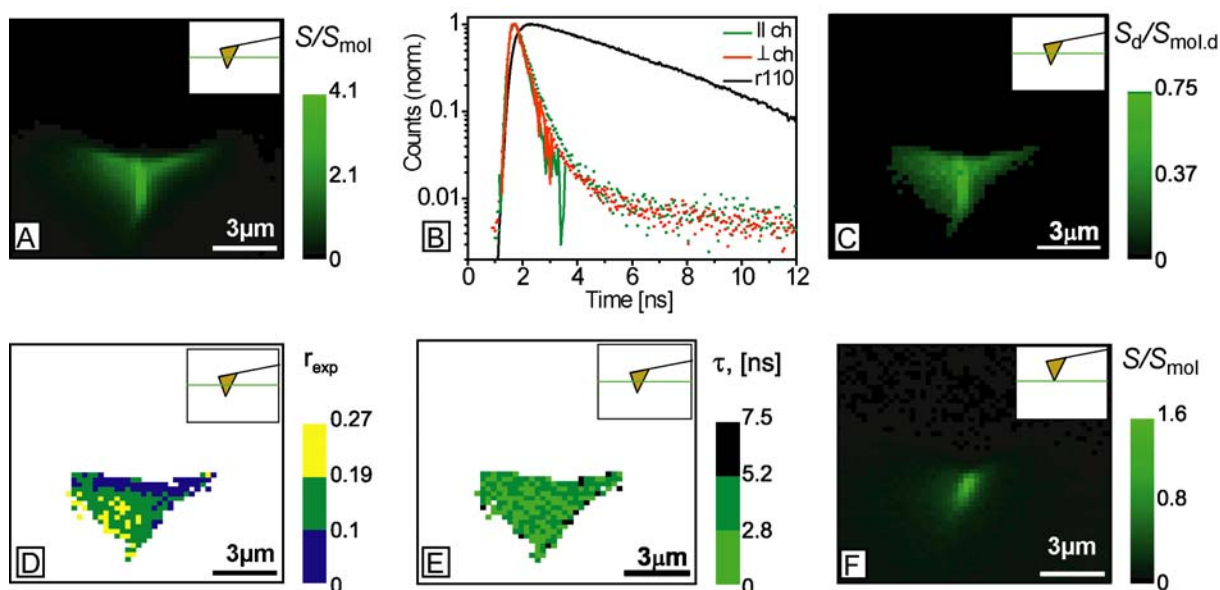


Figure 2-42. MFI analysis of Olympus Biolever tip image corresponding to the z-position $-1.32 \mu\text{m}$ (A) and z-position $0.06 \mu\text{m}$ (F). B) The decay histogram of the tip signal (dots) corresponds mainly to the instrumental function (solid line), indicating a high portion of scattering. For comparison, a decay of Rh110 fluorescence is shown. C) Delayed intensity signal in the range of 2.4–12 ns, normalized to the single molecule signal. D) The anisotropy values had a mean value of $r_{\text{exp}} = 0.13 \pm 0.06$. E) The lifetime image resulting from a single exponential lifetime fit of the delayed signal. For D and E only those pixels are shown for which the delayed signal have at least 20 photons.

2.4.3.4 Nanosensor

Figure 2-43 shows the results for the first Si tip tested, the Si Nanosensors tips. Due to the low signal recorded from the Si tips, the excitation power for these measurements was increased to $14 \text{ kW}/\text{cm}^2$, which increased the measured Rhodamine 110 single molecule signal to 48 kHz. Even at this increased intensity, the signal from the tip was very weak. In Figure 2-43A is recorded at a z-position of $-1.32 \mu\text{m}$. Here the tip is poorly imaged despite the image plane cutting through the tip as shown in the inset. The maximum intensity ratio was 0.022, and Figure 2-43B indicates that the signal decay histogram matches the IRF.

Figure 2-43E shows an intensity ratio image tangent to the apex ($-0.06 \mu\text{m}$). Here the intensity at the apex is almost identical to the intensity of a slice through the tip. The anisotropy (Figure 2-43C) and a single exponential fit lifetime (Figure 2-43D) images shows just few pixels with more than 20 photons in the delayed image (not shown).

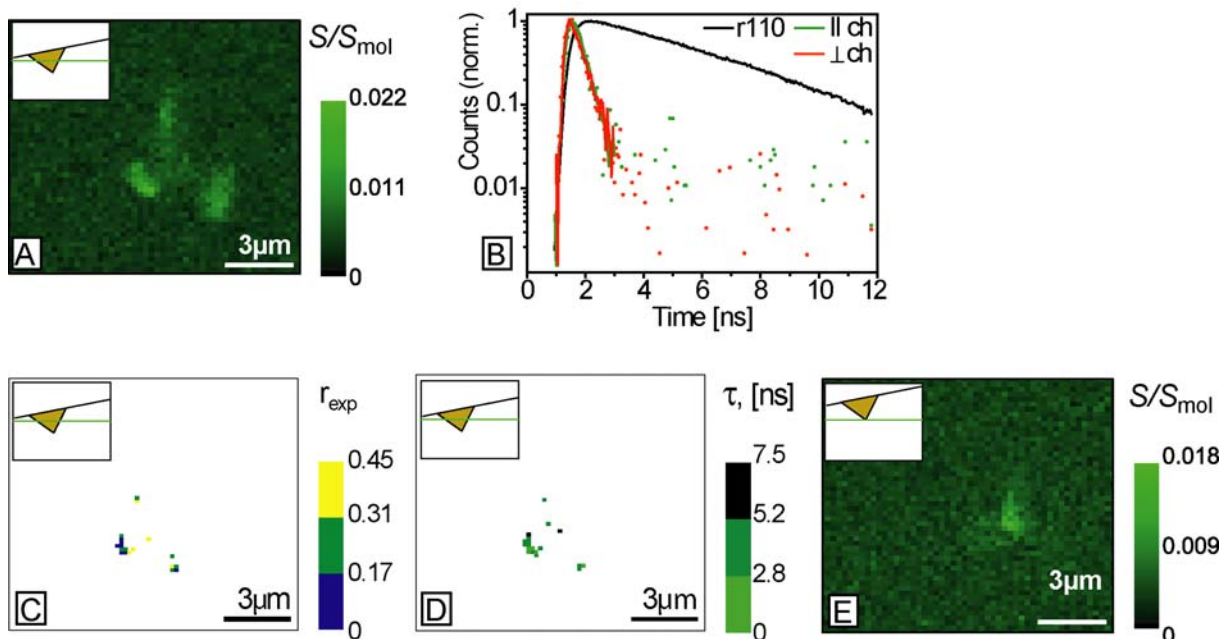


Figure 2-43. MFI analysis of Nanosensor Si tip image corresponding to the z-position $-1.32 \mu\text{m}$ (A) and z-position $0.06 \mu\text{m}$ (E). B) Histogram of the arrival times of photons relative to the laser pulse for the pixels of the tip in image A. The measured signal (dots) overlays the instrumental function (solid line) nearly perfectly, indicating that virtually the entire measured signal is scatter. For comparison, a decay of Rh110 fluorescence is shown. C) The anisotropy image and D) The lifetime image resulting from a single exponential lifetime fit of the delayed signal. For D and E only those pixels are shown for which the delayed signal (2.4–12 ns) have at least 20 photons.

2.4.3.5 Nanotools HDC

The results for the Nanotools HDC tip grown on a Si tip are shown in Figure 2-44. A peak intensity ratio of 0.24 was obtained with an excitation power of $14 \text{ kW}/\text{cm}^2$ at a z-position of $-1.32 \mu\text{m}$. In Figure 2-44A, two spots are visible in the image: the fainter spot is most likely the Si tip, and the brighter spot is the HDC tip. Supporting this assignment, with the image plane tangent ($z = -0.06 \mu\text{m}$) to the tip as shown in Figure 2-44E, only a single spot in the lower position is observed with a signal ratio of 0.09, whereas the upper spot disappears completely.

In Figure 2-44B, the time decay signal of the HDC tip shows a slight but distinct deviation from the IRF. The average anisotropy calculated from this tip is $r_{\text{exp}} = 0.27 \pm 0.11$. The anisotropy image is given in Figure 2-44C. The delayed part of decay histogram, fitted to a single exponential decay model is shown in Figure 2-44D. Only those pixels are used, which have more than 20 photons in delayed part of time-gated decay histogram (1.9–11 ns).

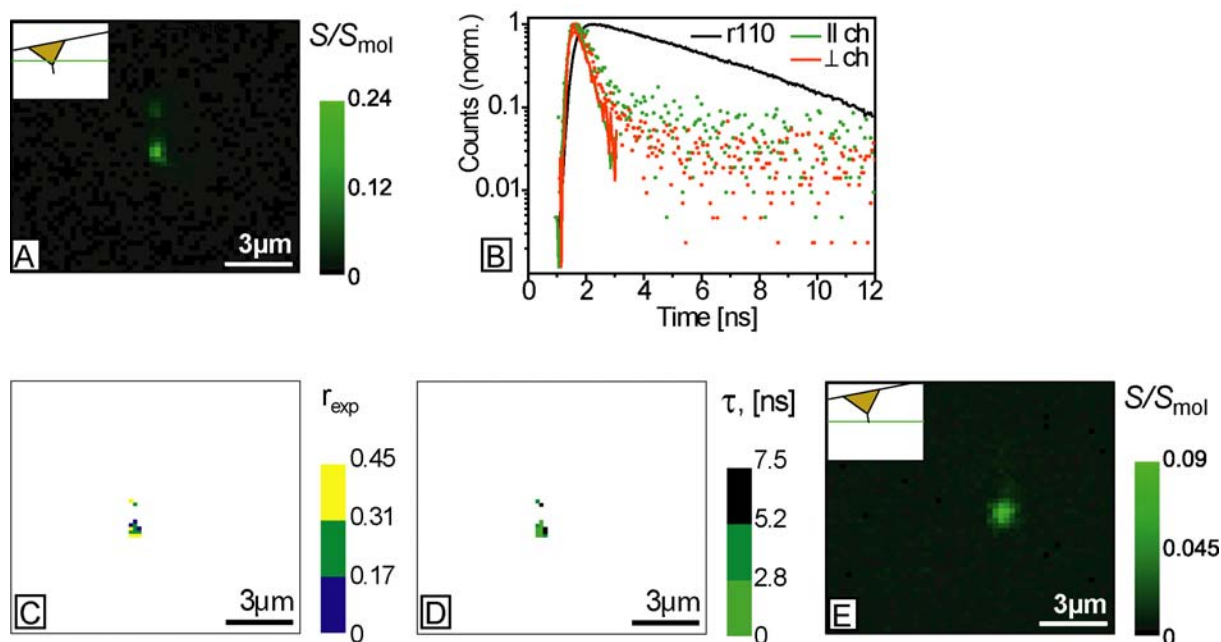


Figure 2-44. MFI analysis of Nanotools HDC tip image corresponding to the z-position $-1.32 \mu\text{m}$ (A) and z-position $0.06 \mu\text{m}$ (E). B) Histogram of the arrival times of photons relative to the laser pulse for the pixels of the tip in image A. The measured signal (dots) does not decay as quickly or as completely as the instrumental function (solid line), suggesting that the HDC tip produces a small amount of fluorescence in addition to the predominant scatter signal. For comparison, a decay of Rh110 fluorescence is shown. C) The anisotropy image and D) The lifetime image resulting from a single exponential lifetime fit of the delayed signal. The mean anisotropy value is calculated to be $r_{\text{exp}} = 0.27 \pm 0.11$. For D and E only those pixels are shown for which the delayed signal (2.4–12 ns) have at least 20 photons.

Each of the tips demonstrated the highest signal at the edges or apex of the tip. The Si_3N_4 tips proved to be brighter than the Si tips and for two of the Si_3N_4 tips, the cantilever itself could be seen in the image even though it should be several microns away from the image plane. The signal from both the Veeco NPG and Olympus Biolever only dropped below the single molecule threshold when the image plane was hundreds of nanometers from the apex of the tip. Both of these cantilevers are gold coated on the tip side according to the manufacturer specifications. The Veeco Microlever, which is gold coated only on the back of the cantilever, demonstrated signal intensity below the single molecule threshold at the apex of the tip. As for the Nanosensors Si tip and the Nanotools HDC tip, both were consistently well below single molecule intensity levels. Figure 2-45 summarizes the results of these observations.

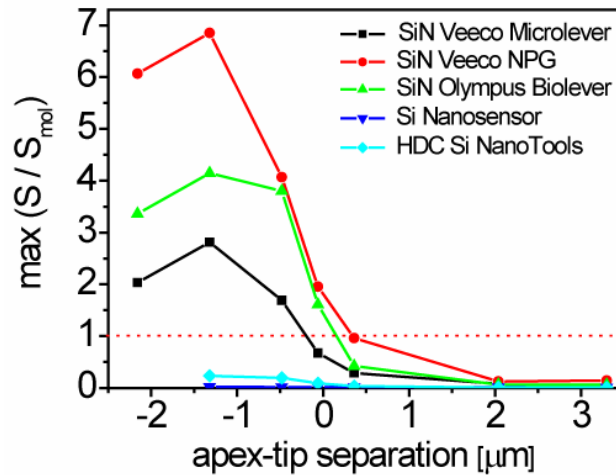


Figure 2-45. Graph of the signal intensity ratio versus z-position for the five cantilevers tested. Normalized intensities were calculated by dividing the measured intensities by the intensity of a single molecule under the same illumination (9.7 kHz for the Si₃N₄ cantilevers, 48 kHz for the Si and HDC cantilevers). The red dashed line indicates the fluorescence intensity of a single Rhodamine 110 molecule (with an intensity ratio by definition of 1).

Cantilevers displayed maximum intensities at $-1.36 \mu\text{m}$, not at the apex as might be expected. The explanation for this phenomenon is the following: the confocal detection volume has some finite dimension, which is estimated above as being 540 nm in diameter and 3 μm tall. As long as the apex remains within this volume, a majority of the photons originating from the apex will be detected. Since measurements indicate the highest intensities occur at the edges, and that the bulk material of the AFM tips produces a higher signal than the surrounding solution, the highest signal should be observed with the apex positioned at one end of the detection volume, and with the rest of the volume extending around and into the tip.

As seen in the various histograms, the time decay behaviour varied from tip to tip. In order to identify and describe the various signal components, each of the decay histograms was fitted to a function, M , which modelled the decay as the sum of background signal, B and R , and a fluorescence signal, F , convoluted with the IRF as described by Brand, et al [73].

$$M(t) = B + R(t) + IRF \otimes F(t, \tau) \quad (2-2)$$

The fluorescence signal $F(t)$ was assumed to be a single exponential decay with lifetime τ and amplitude A . The background signal is composed of a time dependent scattered light component $R(t)$, the signal of which exhibits the shape of the IRF, and a time-independent component B originating from dark counts of the detectors and possibly photons emitted from long lived luminescence states. By fitting the data to this model and allowing the amplitudes of the scatter $R(t)$, constant background B , and fluorescence $F(t)$ components to vary freely,

along with the lifetime of the fluorescence component τ , the contribution of each component to the total signal was determined. The results are presented in Table 2-11, along with the intensity ratios measured for each tip when the detection volume was located at the apex.

Table 2-11. Composition of signal from the respective cantilever tips separated into scatter, background, and fluorescence components according to a single exponential decay model. The tip brightness is defined as the signal intensity recorded at the apex of the tip relative to the signal of a single Rh110 molecule.

Cantilever	% of total signal			Lifetime of fluorescence component	Tip brightness ($S_{\text{apex}}/S_{\text{Rh110}}$)
	Scatter R	Background B	Fluorescence F		
Veeco Microlever	91 %	6 %	3 %	2.8 ns	0.7
Veeco NPG	86 %	6 %	9 %	1.8 ns	1.9
Olympus Biolever	79 %	8 %	13 %	1.0 ns	1.6
Nanosensors Si	49 %	51 %	0 %	-	0.02
Nanotools HDC	52 %	21 %	27 %	0.7 ns	0.08

Of the tips tested, the Nanosensors Si tip exhibited the lowest optical signal, with no observable fluorescence and a scatter component which was no larger than the background signal. The Nanotools HDC cantilevers also exhibited a small total signal, but contained an identifiable short lived fluorescence component and scatter which was 4 times larger than the background. The three Si_3N_4 cantilevers, in contrast, exhibited strong total signals compared to single dyes. They possessed higher scatter signals, higher background, and higher and longer lived fluorescent components. The Veeco Microlever, which was the only Si_3N_4 tip to exhibit a total signal at the apex less than single dye levels, also displayed the lowest percentage of fluorescence. This fact is important to note, since the fluorescence from the tip would be the most difficult of the three components to include in a model function for future experiments. Considering that total signal from the Veeco Microlever was 0.7 times that of a single molecule, and only 3% of this signal was fluorescence, than the amount of fluorescence coming from the tip is only 2% the signal of a single Rh110 dye. The Olympus biolever, in contrast, exhibits a fluorescence signal which is $1.6 \times 13\%$, or 21%, of the intensity of a single dye.

The origin of the scattered signal $R(t)$ is most likely a combination of surface and bulk Raman bands of Si_3N_4 [173]. Some contributions to the background B are due to long lived luminescence as well as slowly decaying excitons located at surface defect sites, local non-stoichiometries and other impurities like hydrogen or oxygen [174-176]. The resemblance of reported luminescence spectra from gold clusters [176] with Figure 2-38 hints at a strong contribution from an inhomogeneous layer of gold impurities on the tip. This can be true even for nominally clean Si_3N_4 tips due to the migration of metal clusters onto the surface of the tip during the deposition process of the reflective (Au) coating on the back of the standard AFM cantilever.

2.4.4 Conclusions

The Multiparameter Fluorescence Imaging (MFI) is developed which can easily be used for 3-dimensional optical imaging studies of single molecules and cells. The MFI is applied to the cantilever tips optical properties investigation. Optical signal of five commercial cantilevers is characterised.

Of the tips tested the Si tip would be the simplest tip to integrate into a single molecule optical measurement due to its low signal intensity and lack of fluorescence. The Nanotools HDC could also be easily integrated even though it exhibits a measurable fluorescence signal, since this signal is no larger than the background count rates. Of the three Si_3N_4 tips tested, the Veeco Microlever would be the most appropriate for single molecule optical application, since its relative brightness is less than unity even at the apex and drops quickly with the use of a short linker. The other tips could also be used in single molecule optical experiments, provided that either time gating or a robust fitting scheme, or a linker separating the dye from the tip is employed to compensate for the additional signal from the tip. The latter solution would be the simplest in terms of the data analysis. Hundreds of nanometers from the apex, all three tips exhibits intensities lower than single dyes.

However, even without a linker, an efficient approach for analyzing the data would be the modelling of the background decay in a multi-component fit of the data with fixed pre-determined background constants. In contrast to the time gating, no fluorescence photons would have to be discarded and minimum shot-noise levels could be achieved. In addition, long-decay time background components such as substrate phosphorescence could be included in the model. The fitting algorithms available to calculate fluorescent lifetimes are robust enough to take into consideration the existence of a background signal with a distinct decay time [73,177].

Single molecule experiments which rely on the calculation of anisotropy values may be compromised by the presence of an AFM tip due to the position and geometry dependant nature of the anisotropy of the signal. Optimal fitting could still be achieved by using a background file which includes tip scattering and background effects; however any experiment which requires repositioning the tip would prevent the use of a constant background file.

As an alternative, tips could be modified or replaced with materials which are more suitable for optical experiments, for example attaching a non-fluorescent bead to the cantilever. The HDC tip provided by Nanotools effectively functions exactly in this manner, since it can in principle be grown on any type of a tip, effectively substituting the HDC properties for the native tip properties.

Finally, it should be noted that the demand for scanned probe imaging and force spectroscopy conflict with the demands for fluorescence microscopy. Commercial cantilevers possessing a low optical signal (Si) do not have small stiffness required for the sensitive force measurements. In addition, good SPM imaging requires sharp tips with low radii of curvature, whereas sharp edges are typically the brightest scattering sources on a tip. When possible, for combined applications, unsharpened and blunt tips should be used.

2.5 High precision distance measurement via fluorescence detection

Conformational changes and fluctuations in molecular interactions are essential for many chemical reactions and biological processes. Distributions of fluctuating properties provide valuable information about the topography of the molecular energy landscape and are critical to understand bimolecular dynamics, protein folding, conformational activity, and non-covalent binding [178-181]. In the last years confocal fluorescence techniques have been considerably used for investigation of molecular fluctuations solution at physiological conditions. Moreover, at single molecule level they can directly study the dynamic behaviour of molecules without ensemble averaging [182,74].

As discussed in Section 1.2, the combination of fluorescence and force spectroscopy techniques can provide complementary data in studies of the structure and dynamics of complex biomolecules. Recently Dietz and Rief have shown that careful force spectroscopy data analysis of a single molecule protein unfolding allows one to measure the intramolecular distance with an angstrom precision [183].

Several attempts were made to provide quantitative distance information in single-molecule fluorescence experiments. Often, Förster (fluorescence) resonance energy transfer (FRET) is used to measure distances in macromolecules. For FRET experiments a single molecule or molecular complex is labelled with two different dyes and the efficiency of energy transfer from one dye to the other is monitored. The transfer efficiency, and hence the fluorescence intensities of both dyes, are sensitive to dye's relative positions, orientations, and fluorescence properties [184]. As such, signal distributions reflect conformational activity and changes in the local environment [74]. Analysis of FRET signal distributions has revealed folding pathways, intermediate structure, and conformational activity in proteins [185-187], RNA [188], and DNA [189].

In the following section FRET data characterization formalism and the theory for FRET data analysis will be given. A central difficulty in extracting molecular information from fluorescence intensity distributions has been the inability to unambiguously distinguish molecular fluctuations from either stochastic variations or background counts, especially when signal counts are low [190]. By including the effects of background and stochastic processes, the shot noise limited shapes of histograms generated from single photon counting data can be predicted with high precision. A probability distribution analysis (PDA) is established for quantitative and precise description of the FRET signal distributions [191].

2.5.1 FRET and PDA formalism

2.5.1.1 Fluorescence Signals

In FRET, a donor molecule, D , is excited and then a part of its energy can be non-radiatively transferred to an acceptor molecule, A . The efficiency of energy transfer, E , is determined by the proximity and orientations of D and A , the spectral overlap between donor emission and acceptor excitation, and the quantum yields of the molecules. E is usually interpreted as the fraction of energy which was transferred to the acceptor, or as the probability that the energy from any given photon absorbed by the donor is transferred to the acceptor.

The amount of energy transfer in FRET experiments can be measured by separating signal photons into two spectral regions corresponding to the donor and acceptor emission spectra. Green and red spectral regions are denoted by the subscripts G and R respectively. A distinction between donor/acceptor and green/red must be made because the terms donor/acceptor refer exclusively to photons which originate via fluorescence of the molecules, whereas the terms green/red are descriptive terms indicating in which channel events are counted, and can equally be applied to either fluorescence, scatter, crosstalk, or non-photon dark counts.

The measured signals are the number of counts in the green and red channels, S_G and S_R , and consist of a number of fluorescence photons arriving at the green/red detectors, F_G and F_{RT} , and a number of background counts, B_G and B_R . The subscript in F_{RT} represents the total fluorescence signal appearing in the red channel, including counts which were emitted by the donor but detected in the red channel (crosstalk). The total number of events (N) counted is given by:

$$N = F_G + F_{RT} + B_G + B_R. \quad (2-3)$$

In the experiment the mean background count rates $\overline{B_G}$ and $\overline{B_R}$ (in kHz) are measured in a clean buffer solution. Also, the spectral crosstalk coefficient (α) is determined from the average signal count rates of a measurement of donor dye in buffer as:

$$\alpha = \frac{(\overline{S_R} - \overline{B_R})}{(\overline{S_G} - \overline{B_G})} \quad (2-4)$$

The notations $\overline{S_G}$, $\overline{S_R}$, $\overline{B_G}$ and $\overline{B_R}$ refer to average count rates, whereas the signals S_G , S_R , B_G and B_R refer only to an integer number of counts in a specified time window.

The detection efficiencies are calculated from the transmission function of the optics, $g'_{optic}(\lambda)$ and the normalized fluorescence spectrum of the dye, $f_{dye}(\lambda)$, according to $g = \int g'_{optic}(\lambda) \times f_{dye}(\lambda) \cdot d\lambda$.

2.5.1.2 Probability Distribution Analysis

FRET signal ratios description

The PDA method calculates the theoretical probability of recording a particular combination of F_G , F_{RT} , B_G , and B_R , from which any intensity based parameter, such as proximity ratio or FRET efficiency, can be derived. The signal ratio is given by the equation (2-5c):

$$\begin{aligned} S_G &= F_G + B_G \\ S_R &= F_{RT} + B_R \\ S_G/S_R &= (F_G + B_G)/(F_{RT} + B_R), \end{aligned} \quad (2-5 \text{ a,b,c})$$

The signal ratio is chosen as the parameter of interest here because the predicted distributions can be compared directly to the uncorrected, unmodified experimental data. Since photon counting results in a finite set of ratio values, the particular values will be denoted by $(S_G/S_R)_i$, and the probability of observing that value by $P(S_G/S_R)_i$. Many $(S_G/S_R)_i$ values can be obtained from several different combinations of F_G , F_{RT} , B_G , and B_R , so $P(S_G/S_R)_i$ is calculated by summing the probability of each combination.

$$P\left(\frac{S_G}{S_R}\right)_i = \sum_{\text{all } F_G, F_{RT}, B_G, B_R \text{ which yield } (S_G/S_R)_i} P(F_G, F_{RT}, B_G, B_R) \quad (2-6)$$

Equation 2-6 can be factored into a product of independent probabilities. B_G and B_R are independent of each other and of the number of fluorescence photons, and so are written as separate factors, $P(B_G)$ and $P(B_R)$. The remaining term, $P(F_G, F_{RT})$, describes the probability of observing a particular combination of green and red photons. This term is equivalent to the probability of observing a total of $F = F_G + F_{RT}$ fluorescence photons times the probability that exactly F_{RT} out of F photons are red; $P(F_G, F_{RT}) = P(F) \times P(F_{RT}|F)$. Making these changes to the equation 2-6 results in

$$P\left(\frac{S_G}{S_R}\right)_i = \sum_{\text{all } F, F_{RT}, B_G, B_R \text{ which yield } (S_G/S_R)_i} P(F)P(F_{RT}|F)P(B_G)P(B_R) \quad (2-7)$$

Photon statistics

The latter three terms in equation 2-7 can be described analytically. First, under the restriction that the data is measured in equal time windows, the probability of recording B_G and B_R background photons per time window, $P(B_G)$ and $P(B_R)$, assuming average number of

counts per time window values of $\langle B_G \rangle$ and $\langle B_R \rangle$ respectively, is given by the Poisson distribution as shown in equation 2–8 [192]. Second, assuming there is a fixed probability, ε , that any given count is recorded in the red channel, the probability of observing exactly F_{RT} red fluorescence photons out of F total fluorescence photons can be expressed as a binomial distribution. $P(F_{RT} | F)$ is written from here on with a subscript ε in equation 2–9 in order to indicate this assumption shown.

$$P_{\langle B \rangle}(B) = \frac{\langle B \rangle^B e^{-\langle B \rangle}}{B!} \quad (2-8)$$

$$P_{\varepsilon}(F_{RT} | F) = \frac{F!}{F_{RT}!(F - F_{RT})!} \varepsilon^{F_{RT}} (1 - \varepsilon)^{F - F_{RT}} \quad (2-9)$$

Apparent FRET efficiency ε

The parameter ε is an apparent FRET efficiency, which take into account the quantum yields, detection efficiencies, and crosstalk of the system. The conventional FRET efficiency describes the ratio of sensitized acceptor events to the total number of donor excitations. If the intensity of fluorescence emissions from D and A is known (F_D and F_A respectively), E can be calculated according to equation 2–10:

$$E = \frac{F_A / \Phi_{FA}}{F_D / \Phi_{FD} + F_A / \Phi_{FA}} \quad (2-10)$$

Φ_{FD} and Φ_{FA} are the fluorescence quantum yields of the donor and the acceptor, respectively. In practice, not all fluorescence emissions are detected. F_G and F_{RT} differ from F_D and F_A by the detection efficiency factors g_G and g_R , respectively. Additionally, the overlap of the donor and acceptor fluorescence spectra results in a fraction of the donor signal appearing in the red channel, characterized by a spectral crosstalk term, α which appears in the equation 2–11:

$$F_G = g_G F_D$$

$$F_{RT} = g_R F_A + \alpha g_G F_D \quad (2-11a,b)$$

Combining equations 2–10 and 2–11, the apparent efficiency can be defined as a function of more conventional fluorescence parameters.

$$\varepsilon = \frac{F_{RT}}{F_G + F_{RT}} = 1 - \frac{1}{1 + \frac{\Phi_{FA} g_R}{\Phi_{FD} g_G} \frac{E}{(1-E)} + \alpha} \quad (2-12)$$

Fluorescence intensity distribution $P(F)$

The final term which needs to be considered in equation 2–7 is the fluorescence intensity distribution $P(F)$. Analytical form has been described in the literature [192], but it

would be simpler to substitute a measurable quantity for $P(F)$. Any term in equation 2–7 is evaluated only after B_G and B_R are specified. This fact suggests that the fluorescence intensity can be calculated as $F = N - B_G - B_R$. Making this substitution, changing the sum to occur over all values for N , and replacing $P(F)$ with $P(N)$ leads to equation 2–13.

$$P\left(\frac{S_G}{S_R}\right)_i = \sum_{\text{all } N, F_{RT}, B_G, B_R \text{ which yield } (S_G/S_R)_i} P(N) P_\varepsilon(F_{RT} | N - B_G - B_R) P_{\langle B_G \rangle}(B_G) P_{\langle B_R \rangle}(B_R) \quad (2-13)$$

The distributions $P_{\langle B_G \rangle}$, $P_{\langle B_R \rangle}$, and P_ε are given by equations 2–8 and 2–9. To obtain $P(N)$, the total intensity distribution histogram can be normalized. $\langle B_G \rangle$ and $\langle B_R \rangle$ are calculated from the mean background count rates. Only ε , remains unknown, and may be determined by using a χ^2 maximum likelihood estimator fit.

FRET fluorescence ratio

Equations 2–8, 2–9, 2–12, and 2–13 provide an analytical expression for the probability of any particular value of $(S_G/S_R)_i$ given $P(N)$, $\langle B_G \rangle$, $\langle B_R \rangle$, and ε . Although ε is a natural parameter in terms of mathematical development, it is not used in the literature. Therefore, instead of ε in subsequent analysis the experimentally related fluorescence ratio, F_G/F_R , will be used. In order to emphasize the distinction between an observed ratio which varies stochastically and the characteristic ratio which defines the distribution, the term "originating value" is introduced, and is denoted by brackets: $\langle F_G/F_R \rangle = [\varepsilon/(1-\varepsilon) - \alpha]^{-1}$. F_R is distinguished from F_{RT} by excluding crosstalk photons, $F_R = F_{RT} - \alpha g_G F_D$, a convention which conforms to previously published reports [126].

Influence of DA-distance

The DA-distance, R_{DA} , influences the FRET efficiency according to the equation:

$$E = \frac{1}{1 + \left(\frac{R_{DA}}{R_0}\right)^6}, \quad (2-14)$$

where R_0 is the Förster radius (see Section 1.1.3).

Equation 2–14 in turn influences ε through equation 2–12. Therefore, equation 2–13 must be extended to include a distribution in ε as a function of R_{DA} as shown in the equation 2–14.

$$P\left(\frac{S_G}{S_R}\right)_i = \int P(\varepsilon(R_{DA})) \sum_{\substack{\text{all } N, F_{RT}, B_G, B_R \\ \text{which yield } (S_G/S_R)_i}} P(N) P_\varepsilon(F_{RT} | N - B_G - B_R) P_{<B_G>}(B_G) P_{<B_R>}(B_R) d\varepsilon \quad (2-15)$$

An expression for $\varepsilon(R_{DA})$ can be derived from equation 2-12 by expressing E in terms of R_0 and R_{DA} . If the distribution for R_{DA} is known, then a distribution for $\varepsilon(R_{DA})$ can be derived which can be used to evaluate equation 2-14.

Assuming a Gaussian distribution of distances [184,193,194] described by an average distance \bar{R}_{DA} and standard deviation in the distance of σ_R , a probability density $P(\varepsilon(R_{DA})) = f_\varepsilon(\varepsilon)$ can be expressed. A probability density $f_R(R_{DA})$ for the donor-acceptor distance in the assumption of the Gaussian distribution is:

$$f_R(R_{DA}) = \frac{1}{\sqrt{2\pi}\sigma_R} \exp\left[-\frac{1}{2\sigma_R^2}(R_{DA} - \bar{R}_{DA})^2\right], \quad (2-16)$$

where \bar{R}_{DA} is the mean value and $\sigma_R = \sqrt{\overline{(R_{DA})^2} - (\bar{R}_{DA})^2}$ is the standard deviation for the Gaussian distribution.

Rearranging equations 2-12 and 2-14, the apparent fluorescence efficiency ε as a function of donor-acceptor separation R_{DA} can be obtained:

$$\varepsilon = \varepsilon(R_{DA}) = 1 - \frac{1}{1 + \alpha + \frac{\Phi_{FA}\mathcal{G}_R}{\Phi_{FD}\mathcal{G}_G} \left(\frac{R_0}{R_{DA}}\right)^6} \quad (2-17)$$

R_{DA} can be expressed as a function of ε :

$$R_{DA}(\varepsilon) = R_0 \left(\frac{\Phi_{FA}\mathcal{G}_R}{\Phi_{FD}\mathcal{G}_G}\right)^{\frac{1}{6}} \frac{1}{\left(\frac{1}{1-\varepsilon} - (1+\alpha)\right)^{\frac{1}{6}}} \quad (2-18)$$

Since $R_{DA}(\varepsilon)$ is an unambiguous function of ε and continuous within the interval $\varepsilon \in (\alpha/(1+\alpha); 1)$, the probability that the distance is in the interval from R_{DA} to $R_{DA} + dR_{DA}$ is identical to the probability that the apparent efficiency is in the interval from ε to $\varepsilon + d\varepsilon$.

$$dP\{\varepsilon, \varepsilon + d\varepsilon\} = dP\{R_{DA}, R_{DA} + dR_{DA}\} \quad (2-19)$$

Accordingly, for probability densities can be written:

$$f_\varepsilon(\varepsilon) = f_R(R_{DA}(\varepsilon)) \frac{dR_{DA}(\varepsilon)}{d\varepsilon} \quad (2-20)$$

That leads us to the analytical equation (see Appendix B) for the apparent fluorescence efficiency probability density $f_\varepsilon(\varepsilon)$, which contains parameters \bar{R}_{DA} and σ_R from the initial Gaussian probability density distribution of donor-acceptor separation:

$$f_\varepsilon(\varepsilon) = P(\varepsilon(R_{DA})) = \frac{R_0}{6\sqrt{2\pi}\sigma_R} \left(\frac{\Phi_{FA}\mathcal{G}_R}{\Phi_{FD}\mathcal{G}_G} \right)^{1/6} \frac{1}{(1-\varepsilon)^2} \left(\frac{1}{1-\varepsilon} - (1+\alpha) \right)^{-7/6} \times \exp \left\{ -\frac{1}{2\sigma_R^2} \left[R_0 \left(\frac{\Phi_{FA}\mathcal{G}_R}{\Phi_{FD}\mathcal{G}_G} \right)^{1/6} \left(\frac{1}{1-\varepsilon} - (1+\alpha) \right)^{-1/6} - \bar{R}_{DA} \right]^2 \right\} \quad (2-21)$$

The above equation can be substituted into equation 2-13 and numerically integrated in order to generate a PDA histogram which is broadened by a Gaussian distribution of R_{DA} distances $P(\varepsilon(R_{DA}))$.

Histograms and PDA fitting

Histograms are generated from $P(S_G/S_R)$ distributions by allocating each $(S_G/S_R)_i$ to a specific bin, summing all $P(S_G/S_R)_i$ values which fall in the same bin, and multiplying by the total number of molecules (or time windows) to be considered. It should be noted here that Poisson distributions have no upper bound, meaning it is possible to have more background photons than total photons. Consequently, for each value of N the Poisson distribution is calculated only up to N total counts, and the sum is subsequently normalized to unity.

For calculating the PDA distributions, $P(N)$ intensity distributions are derived from selected data of each experiment by making a histogram of the total number of photons per window, $N = S_G + S_R$, and dividing the histogram by the total number of time windows. The number of background counts $\langle B_G \rangle$ and $\langle B_R \rangle$ are calculated from \bar{B}_G and \bar{B}_R , respectively, by multiplying by the duration of the time window (1 ms, if otherwise is not specified).

The goodness of fit between the data and the PDA histograms was determined using a χ^2 maximum likelihood test. A Levenberg-Marquadt optimization scheme was used to find the $\langle F_G/F_R \rangle$ which produced the minimum χ^2 . Error bars were established by determining the values of $\langle F_G/F_R \rangle$ for which χ^2 was one higher than the minimum: $\chi^2 = \chi^2_{\min} + 1$. Weighted residuals were calculated as $(data\ histogram - PDA\ histogram) / N_{\text{bin}}^{1/2}$, where N_{bin} is the number of data counts in the respective PDA histogram bins.

2.5.1.3 PDA distributions properties

Several properties of the discrete PDA distributions are demonstrated on the following example: equation 2-13 was evaluated for the arbitrary case of $N = 10$ to 100 photons, $\langle F_G/F_R \rangle = 1.5$, $\langle B_G \rangle = \langle B_R \rangle = 0$, and $\alpha = 0$. The $P(N)$ was taken from the DNA FRET data presented below. All probabilities between 0.5 and 5 are displayed without binning as a comb plot in Figure 2-46. The discrete nature of the distribution leads to two features which introduce binning artefacts in the generation of histograms: probability 'spikes' at certain values, and probability 'voids' around the spikes.

Probability spikes are the result of the redundancy of certain values of the observed signal ratio. The probability voids are observed because efficiency values near the spikes cannot be generated using only integer values between 10 and 100.

As a simple example, consider the case above, but with only $N = 1$ to 10 photons, and each N is equally likely to occur. A value of $S_G/S_R = 1.5$ occurs twice in this set; $3/2$ at $N = 5$ (3.45% chance) and $6/4$ at $N = 10$ (6.27 % chance). An $S_G/S_R = 1$ occurs 5 times, i.e. for every even N , with probabilities 4.80 %, 3.45 %, 2.76 %, 2.32 % and 2.00 %. Given the initial assignment of $\langle F_G/F_R \rangle = 1.5$, it is not surprising that the single most likely event is $S_G/S_R = 1.5$ at $N = 10$. However when summed over all N , the value $P(S_G/S_R = 1.5) = 9.72$ %, which is lower than the 15.33 % chance of observing $S_G/S_R = 1$.

The probability spikes and voids observed in Figure 2-46 lead to histogram distributions which are sensitive to the choice of bin width and position and to histogram distributions which are rough. Figure 2-46 shows two histograms calculated using 49 bins (grey area) and 50 bins (solid line). A one bin change shifts the positions of the maximum and two satellite peaks. As the maximum count N decreases, the dependence of the histogram shape on the bin parameters increases. Additionally, the histogram roughness increases, making it difficult to assign a characteristic shape to the peaks. These problems are typically addressed in single molecule experiments by the use of larger time windows and minimum threshold criteria which serve to smooth the histograms [195], but simultaneously lower time resolution and hide real information.

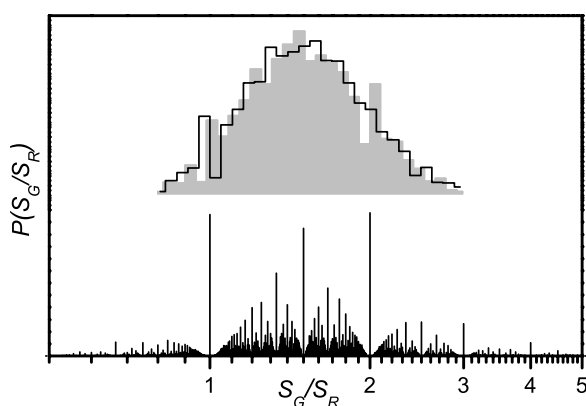


Figure 2-46. (*Bottom*) Comb plot indicating the probability of observing the possible S_G/S_R values. (*Top*) Two histograms composed from the comb plot probabilities, calculated from 0.5 to 5, with 49 bins (solid grey) and 50 bins (black line) showing the change in profile as number of bins change.

The relative sizes of the spikes proved to be very sensitive to $\langle F_G/F_R \rangle$. For example, $P(1)/P(2)$ changes by an order of magnitude, from 20 to 2, as the expected fluorescence ratio $\langle F_G/F_R \rangle$ changes from 0.7 to 1.3 (see Figure 2-47). The model is therefore very sensitive to changes in $\langle F_G/F_R \rangle$ within this range. Considering all of the spikes together over the entire

histogram provides a molecular 'bar code' which provides a sensitive determination of $\langle F_G/F_R \rangle$ over a broad range.

When the expected fluorescence ratio $\langle F_G/F_R \rangle$ is less than unity, then the probability of observing a value of $S_G/S_R = 1$ is much greater than the probability of observing a value of $S_G/S_R = 2$, as shown in the graph by the high probability ratio values at low $\langle F_G/F_R \rangle$. The slope of the curve provides the sensitivity of a fit to $\langle F_G/F_R \rangle$, since small changes in $\langle F_G/F_R \rangle$ result in plots with incorrect relative peak heights. As seen above, the black curve loses its sensitivity to changes in $\langle F_G/F_R \rangle$ beyond $\langle F_G/F_R \rangle = 2$, whereas the dashed light grey line is sensitive up to $\langle F_G/F_R \rangle = 6$. At low values of $\langle F_G/F_R \rangle$, all of the lines increase to infinity, establishing a lower limit of sensitivity of $\langle F_G/F_R \rangle = 0.3$ for the black line and $\langle F_G/F_R \rangle = 1$ for the dashed light grey line. Therefore, each pair of peaks is very sensitive to changes in $\langle F_G/F_R \rangle$ over a different range of values. Since all of these ranges overlap, considering an entire distribution of probabilities provides a sensitive measurement of $\langle F_G/F_R \rangle$ over the entire range of possible values.

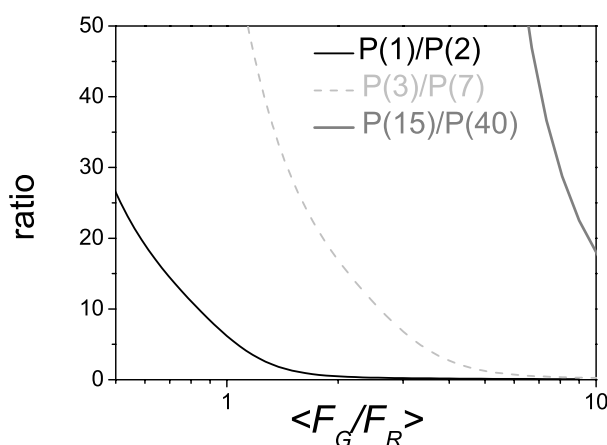


Figure 2-47. Illustration of the sensitivity of two probabilities ratio to the $\langle F_G/F_R \rangle$ value. Comb plots as shown in Figure 2-46 are calculated for many different values of $\langle F_G/F_R \rangle$, given on the X axis above. For each comb plot the ratio of two probabilities is calculated for three pairs of probabilities: $P(S_G/S_R = 1)/P(S_G/S_R = 2)$ (black line), or $P(S_G/S_R = 3)/P(S_G/S_R = 7)$ (dashed light grey), or $P(S_G/S_R = 15)/P(S_G/S_R = 40)$ (dark grey).

2.5.2 PDA application: Single dye FRET studies

2.5.2.1 Atto590 dye: a fixed FRET efficiency

The investigation of the dye Atto590 was designed to simulate a FRET signal with a constant $\langle F_G/F_R \rangle$ (see Figure 2-48). By using a single dye for both the green and red signal, typical problems in FRET measurements such as variations in lifetime, anisotropy, quantum yield, and donor-acceptor distance are excluded. From equation 2–11, the red fluorescence signal consists of two terms corresponding to the two different dyes: an acceptor fluorescence term and a donor crosstalk term. Since there is only one dye in this experiment, only one term is necessary to describe F_{RT} , so the signal can be freely defined as either pure crosstalk ($g_R = 0$) or pure red fluorescence ($\alpha = 0$). Using the latter definition, and recognizing that $F_D = F_A$, and $\Phi_{FD} = \Phi_{FA}$, the expected signal ratio becomes $\langle F_G/F_R \rangle = g_G/g_R$. Assuming the instrumental properties remain constant, the signal ratio is sensitive only to shifts in the emission spectrum.

In the MFD analysis of the raw data single molecule events were distinguished from the 3 – 6 kHz background by an intensity threshold criterion [75]. For Atto590, the single molecule bursts were further subdivided into 1 ms time windows and S_G/S_R was calculated directly. A minimum threshold of $N \geq 20$ photons was set for the Atto590 experiments for consistency with the DNA experiments.

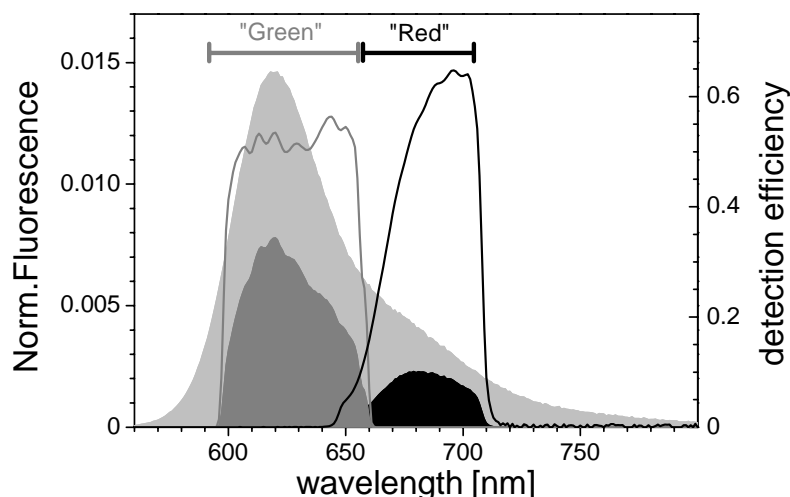


Figure 2-48. The experimental design for the single molecule MFD experiments with the dye Atto590. A FRET signal with a constant $\langle F_G/F_R \rangle$ simulated by dividing the fluorescence spectra of the dye (light grey area) into to channels, called “Green”, indicated by grey detection efficiency curve (smaller wavelength numbers) and “Red”, indicated by black detection efficiency curve (bigger wavelength numbers). The ratio of detected “Green” and “Red” fluorescence signals gives us the F_G/F_R ratio estimated in bulk fluorescence experiment. The detection efficiencies are estimated multiplying the transmittance coefficients of optical filters and dichroics which were used in the optical setup for single molecule detection (see Section 2.1.1.3, Table 2-4) and the manufacturer specifications for the APD sensitivity [130].

The resulting signal ratio histogram for Atto590 isomers 1 in pH6 buffer (see Section 2.2) is shown in Figure 2-49 (bottom, solid grey histogram). Also shown in Figure 2-49 is the best fit PDA histogram computed from equation 2–13 (solid line). It is clear that the theory predicts the shape of the histogram very well, including the positions and the heights of the individual spikes. The best fit, which shows no systematic deviations (see Figure 2-49, top), was determined to have a value of $\langle F_G/F_R \rangle = 4.018 \pm 0.071$. The results of PDA for other Atto590 isomers along with the calculations of the $\langle F_G/F_R \rangle$ ratios from bulk fluorescence spectra are discussed in Section 2.5.2.2.

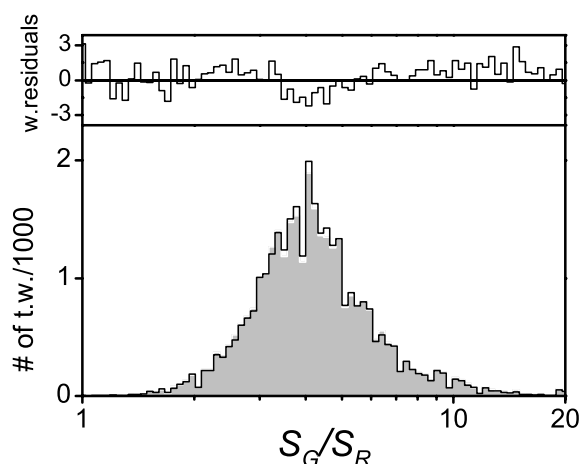


Figure 2-49. Histograms of the number of time windows with particular S_G/S_R values calculated from the data (grey areas) and predicted from the PDA (black line) along with the weighted residuals for best PDA fits (above). Atto590 isomer 1, $\langle F_G/F_R \rangle = 4.018 \pm 0.071$, $\langle B_G \rangle = 3.25$ counts, $\langle B_R \rangle = 0.76$ counts, $\alpha = 0$, $\chi^2 = 1.30$ and $N = 20$ to 444 photons. The standard deviation of $\langle F_G/F_R \rangle$ ratio is estimated when $\chi^2 = 2$.

2.5.2.2 Atto590 dye: a comparison of bulk fluorescence and single molecule FRET measurements

To give the idea of analytical capabilities of PDA applied to single molecule FRET data analysis results of bulk fluorescence measurements of the two isomers of Atto590 dye at two different pH values (6 and 9) are presented in Figure 2-50. Small spectral shifts are observed for the same isomer in different environment conditions. Table 2-12 shows that these spectral shifts are less than 1 nm which is on the order of the bulk fluorescence measurements precision. Simultaneously the spectra of two isomers have distinct spectral shifts of 2-3 nm.

The fluorescence quantum yields (Φ_F) for the fluorescence of the Atto590 dye are calculated as follows:

$$\Phi_{F,dye} = \frac{o.D_{reference}}{o.D_{dye}} \frac{F_{dye}}{F_{reference}} \frac{n_{dye}^2}{n_{reference}^2} \Phi_{F,reference} \quad (2-22)$$

where $\Phi_{F,reference} = 0.95$ is the fluorescence quantum yield of the reference Rh6G dye in ethanol, $o.D_{.dye}$ and $o.D_{.reference}$ are the optical densities at the same wavelength for the Atto590 dye and the reference Rh6G dye respectively, F_{dye} and $F_{reference}$ are total fluorescence intensities of the Atto590 dye and the reference Rh6G dye respectively, and $n_{dye} = 1.333$ and $n_{reference} = 1.359$ are the refraction indices for the dyes medium. The quantum yields values for both isomers and for both pH values are 0.80 ± 0.03 .

The $\langle F_G/F_R \rangle$ ratios are calculated from the spectra in Figure 2-50 and compared to the results of PDA on single molecule fluorescence data. The calculations take into account the transmittance of the optical filters in the smMFD setup (see Section 2.1.1.3, Table 2-4) and the manufacturer specifications for the detection efficiency of the APD [130]. The amount of fluorescence detected in a particular channel (“Green” or “Red”, see Figure 2-48) in the product of the fluorescence spectra and the detection efficiency in a channel. The detection efficiency in a channel is the product of the transmittance/reflectivity of the optical filters in a channel and the APD detection efficiency. The results of $\langle F_G/F_R \rangle$ estimation are listed in Table 2-13. The difference between smFRET PDA ratios and ratios estimated from the bulk fluorescence measurements can arise from:

1. The variations of the APD detection efficiency for different APDs in two channels of the smMFD setup. Manufacturer specifications for the detection efficiency of the APD [130] report the variation between different APD modules to be 15% (at 650 nm). Moreover, the detection efficiencies of the APD also show 5% (at 650 nm) spatial variation within the active area of the detector.
2. The spectral calibration of the steady state fluorescence spectrometer is not perfect.

The value of 15% is taken for the error estimation of the $\langle F_G/F_R \rangle$ ratios calculations from the bulk spectra measurements (see Table 2-13). Thus the $\langle F_G/F_R \rangle$ values estimated by different methods are in agreement within errors.

Single molecule detection and MFD analysis together with PDA propose a new tool for small spectral shifts detection. A properly designed sm FRET measurements allow estimating the influence of the pH value on fluorescence spectrum of the dye. This method can be used to monitor a pH value change within a living cell or to probe the environment of a fluorescent dye.

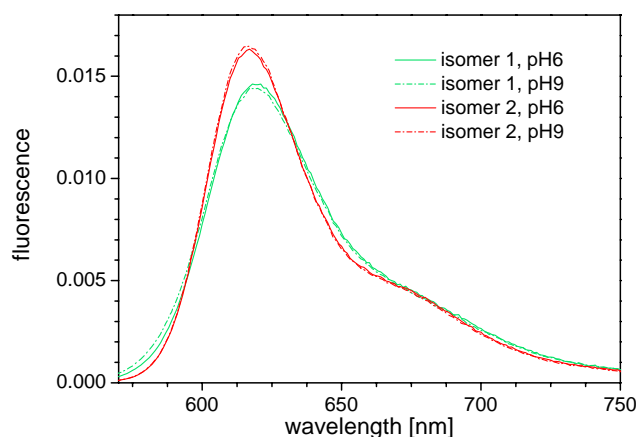


Figure 2-50. The fluorescence spectra of two isomers of Atto590 dye in buffer solutions (see Section 2.2) at two pH values (pH 6 and pH 9).

Table 2-12. The maximal values of normalized spectra presented in Figure 2-50.

	isomer 1	isomer 2
pH 6, spectral max [nm]	619	616
pH 9, spectral max [nm]	619	617

Table 2-13. Atto590 dye FRET histogram analysis. The values obtained for two isomers at pH 6 and pH 9 are listed. A single molecule “sm PDA” columns show fit results of PDA, whereas “bulk” columns show calculations which were done based on normalized fluorescence spectra, transmittance characteristics of the optical filters in single molecule MFD setup and manufacturer specifications for the APD detection efficiency. The parameters of PDA were $\langle B_G \rangle = 3.25$ counts and $\langle B_R \rangle = 0.76$ counts for pH 6, $\langle B_G \rangle = 3.61$ counts and $\langle B_R \rangle = 0.796$ for pH 9, $\alpha = 0$ and $N = 20$ to 444 photons. The standard deviation of $\langle F_G/F_R \rangle$ ratio is estimated when $\chi_{\min}^2 = \chi_{\min}^2 + 1$.

	isomer 1			isomer 2		
	sm PDA		Bulk $\langle F_G/F_R \rangle$	sm PDA		Bulk $\langle F_G/F_R \rangle$
	$\langle F_G/F_R \rangle$	χ_{\min}^2		$\langle F_G/F_R \rangle$	χ_{\min}^2	
pH 6	4.018 ± 0.079	1.23	3.531 ± 0.53	4.399 ± 0.070	0.98	3.824 ± 0.57
pH 9	3.925 ± 0.074	1.16	3.575 ± 0.54	4.349 ± 0.077	0.19	3.926 ± 0.59

2.5.2.3 Goodness of PDA fit and dependence on number of bins and threshold

Illustration of the unambiguity and precision of the PDA fits is shown in the following examples: fits to the Atto590 data histograms were performed either for histograms with different numbers of bins (see Figure 2-51) or for histograms of data which satisfied different minimum number of photons per time window thresholds (see Figure 2-52). In these plots, the best fit of $\langle F_G/F_R \rangle$ values is shown by the black line with opened circles with corresponding values on the left axis, whereas the resulting χ^2 values are shown by the grey line with closed circles with corresponding values on the right axis. The value of $\langle F_G/F_R \rangle$ is largely

insensitive to changes in parameters, varying by less than 1% from the mean value. Although the χ^2 values trend higher as the photon threshold is increased, the threshold increase excludes time windows from analysis, resulting in a poorer statistical sample. The increase from 3.88 to 4.00 in χ^2 may simply reflect this fact (see Figure 2-52).

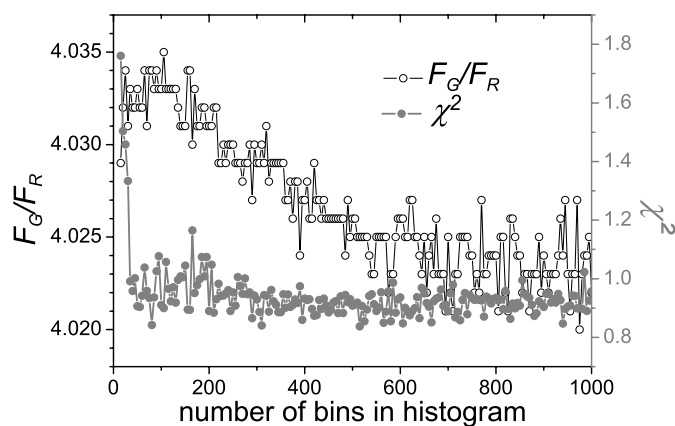


Figure 2-51. $\langle F_G/F_R \rangle$ and χ^2 dependence on the number of bins in the histogram for PDA.

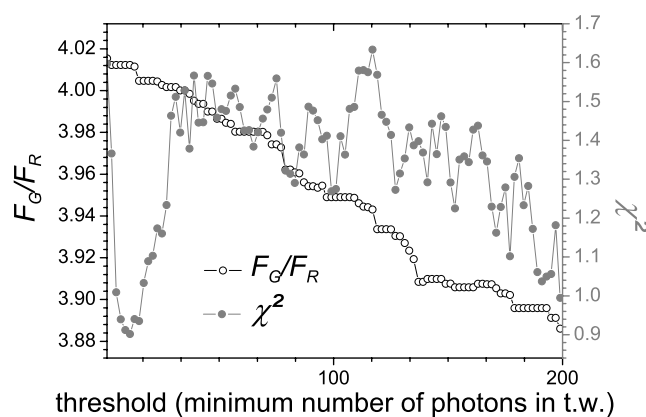


Figure 2-52. $\langle F_G/F_R \rangle$ and χ^2 dependence on the threshold photon count in one time window.

2.5.2.4 Shot Noise Limited Fluorescence Distributions

The result of single dye studies as shown in Figure 2-49 is the ability of the PDA method to fit FRET fluorescence ratios to uncorrected data unambiguously and precisely in a way that is independent of the threshold and the number of bins. The value determined for $\langle F_G/F_R \rangle$ was largely insensitive to changes in either of these parameters, never varying by more than 1% as either the number of bins or minimum number of photons were changed (see Figure 2-51 and Figure 2-52). The insensitivity of $\langle F_G/F_R \rangle$ to the threshold level means that the threshold count criterion can be significantly lowered and the size of the time windows decreased.

The χ^2 was very sensitive to the value of $\langle F_G/F_R \rangle$. The minimum χ^2 value was 1.3 at a ratio of 4.02. The error of the fit was estimated by determining at what $\langle F_G/F_R \rangle$ value did χ^2

increase to 2.3, or one higher than the minimum. This criterion was satisfied at ratio values of 3.95 and 4.09, indicating an error of a 1.8 % in determining the fluorescence ratio.

2.5.3 PDA application: FRET measurement on DNA molecules

Due to bleaching, incomplete labelling, and multiple donor species, the bursts obtained from DNA measurements required two selection steps before analysis.

Step 1 (bleaching correction): Bursts in which dye bleaches are identified by their non-overlapping green and red signals. Averaging the macro time (laboratory time) of all green photons in a burst should produce the same average time T_G as the average macro time of all red photons T_R . In the case of a bleaching event, one dye will fluoresce longer than the other, which will result in different mean macro times. A threshold criterion of ± 0.5 ms for the difference of mean green and red macro times $T_G - T_R$ was used to identify bleached molecules. This step typically reduced the amount of the high FRET ratio signal ($S_G/S_R > 4$) from 27 % to 22 % of the total signal [196].

Step 2 (Selection of an individual donor population): plotting the signal ratio versus donor fluorescence lifetime in the presence of the acceptor, S_G/S_R vs. $\tau_{D(A)}$, for the selected bursts revealed the effects of incomplete labelling and multiple donor lifetimes. According to criteria described in the text for each subensemble, only those molecules are selected for further analysis, which correspond to properly labelled, non-bleached molecules of a single population. These single molecule bursts were further subdivided into 1 ms time windows and S_G/S_R was calculated.

2.5.3.1 Single Dye-DNA construct: fixed FRET efficiency

In order to confirm the homogeneous behaviour of a single dye attached to DNA, D-only labelled DNA was investigated. Here, the crosstalk of $\alpha = 0.01$ is the only source of red fluorescence photons. Performing a MFD analysis on many single-molecule bursts, a look at the obtained S_G/S_R vs. $\tau_{D(A)}$ histogram in Figure 2-53 shows that Alexa488 exists as two species: a long lifetime species with $\tau = 4$ ns (D1), and a minority lifetime species at $\tau = 2$ ns (D2). Although the two species have the same S_G/S_R , the different lifetimes lead to different brightnesses, and consequently to different $P(N)$ distributions. Therefore, only molecules from D1 were selected for time window analysis, as indicated by the vertical line at $\tau = 2.7$ ns in Figure 2-53.

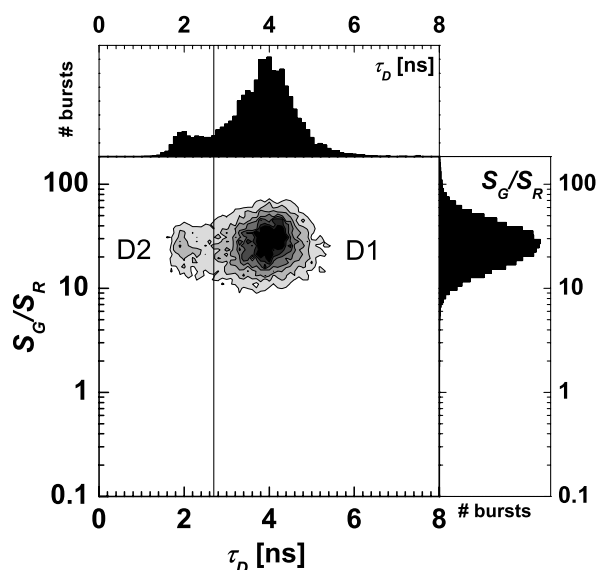


Figure 2-53. S_G/S_R vs. $\tau_{D(A)}$ based selection of D -only DNA construct. Selection rule at $\tau_{D(A)} = 2.7$ ns divides the data into two regions corresponding to two different quantum yields for this dye. Molecules with $\tau_{D(A)} > 2.7$ ns are further analyzed.

A histogram of the S_G/S_R signal after a time window analysis with a window size of 1ms is shown in Figure 2-54 (grey shaded area). The best fit PDA histogram occurs for an $\langle F_G/F_R \rangle = \text{infinity}$, i.e. no red fluorescence (Figure 2-54, black line). The excellent agreement between the theory and experiment validates the assumptions regarding the homogeneity of the system, and that even in the limit of $E = 0$ the PDA method is valid. In particular, the lack of broadening indicates that there is no spectral diffusion or brightness variation within the selected species, confirming that the dye linked to DNA is in a homogeneous environment.

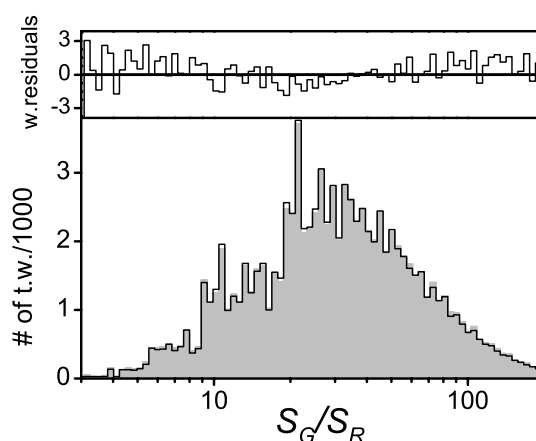


Figure 2-54. Histograms of the number of time windows with particular S_G/S_R values calculated from the data (grey areas) and predicted from the PDA method (black line) along with the weighted residuals for best PDA fits (above). Donor-only labelled DNA. $\langle F_G/F_R \rangle = \infty$, $\langle B_G \rangle = 3.83$ counts, $\langle B_R \rangle = 1.15$ counts, $\alpha = 0.01$; $\chi^2 = 1.36$. $N = 20$ to 444 photons.

2.5.3.2 DNA-dye FRET pair construct: FRET broadening description via distance fluctuations

After verification of a single dye homogeneous behaviour on the time scale of the measurements, the actual FRET *DA*-13 DNA (Section 2.2) was investigated. As with the donor only sample, the existence of two FRET species as shown in Figure 2-55 required a selection procedure which ensured that only species *DA2* was analyzed ($\tau > 1.8$ ns, $S_G/S_R < 4$).

A minimum threshold of $N \geq 20$ photons was set for the DNA analysis primarily to guarantee enough photons for a lifetime analysis, and second to avoid donor-only artefacts. The buffer for the DNA experiment contained a minor contamination species which accounted for ~ 0.6 % of the bursts.

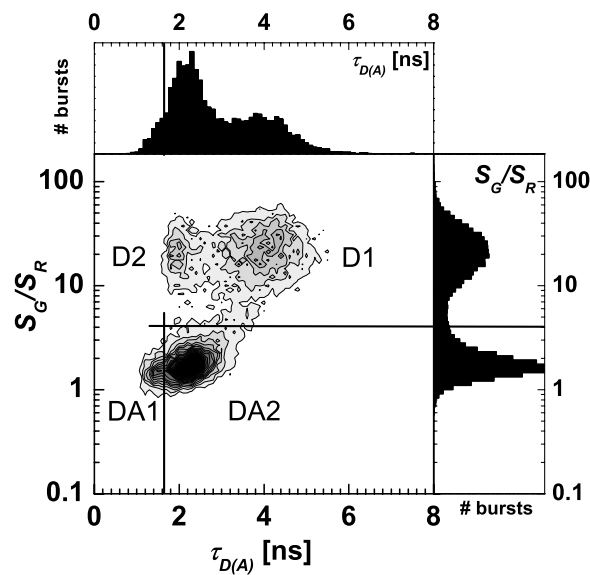


Figure 2-55. S_G/S_R vs. $\tau_{D(A)}$ based selection of *DA*-13 DNA construct (*D* and *A* are 13 bp apart). Two selection criteria were used for this sample ($\tau_{D(A)} > 1.8$ ns, and $S_G/S_R < 4$) due to additional peaks caused by bleaching and incomplete labelling.

A subsequent time window analysis produced an S_G/S_R histogram with a broad peak and a long tail, as shown in Figure 2-56 (grey shaded areas). An attempt to fit the histogram with a single $\langle F_G/F_R \rangle$ value resulted in the dotted line histogram in Figure 2-56A. In this case the PDA method fails to describe the data correctly, indicating a χ^2 value of 124.

There are many possible reasons which may cause a broadening of the S_G/S_R distributions beyond the shot noise limit. Several will be discussed later, but the analysis will be continued here assuming that the broadening is due to fluctuations in the *DA*-distances.

Using equations 2–15 and 2–21, the PDA distribution was fit to the data by varying \bar{R}_{DA} and σ_R . The best fit, shown as the solid line in Figure 2-56A, occurred at values of $\bar{R}_{DA} = 53.9$ Å and $\sigma_R = 2.3$ Å, with no systematic deviation in the weighted residuals (Figure

2-56A, top). The histogram was fit only in the range from $0.5 < S_G/S_R < 4$ because bleaching and blinking of the acceptor dye in some time windows resulted in additional signal at higher ratios (see below).

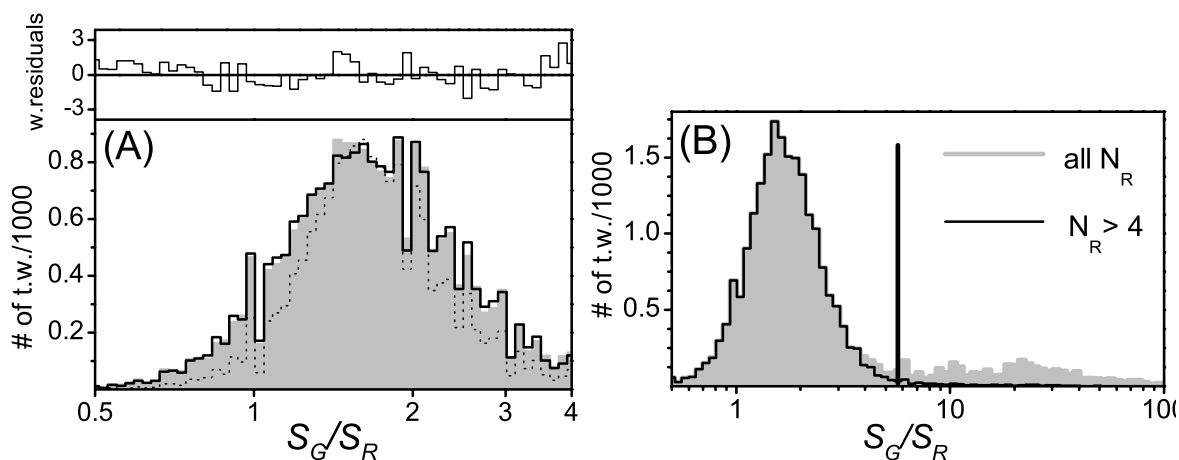


Figure 2-56. Histograms of the number of time windows with particular S_G/S_R values calculated from the *DA-13* DNA data. (A) S_G/S_R histogram calculated from the data (grey area), and predicted from the PDA method for both a fixed fluorescence ratio ($\langle F_G/F_R \rangle = 1.61$, dotted line) and a model Gaussian distance distribution with a centre of $\langle \overline{F_G/F_R} \rangle = 1.58$ and $\sigma_{ratio} = 0.07$ (solid line) which corresponds to an $\overline{R}_{DA} = 53.9 \text{ \AA}$ and $\sigma_R = 2.3 \text{ \AA}$. The data was fit to a Gaussian distribution of distances in the range 0.5 to 4.0. $\langle B_G \rangle = 3.83$ counts, $\langle B_R \rangle = 1.15$ counts, $\alpha = 0.01$, $\Phi_{FA} = 0.32$, $\Phi_{FD} = 0.80$, $g_R/g_G = 2.2$, $\chi^2 = 1.03$. $N = 20$ to 444. A threshold of 20 was chosen to ensure that a $\tau_{D(A)}$ value could be calculated for each time window and to avoid photobleaching events in *DA-13* DNA. (B) Remaining effects of bleaching and blinking in S_G/S_R . The grey histogram shows the S_G/S_R signal as analyzed in (A), but including the long tail at $S_G/S_R > 4$ (vertical line). The black line histogram shows the same data after removing time windows with < 4 red photons, i.e. time windows with only background red photons. The histogram tail corresponding to $S_G/S_R > 4$ is largely removed, whereas the active species peak is not significantly affected, suggesting that the tail is due to time windows with an inactive acceptor.

2.5.3.3 DNA-dye FRET pair construct: other FRET broadening mechanisms

Broadening of the S_G/S_R distribution occurs because the $P(N)$ and/or the P_ϵ distributions in equation 2–13 vary during measurements, causing brightness and/or apparent efficiency fluctuations. There are several mechanisms which can result in such fluctuations. A few of the possible mechanisms are discussed below, but others probably exist.

First, it is possible that the dyes exist in more than one active state. Figure 2-53 demonstrates that Alexa488 has two species with different lifetimes, and Cy5 is known to exhibit double exponential decay behaviour and to possess nonfluorescent intermediates which are capable of quenching the donor [197,198].

Second, the shape of a confocal detection volume is wavelength dependent, so it is possible that the ratio g_G/g_R is position dependent and changes as the molecule diffuses through the focus.

A third possibility is that E changes due to a changing R_0 , either due to spectral shifts in the dyes, changes in Φ_{FD} , or changes in the geometric orientation factor κ^2 .

A fourth mechanism is changes in E caused by a variation in R_{DA} , as already discussed. Each of these broadening possibilities has the time scale on which variations must occur to cause signal broadening.

Time Scales for Dynamics

If a molecule undergoes dynamics at a rate faster than the photon count rate, then consecutive photons are uncorrelated with respect to which state produced them, i.e. the state for each photon is independent and randomly determined. In this case, there is a fixed probability, $P(i)$, that the molecule is in the i^{th} state when a photon is emitted. If the FRET efficiency of the i^{th} state is a constant E_i , then the probability of both being in the i^{th} state and transferring energy is $P(i) \times E_i$. It follows that the expected probability of transferring energy is given by, $\langle E \rangle = \sum_i P(i) \times E_i$, i.e. dynamics result in a constant $\langle E \rangle$, and in the limit of dynamics occurring much faster than photon counting, the signal histograms approach a single shot noise limited PDA distribution. It is therefore sufficient to show that dynamics are fast compared to count rates in order to exclude them as a source of broadening.

Dynamics may also occur on a time scale approaching the size of the time windows used in the analysis. In this case, the likelihood that entire time windows will pass without a dynamic event occurring is significant, and will result in a distinct shot noise limited peak for each species with a long duration. Therefore, slow dynamics result in multiple shot noise limited peaks and are easily recognized.

In these experiments, maximum count rates were typically 100 kHz and a 1 ms time window analysis was used. Only dynamics which occurred within the time scale of 10 – 500 μs could result in broadening.

Multiple States of Alexa488 and Cy5

The two species of Alexa488 (D1 and D2) are clearly resolvable in the burstwise analysis in Figure 2-55, and a time window analysis of either peak produced a shot noise limited distribution. Furthermore, FCS measurements did not show any brightness fluctuations in the 10 – 500 μs range. Therefore, fluctuations in Alexa488 are too slow to cause broadening and are excluded.

Cy5 has been extensively studied for use as an acceptor dye in DNA experiments [129,199]. In these experiments, Cy5 was shown to undergo intersystem crossing to a triplet state and triplet deactivation with rates of $k_{ISC} = 0.5 \times 10^6 \text{ s}^{-1}$, $k_T = 0.2 \times 10^6 \text{ s}^{-1}$, respectively. Cy5 also displays photon dependent isomerization between a strongly fluorescent *trans*-state and a weakly fluorescent *cis*-state. Under the excitation intensities used here, the isomerization rate $k_{ISO} = 0.16 \times 10^6 \text{ s}^{-1}$. An FCS analysis (Figure 2-57) of the red signal did not show any brightness fluctuations in the 10 – 500 μs range. Therefore dynamics of the dyes are ruled out as mechanisms which cause broadening.

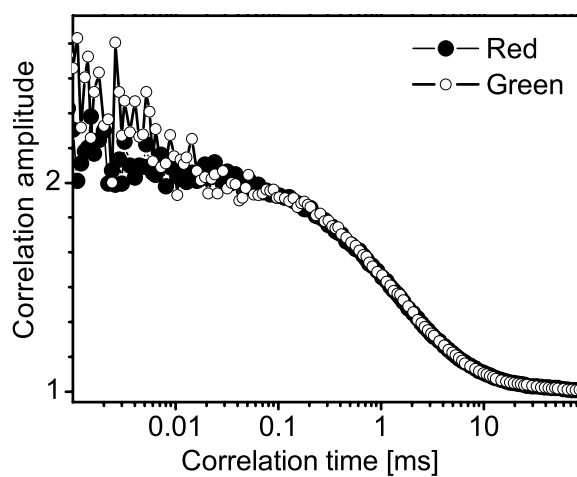


Figure 2-57. Selective FCS studies [200] of DA-13 DNA molecule signals. Open circles correspond to the donor signal and solid circles correspond to the acceptor signal. Fits of the FCS curves determined the donor and acceptor diffusion times to be 1.23 ms and 1.27 ms, respectively, indicating similar detection volumes for the two dyes. The triplet time of Alexa488 and the isomerization time for Cy5 were determined to be 0.9 μs and 5.0 μs , respectively. Neither dye shows dynamics in the time scale 10 – 500 μs .

Inhomogeneous g_G/g_R .

The focus volume can be ideally described by a wavelength dependent 3D Gaussian function [38]. Using two different colour ranges, it is conceivable that the observation foci have different sizes, resulting in a position dependent g_G/g_R . This artefact was avoided by not focusing the optics to a diffraction limited spot size where wavelengths effects become significant, and by illuminating only molecules in a portion of the observation volume near the centre, where a Gaussian volume shows the lowest spatial variation. Thus g_G/g_R remains constant within our ability to measure, which is confirmed by both the FCS measurements in Figure 2-57 indicating no measurable differences in the detection volumes for green and red and in the success of predicting shot noise limited single dye and donor only distributions.

Förster Radius

The Förster radius is calculated as $R_0 = 9870 [\Phi_{FD} J(\lambda) \kappa^2 n^{-4}]^{1/6}$, where n is the index of refraction of the medium, κ^2 is a geometric orientation factor, and $J(\lambda)$ is the overlap integral between the donor emission and acceptor adsorption spectra. Broadening due to changes in Φ_{FD} has already been excluded. Changes in κ^2 could be caused by slow rotational motions of either dye. Previous studies have show that the mean rotational correlation times of Alexa488 and Cy5 attached to DNA are 0.6 ns and 2.3 ns, respectively [129]. These values are too short to cause broadening in these measurements. Finally, a spectral shift for either dye would result in a time varying $J(\lambda)$. A spectral shift would also lead to a change in the detection efficiency, which would be detectable as a fluctuation in intensity. No fluctuations in the 10 – 500 μ s time range were detectable via an FCS analysis (Figure 2-57) for either the green or red signal. Additionally, the donor only measurements specifically verified the lack of spectral shifts in Alexa488. Therefore, spectral shifts, and changes in R_0 altogether, are excluded as sources for the observed broadening.

Cy5 Bleaching

As explained in Section 2.5.3.2, only molecule bursts corresponding to peak DA2 in Figure 2-55 were selected for time windows analysis. After this analysis, time windows appeared with high S_G/S_R values (Figure 2-58). Dividing a burst into time windows lowers the number of photons used to calculate fluorescence parameters. Combined with the random signal variations within a burst, broader histograms are expected. However, despite having enough windows for a good statistical sampling, Figure 2-58 shows a more extreme behaviour. These molecules have distinct populations of time windows with $S_G/S_R \sim 30$, and $\tau_{D(A)}$ values ranging from 2 ns to 4 ns. The heterogeneous $\tau_{D(A)}$ results in brightness fluctuations which make fitting these time windows to a donor-only PDA distribution impossible. Figure 2-59 shows a time trace of a single burst using a sliding window of 100 μ s. This molecule undergoes single step acceptor bleaching (event indicated by a vertical line), resulting in a synchronous rise in green intensity and lifetime. After acceptor bleaching, molecules exhibit an unquenched, donor-only like signal. In addition, Cy5 can enter dark states during a burst and then recover. Dark states have been observed in Cy5 [197,198] and Cy5 attached to DNA [197,201] as intermediates to a bleached state. These studies suggested that there are at least two intermediate states still capable of quenching a donor. A mixing of dark states, fluorescence, and bleached states would explain the $\tau_{D(A)}$ distribution in Figure 2-58.

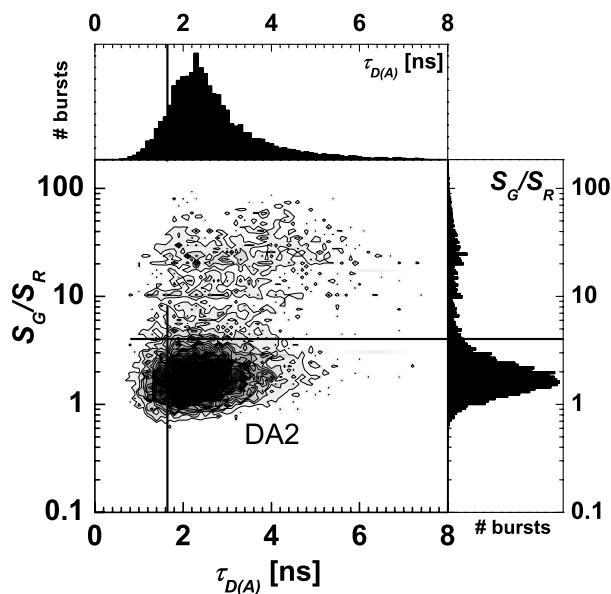


Figure 2-58. S_G/S_R vs. $\tau_{D(A)}$ diagram of *DA-13* DNA signal after time window analysis of species DA2 in Figure 2-55. DA2 remains visible, but a broad, weak signal at $S_G/S_R > 4$ appears with $\tau_{D(A)}$ distributed from 2 ns to 4 ns. The signal is likely due to weakly or nonfluorescent Cy5 molecules, resulting in the high signal ratios. The broad distribution in $\tau_{D(A)}$ indicates a mixture of bleached, inactive Cy5 and dark Cy5 states which are still capable of quenching the donor. Multiple dark states may exist.

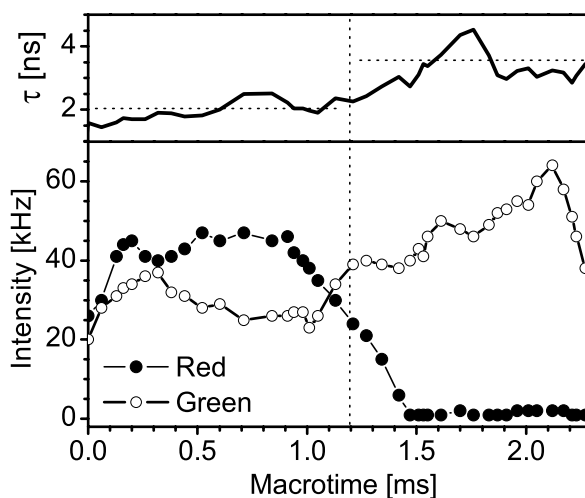


Figure 2-59. Fluorescence signal within a burst. The intensity of the green and red intensities below (solid circles and open circles, respectively) and the lifetime above. Cy5 undergoes single step bleaching, with a simultaneous rise in green intensity and fall in red intensity, together with a corresponding rise in green lifetime. To generate enough points for a visual presentation, the data was calculated from overlapping 1 ms time windows (100 μ s shift), which results in the single step transition (vertical dotted line) being significantly smoothed. Horizontal dotted lines indicate the average lifetimes before and after the transition.

One feature common to the intermediates and the bleached state is that they produce a red signal which is close to background. A look at the red intensity distribution, $P(N_R)$, in Figure 2-60 (grey histogram) reveals two peaks, corresponding to the fluorescent and non-fluorescent states. An overlay of the $P(N_R)$ distribution from the donor only experiment (black line) suggests a selection criterion of $N_R > 4$ will exclude most of the dark Cy5 time windows from the analysis. Furthermore, the existing criterion of $N \geq 20$ for all of the analyses makes it unlikely that a fluorescence active species will produce 4 or fewer red photons, so the FRET time windows should not be affected. Figure 2-56B presents the data as analyzed in Figure 2-56A (grey histogram) and the same data analyzed with the additional $N_R > 4$ criterion. The signal at $S_G/S_R > 4$ has been almost completely removed, while the FRET peak remains virtually unchanged.

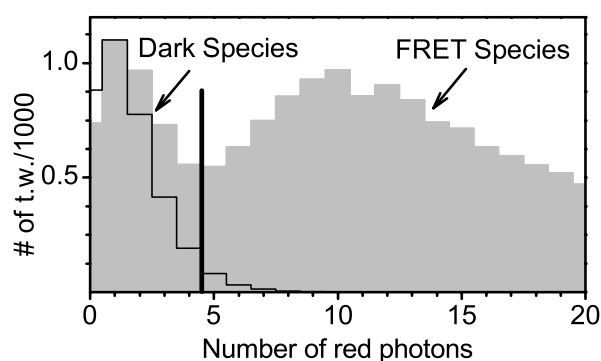


Figure 2-60. Bleaching and blinking in red intensity distributions. The histograms count the number of time windows with a given number of red photons. The grey histogram shows the intensity distribution of the *DA-13* DNA FRET data in Figure 2-56. Two peaks are seen; a low FRET or dark Cy5 species at $N_R < 5$ which most likely contains bleached and dark Cy5 molecules, and a FRET – Cy5 active species. The black line histogram is the intensity distribution of the red signal from the donor only sample shown in Figure 2-54, shown for comparison. The slight difference in the average intensities of the donor only distribution and dark Cy5 species of the *DA-13* DNA (< 1 photon/time window) is likely due to a minimal amount of fluorescence from the dark species.

Basing on the PDA histogram in Figure 2-54, it is possible to estimate the $\sim 6.5\%$ of a donor-only signal has an $S_G/S_R \leq 4$, which when applied to Figure 2-56B suggests that 282 time windows in the FRET peak are actually from the donor only population. Alternatively, Figure 2-60 indicates that $\sim 10\%$ of the donor only time windows ($= 329$) survive the N_R threshold, without commenting on the S_G/S_R value. In practice, only those windows which survive both of these criteria will appear in the filtered histogram in Figure 2-56B (black line). The total difference between the shot noise limited distribution and the data in Figure 2-56A is 6715 time windows, indicating that the number of possible bleached and dark bursts is not large enough to explain the observed broadening.

2.5.4 Fluorescence-based ruler: DNA length estimation

The experiment with a mixture of four DNA constructs labelled with FRET dye pair Alexa488/Cy5 (Section 2.2, dyes) at 5, 9, 13 and 15 bp between them (Section 2.2, DNA samples) is considered to demonstrate the ability of FRET data analysis to determine the distance between two fluorophores [129,202].

Figure 2-61 shows the helical DNA model [129] and the remarkable outcome of the time-resolved single-molecule fluorescence studies. In the experiment molecules of different species [202, page 67-68] mixed together have been easily identified. Although the information about the species is still averaged over the ensemble of molecules and their conformations, the length of molecules in the species can be extracted from the FRET signal ratio S_G/S_R histogram (Figure 2-61, right).

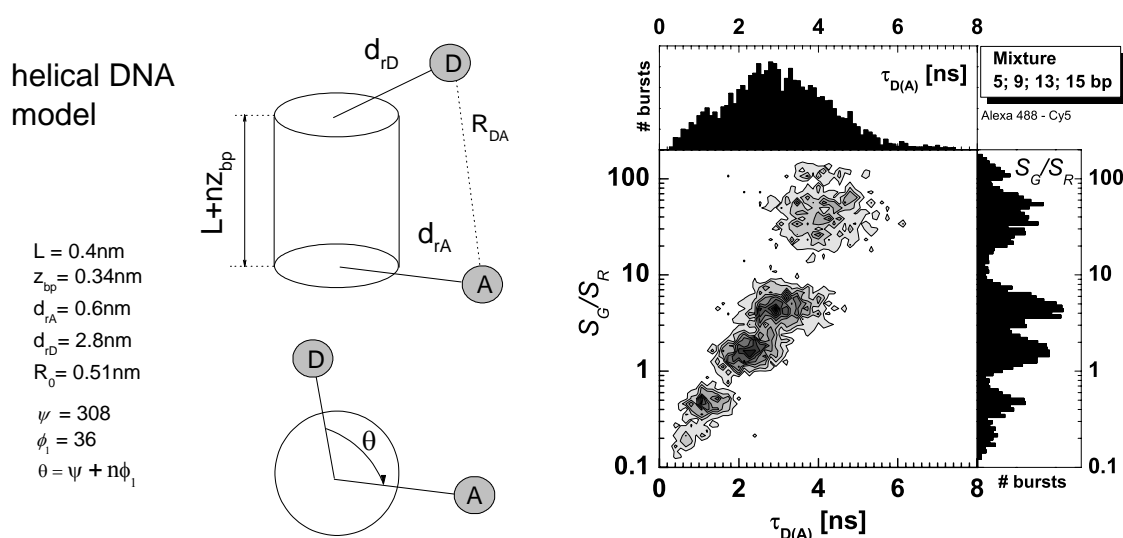


Figure 2-61. Left: the helical DNA model presented by Widengren et al. [129, 202]. Here the double stranded DNA molecule is treated as a cylinder, where L is the distance between projections of the molecular centres of the donor and acceptor fluorophores on the DNA helical axis, z_{bp} is the length between two base-pairs along the helical axis, n is the number of base-pairs, d_{rD} , d_{rA} are normal distances from the donor and acceptor on the helical axis, ψ is the cylindrical angle between the donor and acceptor linker arms and ϕ_1 denotes the cylindrical twist angle of the acceptor linker arm per base-pair. The distance between the donor and acceptor dyes can be calculated from the geometry of the model according to equation 2-23. Right: S_G/S_R vs. $\tau_{D(A)}$ plot for the different base pair number DNA constructs mixture (DA-5, DA-9, DA-13 and DA-15). Fluorescence bursts divided into 1ms time windows and time windows with minimum 100 photons are taken. Four distinct populations corresponding to different molecular constructs species are observed as S_G/S_R changes from 0.1 to 10. The region where $S_G/S_R \sim 100$ corresponds to donor only labelled population. Data is taken from [202, page 98] and a proper scaling is applied.

The average distance (R_{DA}) between the donor (D) and the acceptor (A) dyes attached to the DNA construct can be calculated according to the geometry of the helical DNA model (Figure 2-61, left) by the following equation [129]:

$$R_{DA} = \sqrt{(L + nz_{bp})^2 + (r_A^2 + r_D^2 - 2r_A r_D \cdot \cos(\psi + n\phi_1))} \quad (2-23)$$

The distance between the FRET pair on the DNA construct can be estimated from the fluorescence signal. Considering equations 1-14, 2-5 a,b and 2-11 a,b the FRET efficiency can be written as follows:

$$E = \frac{1}{1 + \left(\frac{R_{DA}}{R_0}\right)^6} = \frac{1}{1 + \frac{\Phi_{FA} g_R}{\Phi_{FD} g_G} \frac{S_G - B_G}{S_R - B_R - \alpha(S_G - B_G)}} \quad (2-24)$$

The relationship between R_{DA} and fluorescence signal ratios can be simplified.

1. if $\alpha = 0$ leads to the relationship

$$\left(\frac{R_{DA}}{R_0}\right)^6 = \frac{\Phi_{FA} g_R}{\Phi_{FD} g_G} \frac{S_G - B_G}{S_R - B_R} = a \frac{S_G - B_G}{S_R - B_R}, \text{ with } a = \frac{\Phi_{FA} g_R}{\Phi_{FD} g_G} \quad (2-25)$$

2. if $\alpha = 0, B_G, B_R = 0$ leads to the relationship

$$\left(\frac{R_{DA}}{R_0}\right)^6 = \frac{\Phi_{FA} g_R}{\Phi_{FD} g_G} \frac{S_G}{S_R} = a \frac{S_G}{S_R}, \text{ with } a = \frac{\Phi_{FA} g_R}{\Phi_{FD} g_G} \quad (2-26)$$

3. if $\alpha = 0, B_G, B_R = 0$ and $\Phi_{FA}, \Phi_{FD}, g_G, g_R = 1$ leads to the relationship

$$\left(\frac{R_{DA}}{R_0}\right)^6 = \frac{S_G}{S_R}, \text{ with } a = 1 \quad (2-27)$$

The case of non-zero background is considered for the FRET data analysis in PDA which also accounts for the shot noise. Other approaches can be generalized describing the FRET fluorescence ratios probability distribution in the same way which was given in Section 2.5.1.2 (see equations 2-16, 2-21). The consideration is based on the Gaussian distribution of for the probability density of the R_{DA} distance. Analogously, other distance distribution [30,187,203] can easily be considered. The probability density function propagation math provides the FRET signals ratio distributions for these cases (see Appendix C). The analytical expressions for the FRET ratios with no background are given by equations 2-28 and 2-29:

$$f(S_G / S_R) = \frac{1}{6\sqrt{2\pi}\sigma_R} a^{\frac{1}{6}} R_0 \left(\frac{S_G}{S_R}\right)^{\frac{5}{6}} \exp\left[-\frac{1}{2\sigma_R^2} \left(a^{\frac{1}{6}} R_0 \left(\frac{S_G}{S_R}\right)^{\frac{1}{6}} - \bar{R}_{DA}\right)^2\right] \quad (2-28)$$

$$f(\log(S_G / S_R)) = \frac{\ln 10}{6\sqrt{2\pi}\sigma_R} a^{\frac{1}{6}} R_0 \cdot 10^{\frac{1}{6} \log \frac{S_G}{S_R}} \cdot \exp\left[-\frac{1}{2\sigma_R^2} \left(a^{\frac{1}{6}} R_0 \cdot 10^{\frac{1}{6} \log \frac{S_G}{S_R}} - \bar{R}_{DA}\right)^2\right] \quad (2-29)$$

Figure 2-62 illustrates the properties of obtained distributions. Whereas the distribution of distances has symmetric Gaussian shape, FRET signal ratios and logarithm of FRET signal

ratios show the asymmetry of the probability density functions. This asymmetry is usually observed on experimental data histograms [180,187,189,202].

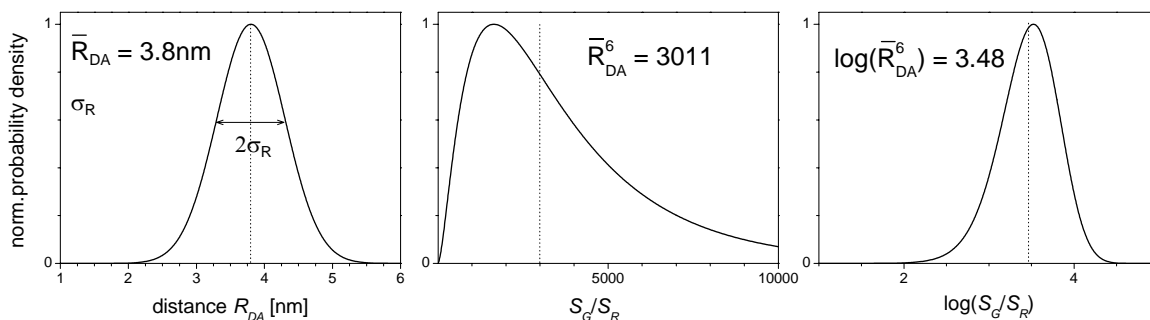


Figure 2-62. Illustration of the probability density function propagation. Initial values, described by symmetric shape Gaussian probability distribution with parameters R_{DA} and σ_R (left graph) becomes different asymmetric shapes for new probability distribution functions, however still can be described with the same initial parameters (R_{DA} , σ_R). Middle graph: initial values are taken to the sixth power (in this case values are proportional to S_G/S_R). Right graph: common logarithm of initial values to the sixth power is taken (obtained values are proportional to $\log(S_G/S_R)$). Dotted lines indicate the positions of the mean DA-distance R_{DA} , as well as the position of the mean value taken to the six power and logarithm of the mean value taken to the six power.

The probability density distributions given by equation 2–28 and 2–29 can be used to describe the DNA constructs mixture sample. The fluorescence signal ratio histogram S_G/S_R of the DNA constructs mixture shown on the right side in Figure 2-61 is analysed. The $\log(S_G/S_R)$ histogram is fitted with the Levenberg-Marquadt optimization algorithm [204] to the sum of five functions given by equation 2–29. Two cases are considered, when $a = 0.88$ (provided by $\Phi_{FA} = 0.32$, $\Phi_{FD} = 0.80$ and $g_R/g_G = 2.2$) and $a = 1$ (provided by $\Phi_{FA} = 1$, $\Phi_{FD} = 1$ and $g_R/g_G = 1$). Distances estimated from the fit of FRET ratios in Gaussian approximation for distance distributions as well as calculated from the theoretical model (equation 2-23) are presented in Table 2-14 and in Figure 2-64. The distance values obtained from the fits are in a good agreement with the theoretical model values for DNA-dyes constructs. The results of the fit with the equation 2-29 and the results obtained via PDA for the DA-13 construct are in a good agreement. This fact indicates a small background signal contribution for each bin of the $\log(S_G/S_R)$ histogram (see Appendix D) and suggest that different values of background counts can result in the same estimation of the fluorescence ratio. Thus, detailed studies of the influence of the background counts on the PDA results are required.

The standard deviations estimated by the fit (σ_R) contain information about a shot noise in fluorescence signal measurements. Although $\sigma_R > \sigma_{PDA}$, the difference between them is occasionally not big for the case of DA-13 construct ($\sigma_{PDA} = 2.3 \text{ \AA}$ and $\sigma_R = 2.7 \text{ \AA}$). This can be explained by the comparable value of $\sigma_{shot} = 3.3 \text{ \AA}$ as estimated for the Atto590 fluorescence ratio histogram fitting (Figure 2-49) by equation 2–29.

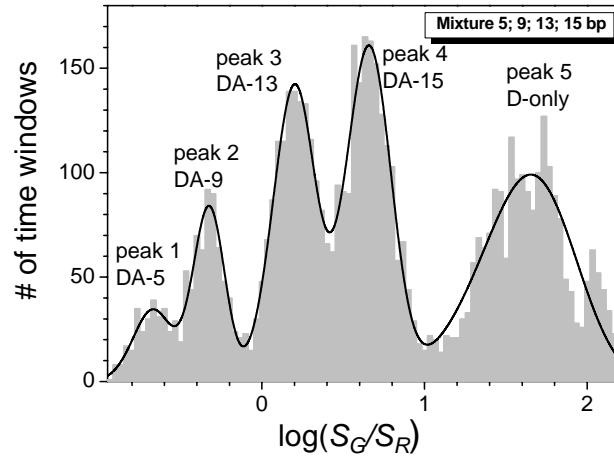


Figure 2-63. S_G/S_R histogram of the number of time windows (grey area) for the experiment, presented in Figure 2-61, vertical histogram. The black line is the result of the fit of five peaks to the efficiency probability distribution function, which is the sum of five functions given by equation 2–29. Equation 2–29 is obtained assuming the model of the Gaussian distribution of distances between donor and acceptor molecules. The value of $a = 0.88$ is based on the experimental parameters for the quantum yields and detection efficiencies $\Phi_{FA} = 0.32$ and $\Phi_{FD} = 0.80$ and $g_R/g_G = 2.2$. The fitting is performed with the Levenberg-Marquadt optimization algorithm and statistical weighting [204].

Table 2-14. Result of the model calculations according to Widengren et al. [129, 202] and FRET analysis of DNA mixture (Figure 2-61). For all fits Förster radius R_0 was 51 Å. Two fits to the sum of five functions (equation 2–29) is performed. For both of them the crosstalk and background assumed to be zero. The quantum yields and detection efficiencies ratio equal unity ($a = 1$) are considered and $\Phi_{FA} = 0.32$ and $\Phi_{FD} = 0.80$ and $g_R/g_G = 2.2$ ($a = 0.88$) are considered. The parameters of PDA were as specified for Figure 2-56.

	bp	R_{DA} [Å] model	fit results, equation 2–29				fit results, PDA	
			$a = 1$		$a = 0.88$		R_{DA} [Å]	σ_{PDA} [Å]
			R_{DA} [Å]	σ_R [Å]	R_{DA} [Å]	σ_R [Å]		
DA-5	5	38.3	39.3	1.8	38.5	1.7	-	-
DA-9	9	44.8	44.9	1.7	43.9	1.6	-	-
DA-13	13	54.3	54.9	2.7	53.8	2.7	53.9	2.3
DA-15	15	63.6	65.4	3.5	64.1	3.4	-	-

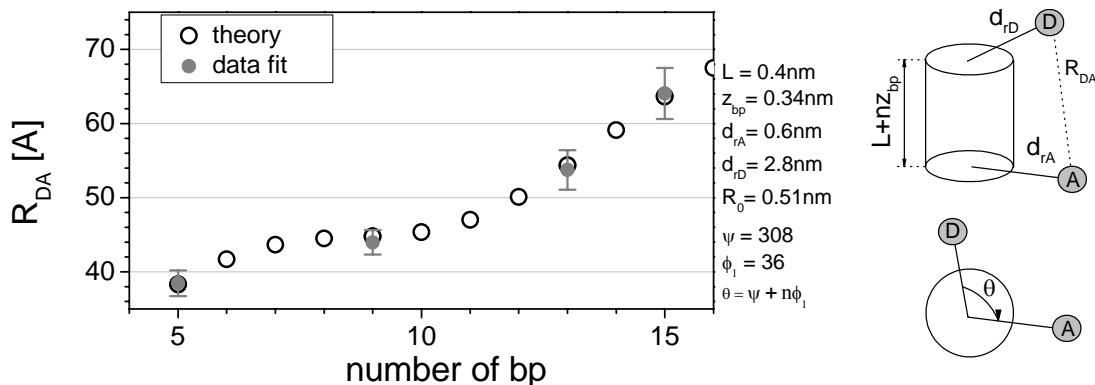


Figure 2-64. Left: Theoretical and calculated from measured data distances between donor and acceptor molecules. Distance values and their standard deviations (grey circles) are obtained from the fit of experimental data (Figure 2-63) with the efficiency probability distribution function according to equation 2–29. Theoretical values (open circles) are calculated according to the model presented by Widengren et al. [129, equation 29]. Right: the helical DNA model (see Figure 2-61).

2.5.5 Conclusions

The PDA predicts the shot noise limited distribution of a two colour FRET signal, thereby describing the minimum width that a FRET signal distribution must have given existing background, crosstalk, and efficiency. Conversely the PDA method can successfully extract the originating value behind shot noise limited FRET signal distributions and determine the underlying fluorescence signal ratio with a precision of better than 2%. Under optimal conditions, this precision translates into a precision in the distance measurements better than 1 % of the Förster radius. FRET distributions which are not shot noise limited are easily identified. For these distributions the PDA method can be used to test the validity of models used to explain the additional broadening. A 5Å distribution broadening due to the mobility of the dyes on flexible linkers is easily revealed. The surprisingly slow linker movements identified here can be rationalized by the existence of a rugged potential surface defined by the presence of the DNA, which hinders the free movement of the dyes.

Information describing the distribution of distances in molecules is valuable in determining protein intermediates and exploring partially folded states and refolding mechanisms. Furthermore, the success of the model even for low photon counts allows both smaller time windows providing higher time resolution, and lower photon thresholds which increases number of bursts which can be used in an analysis.

Especially significant that equations 2–15 and 2–21 fit a distribution of distances to uncorrected experimental data. The background and crosstalk signals are instead added to the PDA distributions, an approach which allows a direct comparison between the model and the data. However, detailed studies of the influence of background counts on PDA results are still required.

The PDA is also applied to study spectral shifts of fluorescent molecules, which makes the method attractive for pH monitoring in a living cell or for probing a microenvironment of fluorescent molecules.

2.6 Force spectroscopy of single DNA molecules

This chapter establishes the force spectroscopy. The experiments are realized in a combined optical microscopy and AFM setup and also reports on mechanical noise of the equipment. The results of force pulling on DNA molecules deposited on different surfaces are presented. Reproducible consecutive pulling on single DNA molecule is achieved. The influence of selected DNA binding dye (SYBR Green I) on force curves is investigated.

Various approaches to force spectroscopy and simultaneous force/fluorescence spectroscopy experimental configuration are given. Non-functionalized and functionalized DNA molecules depositions on functionalized surface and on a cantilever have been tested and the results are presented.

2.6.1 DNA molecules

Why DNA molecules?

Well studied mechanical properties of DNA molecules, and the ability to create DNA constructs having various sequences and modifications, offer an excellent test sample for the control experiments of a new experimental technique. At the same time the important role of DNA molecules in cell replication and protein building makes them an attractive object for scientific research. Thus DNA molecules were chosen for the experiments further on described.

History and structure

Deoxyribonucleic acid (DNA) is a macromolecule containing the information that is necessary for an organism to be replicated. It serves as a template for self replication and it is located in nucleolus of the cells. The information can be translated to build proteins with various functions. These proteins serve as catalyst of chemical reactions in cells. DNA was discovered in 1869 by F.Miescher. In 1962 James D.Watson, Francis H.C. Crick and Maurice H.F. Wilkins received the Nobel Prize for Physiology or Medicine for their discovery of the DNA double helix structure. Since then DNA is known as a polymer which consists of a sugar-phosphate-backbone and bases attached to the backbone. Deoxyribose molecules are connected by phosphate bridges which results in a chain with alternating ribose and phosphate units. In the case of DNA there are four different bases connected to ribose: Adenine (A), Cytosine (C), Guanine (G) and Thymine (T). The complex of a base connected to a sugar is called a nucleoside. The complex of a base, a sugar and a phosphate is called a nucleotide. DNA is a long chain of nucleotides.

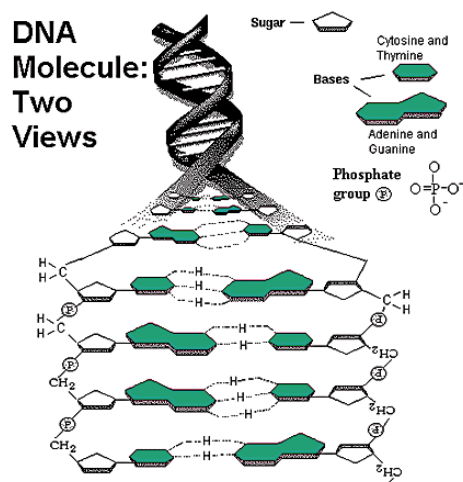


Figure 2-65. Schematic representation of DNA molecule structure (the picture is taken from: http://www.accessexcellence.org/RC/VL/GG/dna_molecule.html). The DNA structure is illustrated by a right handed double helix with 10 nucleotide pairs per helical turn. Each spiral strand, composed of a sugar phosphate backbone and attached bases, is connected to a complementary strand by hydrogen bonds between the paired bases.

The primary structure of the molecule is determined by the sequence of bases along the chain. It serves as genetic information (three consecutive bases encode one amino-acid). In nature DNA often occurs as a duplex in which two strands form a double helix with a right-handed twist. In a double helix, base pairs (bp) are formed between the opposing strands (secondary structure). According to Watson and Crick there are AT and GC pairs, so that the two strands are complementary to each other because each base has only one possible binding partner. The bases are turned inside the helix where the hydrogen bonds can be established, two for AT and three for GC. The bases are in perpendicular orientation to the helix axis. The helix length increases by 0.34 nm per bp. The helix consists of 10 bp per turn and is approximately 2 nm in diameter, which corresponds to a nucleotide length of 0.7–0.8 nm.

The phosphate bridges connect in inequivalent positions to neighbouring sugars (3'- and 5'-position). It makes a difference between directions along the nucleotide chain. Primary structures can only be compared when the direction is known, 3'-5' or 5'-3'. At the 3'-end of a strand, the nucleotide ends without a phosphate group at the 3'-position. At the 5'-end strand ends with a phosphate group at the 5'-position. The two strands of a double helix are normally antiparallel: starting at the same helix end, one strand runs in 3'-5'-direction and the other in 5'-3'-direction.

2.6.2 Force spectroscopy: experimental procedure and protocol

The experimental realization of force spectroscopy experiments includes sample surface preparation and DNA molecule deposition. AFM alignment (for force spectroscopy experiment) or optical setup and AFM alignment (for simultaneous force and fluorescence spectroscopy) is followed by the calibration of an AFM cantilever. After the initial setup, a molecule suitable for the experiment can be found and force or simultaneously force and fluorescence can be detected.

2.6.2.1 Sample preparation approaches

Sample surface (glass) preparation, including surface cleaning and modification, is described in detail in Section 2.3. Briefly, glass surfaces were modified with silane molecules which have active chemical groups. This allows non-covalent binding of negatively charged DNA to the APTES modified surface and the formation of covalent bonds between functionalized DNA molecules and a GOPTS modified surface. In addition, pulling experiments were performed on DNA molecules adsorbed on gold coated glass surface [205]. Cleaned glass surfaces were covered in vacuum (10^{-6} bar) with ~ 2 nm chromium and then with ~ 40 nm gold. Sample preparation approaches are illustrated in Figure 2-66.

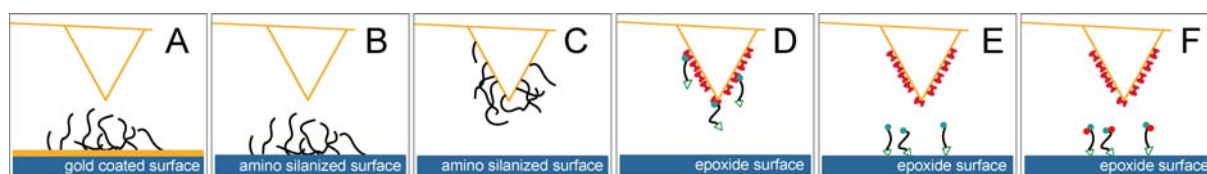


Figure 2-66. Illustration of various sample preparation approaches used for force spectroscopy and SFPS experiments. DNA molecules non-specifically adsorbed on gold coated surface (A); non-specifically adsorbed on APTES modified surface (B); non-specifically adsorbed on cantilever tip (C); specifically bound to an avidin modified cantilever surface via biotin-avidin interaction (D); covalently linked to GOPTS modified surface (E,F). Differently functionalized DNA with additional single dye molecule attached tested in the last approach (F).

Sample preparation and the experiment are closely connected. Thick DNA layer necessary for force spectroscopy experiment can be prepared on gold coated surfaces or silane modified glass surfaces.

As already discussed in Section 2.3.5, biomolecules can be imaged on flat surfaces with high spatial resolution. Providing there is a good enough resolution, different point of a molecule can be addressed for force spectroscopy. Such experiments have been demonstrated on flat mica surface [206,207]. The combination of force and fluorescence experiments requires transparent substrates (e.g. glass). However, glass surfaces have shown roughness comparable to the thickness of DNA molecules, making it difficult to realize this approach in combined experiments (Section 2.3). Nevertheless it can be realized for molecules larger than surface roughness features.

Another approach for pulling on DNA molecules is the localization of a sample for force spectroscopy using the fluorescence or the light scattering signal. Optical localization has poorer spatial resolution and requires higher separation of molecules on the surface. The advantage of this approach is that unsuccessful experiment on one spot does not forbid performing the experiment on the other spot of the sample. Finally, sample molecules can be at first adsorbed on the cantilever tip and then brought in contact with the surface.

2.6.2.2 Cantilever cleaning and modification

AFM cantilevers can be treated differently for different force spectroscopy experiments, and the tip treatment varies to create sites reactive to DNA molecule.

If non-covalent attachment is desired, cantilever tips are cleaned prior to experiments in a UVO cleaner (Model 42.220, Jelight Company Inc., CA, USA) at full power for 30min or treated with APTES silane (Section 2.3.3).

Alternative cantilever preparation protocols for covalent DNA molecules attachment are more complex. If DNA molecules have biotin sites then the cantilevers require more complex modification. As described in literature, cantilevers can be incubated in biotinaminodocaproyl-labelled bovine serum albumin (BSA-biotin) [84,208]. A BSA layer tightly adsorbs to the surface or can be fixed with gluteraldehyde. Further treatment with an avidin (or streptavidin) solution produces cantilevers ready to pick up a biotinlabelled DNA molecule. Alternatively avidin molecules can be directly attached to APTES surfaces via electrostatic interactions. The following cantilever treatments, which are modifications of reported protocols [84,208,209], were used in this thesis:

Protocol 1: Cantilever tip modification with avidin

- | | |
|---|----------|
| 1. Cantilever immersion in acetone | 5 min |
| 2. Irradiation with UV light | 30 min |
| 3. APTES liquid phase silanization (see Section 2.3.3) | |
| 4. Incubation in 1 ml streptavidin 1-4mg/ml in PBS buffer at room temperature | 2 h |
| 5. Rinsing the tip with PBS buffer to remove unbound streptavidin | 10 times |

Protocol 2: Cantilever tip modification with avidin

- | | |
|--|----------|
| 1. Cantilever immersion in acetone | 5 min |
| 2. Irradiation with UV light | 30 min |
| 3. APTES liquid phase silanization (see Section 2.3.3) | |
| 5. Incubation in 50µl Biotin-BSA, 1mg/ml in PBS, 10mM, 150mM NaCl, 1mMEDTA, pH 8.0-8.17, at 37°C | 24 h |
| 6. Rinsing in PBS, 10mM, 150mM NaCl, 1mMEDTA, pH 8.0-8.17 | 6 times |
| 7. Fixing in 1%gluteraldehyde solution | 30 sec |
| 8. Incubation in 50 µl streptavidin 1-4mg/ml in PBS at room temperature | 2 h |
| 9. Rinsing the tip with PBS buffer to remove unbound streptavidin | 10 times |

2.6.2.3 Force spectroscopy measurements

The custom built force spectroscopy setup based on a PicoPlus AFM (see Figure 2-1) and was described in Section 2.1.3. Briefly, the deflection of the cantilever is amplified and digitized by a 20 MHz 16 bit computer board. The same board controls the piezo voltage. Due to computer board noise limitations, acquisition rates are limited to a set of experimentally determined rate with low electronic noise. Custom-written LabView “PicoPull” software (see Appendix E) is responsible for the AFM controller, the computer board communication, data acquisition and storage. It is capable of real-time deflection signal monitoring and simultaneous spectral power density function calculations. Information about the programs used for the analysis is also given in Section 2.1.3 and in Appendix E.

Before the first approach of the AFM tip to the surface, the spring constant of each lever is calibrated by measuring the amplitude of thermal oscillations and the sensitivity of the optical lever detection scheme.

2.6.2.4 Calibration of AFM cantilevers

Measurements of force in atomic-force spectroscopy rely on the cantilever spring constant calibration. The thermal oscillations method (Section 1.3.2.4) was chosen among others for this purpose. The position of a soft cantilever fluctuates due to thermal oscillations which can be detected by measuring the cantilever deflection. The current experimental force spectroscopy setup allows the sampling of the deflection at a frequency up to 2.5 MHz. Beyond this value, electronic and digitalization noises have a strong impact. The accessible frequency range allows detecting of several eigenmodes of the cantilever vibration. This can be resolved in a time trace of the deflection signal (Figure 2-67). Fast Fourier transformations (FFT) [210] on the time trace lead to spectral power density function (Figure 2-68). It reflects the amplitude of thermal oscillations of the cantilever.

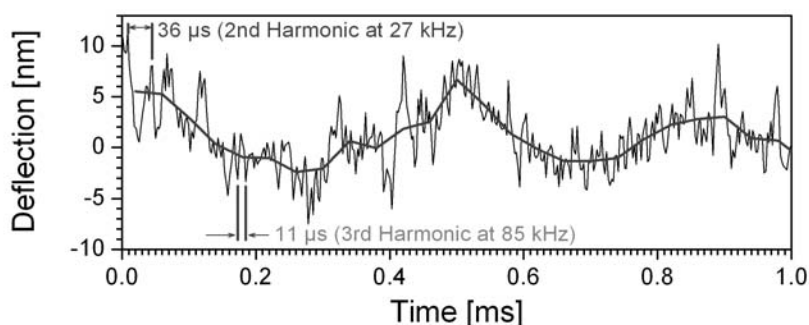


Figure 2-67. Time trace of the cantilever deflection. Veeco microlever B cantilever. Manufacturer specified resonance frequency in air is 12 Hz. In solution this frequency is substantially lowered due to velocity damping. The obtained signal quality is good enough to resolve the 3rd harmonic of cantilever resonance frequency.

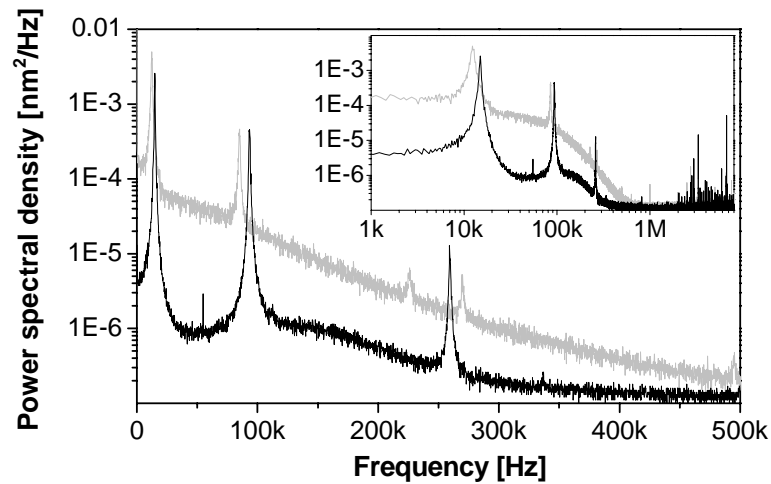


Figure 2-68. Power spectral density of the cantilever oscillations obtained for the Veeco Microlever cantilever B in air. Several peaks, corresponding to higher oscillation eigenmodes are observed. The black power curve illustrates the improvement of the experimental setup by using a stable intensity fiber coupled IR laser for the cantilever deflection measurements. The light gray curve corresponds to the optical lever scheme with the standard PicoSPM I red laser. The insert represents the oscillation amplitude in a broader frequency range. The influence of electronic and digitalization noise is observed at frequencies >2.5 MHz.

The power spectral density function is used for a cantilever spring constant estimation, calculating the area under the first fundamental eigenmode or performing a fit to the function (equation 1-36) described in Section 1.2.4.

Spring constant calibration

1. Obtain a near diffraction limited IR laser spot on the back side of the cantilever (The size can be monitored with the CCD camera or IR camera in the inverted optical microscope). The typical diameter of the focused IR laser spot is less than $1\mu\text{m}$.
2. Position the laser spot on the cantilever in such a way, that the ratio of cantilever chip-spot distance/cantilever length is in the range of 0.8-0.9.
3. Obtain a power density spectrum for cantilever thermal motion. It is available in PicoPull software in $[\text{V}^2/\text{Hz}]$.
4. Calibrate the photodiode sensitivity by performing a force curve with a cantilever in contact with a hard surface. Estimate $\text{InvOLS} = \text{InvOLS}_{\text{end}}$ from the slope of the force curve. The dimension of InvOLS is $[\text{nm}/\text{V}]$.
5. Calculate the $\text{InvOLS}_{\text{free}} = \chi \cdot \text{InvOLS}_{\text{end}}$. Use the correction factor χ (calibration graph is provided by Proksch et al. [115]). For Veeco microlevers B-E and IR diffraction limited laser, it is usually within values of 1.05–1.09.
6. Convert the power density spectrum into $[\text{nm}^2/\text{Hz}]$ units using $\text{InvOLS}_{\text{free}}$ value and calculate the area under the first resonance peak, corresponding to the first eigenmodes

of the cantilever. A practical integration bandwidth for Veeco microlevers B-E is usually $150 \text{ Hz} - 3 \cdot \omega_0 \text{ Hz}$.

7. Calculate the first approximation for a cantilever spring constant: $k = \frac{k_B T}{(\text{FFT area})}$.
8. Introduce the correction factors depending on the cantilever and experimental geometry and conditions. For Veeco microlevers at 22°C it is usually 0.8 (lever B) and 0.65 (lever C) (see Section 1.3.2.4).

Alternatively, fitting of the cantilever oscillations spectral power density function to equation 1–35 including noise contribution provide parameters for cantilever spring constant estimation.

Results of spectral power density measurements for Veeco microlevers C in air and in water are shown in Figure 2-69. Spring constants are calculated by the power spectral density integration and estimated from the parameters of the fit to equation 1–36 including the white and $1/f$ noise contributions. Providing the correction coefficient specified in step 8 of the spring constant estimation procedure is 0.65 for all calculations, the stiffness of the cantilever was found to be in water: 7.5 pN/nm (numerical integration) and 8.1 pN/nm (fitting); and in air: 10.7 pN/nm (numerical integration) and 9.2 pN/nm (fitting).

The difference in the spring constant estimation between the two methods (integration and Levenberg-Marquardt fitting [204]) is 4-16%, and for different media (air and water) is 14-37%. The main source of error for a spring constant comes from the error in the deflection constant (InvOLS) estimation. InvOLS can change for the time of an experiment. Variations are caused by changes in the optical lever deflection scheme alignment. Possible sources of misalignment are evaporation of buffer in the fluid cell and readjustment of the photodiode in the optical lever deflection detection scheme.

However, the cantilever calibration is realized in the same manner for all force spectroscopy measurements. That makes qualitative analysis reliable and allows one to correct the calibration for precise quantitative characterization. Calibrated force sensitivity provides a tool for single molecule event recognition in experiments on DNA molecules.

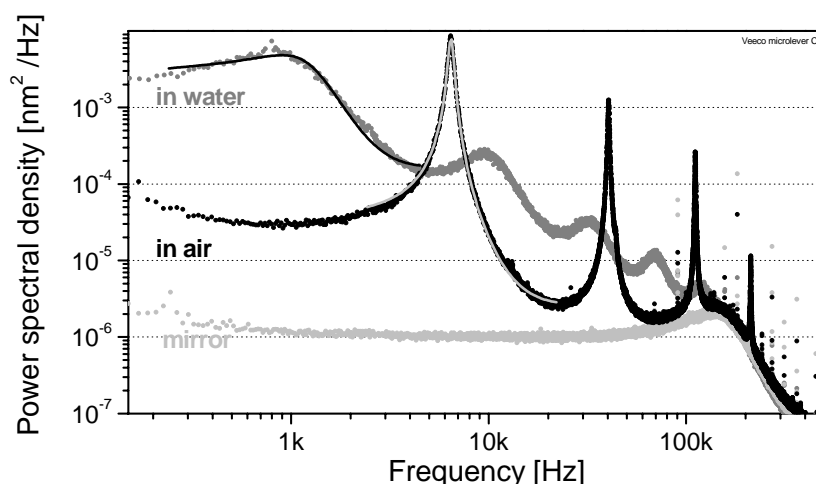


Figure 2-69. Power spectral density of the cantilever oscillations. Veeco microlever cantilever (lever C) in air and water. Several peaks, corresponding to different oscillation eigenmodes are observed. Power spectral density of the reflection from the cantilever chip (mirror) is shown with light grey colour. This measurement corresponds to a deflection unaffected by thermal Brownian motion. The Levenberg-Marquardt fitting with the statistical weighting [204] to equation 1–36 is performed for the first peaks of the power spectrum. Cantilever spring constants, estimated by numerical integration (according to procedure, presented in the text) and from the fit were found. The values are correspondingly 7.5 pN/nm and 8.1 pN/nm (in water) and 10.7 pN/nm and 9.2 pN/nm (in air). Specified by manufacturer cantilever spring constant is 10 pN/nm.

2.6.3 Pulling on DNA molecules

Mechanical properties of DNA molecules

The mechanical stability of single DNA molecules under various conditions can be probed with the force spectroscopy [4,205,211,212]. Typical characteristic force versus distance curve obtained on a single DNA molecule delivers the information about structural changes of the molecule. A dsDNA molecule shows almost no force change while being straightened to its contour length. Further elongation results in elastic stretching of the B-form and is followed by a plateau with increased force attributed to the conformational change from B-form into the so called S-form (stretched form) [213,214]. This force is measured with high precision by optical tweezers technique and was found to be 65 pN. A structural B-S transition is followed by a next conformational change, where the double stranded DNA melts into two single stranded DNAs. The ssDNA molecules can be further extended until they rupture or relax. The relaxed molecule re-hybridizes into dsDNA and can be pulled again showing similar structural changes. In a number of experiments it has been shown that DNA mechanics are sequence depend [215]. The buffer's pH value and the salt concentration influence the B-S transition force of a DNA molecule [216,217]. The pulling rate and the waiting time between consecutive pulls have a strong impact on the melting transition force

and the hysteresis in a B-S transition [205]. Thus, special attention should be paid to keep experimental conditions constant for a reliable comparison of force spectroscopy results.

2.6.3.1 DNA on gold surfaces

A logical step in the force spectroscopy establishment is the pulling on a single DNA on gold surfaces. This is an easy and reliable sample preparation method reported by many research groups. The results of force spectroscopy experiments with λ digest DNA molecules deposited at a concentration of 100 $\mu\text{g}/\text{ml}$ in TRIS buffer on a gold surface are shown in Figure 2-70. A double stranded DNA molecule, approximately 1.2 μm long, is stretched from its B form into S at a constant force, melted into two single-stranded molecules at a force range of 100–300 pN and ruptured at a 800pN force after a short extension.

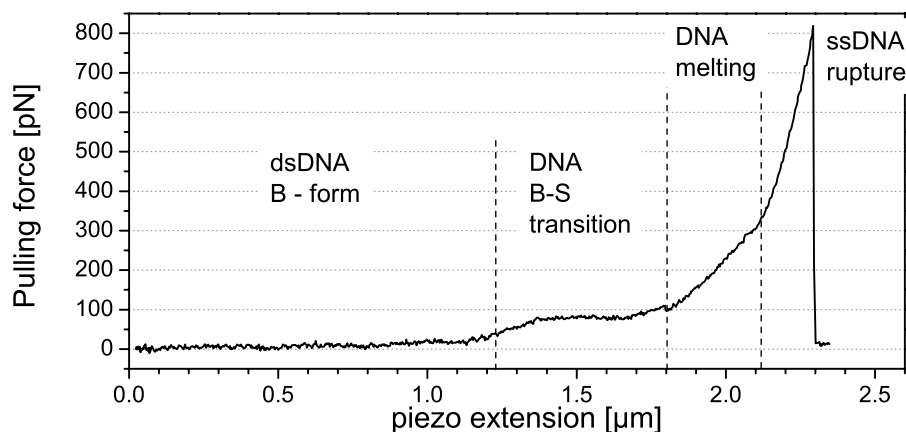


Figure 2-70. Force versus extension curve for a dsDNA molecule obtained on a fragment of λ digest DNA adsorbed on a gold surface in atomic force spectroscopy experiment. DNA molecules are deposited on the surface at a concentration of 100 $\mu\text{g}/\text{ml}$ in 10mM TRIS buffer, 150mM NaCl, 1mM EDTA, pH8.0. Veeco cantilever (lever C) is used for the experiment. Cantilever spring constant of 10 pN/nm is specified by the manufacturer. Pulling rate is 1 $\mu\text{m}/\text{s}$.

2.6.3.2 DNA on APTES glass. Influence of the dye

Force spectroscopy experiments performed on DNA molecules on transparent silane-modified glass surfaces have shown good results. Stretching of the λ digest DNA between APTES surface and APTES modified cantilever tip is shown in Figure 2-71. A Veeco cantilever, lever B, with stiffness of 20 pN/nm was used for the experiment. The cantilever deflection is acquired at a rate of 10 MHz and low pass filtered at 25 kHz, which is twice the resonance frequency of the cantilever in air. A Levenberg-Marquardt fitting [204] to the wormlike chain model (WLC, Section 1.3.3.1, equation 1–62) is performed for the force vs. tip-surface separation curve at low forces. That is a valid approximation of dsDNA molecule as a uniform flexible rod [123,218-220]. The fit results in a dsDNA contour length of 484 nm

and a persistence length of 42 nm. This persistence length is in good agreement with values reported in literature [123,217,221].

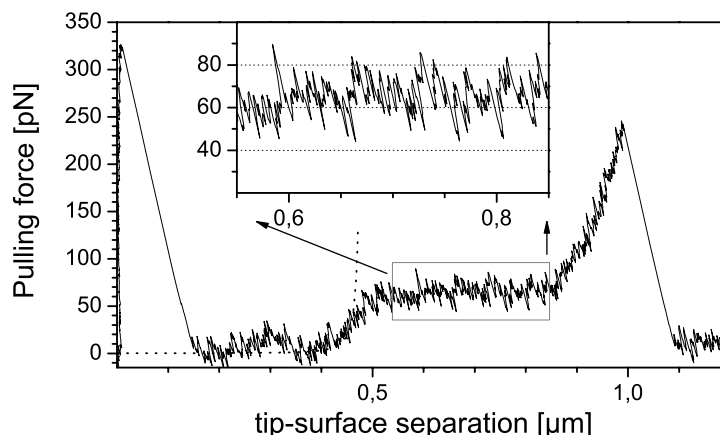


Figure 2-71. Force versus tip-surface separation for a dsDNA molecule obtained on λ digest DNA adsorbed on gold surface in atomic force spectroscopy experiment. DNA molecules are deposited on the surface at a concentration of 100 $\mu\text{g/ml}$ in 10mM TRIS buffer, 150mM NaCl, 1mM EDTA, pH8.0. A Veeco cantilever (lever B) is used for the experiment. The cantilever spring constant is 20 pN/nm as specified by manufacturer. Pulling rate is 1 $\mu\text{m/s}$. The dotted line represents the Levenberg-Marquardt fitting with the statistical weighting [204] to the WLC model which yields a persistence length of 42 nm and a contour length of 484 nm. Insert shows the zoomed BS plateau. Force fluctuations reach values of 40 pN. The curve is averaged over a time window of 40 μs (low pass filtering below 25 kHz).

Influence of the binding agents on the DNA mechanics

DNA molecules in the presence of binding molecules show variations in the characteristic shape of the force spectroscopy curves. Various small binding agents possessing different binding modes have been recently studied [221-227]. Generally groove binding, intercalation and crosslinking modes are possible.

The groove binding mode is valid for small, positively charged molecules. It may occur in the minor groove of dsDNA, and only requires a slight change of the double helix conformation. The characteristics of the DNA pulling curve are mostly conserved: its structural transitions remain. However, the B-S plateau force value may be changed up to 60% in comparison to free DNA [223-224,227]. An increase or decrease of the force depends on the dsDNA sequence and the binding agent. The contour length is influenced up to 3.1%, as reported in literature [221]. Major groove binding agents normally show bigger effects upon binding [222].

Cross-linking takes place between two neighbouring base pairs or between base pairs separated by other pairs. Cross-linking has effects similar to intercalation, but is more dependent on the DNA sequence [222,225].

Intercalation is a different small agents binding mode, characterized by the planar parts of binders stacking between DNA base pairs. The B-S transition almost vanishes and the

contour length increases. The strength of the effect as reported depends on the intercalator concentration [225,227].

The binding agent used in the frame of this thesis is the SYBR Green I fluorescent dye. The fluorescence properties of the dye are given in the material Section 2.2. It is known from fluorescence measurements that this dye has two binding modes, depending on the concentration per DNA bp [228]. Intercalation takes place at low dye/bp ratios, less than 0.15, and groove binding dominates at higher concentrations. The influence of this dye on the DNA mechanical properties is not studied in detail. However, some results of optical tweezers experiments indicate BS transition force and an increase in the WLC persistence length [224]. Force hysteresis between the retraction and approach (relaxation) in force-distance curves is also reported in this paper.

A typical result of DNA molecule extension force versus tip-surface separation is shown in Figure 2-72. Here λ digest DNA molecules are deposited on an APTES modified glass surface. A single DNA molecule is picked up and stretched by the APTES coated AFM cantilever. Fitting the low force regime part of the curve to the WLC model (equation 1-62), a contour length of 1.871 μm and a persistence length of 22 nm are estimated. A DNA molecule in S-form can be elongated up to 3.2 μm , which is 1.7 times the contour length.

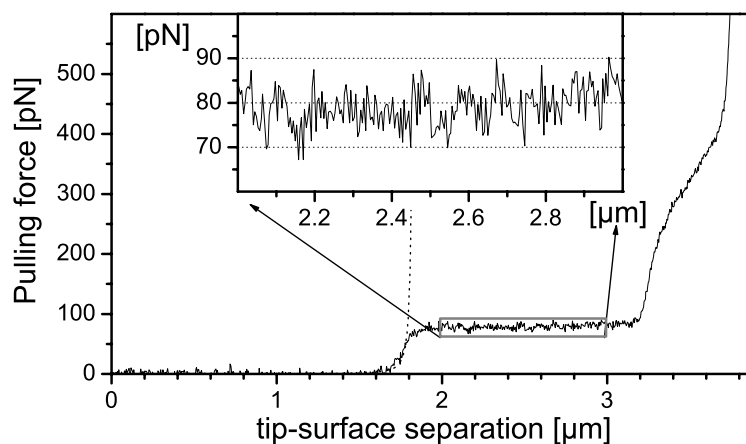


Figure 2-72. Force versus tip-surface separation for dsDNA molecule obtained on λ digest DNA adsorbed on APTES functionalized surface in the presence of SYBR Green I fluorescent dye in solution. DNA molecules are deposited on the surface at a concentration of 4.3 $\mu\text{g}/\text{ml}$ in 10mM PBS buffer, 150mM NaCl, 1mM EDTA, pH8.16. A Veeco cantilever (lever C) is used as a force sensor. Thermal calibration method provides cantilever spring constant of 8.5 pN/nm. Pulling rate is 1.5 $\mu\text{m}/\text{s}$. The dotted line represents the Levenberg-Marquardt fitting with the statistical weighting [204] to the WLC model which yields a persistence length of 22 nm and a contour length of 1871 nm. Insert shows the zoomed BS plateau. Force fluctuations (min to max) for B-S plateau reach values of 38 pN. The curve is averaged over a time window of 3 ms (low pass filtering below 0.333 kHz).

The average concentration of the dye SYBR Green I on solution was 0.28-0.55 dyes/bp. The average dyes/bp values are calculated based on the total amount of dsDNA and the dye in solution without consideration of fluid cell surface adsorption and buffer evaporation effects.

Comparing the result obtained for unlabelled λ digest DNA (Figure 2-71), the persistence length is smaller. A similar decrease is already previously reported for groove binders [221,224].

A single DNA molecule attached between the APTES modified tip and the surface can be stretched and relaxed many times, allowing the observation of molecule's mechanical properties with time (Figure 2-73). Retraction from the surface is followed by approach without any time delay between them. The next retraction-approach pair is performed after a short delay, approximately 1-2 seconds. During this delay the force spectroscopy data is saved.

Several effects are observed in force curves in Figure 2-73:

1. A hysteresis of the B-S transition position in the retraction and approach curves.
2. An increased B-S transition force in the retraction curves.
3. Reannealing into a complete double helix in the retraction curves.
4. Other features.

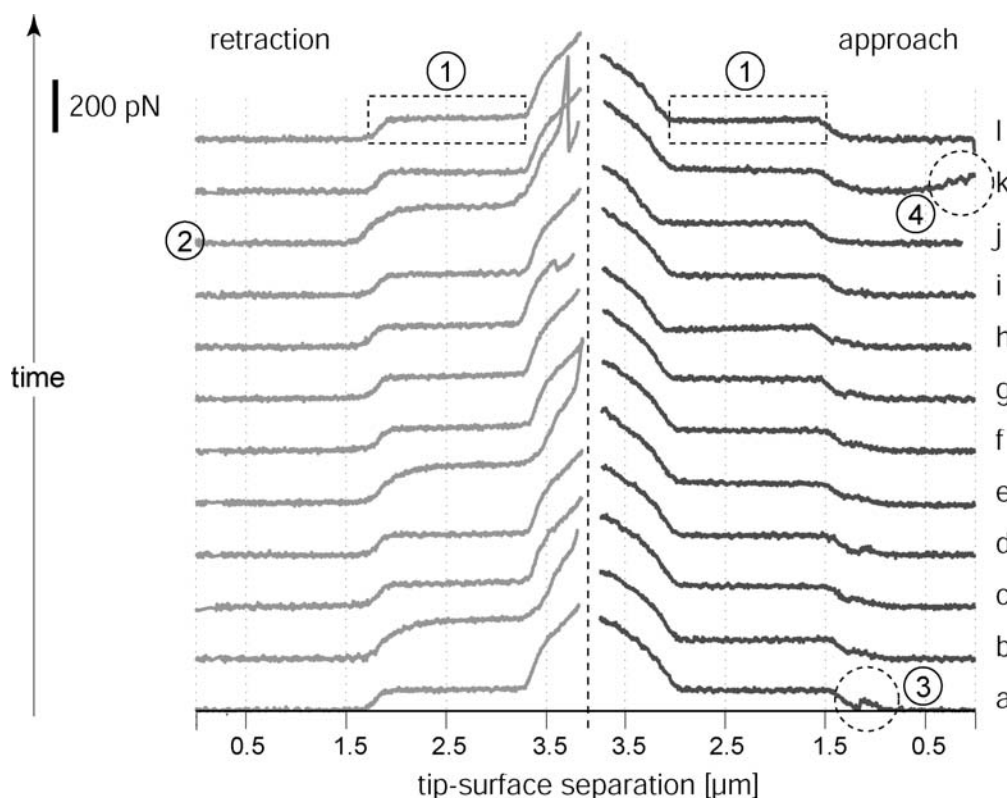


Figure 2-73. Series of force versus tip-surface separation curves obtained on λ digest DNA adsorbed on APTES functionalized surface. The vertical dashed line separates the retraction and approach part of a single pulling experiment. For presentation purposes parts of retraction curves at the end and approach curves in the beginning are not shown. Several features marked in the figure (1-4) are discussed in the text. DNA molecules are deposited on the surface at a concentration of 4.3 $\mu\text{g/ml}$. SYBR Green I fluorescent dye is present in solution at an average concentration of 0.28 dyes/bp. Pulling is performed in 10mM PBS buffer, 150mM NaCl, 1mM EDTA, pH8.0. Pulling rate is 1.5 $\mu\text{m/s}$. A Veeco cantilever (lever C) with a spring constant of 8.5 pN/nm is used.

A hysteresis of the B-S transition between the retraction and approach curves is recognizable in Figure 2-73 (number 1). Although the hysteresis can originate from real dynamics of DNA molecules, it is most probably arising from the hysteresis of the piezo scanner. Active closed loop piezo position feedback would help to solve this problem. Due to the piezo drift during the time delay between two consecutive pulls, the piezo hysteresis is compensated. Therefore the start of the B-S transitions in the retraction curves occurs at the same position of $\sim 1.8 \mu\text{m}$.

Strong electrostatic adsorption of DNA molecules to APTES surface results in different attachment of molecular ends to the surface. This effect can be observed in the retraction curves (b), (e), (j), see Figure 2-73 (number 2). Here the pulling force is higher than the typical B-S transition force for a single DNA (for example, a). It can be explained by the DNA attached with both strands to the surface or to the tip [205]. However such connections are weak and can be ruptured (retraction, j) leaving just one attachment for a single DNA molecule on the tip and on the surface. In addition, all relaxation curves show forces corresponding to a single DNA molecule that is attached at only one strand.

Another effect observed in Figure 2-73 (number 3) indicates the different reannealing [205,215] for various approach curves at the end of the B-S transition. Although the same DNA molecule is stretched and relaxed at a constant pulling rate, the reannealing process is different. The difference can be influenced by the presence of the dye in the buffer.

A non-perfect setup operation can lead to features (Figure 2-73, number 4) which have no reasonable meaning. Such features can be excluded from the presentation or analysis.

Force histograms

Pulling force histograms are created to assist the statistical analysis of force spectroscopy data. Histograms are constructed by counting the number of experimental points in a given force interval for the whole force curve. Most frequently occurring values produce peaks resulting in the calculations of mean force values and deviations. If the different forces correspond to different B-S plateaus in the curves, they will be separated on the pulling force histogram. The illustration is given in Figure 2-74. Retraction and approach curves together with force histograms are scaled within arrange of 0–500 pN. The B-S plateau in the retraction curve shows peak at 120-150 pN, while the approach curve demonstrates the B-S plateau at 60-80 pN.

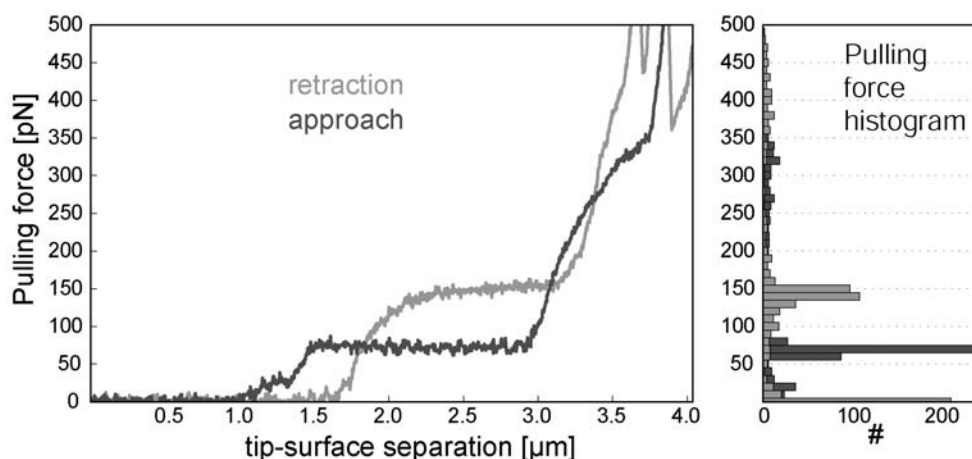


Figure 2-74. Force versus tip-surface separation for dsDNA molecule obtained on λ digest DNA adsorbed on APTES functionalized surface (left). DNA molecules are deposited on the surface at a concentration of 4.3 $\mu\text{g/ml}$. SYBR Green I fluorescent dye present in solution at an average concentration of 0.28 dyes/bp. Pulling is performed in 10mM PBS buffer, 150mM NaCl, 1mM EDTA, pH8.16. A Veeco cantilever (lever C) with a spring constant of 8.5 pN/nm is used for the experiment. Retraction and approach (relaxation) curves are shown. Histograms of pulling force (right) clearly indicate the force values of B-S transitions in retraction and approach curves.

Force histograms and SYBR Green I binding

Pulling force histograms provide the tool for statistical analysis of force curves and studies of the influence of SYBR Green I binding on dsDNA B-S transition. In the experiments DNA molecules were stretched and relaxed at different concentrations of the dye in solution. Table 2-15 and Figure 2-75 present results of 72 successful pulls on λ digest DNA adsorbed on APTES functionalized surface (A) and 40 pulls on modified DNA molecules (NHdna3BioA12, Table 2-6) adsorbed on a GOPTS modified surface (B). The average dye concentration in the first case is 0.28–0.55 dyes/bp, while in the second case it is 1-2 dyes/bp.

Normalized force histograms reveal two main peaks around 0 pN (peak “0”) and in the range of 60-80 pN (peak “1”). These peaks show force distributions of dsDNA in B-form and DNA B-S transition respectively. The interpretation of peaks with higher forces is difficult, since they can result from different effects:

1. dsDNA melting transition.
2. Pulling on a dsDNA molecule attached to the surface with one or with two strands.
3. Pulling on more than one DNA molecule.

Figure 2-75, A illustrates this situation with peaks “2” within force values of 100-130 pN (retraction) and peak “3” within forces values of 140-180 pN. Peak “3” has twice the force of peak “1” and can correspond to B-S transition for pulling on two DNA molecules, while peak “2” corresponds to melting force distribution of a single dsDNA.

Nonspecific interactions between the tip and the surface, as well as pulling on short DNA result in an offset in force histograms and in peak distortions. The force curves are

usually “dirty” in between peak “0” and peak “1” which shifts peak “0” to higher values and increases the offset between the two peaks. Such a situation is illustrated in Figure 2-75, (B).

Table 2-15. Max counts values for cumulative histograms presented in Figure 2-75. The values used for the normalization are marked with bold font. Forces of two experiment types are histogrammed with 5 pN force binning. These are (A) 72 pulls on λ digest DNA on APTES surface and (B) 40 pulls on modified DNA molecules on GOPTS surface. Cantilever spring constants were estimated to be 8.5 pN/nm and 9.9 pN/nm respectively.

	(A) λ digest DNA		(B) modified DNA	
	peak “0”	peak “1”	peak “0”	peak “1”
Retraction	9246 counts	5114 counts	3468 counts	726 counts
Approach	10953 counts	3534 counts	8680 counts	1091 counts

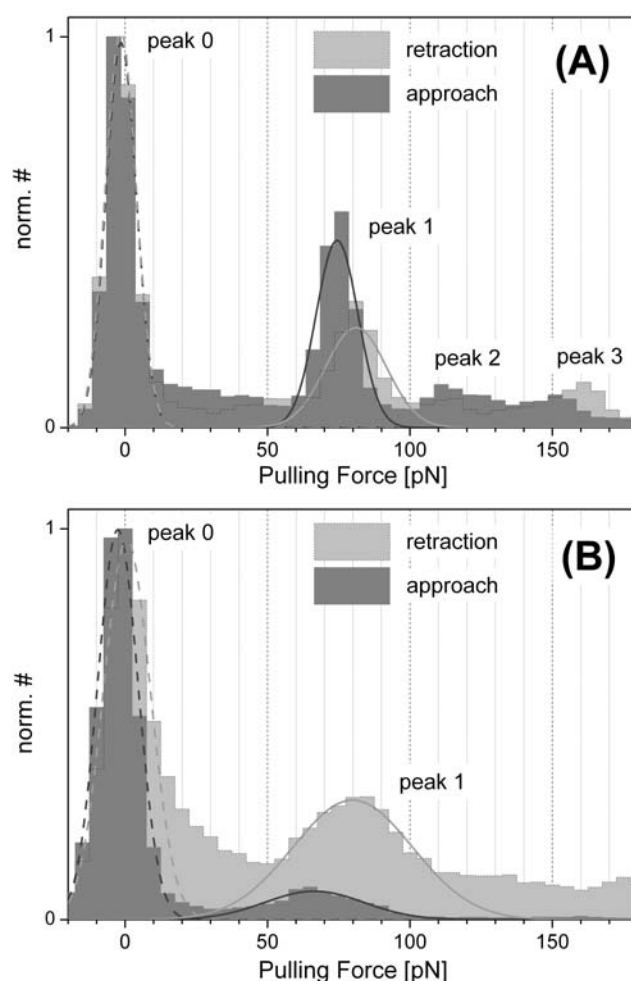


Figure 2-75. Cumulative normalized force histograms of many pulls performed on λ digest DNA adsorbed on APTES (A) and modified DNA molecules adsorbed on GOPTS (B). Retraction force histograms are shown with light grey colour and dotted lines where it is behind the approach histogram. Approach histograms are dark grey. (A) Concentrations of the dye were 0.28–0.55 dyes/bp and cantilever spring constant was 8.5 pN/nm. (B) Concentrations of the dye were 1–2 dyes/bp. Peaks “0” correspond to pulling on dsDNA in B-form. Peaks “1” correspond to DNA B-S transition. Peaks “2” and “3” can correspond to melting transition and to multiple DNA pulling. Cantilever spring constant was 8.5 pN/nm (A) and 9.9 pN/nm (B). Experimental histogram peaks are fitted with the Levenberg-Marquardt algorithm with the weighting of 1 [204] to the Gaussian model (equation 2–30). The results of the fit are listed in Table 2-16.

A quantitative analysis of force histograms is performed by Levenberg-Marquardt fitting [204] of peaks corresponding to dsDNA in B-form (peaks “0”) and DNA B-S transition (peaks “1”) with Gaussian distributions. The fitting function defines the normalized number of counts in force histogram (norm.#) as follows:

$$\text{norm.\#} = \frac{\text{const.}}{\sigma} \exp\left(-\frac{2}{\sigma^2}(F - F_{\text{mean}})^2\right) \quad (2-30)$$

where F is the pulling force, F_{mean} is the mean pulling force, σ is the standard deviation and const. is the normalization constant. The results of the fit are given in Table 2-16. The fitting range for each peak is chosen based on the approximate position of the peak and the offset in the pulling force histogram. The variations of 10-30 pN in the fitting range influence the value of σ , but do not change the F_{mean} value. The accuracy of F_{mean} is insured by the large number of pulling experiments on the same DNA molecules. The value of σ is influenced by the precision and the accuracy of the force curve measurements. It depends on the thermal motion of the cantilever and real variations in the B-S transition force.

Table 2-16. Results of the Gaussian fit of equation 2–30 to the data presented in Figure 2-75 with weighting coefficients equal 1. (A) represents the analysis of 72 pulls on λ digest DNA and (B) and represents analysis of 40 pulls on modified DNA molecules (NHdna3BioA12, Table 2-6). Cantilever spring constant was 8.5 pN/nm (A) and 9.9 pN/nm (B).

		(A) λ digest DNA 0.28–0.55 dye/bp		(B) modified DNA 1–2 dye/bp	
		peak “0”	peak “1”	peak “0”	peak “1”
Retraction	Fitting range	-20 to 20 pN	50 to 150 pN	-20 to 10 pN	55 to 115 pN
	F_{mean}	-1.5 ± 0.4pN	81.1 ± 1.1pN	0.9 ± 0.6pN	78.8 ± 0.8pN
	Σ	10.9 ± 0.6pN	21.4 ± 2.1pN	17.6 ± 1.0pN	43.5 ± 2.0pN
Approach	Fitting range	-20 to 20 pN	50 to 100 pN	-20 to 20 pN	40 to 100 pN
	F_{mean}	-1.4 ± 0.6pN	74.4 ± 1.2pN	-2.6 pN ± 0.5pN	64.9 ± 1.0pN
	σ	10.7 ± 0.9pN	14.7 ± 2.2pN	14.6 ± 0.8pN	36.7 ± 2.0pN

Table 2-17. Results of the B-S transition plateau height calculations of the data in Table 2-16. (A) represents the analysis of 72 pulls on λ digest DNA and (B) represents the analysis of 40 pulls on modified DNA molecules (NHdna3BioA12, Table 2-6). Cantilever spring constant was 8.5 pN/nm (A) and 9.9 pN/nm (B).

	(A) λ digest DNA, 0.28–0.55 dye/bp B-S plateau height (F_{BS})	(B) modified DNA, 1–2 dye/bp B-S plateau height (F_{BS})
Retraction	82.6 ± 1.2pN	77.9 ± 1.0pN
Approach	75.8 ± 1.3pN	67.5 pN ± 1.1pN
Difference retraction-approach	6.8 ± 1.7pN	10.4 ± 1.5pN

The B-S transition plateau height (F_{BS}) is defined as the difference between the F_{mean} values of peak “1” and peak “0” for each sample for retraction and approach force histograms (Table 2-17). It is given by the following equation:

$$F_{BS} = F_{mean}(\text{peak "1"}) - F_{mean}(\text{peak "0"}) \quad (2-31)$$

The error of the B-S transition force (σ_{BS}) is defined from the errors of F_{mean} values for peak “1” ($\sigma_{Fmean}(\text{peak "1"})$) and peak “0” ($\sigma_{Fmean}(\text{peak "0"})$) as follows:

$$\sigma_{BS} = \sqrt{\sigma_{Fmean}^2(\text{peak "1"}) + \sigma_{Fmean}^2(\text{peak "0"})} \quad (2-32)$$

The difference of the mean of B-S transition forces between two concentrations (3.5 times) of SYBR Green I on DNA molecules is resolved in Table 2-17. For the higher concentration of the dye the mean of B-S transition force is higher (10.4 ± 1.5 pN against 6.8 ± 1.7 pN). That suggests the SYBR Green binding stabilizes the structure of DNA molecule and increases the structural transition force in a DNA molecule. The dye detaches after the DNA stretching and the relaxation is performed at the force close to the B-S transition force of a clean DNA.

Assuming the force variations in different experiments arise from the cantilever calibration, the B-S transition forces on approach curve can be rescaled to be equal to 65 pN [215]. This assumption would lead to plateau heights with force difference of 5.8 pN (Figure 2-75, (A)) and 10 pN (Figure 2-75, (B)) or 8.9% and 15% of the B-S transition force.

2.6.4 Conclusion

The force spectroscopy technique is established. The custom-build setup is based on a commercial AFM system and an additional acquisition board. The feasibility of experiments on single DNA molecules reveal structural transitions in the molecule upon the applied force. An AFM cantilever spring constant estimation influences the quantitative analysis of force spectroscopy data and can lead to 16% variations in force. The main source of the cantilever calibration uncertainties is the optical lever sensitivity estimation.

The influence of the SYBR Green I groove binder is studied. Pulling force histograms are introduced for force spectroscopy data analysis. The results were found to be consistent with previous optical tweezers reports on dsDNA force spectroscopy using this dye, which indicate a hysteresis between the retraction and approach force curves [224]. The force of the structural B-S transition is increased up to 8.9% upon SYBR Green I binding at an average concentration of 0.28–0.55 dyes/bp and 15% upon SYBR Green I binding at an average concentration of 1-2 dyes/bp (comparing to the literature value of the B-S transition force of 65 pN [215]).

2.7 Simultaneous force spectroscopy and fluorescence measurements

An approach to perform simultaneous pulling on single macro molecule and fluorescence detection is described. Combined experiments on DNA molecules are performed. Constrains of the present experimental setup are discussed and further improvement are suggested.

2.7.1 Fluorescence-directed localization of molecules

Developments in the deposition of biological macro-molecule on transparent substrates, availability of a force spectroscopy and improvements of fluorescence spectroscopy techniques suggest the possibility of combined force and fluorescence studies.

To start, the optical setup and AFM must be co-aligned followed by the calibration of the AFM cantilever spring constant. The combination of piezo stages facilitates aligning the sample molecules and the cantilever tip (Figure 2-1). Alignment can be controlled by either the PicoScan software (AFM piezo positioning), the custom-written ControlPI program (piezo X-Y-Z stage) or manually (X-Y translation stage and sample pushers). A visualization of the piezo manipulations is realized by switching to a wide-field evanescent illumination and fluorescence detection via a single fluorophore-sensitive CCD camera.

Sample preparation approaches are described in Section 2.6.2.1. As illustrated in Figure 2-66, C and D, DNA molecules can be deposited on the AFM cantilever tip by cantilever immersion in a DNA solution. Functionalized tips containing DNA molecules are then positioned on the optical axis for a combined experiment. Although this particular approach is easy to realize, there are several disadvantages. In the case of non-specific DNA adsorption on the cantilever, the attachment for untreated cantilever can be loose. APTES modified cantilever may have too many DNA on the tip, so that it is difficult to obtain only a single DNA molecule attached between the surface and the AFM probe. In the case of reversible complex formation between the avidin-coated tip and a biotinylated DNA, each contact of the tip with the surface can lead to DNA detachment or denaturation. Vice versa, too little DNA attached makes it difficult to find the attachment point and thus to locate the DNA functionalized tip on the optical axis. Nevertheless, successful experiments have been performed using this approach. The wide-field fluorescence images of the cantilever (Veeco microlever, C) functionalized according to the protocol 1 (Section 2.6.2.2) are given in Figure 2-76. The amount of DNA molecules adsorbed on the cantilever tip (Figure 2-76,A) is

difficult to estimate due to a bright fluorescence signal from the modified tip itself. However, it can be expected to have the same average surface coverage as on the other regions of the cantilever (Figure 2-76,B,C). Accurate characterization of the cantilever tip functionalization can be achieved using the confocal scanning imaging technique (Section 2.4.3).

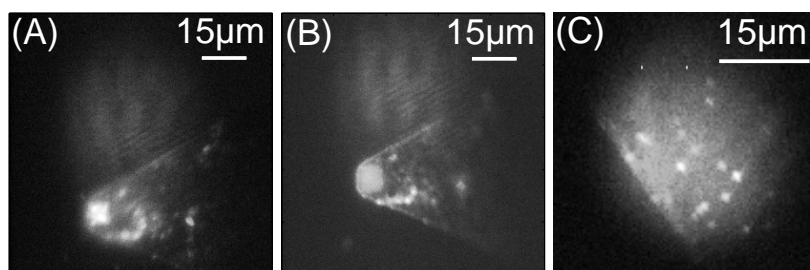


Figure 2-76. Wide-field fluorescence images of the GOPTS modified AFM cantilever. DNA molecules (NHdna3BioA) were deposited on the cantilever immersing it for 24h in the PBS buffer solution, containing 1 $\mu\text{g/ml}$ DNA. SYBR Green I fluorescent dye is at the concentration of 2 μM . Excitation light is delivered with frustrated evanescent excitation.

Different to the “on-the-tip” preparation approach, molecules can be first bound to the surface (Figure 2-66, B and E,F). Results of surface preparation techniques demonstrating well separated DNA molecules were described in Section 2.3.6. Experimental alignment can be achieved by either (1) addressing molecules with the AFM tip and bringing them together on the optical axis (Figure 2-77) or (2) aligning the cantilever tip on the optical axis, retracting it and bringing the molecules under the tip by moving the sample plate (Figure 2-78).

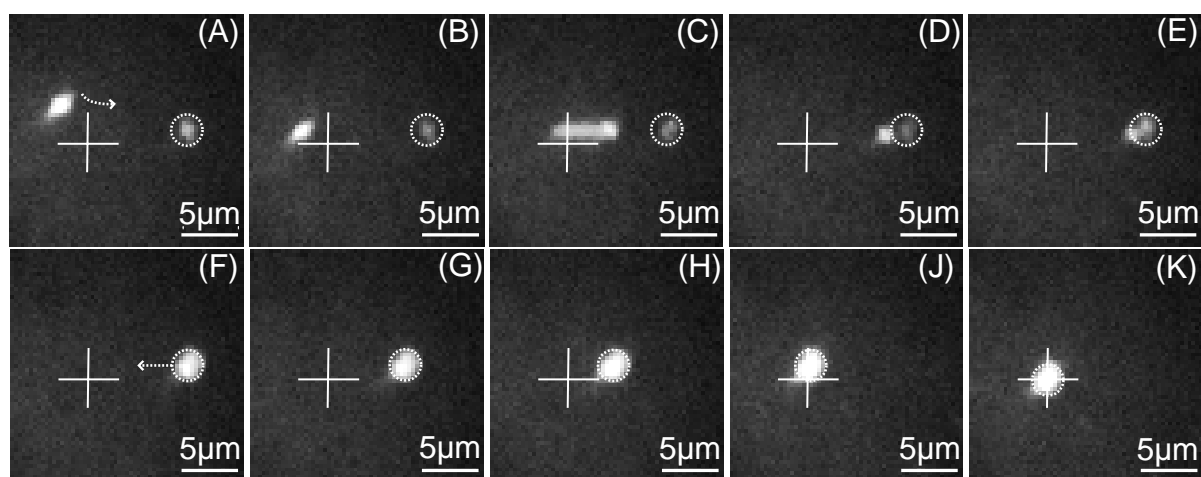


Figure 2-77. Illustration of the alignment procedure, when the AFM tip is moved towards a molecule bound to the surface (A-E), afterwards the whole AFM is brought on the optical axis (F-K). A cross represents the optical axis, which is perpendicular to the image. A dotted circle shows the location of the DNA molecule. DNA molecules (NHdna3BioA) is adsorbed on a GOPTS surface and labelled with SYBR Green I dye at a concentration of 0.2 μM . The tip is 1 μm above the surface (A-E) and directly on the surface (F-K).

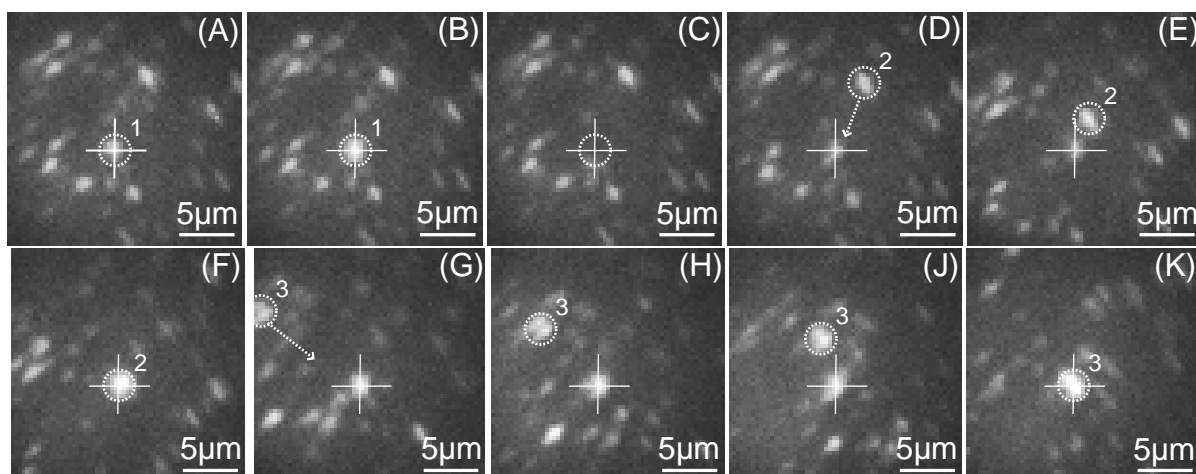


Figure 2-78. Illustration of the alignment procedure, when the AFM tip is kept on the optical axis and the fluorescence spot, corresponding to a molecule adsorbed on the surface, is positioned under the tip. DNA molecules (NHdna3BioA) adsorbed on GOPTS surface and labelled with SYBR Green I dye at a concentration 0.2–2 μM . A cross represents the optical axis which is perpendicular to the image. Dotted circles with numbers show molecules which are consequently brought on the optical axis and pulled with the AFM cantilever. (A) molecule (1) on optical axis, the tip is retracted. (B) molecule (1) and the tip are on the surface. (C) molecule (1) has disappeared, the tip is retracted. (D,E,F) a new molecule (2) is moved on optical axis, while the tip is close to the surface. (G,H,J,K) another molecule (3) is located.

2.7.1.1 Mechanical manipulation of DNA molecules

A DNA molecule caught between the surface and the tip can be manipulated with the AFM probe. Figure 2-79 shows attachment of a dsDNA (NHdna3Bio), $\sim 2\mu\text{m}$ long, between the avidin-coated tip and GOPTS silanized coverglass. The brightest spot in the images is the scattering and/or luminescence originating from the AFM tip. The bright signal is not only due to the emission of the Si_3N_4 itself but also to additional stained DNA not being bound to the cover glass but to the tip. This luminescence dictates a minimum useful distance between the tip and optical observation volume element for single molecule studies of the order of one micron. As a result of manipulation with the tip, the dsDNA molecule is stretched up to 4–5 μm and ruptured (Figure 2-79, last image).

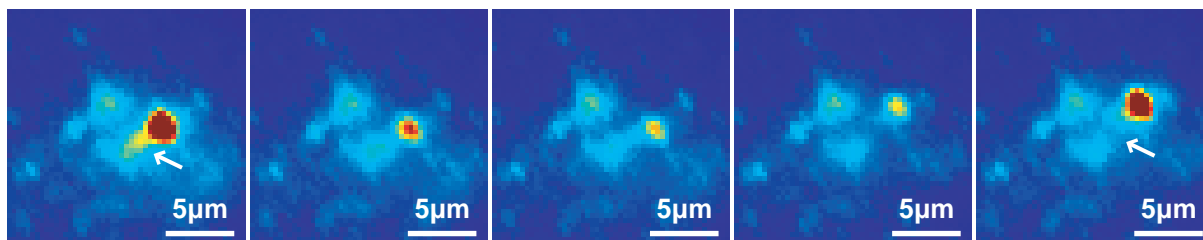


Figure 2-79. DNA molecule manipulation. Brightest spot is a AFM cantilever. An arrow indicates a dsDNA molecule (NHdna3Bio) captured between the avidin-functionalized tip (via reversible avidin-biotin bonds) and a GOPTS covered glass (via covalent bond formation). DNA is stained with SYBR Green I fluorescent dye, $\sim 2\mu\text{M}$ concentrated in PBS buffer. Luminescence excitation is obtained via evanescent light. Other luminescent spots correspond to other molecules bound to the surface.

2.7.1.2 AFM hysteresis influence on manipulations

The main source of an instrumental limitation for a combined experiment realization is the AFM piezo hysteresis. First, hysteresis appears when the AFM tip is moved in the X-Y plane. That property decreases the ability to precisely address a fluorescent object on the surface. The illustration of the hysteresis in X-Y translation is shown in Figure 2-80. Moving the AFM piezo in X-Y for 10 μm does result in different actual translation. The change of the cantilever brightness can be attributed to the excitation intensity of the evanescent wave change and also to the AFM piezo translation in Z. Another example, illustrating the X-Y position change due to Z translation is given in Figure 2-81. The cantilever which is 1 μm above the glass surface is positioned above the luminescent spot (position 2). After this it is brought in contact with the surface. A force curve, in this case a 4 μm retraction followed by a 4 μm approach, is performed. The position of the spot in X-Y plane has moved approximately 2 μm (position 3).

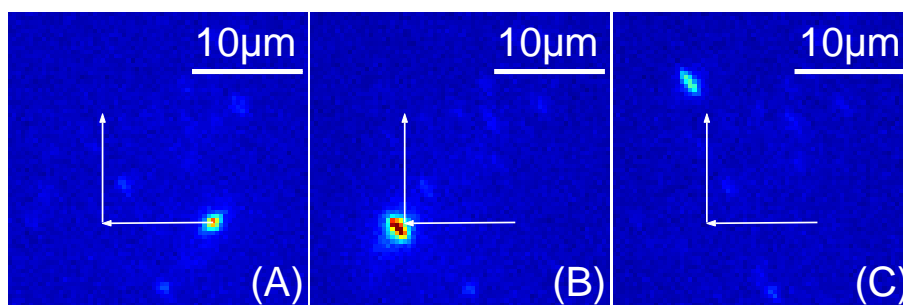


Figure 2-80. Illustration of the AFM piezo hysteresis in X-Y translation. The bright spot indicates the position of the cantilever tip. The tip is supposed to move 10 μm to the left (B) and then 10 μm to the top (C), as shown by the arrows. However, the actual displacement is different.

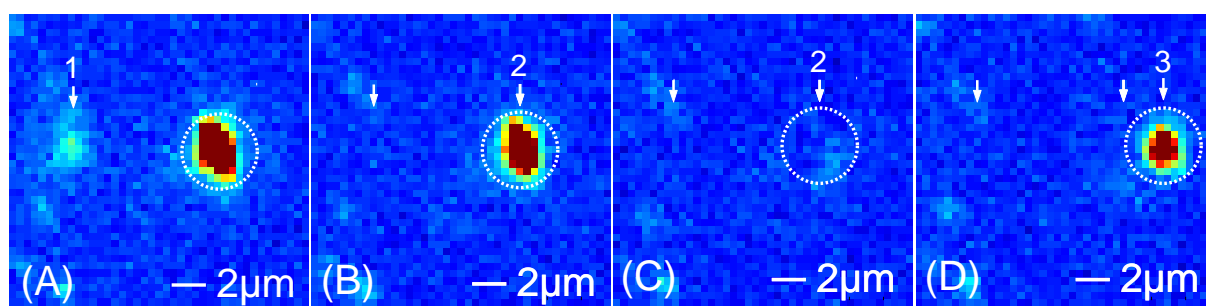


Figure 2-81. Illustration of the AFM piezo hysteresis in X-Y due to piezo translation in Z. (A) The cantilever tip positions are shown with arrows. The cantilever is about 1 μm above the surface. A circle indicates the position of a luminescent object on the surface. (B) The cantilever is moved from position 1 to position 2. (C) A force curve, 4 μm retraction, is performed. A bright luminescent object on the surface is picked up with the cantilever. (D) The cantilever is brought into contact with the surface again. The luminescent spot has moved to position 3 as a result of piezo Z-translation.

The observed hysteresis eliminates one of the fluorescence-directed molecules localization approaches for the realization of simultaneous atomic-force spectroscopy and confocal fluorescence detection, described in Section 2.7.1 and illustrated in Figure 2-77.

Additional piezo translation in the X-Y plane is an undesirable effect, affecting the fluorescent molecule positioning on the optical axis and in the confocal detection volume. However, combining fluorescence CCD imaging under evanescent wave excitation and AFM manipulation, the hysteresis can be measured down to distances resolved by optics. Additionally, some kind of piezo hysteresis compensation and control of piezo translation, e.g. a close loop control, would help to make this approach reproducible.

For the combination of AFM force spectroscopy with confocal fluorescence detection and simultaneous measurements, the approach illustrated in Figure 2-78 is more appropriate. It was found that the X-Y hysteresis can be minimized by performing several piezo Z-translation with the full piezo range. Afterwards the cantilever does not change its position of the dimensions of optical resolution. That is why the alignment of the cantilever on the optical axis followed by a sample molecule translation under the cantilever is preferred for the experimental realization in the present setup.

2.7.2 Simultaneous force and fluorescence spectroscopy experiments on single DNA molecules

The tip and immobilized DNA molecule aligned on the optical axis allow for simultaneous single molecule force and MFD spectroscopy. An experiment can be illustrated by the following scheme (Figure 2-82). The fluorescence detection volume is positioned above the surface at a distance described by the focus-surface separation (FS). The geometrical parameters of the detection volume depend on the laser focus and the size of the confocal pinhole as listed in Section 2.1.1. Force curves are performed by moving the AFM tip away and towards the surface. Its position is characterized by the tip-surface separation (TS) and the relative position of the tip and the focus – the tip-focus separation (TF). Depending on the relative positions of all elements, different contributions of scattering and luminescent signal from the cantilever tip are expected. The signal from the untreated cantilevers, studied in Section 2.4.3 can serve as an example. Fluorescence signal curves, presented in Figure 2-45, define fluorescence calibration curves for the tip apex of an untreated AFM cantilever. Equally shaped curves were obtained performing continuous retraction and approach with the fixed x-y position of the cantilever (results are not shown). These curves can be used to estimate a useful piezo position range and focus-surface separation for simultaneous force and fluorescence spectroscopy experiments. For example, if the focus-surface separation is 3 μm (Figure 2-82, A), and the tip is moved from the surface up to 6 μm , all possible fluorescence intensities will be probed (Figure 2-82, light grey area).

For some of them the fluorescence signal of the tip will dominate the signal from dye molecules bound to a DNA. The bigger the tip-focus separation the smaller the signal contribution from an unmodified tip. Decreasing the focus–surface separation would shift the calibration curve to the left and limit the accessible negative tip-focus separation region (Figure 2-82, dark grey area). This will increase the signal to noise ratio for single molecule detection. However, moving the focus too close to the glass surface would increase the background contribution due to the light scattering in glass.

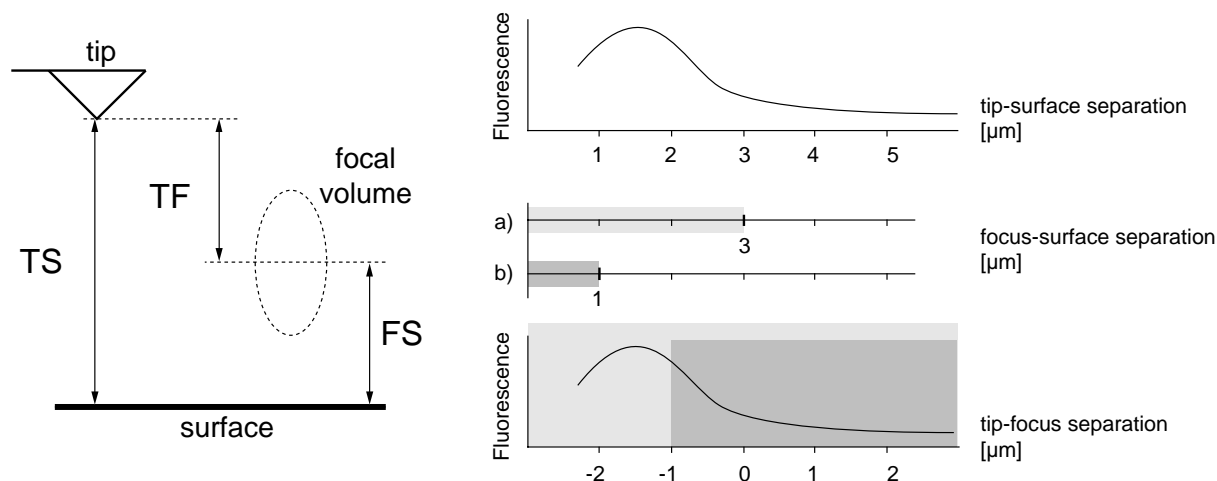


Figure 2-82. Schematic representation of the confocal fluorescence detection in a combined AFM and optical microscope setup (left). The position of the tip is defined by a tip-surface separation (TS) and an AFM tip-focus separation (TF). The position of the optical focal volume is defined by a focus-surface separation (FS). A single molecule detection calibration curve defines the amount of fluorescence at different TS or TF separations (right). Light (a) and dark (b) areas indicate the position of the focus above the surface and define the assessable separation ranges, as well as the maximum fluorescence values.

Explicit fluorescence signal characterization under confocal detection conditions would require several fluorescence calibration curves: signal contributions from the surface and from the tip. Due to the cantilever geometry, these curves will be quantitatively different for different positions on the tip. Moreover, the number of fluorescent molecules bound to the cantilever would dramatically change the background signal. The absence of a precise cantilever position determination (i.e. closed loop) in the present setup makes the task of obtaining the fluorescence calibration curves impractical. However, useful qualitative information for planning an experiment and simple analysis can be extracted from the shape of the fluorescence calibration curves.

2.7.2.1 Pulling on many molecules: sample misalignment

Pulling on many molecules as well as an uncertainty of DNA attachment on the tip are illustrated in the following experiments. The dsDNA molecules modified for specific attachment (NHdna3Bio) are prepared on a cantilever tip. The tip is positioned above the

surface on the optical axis and pulling is performed. The position of the cantilever is readjusted after several pulls in order to compensate for the piezo hysteresis and to keep the cantilever on the optical axis.

In general, as specified by the manufacturer, the length of dsDNA is 2 μm , and the height of the AFM tip is 3 μm . That allows several DNA molecules being close to the tip apex to bind to a GOPTS surface (Figure 2-83, A). The fluorescence light from these molecules, as well as the fluorescence from the molecules left on the surface will produce “noise” on the signal. This case is illustrated in Figure 2-84 A. Here first pulls have shown several pulling events originating from many DNA molecules on the tip. The force events observed (black curve) can hardly be correlated with fluorescence events (light grey curve). However, one of the fluorescence peaks corresponds to a high force rupture event ($\sim 0.75 \mu\text{m}$, 800pN). The overall fluorescence signal decreases in the retraction part and increases in the approach, which can be the contributions of a fluorescence signal from the DNA molecules left on the surface and the signal coming from the AFM tip. The small focus-surface separation (FS = 0.5 μm) suggests that the maximum fluorescence signal from the AFM tip emerges close to the surface, and decreases monotonically with the piezo position above the surface.

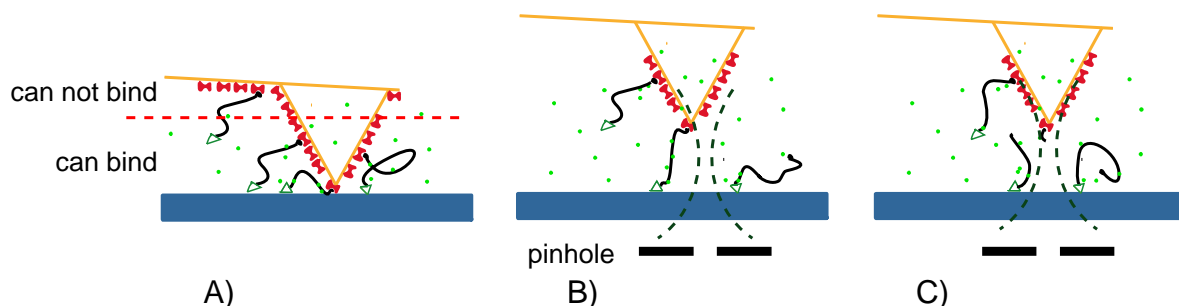


Figure 2-83. Schematic illustrations of pulling experiments. (A) Finite sizes of DNA molecules and the cantilever tip limit the positions on the cantilever, where molecules can bind later to a surface. The allowed area for binding of molecules is still big and many molecules can simultaneously be connected between the tip and the surface. (B) The fluorescence detection volume and the attachment point of a DNA molecule on the tip can be misaligned. (C) After all DNA molecules have been ruptured or detached AFM, the cantilever is no longer useful for the combined experiment.

Single DNA stretching was performed also at different position on the sample (Figure 2-84 B). Here, the focus was positioned on the surface and the maximum signal from the cantilever tip apex is expected on the surface. However, different shapes of the fluorescence signal suggest that a different point on the tip, not the tip apex, was positioned on the optical axis (Figure 2-83 B). The total fluorescence intensity is lower than in the case illustrated in Figure 2-84 (A), proposing no molecules were left on the surface. At this position, the almost identical shapes of the fluorescence curves for retraction and approach indicates that the pulled molecule was not placed within the detection volume (Figure 2-83 B). The following experiment, with no molecules were attached between the tip and the surface (Figure 2-83 C),

and a comparable shape of the fluorescence curve are observed. The focus in Figure 2-84 (C) is 0.5 μm above the surface, in contrast to the previous measurement. That shifts the local maximum from 2.5 μm piezo position (see Figure 2-84 B) to 3 μm (see Figure 2-84 C). Other features in the fluorescence curves are also translated as expected.

Although a single DNA molecule is pulled in the combined experiment (see Figure 2-84 B), the corresponding fluorescence signal is hard to interpret. An analysis of the fluorescence anisotropy and the fluorescence lifetime traces also do not reveal significant effects.

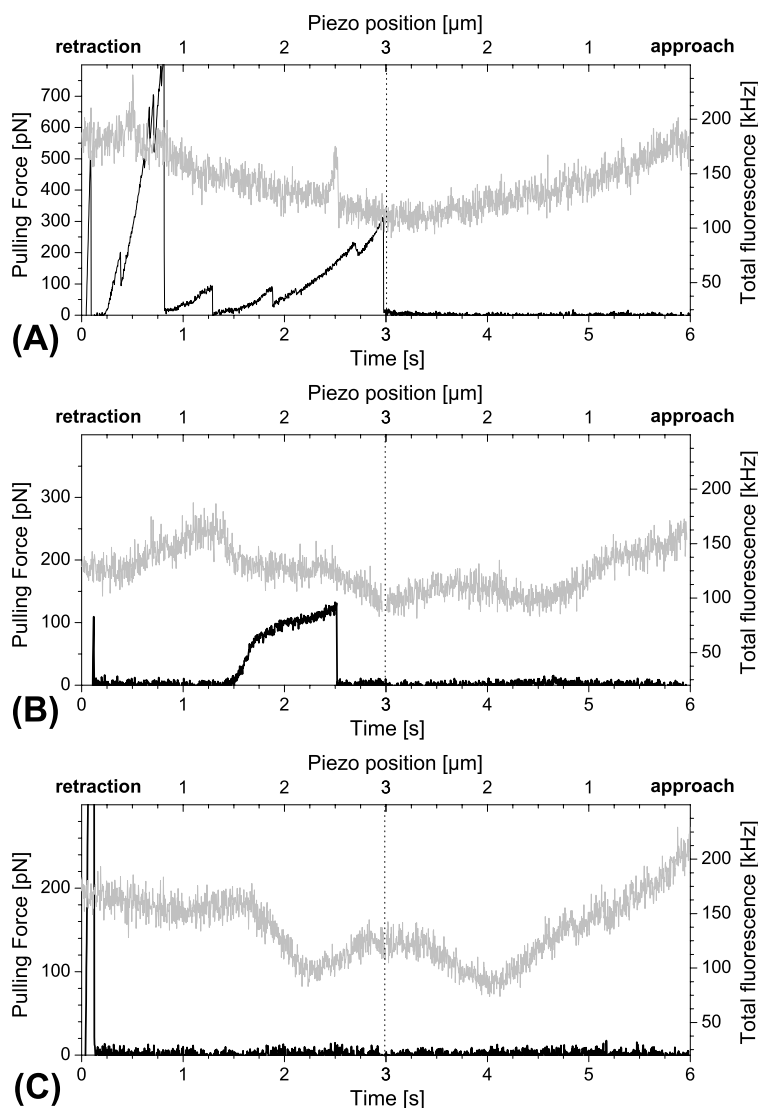


Figure 2-84. Results of simultaneous AFM pulling and fluorescence detection. For each experiment A,B,C the pulling force (black line) and the total fluorescence signal (light grey line) are shown as a function of time (bottom scale) and piezo position (top scale). A dotted line marks the separation between retraction (left) and approach (right) within the pulling curves. (A) The retraction curve indicates a pulling on many molecules. Focus-surface separation (FS) is 0.5 μm . (B) The retraction curve indicates a pulling on a single dsDNA molecule. Focus-surface separation (FS) is 0 μm . (C) No pulling events are observed and focus-surface separation (FS) is 0.5 μm . For all experiments the concentration of SYBR Green I dye was 0.2-1 μM , and excitation power 1.12 kW/cm^2 . Pulling is performed in 10mM PBS buffer, 150mM NaCl, 1mM EDTA, pH8.0. A Veeco cantilever (lever C) with a spring constant of 12 pN/nm is used for the experiment.

2.7.2.2 Consecutive dsDNA pulls and fluorescence detection

Simultaneous force and fluorescence measurements require fluorescence signal detection while reversibly stretching and relaxing a single DNA molecule many times. Reversible force measurements were demonstrated in Section 2.6.3.2 (see Figure 2-73). Experiments with the different types of DNA molecules are illustrated in Figure 2-85. Specifically modified dsDNA molecules (NHdna3Bio12) are prepared on a cantilever tip. The consecutive pulling to various increasing piezo distances is performed (a-h). The left side of the figure represents the retraction and the right side shows the approach. The dotted lines mark the turning points of the force curves. There is no delay between stop of the retraction and start of the approach, and two dotted lines for one force curve can be superposed on the time axis.

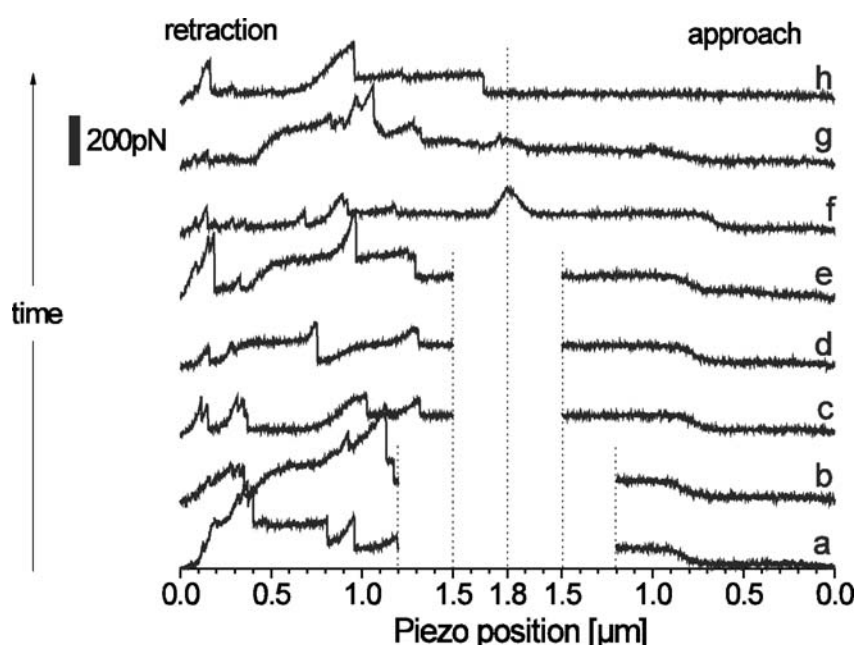


Figure 2-85. Series of force versus piezo position curves obtained on specifically modified dsDNA (NHdna3Bio12, Table 2-6) bound between a biotinylated AFM probe and a GOPTS functionalized surface. DNA extension is increased from (a,b) to (c,d,e) and to (f,g,h) until the detachment of a DNA molecule. Dotted lines mark the separation between the retraction (on the left) and approach parts (on the right). Pulling is performed in 10mM PBS buffer, 150mM NaCl, 1mM EDTA, pH8.0. A Veeco cantilever (lever C) with a spring constant of 9.9 pN/nm is used for the experiment.

Although the retraction curves are “noisy” and reveal many molecules sticking between the tip and the surface, the approach curves always show a force corresponding to single molecule. Moreover, in the retraction curve the B-S transition is observed at the same piezo position. This indicates a consecutive pulling on the same dsDNA. However, the length of all dsDNA molecules is less than the manufacturer specified 2 μm . That suggests partially denaturated DNA molecules. Performing AFM imaging in tapping mode, mainly DNA fragments smaller than 6000bp (2 μm) were discovered (results are not shown).

For each pull in Figure 2-85 a corresponding fluorescence signal is recorded. Several curves (Figure 2-85, b, f, h) are presented in Figure 2-86. The total fluorescence signal decreases with time, while the AFM tip is moved away and towards the surface. Each consecutive pull is delayed for 1-2 minutes (during this time the experimental data are saved). The intensity drop can be explained either by the cantilever geometry change in the detection volume or the fluorescence photobleaching of the molecules on the tip. The changes in the tip geometry can be considered if fluorescence calibration curves are obtained. This task can be accomplished by performing an AFM tip raster scan with retraction and approach in each point (force-volume) and measuring the fluorescence signal. A tip uniformly covered with fluorophores, can be used for this purpose.

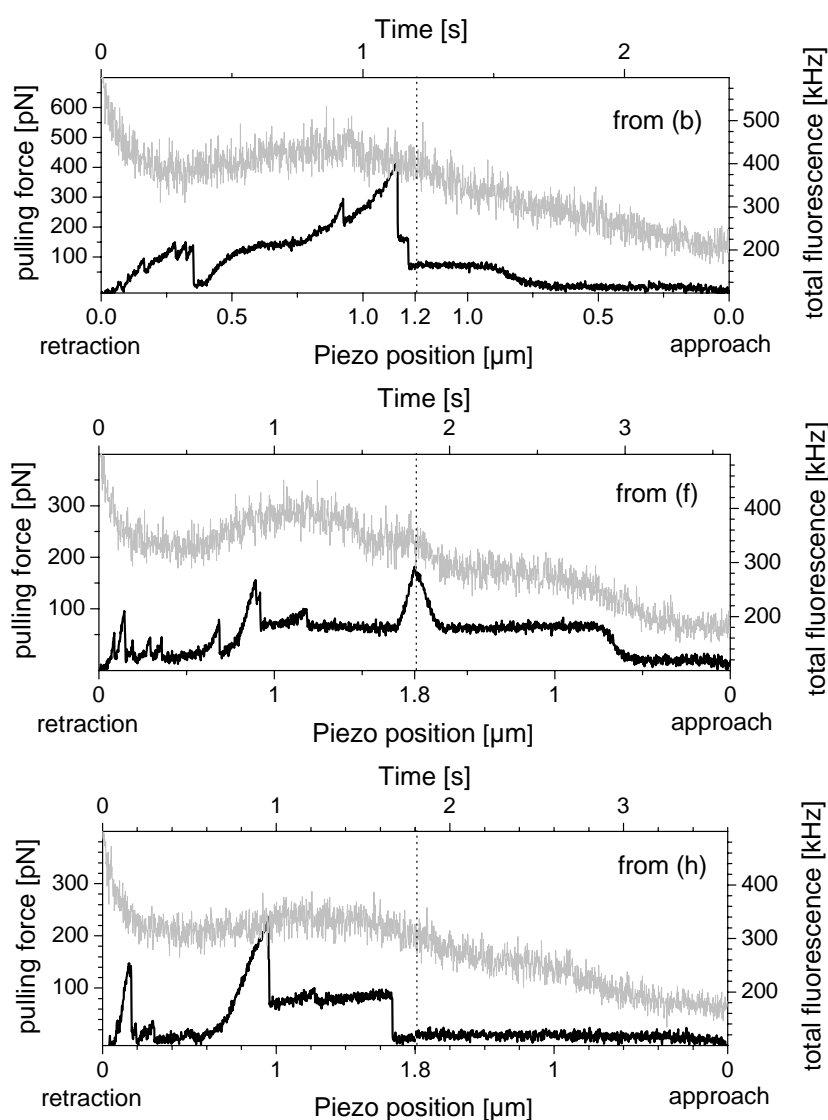


Figure 2-86. Results of simultaneous AFM pulling and fluorescence detection. From the top to the bottom consecutive pulls (Figure 2-85, b, f, h) are shown. Pulling force (black line) and total fluorescence signal (light grey line) are presented as a function of time (top scale) and piezo position (bottom scale). Dotted lines mark the separation between retraction (left) and approach (right) parts within the pulling curves. Concentration of SYBR Green I fluorescent dye in solution is $2 \mu\text{M}$. The excitation power is $\sim 0.5 \text{ kW/cm}^2$.

However, one can assume the ideal case where the observation spot on the tip surface does not change as the cantilever moves. In this case the fluorescence signal decreases with time due to photobleaching. The photobleaching contribution can be estimated by analyzing the fluorescence signal at similar piezo positions. Figure 2-87 depicts the result of an exponential fit (A) to the total fluorescence for the experimental data given in Figure 2-85, f. The fluorescence signal (S) in presence of quenching is described by the following equation:

$$S = S_0 \cdot \exp(-t/t_q) \quad (2-33)$$

where S_0 is the initial fluorescence signal at time “0” and t_q is the characteristic quenching time. A corrected fluorescence trace calculated (B) by the following equation is also shown in Figure 2-87, B.

$$S_{corr} = \frac{S_{not\ corr}}{\exp(-t/t_q)} \quad (2-34)$$

where S_{corr} is the corrected total fluorescence and $S_{not-corr}$ is the experimental data total fluorescence.

The fast fluorescence signal decay in the range of 0–0.25 s (Figure 2-87, region 1) is not completely removed, suggesting a more complex model. However, the detectable correlations between the fluorescence signal and force events are observed. The fluorescence increase in the range of 0.5–1.5 s (region 2) and in the range of 2–3 s (region 4) coincides with dsDNA B-S transitions. In these regions dsDNA undergoes a length change of almost a factor of 2 and a correspondingly bigger or smaller part of the single DNA molecule is located in the detection volume. Since the fluorescence signal does not change accordingly but rather stays constant, either a variation of the concentration of the dye molecules on the DNA or a change of the dyes fluorescence properties upon stretching the DNA could be inferred. The latter is unlikely (the fluorescence quantum yield of SYBR Green I on DNA free in solution was reported to be 0.69 for dsDNA and 0.39 for ssDNA) [229], therefore an increased dye to base pair ratio on DNA upon stretching has to be concluded in both regions.

The fluorescence increase in the range of 1.5–2 s (region 3) coincides with DNA strand melting. The effect can be caused by the SYBR Green I concentration increase on stretched dsDNA and ssDNA molecules. However, the dye has a 57% lower quantum yield upon binding to ssDNA [229]. In addition, reported results [228] predict a 25% fluorescence decrease at the average concentration of SYBR Green I dyes of 1–2 dyes/bp which is used here. The fluorescence anisotropy has shown no features that can be attributed to changes in the local environment or binding conditions of the dye (data are not shown).

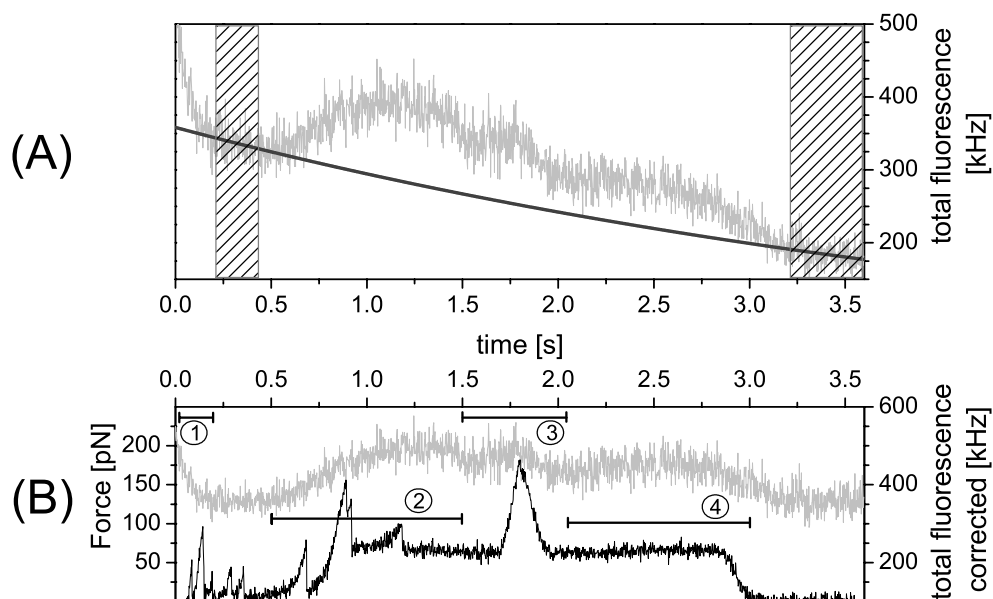


Figure 2-87. Photobleaching correction of a fluorescence trace in a combined experiment (Figure 2-85, f and Figure 2-86). The uncorrected fluorescence signal is shown with a grey curve (A). A black curve in (A) indicates the exponential fit (equation 2-33) of the fluorescence data at comparable piezo positions which are indicated by shaded areas (0.2-0.4 s and 3.2-3.6 s). The parameters of the fit are $S_0 = 358$ kHz, $t_q = 5.1$ s. A grey curve in (B) presents the corrected fluorescence trace (equation 2-34). A black curve in (B) shows the force during the cantilever retraction and approach. Region 1 indicates remained fast fluorescence decrease, fluorescence in regions 2 and 4 coincides with dsDNA B-S transitions, and fluorescence in region 3 coincides with DNA strand melting.

2.7.2.3 DNA rupture. Fluorescence intensity and lifetime change

Clear coincidences of abrupt changes in force and fluorescence were observed for various sample preparations and can be classified into two types. The classification of these results is mainly based on the mechanical part of the combined experiment.

The first type is when the cantilever tip which is densely covered with molecules can jump out of contact with the surface at small piezo positions (Figure 2-88 top and bottom, 0–0.4 μm). Sudden cantilever jumps lead to a change in the cantilever position and the tip geometry inside the detection volume. An unphotobleached area of the tip will be introduced into the detection volume, increasing the fluorescence signal.

The second type of correlation between the abrupt force events and the fluorescence events happens at larger piezo positions (Figure 2-88 top 0.8–1 μm and bottom 1.4–1.6 μm). They are more likely to be explained by mechanical rupture of pulled molecules. The fluorescence signal intensity report changes of the dye fluorescence emission properties upon conformational changes caused by a mechanical rupture. The conformational change in the structure of a single DNA molecule induced by a force would change the fluorescence properties of a dye. As reported [229], the fluorescence lifetime of SYBR Green I dye on ssDNA is shorter than on a dsDNA molecule. After passing through the mechanically induced

B-S transition, the DNA molecule consists of two single strands. The binding properties of the dye will be changed and the fluorescence signal would be a mixture of the fluorescence signals of the dye on a dsDNA and a ssDNA. After the ssDNA ruptures, molecule fragments left on the surface and the tip would re-hybridise to a dsDNA molecule. The molecule re-hybridisation will lead to a change in binding conditions and an increase of fluorescence lifetime and intensity.

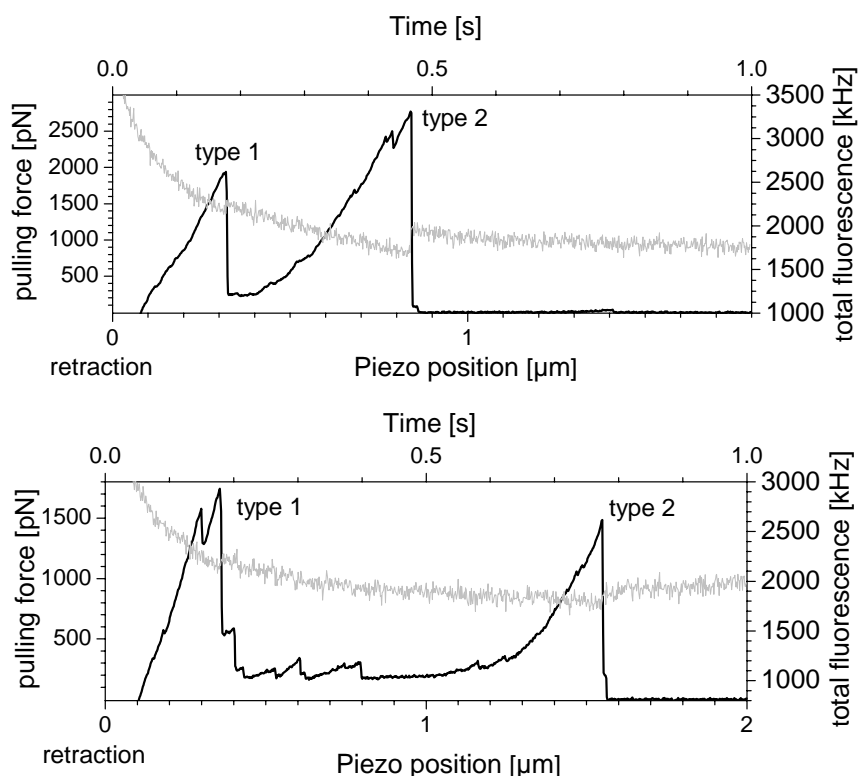


Figure 2-88. Results of simultaneous AFM pulling and fluorescence detection. Pulling force (black line) and total fluorescence signal (light grey line) are presented as a function of time (top scale) and piezo position (bottom scale). Abrupt force and fluorescence events coincide divided into two types. Type 1 are events at small piezo positions, which can be explained by cantilever jumps out of contact with the surface. Type 2 are events at larger position, which can be explained by the mechanical rupture of DNA molecules. The concentration of SYBR Green I fluorescent dye in solution is $4 \mu\text{M}$. The excitation power is $\sim 6 \text{ kW}/\text{cm}^2$. Focus-surface separation is $1 \mu\text{m}$.

However, the presence of the AFM tip can cause fluorescence quenching of the dye close to the cantilever. In addition, the optical signal from the tip itself is intense and has a short lifetime (Section 2.4.3). Effects of the tip scattering and fluorescence as well as tip induced fluorescence quenching and fluorescence enhancement would compete with fluorescence of the dye.

An experiment demonstrating the fluorescence intensity and the fluorescence lifetime change while stretching a single DNA is presented in Figure 2-89. Fluorescence decay histograms are generated at each point of the fluorescence trace (Figure 2-89, grey line) and fitted to a single exponential model function, taking into account background scattering and

the instrumental response function (as explained in Section 2.4.3). The fluorescence lifetime jump is observed as the DNA molecule ruptures. The lifetime of the SYBR Green I dye is reported to be 4.78 ns and 2.26 ns on dsDNA and ssDNA accordingly [229]. Since the lifetime values are too short to belong to the fluorescence of the dye bound to DNA, it is hard to judge whether the lifetime jump is caused by the change in fluorescent properties of the dye or by the sudden tip movement causing different amount of fluorescence quenching.

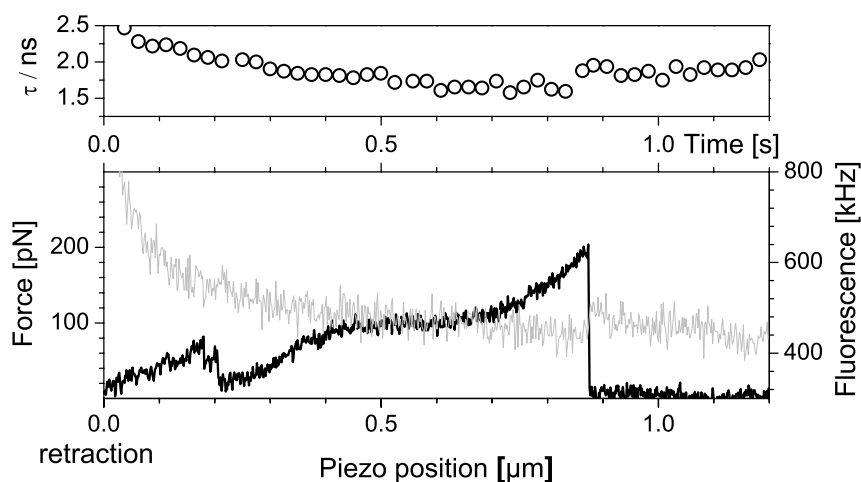


Figure 2-89. Combined force and fluorescence data (left). The force curve (black line) shows a single DNA molecule being stretched and ruptured. The fluorescence intensity reveals the abrupt signal increase upon DNA rupture (grey curve). The fluorescence lifetime for a 25 ms time windows is shown in with open circles. The concentration of SYBR Green I fluorescent dye in solution is 0.6-1 μM . The excitation power is $\sim 0.5 \text{ kW/cm}^2$. Focus-surface separation is 0.5 μm .

2.7.3 Conclusions and outlook

The effect of the piezo hysteresis in the sample plane is quantified. It can reach values of 5 μm , depending on the history of the piezo movements. The AFM piezo hysteresis has to be controlled for the precise optical alignment and the addressing of fluorescent molecules on the surface with the AFM tip. The piezo hysteresis in the sample plane can be eliminated when a series of full piezo range movement perpendicular to the surface is performed.

Several experimental approaches to realize simultaneous force spectroscopy and multiparameter fluorescence detection have been demonstrated. Successful experiments are performed depositing DNA molecules on the tip or on the surface. The fluorescence of the modified AFM cantilever tips needs to be better characterized to quantify the modification procedures of the AFM cantilevers.

The data analysis of the combined experiment includes the correlation on the time scale of the force events and the changes in fluorescence parameters. Additional dimension (force values) is added to the standard two-dimensional MFD histograms.

Although commercial specifically modified DNA molecules were found to have variations in length and thus possess hardly predictable binding properties, the consecutive pulling on a single DNA molecule (more than 10 pulls) and the simultaneous optical signal registration were achieved. The intensity decrease of the fluorescence of the DNA binding dye is detected upon stretching the DNA molecules. The abrupt fluorescence intensity and the fluorescence lifetime increase accompany the rupture of a single DNA molecule.

The method of the fluorescence-directed localization and force spectroscopy can be implemented to study other biological molecules. Different sample preparations strategies and various surface chemistries as antigen-antibody interaction [136,230,231] can be used for the molecule attachment. Long Si or carbon cantilever tips are preferred for the experiments in order to minimize the influence of the tip's fluorescence signal. Sharp AFM probes and their proper chemical treatment will also limit the attachment area of molecules on the tip.

The combination of force spectroscopy and FRET probability distribution analysis propose high spatial resolution in both mechanical and fluorescence measurements of the combined experiment.

Literature:

1. Feynman R.P., "There's plenty of room at the bottom" *Engineering and Science*, 1960.
2. Tamarat Ph., Maali A., Lounis B., Orrit M., "Ten years of single-molecule spectroscopy" *J.Phys.Chem.A* 104 (2000) pp.2-15.
3. Moerner W.E. "A dozen of years of single-molecule spectroscopy in physics, chemistry, and biophysics" *J.Phys.Chem.B* 106 (2002) pp.910-927.
4. Clausen-Schaumann H., Seitz M., Krautbauer R., Gaub H.E., "Force spectroscopy with single bio-molecules" *Current Opinions in Chemical Biology* 4 (2000) pp.524-530.
5. Bustamante C., Bryant Z., Smith S.B., "Ten years of tension: single-molecule DNA mechanics" *Nature* 421 (2003) pp.423-427.
6. Wallace M.I., Molloy J.E., Trentham D.R., "Combined single-molecule force and fluorescence measurements for biology" *J.Biology* 2:4 (2003).
7. Weiss S., "Fluorescence spectroscopy of single biomolecules" *Science* 283 (1999) pp.1676-1683.
8. Hillner P.E., Radmacher M., Hansma P.K., "Combining atomic force and scanning reflection interference contrast microscopy" *Scanning* 17 (1995) pp.144-147.
9. Kolodny L.A., Willard D.M., Carillo L.L., Nelson M.W., Van Orden A., "Spatially correlated fluorescence/AFM of individual nanosized particles and biomolecules" *Anal.Chem.* 73 (2001) pp.1959-1966.
10. Noy A., Huser T.R., "Combined force and photonic probe microscope with single molecule sensitivity" *Rev.Sci.Instrum.* 74 (2003) pp.1217-1221.
11. Hernando J., de Witte P.A.J., van Dijk E.M.H.P., Korterik J., Nolte R.J.M., Rowan A.E., Garcia-Parajo M.F., van Hulst N.F., "Investigation of perylene photonic wires by combined single-molecule fluorescence and atomic force microscopy" *Angew.Chem.* 43 (2004) pp.4045-4049.
12. Burns A.R., "Domain structure in model membrane bilayers investigated by simultaneous atomic force microscopy and fluorescence imaging" *Langmuir* 19 (2003) pp.8358-8363.
13. Gorelik J., Shevchuk A., Ramalho M., Elliot M., Lei C., Higgind C.F., Lab M.J., Klenerman D., Krauzewicz N., Korchev Y., "Scanning surface confocal microscopy for simultaneous topographical and fluorescence imaging: Application to single virus-like particle entry into a cell" *Proc.Natl.Acad.Sci.USA* 99 (2002) pp.16018-16023.

14. Nishida S., Funabashi Y., Ikai A., "Combination of AFM with an objective-type total internal reflection microscope (TIRFM) for nanomanipulation of single cells" *Ultramicroscopy* 91 (2002) pp.269-274.
15. Ishii Y., Kimura Y., Kitamura K., Tanaka H., Wazawa T., Yanagida T., "Imaging and nano-manipulation of single actomyosin motors at work" *Clin.Exper.Pharm.Physiol.* 27 (2000) pp.229-237.
16. Hugel T., Holland N.B., Cattani A., Moroder L., Seitz M., Gaub H.E., "Single-molecule optomechanical cycle" *Science* 296 (2002) pp.1103-1106.
17. Shivashankar G.V., Libchaber A., "Single molecule grafting and manipulation using a combined atomic force microscope and an optical tweezers" *Appl.Phys.Lett.* 71 (1997) pp.2327-2329.
18. Yang T.J., Lessard A., Quake S.R., "An apertureless near-field microscope for fluorescence imaging" *Appl.Phys.Lett.* 76 (2000) pp.378-380.
19. Trabesinger W., Kramer A., Kreiter M., Hecht B., Wild U.P., "Single-molecule near-field optical energy transfer microscopy" *Appl.Phys.Lett.* 81 (2002) pp.2118-2120.
20. Clark S.C., Walz J.Y., Ducker W.A., "Atomic force microscopy colloid-probe measurements with explicit measurement of particle-solid separation" *Langmuir* 20 (2004) pp.7616-7622.
21. Sakar A., Robertson R.B., Fernandez J.M., "Simultaneous atomic force microscope and fluorescence measurements of protein unfolding using a calibrated evanescent wave" *Proc.Natl.Acad.Sci.USA* 101 (2004) pp.12882-12886.
22. Hards A., Zhou C., Seitz M., Bräuchle C., Zumbusch A., "Simultaneous AFM manipulation and fluorescence imaging of single DNA strands" *Chem.Phys.Chem.* 6 (2005) pp.534-540.
23. Lang M.J., Fordyce P.M., Block S.M., "Combined optical trapping and single-molecule fluorescence" *J.Biology* 2:6 (2003).
24. Lang M.J., Fordyce P.M., Engh A., Neuman K.C., Block S.M., "Simultaneous, coincident optical trapping and single-molecule fluorescence" *Nature Methods* 1 (2004) pp.1-7.
25. Born M., Wolf E., "Principles of optics" Pergamon Press, 1980.
26. Loudon R., "The quantum theory of light" Oxford, 2000.
27. Wiedemann E., *Wied. Ann.d.Phys.* 34 (1888) p.446.
28. Valeur B., "Molecular fluorescence: Principles and applications" Wiley-VCH, 2002.
29. Stepanov "Vavilov law" *U.F.N.* LVIII (1956) pp.1-33.

30. Lakowicz J.R., "Principles of fluorescence spectroscopy" Kluwer Academic, 1999.
31. Lakowicz J.R., "Topics in fluorescence spectroscopy" Plenum press, 1991.
32. Van der Meer B.W., Cooker G., Chen S.-Y., "Resonance energy transfer: theory and data" VCH publishers, 1994.
33. Selvin P.R., "Fluorescence resonance energy transfer" *Methods in Enzymology* 246 (1995) pp.300-334.
34. Fung B.K.K., Stryer L., "Surface density determination in membranes by fluorescence energy transfer" *Biochemistry* 17 (1978) pp.5241-5248.
35. Elson E.L., Magde D., "Fluorescence correlation spectroscopy I. Conceptual basis and theory" *Biopolymers* 13 (1974) pp.1-27.
36. Magde D., Elson E.L., Webb W.W., "Fluorescence correlation spectroscopy II. An experimental realization" *Biopolymers* 13 (1974) pp.29-61.
37. Qian H., Elson E.L., "Analysis of confocal laser-microscope optics for 3-D fluorescence correlation spectroscopy" *Appl.Optics* 30 (1991) pp.1185-1195.
38. Rigler R., Metz Ü., Widengren J., Kask P., "Fluorescence correlation spectroscopy with high count rate and low background: analysis of translational motion" *Eur.Biophys.J.* 22 (1993) pp.169-175.
39. Widengren J., Rigler R., "Fluorescence correlation spectroscopy as a tool to investigate chemical reactions in solutions and on cell surfaces" *Cell.Molec.Biology* 44 (1998) pp.857-879.
40. Widengren J., Rigler R., "Mechanisms of photobleaching investigated by fluorescence correlation spectroscopy" *Bioimaging* 4 (1996) pp.149-157.
41. Valeur B., Brochan J.-C., "New trends in fluorescence spectroscopy: Applications to chemical and life sciences" Springer, 1994.
42. Krichevsky O., Bonnet G., "Fluorescence correlation spectroscopy: the technique and its applications" *Rep.Prog.Phys.* 65 (2002) pp.251-297.
43. Metz Ü., Rigler R., "Submillisecond detection of single rhodamine molecules in water" *J.Fluorescence* 4 (1994) p.259.
44. Rigler R., Elson E.L., "Fluorescence correlation spectroscopy" Springer, 2001.
45. Starchev K., Ricka J., Buffle J., "Noise on fluorescence correlation spectroscopy" *J.Coll.Inter.Sci.* 233 (2001) pp.50-55.
46. Wohland T., Rigler R., Vogel H., "The standard deviation in fluorescence correlation spectroscopy" *Biophysical J.* 80 (2001) pp.2987-2999.

47. Kask P., Günter R., Axhausen P., “Statistical accuracy in fluorescence fluctuation experiments” *Eur.Biopys.J.* 25 (1997) pp.163-169.
48. Qian H., “On the statistics of fluorescence correlation spectroscopy” *Biophys.Chem.* 38 (1990) pp.49-57.
49. Koppel D.E., “Statistical accuracy in fluorescence correlation spectroscopy” *Phys.Rev.E* 10 (1974) pp.1938-1945.
50. Hess S.T., Webb W.W., “Focal volume optics and experimental artefacts in confocal fluorescence correlation spectroscopy” *Biophysical J.* 83 (2002) pp.2300-2317.
51. Brown E.B., “Modern Optics” Reinhold publishing Co., 1965.
52. Olympus Microscopy Research Center (<http://olympusmicro.com>).
53. Nikon Microscopy Tutorials (<http://microscopyu.com>).
54. Driscoll W.G. and Vaughan W., eds, “Handbook of optics” McGraw-Hill, 1978.
55. Pawley J.B., “Handbook of biological confocal microscopy” Plenum press, 1996.
56. Abbe E., “Beiträge zur Theorie des Mikroskops und der mikroskopischen Wahrnehmung” *Schultzes.Arc.Mikr.Anat.* 9 (1873) pp.413-468.
57. Abbe E., “Note on the proper definition of the amplifying power of a lens or a lens system” *J.R.Microsc.Soc.* 4 (1884) pp.348-351.
58. Lord Rayleigh “Investigations in optics, with special reference to the spectroscope” *Philos.Mag.* 8-9 (1879, 1880) pp. 261-274, 403-411, 477-486, 40-55.
59. Minsky M., U.S. Patent #3013467, 1957.
60. Minsky M., “Memoir on inventing the confocal scanning microscope” *Scanning* 10 (1988) pp.128-138.
61. Newton I., “Optics” Dover, 1952.
62. de Fornel F., “Evanescent waves from Newtonian optics to atomic optics” Springer, 2001.
63. Goos F., Hänchen M., “Ein neuer und fundamentaler Versuch zur Totalreflexion” *Ann.Phys.Lpz.* 1 (1947) pp.333-346.
64. Lotsch H.K.V., “Beam displacement at total reflection: The Goos–Hänchen effect.” *Optik* 32 (1970-1971) pp.116–137, 189–204, 299–319, 553–569.
65. Fedorov F.I., *Dokl.Akad.Nauk.SSSR* 105 (1955) p.465.
66. Imbert C., “Calculation and experimental proof of the transverse shift induced by total internal reflection of a circularly polarized light beam” *Phys.Rev.D* 5 (1972) p.787.
67. Achmanov S.A., Nikitin C.Y., “Physical Optics” Nauka, 1998.

68. Stout A.L., Axelrod D., "Evanescent field excitation of fluorescence by epi-illumination microscopy" *Appl.Opt.* 28 (1989) p.5237-5242.
69. O'Connor D.V., Phillips D., "Time-Correlated Single Photon Counting" Academic, 1984.
70. Bekker W., "Advanced time-correlated single photon counting techniques" Springer, 2005.
71. Kühnemuth R., Seidel C.A.M., "Principles of single molecule multiparameter fluorescence spectroscopy" *Single Mol.* 2 (2001) pp.251-254.
72. Zander C., Sauer M., Drexhage K.H., Ko D.-S., Schulz A., Wolfrum J., Brand L., Eggeling C., Seidel C.A.M., "Detection and characterization of single molecules in aqueous solution" *Appl.Phys.B* 63 (1996) pp.517-523.
73. Brand L., Eggeling C., Zander C., Drexhage K.H., Seidel C.A.M., "Single-molecule identification of Coumarin-120 by time-resolved fluorescence detection: Comparison of one- and two-photon excitation in solution" *J.Phys.Chem.A* 101 (1997) pp.4313-4321.
74. Eggeling C., Fries J.R., Brand L., Günter R., Seidel C.A.M., "Monitoring conformational dynamics of a single molecule by selective fluorescence spectroscopy" *Proc.Natl.Acad.Sci.USA* 95 (1998) pp.1556-1561.
75. Eggeling C., Berger S., Brand L., Fries J.R., Schaffer J., Volkmer A., Seidel C.A.M., "Data registration and selective single-molecule analysis using multi-parameter fluorescence detection" *J.Biotechnology* 86 (2001) pp.163-180.
76. Felekyan S., Kühnemuth R., Kudryvtsev V., Sandhagen C., Becker W., Seidel C.A.M., "Full correlation from picoseconds to seconds by time-resolved and time-correlated single photon detection" *Rev.Sci.Instrum.* 76 (2005) p.083104.
77. Binning G., Rocher H., Gerber C., Weibel E., "Surface studies by scanning tunneling microscopy" *Phys.Rev.Lett.* 49 (1982) pp.57-61.
78. Binning G., Smith D., "Single-tube three dimensional scanner for scanning tunneling microscopy", *Rev.Sci.Intstrum.* 57 (1986) pp.1688-1689.
79. Binning G., Rocher H., "Scanning tunneling microscopy" *Helv.Phys.Acta* 55 (1982) p.726-735.
80. Binning G., Gerber C., Stoll E., Albrecht T.R., Quate C.F., "Atomic resolution with the atomic force microscope." *Europhys.Lett.* 3, (1987), p.1281-1286.
81. Sarid D., "Scanning Force Microscopy" Oxford University press, 1994.
82. Bonnell D.A., "Scanning probe microscopy and Spectroscopy" Wiley-VCH, 2001.

83. Morris V.J., Kirby A.R., Gunning A.P., "Atomic force microscopy for biologist" Imperial college press, 2001.
84. ed. Colton R.J., Engel A., Frommer J., Gaub H.E., Gewirth A.A., Guckenberger R., Heckl W., Parkinson B., Rabe J., "Procedures in scanning probe microscopes" Wiley-VCH, 1998.
85. Giessibl F.J., "Advances in atomic force microscopy" *Rev.Mod.Phys.* 75 (2003) pp.949-983.
86. Binning G., Quate C.F., Gerber Ch., "Atomic force microscope" *Phys.Rev.Lett.* 56 (1986) pp.930-933.
87. Israelachvili J.N., "Intermolecular and surface forces" Academic Press, 1992.
88. Albrecht T.R., Akamine S., Carver T.E., Quate C.F., "Microfabrication of cantilever styli for the atomic force microscope" *J.Vac.Sci.Technol.A* 8 (1990) p.3386-3396.
89. Harris J.G.E., Awschalom D.D., Maranowski K.D., Gossard A.C., "Fabrication and characterization of 100-nm-thick GaAs cantilevers" *Rev.Sci.Instrum.* 67 (1996) pp.3591-3593.
90. Wenzler L.A., Moyes G.L., Beebe T.P., "Improvements to atomic force microscopy cantilevers for increased stability" *Rev.Sci.Instrum.* 67 (1996) pp.4191-4197.
91. Vesenka J., Miller R., Henderson E., "Three-dimensional probe reconstruction for atomic force microscopy" *Rev.Sci.Instrum.* 65 (1994) pp.2249-2251.
92. Villarrubia J.S., "Algorithms for scanned probe microscopy image simulation, surface reconstruction and tip estimation" *J.Res.Natl.Inst.Stand.Technol.* 102 (1997) pp.425-454.
93. Wolter O., Bayer Th., Greshner J., "Micromachined silicon sensors for scanning force microscopy" *J.Vac.Technol. B* 9 (1991) p.1353-1357.
94. Fowles G.L., "Analytical mechanics" CBS College Publishing, 1986.
95. Saulson P.R., "Thermal noise in mechanical experiments" *Phys.Rev.D* 42 (1990) p.2437-2445.
96. Anczykowski B., Schäfer A., "Q-control" NanoAnalytics information booklet 2003.
97. Levy R., Maaloum M., "Measuring the spring constant of atomic force microscope cantilevers: thermal fluctuations and other methods" *Nanotechnology* 13 (2000) pp.33-37.
98. Gittes F., Schmidt C.F., "Thermal noise limitations on micromechanical experiments" *Eur.Biophys.J.* 27 (1998) pp.75-81.

99. Burnham N.A., Chen X., Hodges C.S., Matei G.A., Thoreson E.J., Roberts C.J., Davies M.C., Tendler S.J.B., "Comparison of calibration methods for atomic-force microscopy cantilevers" *Nanotechnology* 14 (2003) pp.1-6.
100. Holbery J.D., Eden V.L., Sarikaya M., Fisher R.M., "Experimental determination of scanning probe microscope cantilever spring constants utilizing a nanoindentation apparatus" *Rev.Sci.Instrum.* 71 (2000) p.3769.
101. Asylum Application Notes:
<http://www.asylumresearch.com/Applications/CantileverCal/CantileverCal.shtml>
102. Cleveland J.P., Manne S., Bocek D., Hansma P.K., "A nondestructive method for determining the spring constant of cantilevers for scanning force microscopy" *Rev.Sci.Instrum.* 64 (1993) p.403-405.
103. Sader J.E., Larson I., Mulvaney P., White L.R., "Method for the calibration of atomic force microscope cantilevers" *Rev.Sci.Instrum.* 66 (1995) p.3789.
104. Senden T.J., Ducker W.A., "Experimental determination of spring constants in atomic force microscopy" *Langmuir* 10 (1994) pp.1003-1004.
105. Maeda N., Senden T.J., "A method for the calibration of force microscopy cantilevers via hydrodynamic drag" *Langmuir* 16 (2000) pp.9282-9286.
106. Craig V.S.J., Neto C., "In situ calibration of colloid probe cantilevers in force microscopy: hydrodynamic drag on a sphere approaching a wall" *Langmuir* 17 (2001) pp.6018-6022.
107. Li Y.Q., Tao N.J., Pan J., Garcia A.A., Lindsay S.M., "Direct measurement of interaction forces between colloidal particles using the scanning force microscope" *Langmuir* 9 (1993) pp.637-641.
108. Torii A., Sasaki M., Hane K., Okuma S., "A method for determining the spring constant of cantilevers for atomic force microscopy" *Meas.Sci.Tech.* 7 (1996) p.179-185.
109. Press W.H., Flannery B.P., Teukolsky S.A., Vetterling W.T., "Numerical recipes in C: the art of scientific computing" Cambridge University Press, 1982.
110. Weissman M.B., "1/f noise and other slow, nonexponential kinetics in condensed matter" *Rev.Mod.Phys.* 60 (1988) pp.537-571.
111. Rios P.D.L., Zhang Y.-C., "Universal 1/f noise from dissipative self-organized criticality models" *Phys.Rev.Lett.* 82 (1999) pp.472-474.
112. Hutter J.L., Benchoefer J., "Calibration of atomic-force microscope tips" *Rev.Sci.Instrum.* 64 (1993) p.1868.

113. Butt H.J., Jaschke M., "Calculation of thermal noise in atomic force microscopy" *Nanotechnology* 6 (1995) pp.1-7.
114. Stark R.W., Drobek T., Heckl W.M., "Thermomechanical noise of a free v-shaped cantilever for atomic-force microscopy" *Ultramicroscopy* 86 (2001) pp.207-215.
115. Proksch R., Schäffer T.E., Cleveland J.P., Callahan R.C., Vivani M.B., "Finite optical spot size and position corrections in thermal spring constant calibration" *Nanotechnology* 15 (2004) pp.1344-1350.
116. Schäffer T.E., "Calculation of thermal noise in an atomic force microscope with a finite optical spot size" *Nanotechnology* 16 (2005) pp.664-670.
117. Sader J.E., White L., "Theoretical analysis of the static detection of plates for atomic force microscope applications" *J.Appl.Phys.* 74 (1993) pp.1-9.
118. Sader J.E., Chon J.W.M., Mulvaney P., "Calibration of rectangular atomic force microscope cantilevers" *Rev.Sci.Instrum.* 70 (1999) p.3967.
119. Sader J.E., "Frequency response of beams immersed in viscous fluids with applications to the atomic force microscope" *J.Appl.Phys* 84 (1998) p.64.
120. Calibration method of Sader, at Melbourne University,
<http://www.ampc.ms.unimelb.edu.au/afm/>
121. Doi M., "Introduction to polymer physics" Clarendon press, 1996.
122. Rubinstein M., Colby R.H., "Polymer physics", University press, 2003.
123. Marko J.F., Siggia E.D., "Stretching DNA", *Macromolecules* 28 (1995) p.8759.
124. Janshoff A., Neitzert M., Oberdörfer Y., Fuchs H., "Force spectroscopy of molecular systems – single molecule spectroscopy of polymers and biomolecules" *Angew.Chem.* 39 (2000) pp.3212-3237.
125. Margittai M., Widengren J., Schweinberger E., Schröder G. F., Felekyan S., Haustein E., König M., Fasshauer D., Grubmüller H., Jahn R., Seidel C.A.M., "Single-molecule fluorescence resonance energy transfer reveals a dynamic equilibrium between closed and open conformations of syntaxin 1" *Proc.Natl.Acad.Sci.U.S.A.* 100 (2003) pp.15516-15521.
126. Rothwell P.J., Berger S., Kensch O., Felekyan S., Antonik M., Wöhrl B.M., Restle T., Goody R.S., Seidel C.A.M., "Multiparameter single-molecule fluorescence spectroscopy reveals heterogeneity of HIV-1 reverse transcriptase: primer/template complexes" *Proc.Natl.Acad.Sci.U.S.A.* 100 (2003) pp.1655-1660.

127. Eggeling C., Widengren J., Rigler R., Seidel C.A.M., "Photobleaching of fluorescent dyes under conditions used for single-molecule detection: evidence of two-step photolysis" *Anal.Chem.* 70 (1998) pp.2651-2659.
128. Rigler R., Mets Ü., Widengren J., Kask P., *Eur.Biophys.J.* 22 (1993) pp.169-175.
129. Widengren J., Schweinberger E., Berger S., Seidel C.A.M., "Two new concepts to measure Fluorescence Resonance Energy Transfer via Fluorescence Correlation Spectroscopy: theory and experimental realizations" *J.Phys.Chem.A* 105 (2001) pp.6851-6866.
130. Datasheet for single photon counting module SPCM-AQR series, PerkinElmer, <http://optoelectronics.perkinelmer.com/content/Datasheets/SPCM-AQR.pdf>
131. Gaiduk A., Kühnemuth R., Antonik M., Seidel C.A.M., "Optical characteristics of atomic force microscopy tips for single-molecule fluorescence applications" *Chem.Phys.Chem.* 6 (2005) pp.976-983.
132. Semin D.J., Rowlen K.L., "Influence of vapour deposition parameters on SERS active Ag film morphology and optical properties" *Anal.Chem.* 66 (1994) pp.4324-4331.
133. Metzger S., Natesan M., Yanavich C., Schneider J., Lee G.U., "Development and characterization of surface chemistries for microfabricated biosensors" *J.Vac.Sci.Technol.A* 17 (1999) pp.2623-2628.
134. Rogers Y.-H., Jiang-Baucom P., Huang Z.-J., Bogdanov V., Anderson S., Boyce-Jacino M.T., "Immobilization of oligonucleotides onto a glass support via disulfide bonds: a method for preparation of DNA microarrays" *Anal.Biochem.* 266 (1999) pp.23-30.
135. Eggers M., Hogan M., Reich R.K., Lamture J., Ehrlicj D., Hollis M., Kosicki B., Powdrill T., Beattie K., Smith S., Varma R., Gangadharan R., Mallik A., Burke B., Wallace D., "A microchip for quantitative detection of molecules utilizing luminescent and radioisotope reporter groups" *BioTechniques* 17 (1994) pp.516-523.
136. Beaucage S.L., "Strategies in the preparation of DNA oligonucleotide array for diagnostic applications" *Current Medical Chemistry* 8 (2001) pp.1213-1244.
137. Zammattéo N., Jeanmart L., Hamels S., Courtois S., Louette P., Hevesi L., Remacle J., "Comparison between different strategies of covalent attachment of DNA to glass surfaces to build DNA microarrays" *Anal. Biochem.* 280 (2000) pp.143-150.
138. Chan V., McKenzie S.E., Surrey S., Fortina P., Graves D.J., "Effect of hydrophobicity and electrostatics on adsorption and surface diffusion of DNA oligonucleotides at liquid/solid interfaces" *J.Coll.Inter.Sci.* 203 (1998) pp.197-207.

139. Lösche M., "Protein monolayers at interfaces" *Current Opinion in Solid State and Material Science* 2 (1997) pp.546-556.
140. Wasserman S.R., Tao Y.-T., Whiteside G.M., "Structure and reactivity of alkylsiloxane monolayers formed by reaction of alkyltrichlorosilanes on silicon substrates" *Langmuir* 5 (1989) pp.1074-1087.
141. Tripp C.P., Hair M.L., "An infrared study of the reaction of octadecyltrichlorosilane with silica" *Langmuir* 8 (1992) pp.1120-1126.
142. Mellott N.P., Brantley S.L., Hamilton J.P., Pantano C.G., "Evaluation of surface preparation methods for glass" *Surface and interface analysis* 31 (2001) pp.362-368.
143. Bikermann J.J., "Surface chemistry. Theory and applications" NewYork 1958.
144. Meyer E., Haefke H., Güntherod H.-J., Anderson O., Bange K., "Surface topography of polished and oxide-coated BK-7 glasses investigated by atomic force microscopy" *Glastech. Ber.* 66 (1993) pp.30-37.
145. Radlein E., Frischat G.H., "Atomic force microscopy as a tool to correlate nanostructure to properties of glasses" *J. Non-Crystalline Solids* 222 (1997) pp.69-82.
146. Eske L.D., Galipeau D.W., "Characterization of SiO₂ surface treatments using AFM, contact angles and novel dewpoint technique" *Colloids and Surfaces A* 154 (1999) pp.33-51.
147. Gupta P.K., Inniss D., Kurkjian C,R,m Zhong Q., "Nanoscale roughnes of oxide glass surfaces" *J.Non-Crystalline Solids* 262 (2000) pp.200-206.
148. Torres D.B., Pantano C.G., Barnes A., "Coating and etching glass substrates for DNA microarray" National nanofabrication users network, Penn State Nanofabrication facility, pp. 40-41.
149. Vigil, Xu Z., Steinberg S., Israelachvili J., "Interactions of silica surfaces" *J. of Colloid and Interface Science* 165 (1994) pp.367-385.
150. McGraw-Hill Annual Review of Technology covering all forms of CO₂ cleaning.
151. Schweinberger E., Berger S., personal communication, 2001.
152. Allemand J.-F., Bensimon D., Jullien L., Bensimon A., Croquette V., "pH-dependent specific binding and combing of DNA" *Biophysical J.* 73 (1997) pp.2064-2070.
153. Ha T., "Single-molecule fluorescence resonance energy transfer" *Methods* 25 (2001) pp.78-86.
154. Pavlovich E., Quist A.P., Gelius U., Oscarsson S., "Surface functionalization of silicon oxide at room temperature and atmospheric pressure" *J. of Colloid and Interface Science* 254 (2002) pp.200-203.

155. Roberts M.J., Bentley M.D., Harris J.M., "Chemistry for peptide and protein PEGylation" *Adv.DrugDeliv.Reviews* 54 (2002) pp.459-476.
156. Löcher F., Ruckstuhl T., Jaworek T., Wegner G., Seeger S., "Immobilization of biomolecules on Langmuir-Blodgett films of regenerative cellulose derivatives" *Langmuir* 14 (1998) pp.2786-2789.
157. Piehler J., Brecht A., Valiokas R., Leidberg B., Gauglitz G., "A high-density poly(ethylene glycol) polymer brush for immobilization on glass-type surfaces" *Biosensors and Bioelectronics* 15 (2000) pp.473-481.
158. Rivetti C., Guthold M., Bustamante C., "Scanning force microscopy of DNA deposited onto mica: equilibration versus kinetic trapping studied by statistical polymer chain analysis" *J.Mol.Biol.* 264 (1996) pp.919-932.
159. Rippe K., Mücke N., Langowski J., "Molecules in motion_ imaging DNA with the scanning force microscope in aqueous solution" *Bioforum Intern.* 1 (1997) pp.42-44.
160. Dahlgren P.R., Lubchenko Y.L., "Atomic force microscopy study of the effects of Mg^{2+} and other divalent cations on the end-to-end DNA interactions" *Biochemistry* 41 (2002) pp.11372-11378.
161. Balladur V., Theretz A., Mandrand B., "Determination of the main forces driving DNA oligonucleotide adsorption onto aminated silica wafers" *J.Coll.Inter.Sci.* 194 (1997) pp.408-418.
162. Belosludtsev Y., Iverson B., Lemeshko S., Eggers R., Wiese R., Lee S., Powdrill T., Hogan M., "DNA microarrays based on noncovalent oligonucleotide attachment and hybridization in two dimensions" *Anal.Biochem.* 292 (2001) pp.250-256.
163. Ferguson J.A., Boles T.C., Adams C.P., Walt D.R., "A fiber-optic DNA biosensor microarray for the analysis of gene expression" *Nature Biotech.* 14 (1996) pp.1681-1684.
164. Ji M., Hou P., Lu Z., He N., "Covalent immobilization of DNA onto functionalized mica for atomic force microscopy" *J.Nanosci.Nanotech.* 6 (2004) pp.580-583.
165. Abney J.R., Scalettar B.A., Thompson N.L., "Evanescent interference patterns for fluorescence microscopy" *Biophys.J.* 61 (1992) p.542-552.
166. Kramer A., Trabesinger W., Hetch B., Wild U.P., "Optical near-field enhancement at a metal tip probed by a single fluorophore" *Appl.Phys.Lett.* 80 (2002) pp.1652-1654.
167. Trabesinger W., Kramer A., Kreiter M., Hecht B., Wild U.P., "Single-molecule near-field optical energy transfer microscopy with dielectric tips" *J.Microscopy* 209 (2003) pp.249-253.

168. Azoulay J., Debarre A., Richard A., Tchenio P., "Field enhancement and apertureless near-field optical spectroscopy of single molecules" *J.Microscopy* 194 (1999) pp.486.
169. Fluorescein equivalents in our yellow-green-fluorescent FluoSpheres beads. Handbook <http://probes.invitrogen.com/handbook/tables/0731.html>
170. Kinoshita S., Kushida T., "Subnanosecond of fluorescence-lifetime measuring system using single photon counting method with mode-locked laser excitation" *Rev.Sci.Instrum.* 52 (1981) pp.572-575.
171. Viera G., Huet S., Boufendi L., "Effects of ion energy on the crystal size and hydrogen bonding in plasma-deposited nanocrystalline silicon thin films" *J.Appl.Phys.* 90 (2001) pp.4175-4183.
172. Koshioka M., Sasaki K., Masuhara H., "Time-dependent fluorescence depolarization analysis in three-dimensional microspectroscopy" *Appl.Spectrosc.* 49 (1995) pp.224-228.
173. Krimmel, E. F. and Hockings, E. F. Schöberg, D. 8[Silicon B5b2]. 1997. Berlin, Heidelberg, New York, Springer Verlag. Gmelin Handbook of Inorganic Chemistry.
174. Mo C.-M., Zhang L., Xie C., Wang T., "Luminescence of nanometer-sized amorphous silicon nitride solids" *J.Appl.Phys.* 73 (1993) pp.5185-5188.
175. Price K.J., McNeil L.E., Suvkanov A., Irene E.A., MacFarlane P. J., Zvanut M.E., "Characterization of the luminescence center in photo- and electroluminescent amorphous silicon oxynitride films" *J.Appl.Phys.* 86 (1999) pp.2628-2637.
176. Khriachtchev L., Heikkila L., Kuusela T., "Red photoluminescence of gold island films" *Appl.Phys.Lett.* 78 (2001) pp.1994-1996.
177. Maus M., Cotlet M., Hofkens J., Gensch T., De Schryver F.C., Schaffer J., Seidel C.A.M., "An experimental comparison of the Maximum Likelihood Estimation and Nonlinear Least-Squares fluorescence lifetime analysis of single molecules" *Anal.Chem.* 73 (2001) pp.2078-2086.
178. Haas E., "The study of protein folding and dynamics by determination of intramolecular distance distributions and their fluctuations using ensemble and single-molecule FRET measurements" *ChemPhysChem* 6 (2005) pp.858-870.
179. Dahan M., Deniz A.A., Ha T.J., Chemla D.S., Schultz P.G., Weiss S., "Temporal fluctuations of fluorescence resonance energy transfer between two dyes conjugated to a single protein" *Chem.Phys.* 247 (1999) pp.85-106.
180. Kapanidis A.N., Laurence T.A., Lee N.K., Margeat E., Kong X.X., Weiss S., "Alternating-Laser excitation of single molecules" *Acc.Chem.Res.* 38 (2005) pp.523.

181. Lu H.P., "Probing single-molecule protein conformational dynamics" *Acc.Chem.Res.* 38 (2005) pp.557-565.
182. Ha T., Enderle T., Ogletree D.F., Chemla D.S., Selvin P.R., Weiss S., "Probing the interaction between two single molecules: fluorescence resonance energy transfer between a single donor and a single acceptor" *Proc.Natl.Acad.Sci.U.S.A.* 93 (1996) pp.6264-6268.
183. Dietz H., Rief M., "Protein structure by mechanical triangulation" *Proc.Natl.Acad.Sci.U.S.A.* 103 (2006) pp.1244-1247.
184. van der Meer, B. W.; Cooker, G.; Chen, S. Y. *Resonance Energy Transfer: Theory and Data*, VCH Publishers: New York, 1994.
185. Diez M., Zimmermann B., Börsch M., König M., Schweinberger E., Steigmiller S., Reuter R., Felekyan S., Kudryavtsev V., Seidel C.A.M., Gräber P., "Proton powered subunit rotation in single membrane-bound F₀F₁-ATP synthase" *Nat.Struct.Mol.Biol.* 11 (2004) pp.135-141.
186. Schuler B., Lipman E.A., Eaton W.A., "Probing the free-energy surface for protein folding with single-molecule fluorescence spectroscopy" *Nature* 419 (2002) pp.743-747.
187. Schuler B., Lipman E.A., Steinbach P.J., Kumke M., Eaton W.A., "Polyproline and the "spectroscopic ruler" revisited with single-molecule fluorescence" *Proc.Natl.Acad.Sci.U.S.A.* 102 (2005) pp.2754-2759.
188. Xie Z., Srividya N., Sosnick T.R., Pan T., Scherer N.F., "Single-molecule studies highlight conformational heterogeneity in the early folding steps of a large ribozyme" *Proc.Natl.Acad.Sci.U.S.A.* 101 (2004) pp.534-539.
189. Deniz A.A., Dahan M., Grunwell J.R., Ha T.J., Faulhaber A.E., Chemla D.S., Weiss S., Schultz P.G., "Single-pair fluorescence resonance energy transfer on freely diffusing molecules: Observation of Forster distance dependence and subpopulations" *Proc.Natl.Acad.Sci.U.S.A.* 96 (1999) pp.3670-3675.
190. Gopich I., Szabo A., "Photon counting histograms for diffusing fluorophores" *J.Chem.Phys.B* 109 (2005) pp.17683-17688.
191. Antonik M., Felekyan S., Gaiduk A., Seidel C.A.M., "Separating structural heterogeneities from stochastic variations in fluorescence resonance energy transfer distributions via photon distribution analysis" *J.Phys.Chem.* 110 (2006) pp.6970-6978.
192. Fries J.R., Brand L., Eggeling C., Köllner M., Seidel C.A.M., "Quantitative identification of different single molecules by selective time-resolved confocal

- fluorescence spectroscopy” *J.Phys.Chem.A* 102 (1998) pp.6601-6613.
193. Parkhurst L.J., Parkhurst K.M., Powell R., Wu J., Williams S., “Time-resolved fluorescence resonance energy transfer studies of DNA bending in double-stranded oligonucleotides and in DNA-protein complexes” *Biopolymers* 61 (2002) pp.180-200.
 194. Laurence T.A., Kong X., Jäger M., Weiss S., *Proc.Natl.Acad.Sci.U.S.A.* 102 (2005) Supporting Appendixes.
 195. Watkins L.P., Yang H., “Information bounds and optimal analysis of dynamic single molecule measurements” *Biophys.J.* 86 (2004) pp.4015-4029.
 196. Eggeling C., Widengren J., Brand L., Schaffer J., Felekyan S., Seidel C.A.M., “Analysis of photobleaching in single-molecule multicolor excitation and Förster Resonance Energy Transfer measurements” *J.Phys.Chem.A* 110 (2006) pp.2979-2995.
 197. Heilemann M., Margeat E., Kasper R., Sauer M., Tinnefeld P., “Carbocyanine dyes as efficient reversible single-molecule optical switch” *J.Am.Chem.Soc.* 127 (2005) pp.3801-3806.
 198. Bates M., Blosser T.R., Zhuang X., “Short-range spectroscopic ruler based on a single-molecule optical switch” *Phys.Rev.Lett.* 94 (2005) p.108101.
 199. Widengren J., Schwille P., “Characterization of Photoinduced Isomerization and Back-Isomerization of the Cyanine Dye Cy5 by Fluorescence Correlation Spectroscopy” *J.Phys.Chem.A* 104 (2000) pp.6416-6428.
 200. Böhmer M., Wahl M., Rahn H.J., Erdmann R., Enderlein J., “Time-resolved fluorescence correlation spectroscopy” *Chem.Phys.Lett.* 353 (2002) pp.439-445.
 201. Ha T., Xu J., “Photodestruction intermediates probed by an adjacent reporter molecule” *Phys.Rev.Lett.* 90 (2003) pp.223002-1-223002-4.
 202. Schweinberger E., “Multidimensionale einzelmolekül-fluoreszenz-spektroskopie von fluoreszenzmarkierten biomolekülen”, Dissertation, Göttingen 2002.
 203. Laurence T.A., Kong X., Jäger M., Weiss S., “Probing structural heterogeneities and fluctuations of nucleic acids and denaturated proteins” *Proc.Natl.Acad.Sci.U.S.A.* 102 (2005) pp.17348-17353.
 204. Origin help: www.originlab.com
 205. Clausen-Schaumann H., Rief M., Tolksdorf C., Gaub H.E., “Mechanical stability of single DNA molecules” *Biophys.J* 78 (2000) pp.1997-2007.
 206. Anselmetti D., Fritz J., Smith B., Fernandez-Busquets X., “Single molecule DNA biophysics with atomic force microscopy” *Single Mol.* 1 (2000) pp.53-58.
 207. Asylum Research: www.asylumresearch.com/ImageGallery/Litho/Litho.shtml#7

208. Yuan C., Chen A., Kolb P., Moy V.T., "Energy landscape of streptavidin-biotin complexes measured by atomic force microscopy" *Biochemistry* 39 (2000) pp.10219-10223.
209. Wong J., Chilkoti A., Moy V.T., "Direct force measurements of the streptavidin-biotin interaction" *Biomol.Engineering* 16 (1999) pp.45-55.
210. Eric W. Weisstein. "Fast Fourier Transform." From [MathWorld](http://mathworld.wolfram.com/FastFourierTransform.html), A Wolfram Web Resource. <http://mathworld.wolfram.com/FastFourierTransform.html>
211. Bustamante C., Smith S.B., Liphardt J., Smith D., "Single-molecule studies of DNA mechanics" *Curr.Opin.Struct.Biol.* 10 (2000) pp.523-543.
212. Strick T.R., Dessinges M.-N., Charvin G., Dekker N.H., Allemand J.-F., Bensimon D., Croquette V., "Stretching of macromolecules and proteins" *Rep.Prog.Phys.* 66 (2003) pp.R1-R45.
213. Konrad M.W., Bolonick J.I., "Molecular dynamics simulation of DNA stretching is consistent with the tension observed for extension and strand separation and predicts a novel ladder structure" *J.Am.Chem.Soc.* 118 (1996) pp.10989-10994.
214. Lebrun A., Lavery R., "Modelling extreme stretching of DNA" *Nuc.Acid.Res.* 24 (1996) pp.2260-2267.
215. Rief M., Clausen-Schaumann H., Gaub H.E., "Sequence-dependent mechanics of single DNA molecules" *Nature Struc. Biology* 6 (1999) 346-349.
216. Williams M.C., Wenner J.R., Rouzina I., Bloomfield V.A., "Effect of pH on the overstretching transition of double-stranded DNA: evidence of force-induced DNA melting" *Biophys.J.* 80 (2001) pp.874-881.
217. Wenner J.R., Williams M.C., Rouzina I., Bloomfield V.A., "Salt dependence of the elasticity and overstretching transition of single DNA molecule" *Biophys.J.* 82 (2002) pp.3160-3169.
218. Smith S.B., Cui Y., Bustamante C., "Overstretching B-DNA: the elastic response of individual double-stranded and single-stranded DNA molecules" *Science* 271 (1996) pp.795-799.
219. Wang M., Yin H., Landick R., Gelles J., Block S.M., "Stretching DNA with optical tweezers" *Biophysical J.* 72 (1997) pp.1335-1346.
220. Zhou H., Zhang Y., Ou-Yang Z., "Elastic property of single double-stranded DNA molecules: theoretical study and comparison with experiments" *Phys.Rev.E* 62 (2000) pp.1045-1058.

221. Sischka A., Toensing K., Eckel R., Wilking S.D., Sewald N., Ros R., Anselmetti D., "Molecular mechanisms and kinetics between DNA and DNA binding ligands" *Biophysical J.* 88 (2005) pp.404-411.
222. Ros R., Eckel R., Bartels F., Sischka A., Baumgarth B., Wilking S.D., Pühler A., Sewald N., Becker A., Anselmetti D., "Single molecule force spectroscopy on ligand-DNA complexes: from molecular binding mechanisms to biosensor applications" *J.Biotechnology* 112 (2004) p.5-12.
223. Eckel R., Ros R., Wilking S.D., Sewald N., Anselmetti D., "Identification of binding mechanisms in single molecule-DNA complexes" *Biophysical J.* 85 (2003) pp.1968-1973.
224. Hursale S., Grange W., Hegner M., "DNA mechanics affected by small DNA interacting ligands" *Single Mol.* 2-3 (2002) pp.91-96.
225. Krautbauer R., Clausen-Schaumann H., Gaub H.E., "Cisplatin changes the mechanics of single DNA molecules" *Angew.Chem.Int.Ed.* 39 (2000) pp.3912-3915.
226. Krautbauer R., Pope L.H., Schrader T.E., Allen S., Gaub H.E., "Discriminating small molecules DNA binding modes by single molecule force spectroscopy" *FEBS Lett.* 510 (2002) pp.155-158.
227. Krautbauer R., Fischerländer S., Allen S., Gaub H.E., "Mechanical fingerprinting of DNA drug complexes" *Single Molecules.* 2-3 (2002) pp.97-103.
228. Zipper H., Brunner H., Bernhagen J., Vitzthum F., "Investigations on DNA intercalation and surface binding by SYBR Green I, its structure determination and methodological implications" *Nucleic Acids Research* 32 (2004) p.e103.
229. Cosa G., Focsaneanu K.-S., McLean J.R.N., McNamee J.P., Scaiano J.C., "Photophysical properties of fluorescent DNA-dye bound to single and double-stranded DNA in aqueous buffered solution" *Photochem.Photobiol.* 73 (2001) pp.585-599.
230. Stevens M.M., Allen S., Davies M.C., Roberts C.J., Schacht E., Tendler S.J.B., VanSteenkiste S., Williams P.M., "The development, characterization and demonstration of a versatile immobilization strategy for biomolecular force measurements" *Langmuir* 18 (2002) pp.6659-6665.
231. Biebricher A., Paul A., Tinnefeld P., Gölzhäuser A., Sauer M., "Controlled three-dimensional immobilization of biomolecules on chemically patterned surfaces" *J.Biotechnology* 112 (2004) pp.97-107.

Appendix A: solid substrates AFM imaging statistics

sample (details in Section 2.3)	figure#	field of view [μm]	mean height [nm]	Rp-v [nm]	RMS [nm]
quartz test sample from Olympus	2-2	7.5 \times 7.5	2.1	85.93	3.4
quartz test sample from Olympus	2-3	7.5 \times 7.5	1.2	8.26	1.35
glass from Mendel	2-4	7.5 \times 7.5	0.6	12.3	0.73
quartz test sample from Mendel	2-5	7.5 \times 7.5	1.0	42.69	1.18
glass cleaned via A (see Table 2-8)	2-6	7.5 \times 7.5	0.7	17.93	0.81
glass cleaned via B (see Table 2-8)	2-7	7.5 \times 7.5	0.6	5.48	0.65
glass cleaned via C (see Table 2-8)	2-8	1.0 \times 1.0	0.28	1.69	0.32
quartz cleaned via D (see Table 2-8)	2-9	7.5 \times 7.5	0.53	1.44	0.55
glass cleaned via E (see Table 2-8)	2-10	6 \times 6	1.1	4.49	1.23
Dicarboxy-PEG modified glass	2-14 left	7.5 \times 7.5	1.7	57.9	2.57
Dicarboxy-PEG modified glass	2-14 right	0.9 \times 0.9	0.56	2.19	0.61
Carboxy-Methoxy-PEG glass	2-15 left	2.0 \times 2.0	1.9	22.3	4.35
Carboxy-Methoxy-PEG glass	2-15 right	0.5 \times 0.5	0.2	12.5	1.5
Amino-Hydroxy-PEG glass	2-16 left	7.5 \times 7.5	1.4	68.3	2.6
Amino-Hydroxy-PEG glass	2-16 right	1.04 \times 1.04	0.67	2.3	0.72
Amino-Methoxy-PEG glass	2-17 left	7.5 \times 7.5	4.2	15.5	9.7
Amino-Methoxy-PEG glass	2-17 right	1.65 \times 1.65	0.58	3.7	0.62
Diamino-PEG modified glass	2-18 left	7.5 \times 7.5	3.2	14.2	5.9
Diamino-PEG modified glass	2-18 right	1.15 \times 1.15	3.4	2.0	0.37
MMI LB8 BioChip	2-19 left	7.5 \times 7.5	3.5	46.1	4.1
MMI LB8 BioChip	2-19 right	2.0 \times 2.0	3.9	24.3	4.3
λ -DNA molecules adsorbed on mica	2-20 left	5.0 \times 5.0	0.69	5.3	0.84
λ -DNA molecules adsorbed on mica	2-20 right	0.95 \times 0.95	0.69	3.8	0.82
λ -DNA adsorbed on APTES glass	2-21 left	7.5 \times 7.5	0.57	38.3	1.0
λ -DNA adsorbed on APTES glass	2-21 right	7.5 \times 7.5	1.3	44.5	2.1

The image analysis is performed with the commercial PicoScan software. Prior to calculations, all images were levelled (corrected for sample tilt) in the same manner.

Appendix B: Apparent fluorescence efficiency probability density

In the following appendix transformations of equation 2–20 in the text are shown:

$$f_{\varepsilon}(\varepsilon) = f_R(R_{DA}(\varepsilon)) \frac{dR_{DA}(\varepsilon)}{d\varepsilon} \quad (\text{A. 1})$$

The probability density $f_R(R_{DA})$ for the donor-acceptor distance in the assumption of the Gaussian distribution is given by equation 2–15 as follows:

$$f_R(R_{DA}) = \frac{1}{\sqrt{2\pi}\sigma_R} \exp\left[-\frac{1}{2\sigma_R^2}(R_{DA} - \bar{R}_{DA})^2\right] \quad (\text{A. 2})$$

where \bar{R}_{DA} is the mean value and $\sigma_R = \sqrt{R_{DA}^2 - \bar{R}_{DA}^2}$ is the standard deviation for the Gaussian distribution.

The apparent fluorescence efficiency is given by equation 2–17 as follows:

$$\varepsilon = \varepsilon(R_{DA}) = 1 - \frac{1}{1 + \alpha + \frac{\Phi_{FA}g_R}{\Phi_{FD}g_G} \left(\frac{R_0}{R_{DA}}\right)^6} \quad (\text{A. 3})$$

From the above equation R_{DA} can be expressed as a function of ε in the following steps:

$$\frac{1}{1 - \varepsilon} = 1 + \alpha + \frac{\Phi_{FA}g_R}{\Phi_{FD}g_G} \left(\frac{R_0}{R_{DA}}\right)^6$$

Rearranging brings to equation 2–18 in Section 2.5.1.2:

$$R_{DA} = R_0 \left[\frac{\Phi_{FD}g_G}{\Phi_{FA}g_R} \left(\frac{1}{1 - \varepsilon} - 1 - \alpha \right) \right]^{-1/6} \quad (\text{A. 4})$$

Thus the derivative $\frac{dR_{DA}(\varepsilon)}{d\varepsilon}$ can be calculated as follows:

$$\begin{aligned} \frac{dR_{DA}(\varepsilon)}{d\varepsilon} &= R_0 \left(\frac{\Phi_{FD}g_G}{\Phi_{FA}g_R} \right)^{1/6} \left(-\frac{1}{6} \right) \left[\frac{1}{1 - \varepsilon} - 1 - \alpha \right]^{-7/6} \frac{1}{(1 - \varepsilon)^2} \cdot (-1) \cdot (-1) = \\ &= -\frac{R_0}{6} \left(\frac{\Phi_{FD}g_G}{\Phi_{FA}g_R} \right)^{1/6} \left[\frac{1}{1 - \varepsilon} - 1 - \alpha \right]^{-7/6} \frac{1}{(1 - \varepsilon)^2} \end{aligned} \quad (\text{A. 5})$$

Inserting parts of (A. 4) into (A. 2) gives the following equation:

$$f_R(R_{DA}(\varepsilon)) = \frac{1}{\sqrt{2\pi}\sigma_R} \exp \left[-\frac{1}{2\sigma_R^2} \left(R_0 \left[\frac{\Phi_{FD}g_G}{\Phi_{FA}g_R} \left(\frac{1}{1-\varepsilon} - 1 - \alpha \right) \right]^{-1/6} - \bar{R}_{DA} \right)^2 \right] \quad (\text{A. 6})$$

Combination of equations (A. 6) and (A. 5) in equation (A. 1) gives the final expression for the apparent fluorescence efficiency probability density $f_\varepsilon(\varepsilon)$:

$$f_\varepsilon(\varepsilon) = \frac{R_0}{6\sqrt{2\pi}\sigma_R} \left(\frac{\Phi_{FA}g_R}{\Phi_{FD}g_G} \right)^{1/6} \frac{1}{(1-\varepsilon)^2} \left(\frac{1}{1-\varepsilon} - (1+\alpha) \right)^{-7/6} \times \exp \left\{ -\frac{1}{2\sigma_R^2} \left[R_0 \left(\frac{\Phi_{FA}g_R}{\Phi_{FD}g_G} \right)^{1/6} \left(\frac{1}{1-\varepsilon} - (1+\alpha) \right)^{-1/6} - \bar{R}_{DA} \right]^2 \right\} \quad (\text{A. 7})$$

The above obtained equation (A. 7) is identical to equation 2–21 in the text and used for further calculations.

Appendix C: Fluorescence ratio probability density

The probability density $f_R(R_{DA})$ for the donor-acceptor distance (R_{DA}) in the assumption of Gaussian distribution is given by equation 2–15:

$$f_R(R_{DA}) = \frac{1}{\sqrt{2\pi}\sigma_R} \exp\left[-\frac{1}{2\sigma_R^2}(R_{DA} - \bar{R}_{DA})^2\right] \quad (\text{A. 8})$$

where \bar{R}_{DA} is the mean value and $\sigma_R = \sqrt{R_{DA}^2 - \bar{R}_{DA}^2}$ is the standard deviation for the Gaussian distribution.

Consider two variables Ψ and Ω , defined as the functions $\varphi|_{linear}$ and $\varphi|_{\log}$ of R_{DA} :

$$\Psi = \varphi|_{linear}(R_{DA}) = \frac{1}{a} \left(\frac{R_{DA}}{R_0} \right)^6 \quad (\text{A. 9})$$

$$\Omega = \varphi|_{\log}(R_{DA}) = \log\left(\frac{1}{a} \left(\frac{R_{DA}}{R_0} \right)^6 \right) \quad (\text{A. 10})$$

where a and R_0 are constants.

R_{DA} can be expressed by the inverse functions of Ψ and Ω :

$$R_{DA}(\Psi) = a^{\frac{1}{6}} R_0 (\Psi)^{\frac{1}{6}} \quad (\text{A. 11})$$

$$R_{DA}(\Omega) = a^{\frac{1}{6}} R_0 \cdot 10^{\frac{1}{6}\Omega} \quad (\text{A. 12})$$

Since $R_{DA}(\Psi)$ and $R_{DA}(\Omega)$ is an unambiguous continuous function of Ψ and Ω , the probabilities that the distance is in the interval from R_{DA} to $R_{DA} + dR_{DA}$ are identical to the probabilities that Ψ and Ω are in the intervals from Ψ to $\Psi + d\Psi$ and Ω to $\Omega + d\Omega$ respectively:

$$dP\{\Psi, \Psi + d\Psi\} = dP\{R_{DA}, R_{DA} + dR_{DA}\} \quad (\text{A. 13})$$

$$dP\{\Omega, \Omega + d\Omega\} = dP\{R_{DA}, R_{DA} + dR_{DA}\} \quad (\text{A. 14})$$

Accordingly, for probability densities for distributions of Ψ and Ω can be written as follows:

$$f(\Psi) = f_R(R_{DA}(\Psi)) \frac{dR_{DA}(\Psi)}{d\Psi} \quad (\text{A. 15})$$

$$f(\Omega) = f_R(R_{DA}(\Omega)) \frac{dR_{DA}(\Omega)}{d\Omega} \quad (\text{A. 16})$$

The derivatives for the case of Ψ and Ω ratios will be:

$$\frac{dR_{DA}(\Psi)}{d\Psi} = \frac{d}{d\Psi} \left(a^{\frac{1}{6}} R_0 (\Psi)^{\frac{1}{6}} \right) = \frac{1}{6} a^{\frac{1}{6}} R_0 (\Psi)^{-\frac{5}{6}} \quad (\text{A. 17})$$

$$\frac{dR_{DA}(\Omega)}{d\Omega} = \frac{d}{d\Psi} \left(a^{\frac{1}{6}} R_0 \cdot 10^{\frac{1}{6}\Omega} \right) = a^{\frac{1}{6}} R_0 \cdot 10^{\frac{1}{6}\Omega} \cdot \ln 10 \quad (\text{A. 18})$$

That leads us to the analytical equations for the probability densities $f(\Psi)$ and $f(\Omega)$, containing parameters \bar{R}_{DA} and σ_R from the initial Gaussian probability density distribution of the donor-acceptor separation:

$$f(\Psi) = \frac{1}{6\sqrt{2\pi}\sigma_R} a^{\frac{1}{6}} R_0 (\Psi)^{-\frac{5}{6}} \exp \left[-\frac{1}{2\sigma_R^2} \left(a^{\frac{1}{6}} R_0 (\Psi)^{\frac{1}{6}} - \bar{R}_{DA} \right)^2 \right] \quad (\text{A. 19})$$

$$f(\Omega) = \frac{\ln 10}{6\sqrt{2\pi}\sigma_R} a^{\frac{1}{6}} R_0 \cdot 10^{\frac{1}{6}\Omega} \cdot \exp \left[-\frac{1}{2\sigma_R^2} \left(a^{\frac{1}{6}} R_0 \cdot 10^{\frac{1}{6}\Omega} - \bar{R}_{DA} \right)^2 \right] \quad (\text{A. 20})$$

APPENDIX D: FRET ratio histograms background correcting procedure for PDA

Atto590, D-only labelled DNA and donor-acceptor labelled DNA (DA-13) were corrected for background counts originating from the buffer solution. Background histograms were generated from the buffer-only measurement using the same selection and binning parameters as for the data, and were subtracted from data histograms. Background corrected data histograms were used for comparison with the PDA and results are presented in Figure 2-49, Figure 2-54, Figure 2-56. The total counts in these background histograms were $\sim 10^2$ time windows, whereas the data histogram contained $\sim 10^4$ time windows. Therefore, the background signal and resulting correction cannot account for any of the deviations between the data and the PDA histograms shown in the main text.

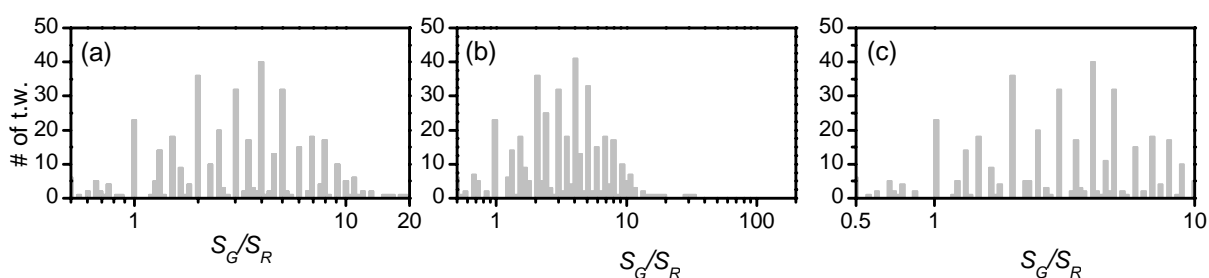


Figure A-1. Histograms calculated from buffer solutions used for single molecule fluorescence experiments with Atto590, showing the number of time windows which have a given signal ratio value (a), D-only (Alexa488) labelled DNA (b) and donor-acceptor labelled DNA (DA-13) (c) molecules. # of t.w. is a number time windows abbreviation.

Appendix E: Description of custom-written software

Hardware control and analysis programs described in the following appendix are written in the Windows-based development package LabView, version 7 (National Instruments) and MatLab, version 6.5 (MathWorks). Experimental data were prepared for the presentation in Origin, version 7.5 (OriginLab Corporation, Northampton, MA).

ControlPI

ControlPI is the LabView based, custom-written program which allows 3 axis piezo and acusto-optical modulator (laser power adjustment) control via RS232 connection.

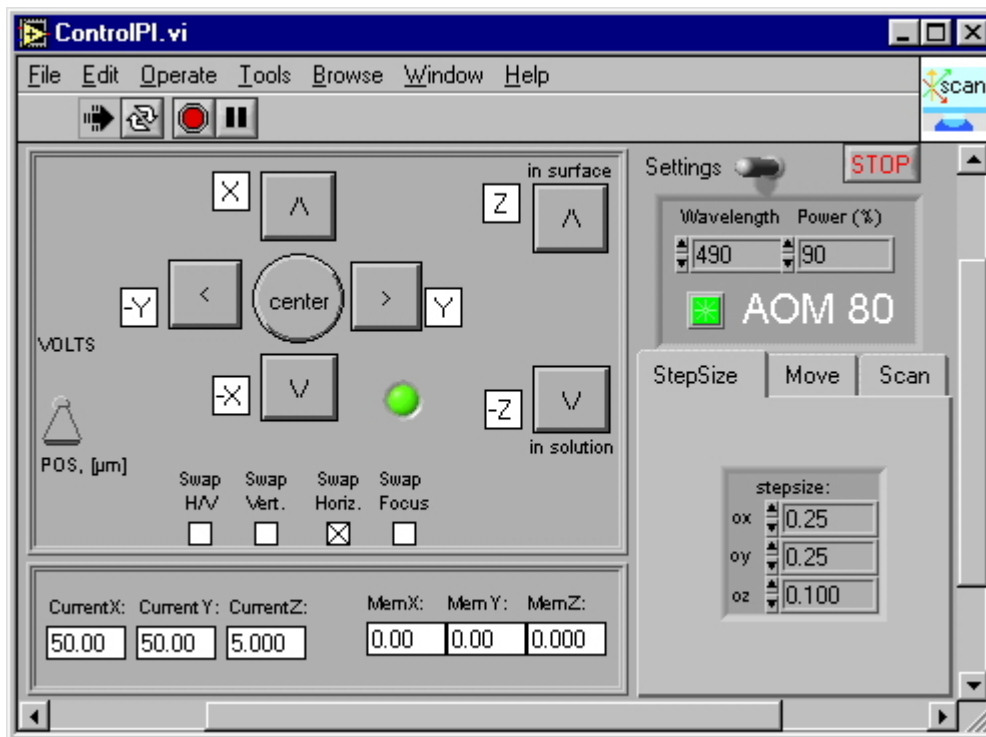


Figure A–2. Control panel of the ControlPI program, controlling piezos and acusto-optical modulator.

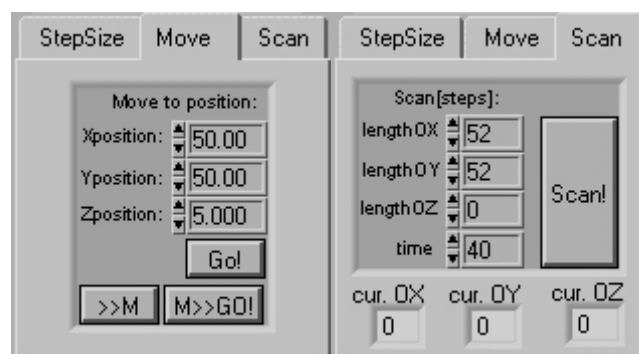


Figure A–3. Piezos can be moved manually (keyboard or mouse) with adjustable step size (StepSize tab) and to a specified position (Move tab). Piezo position can also be kept in a memory and restored. Automatic scanning mode is realized in Scan tab.

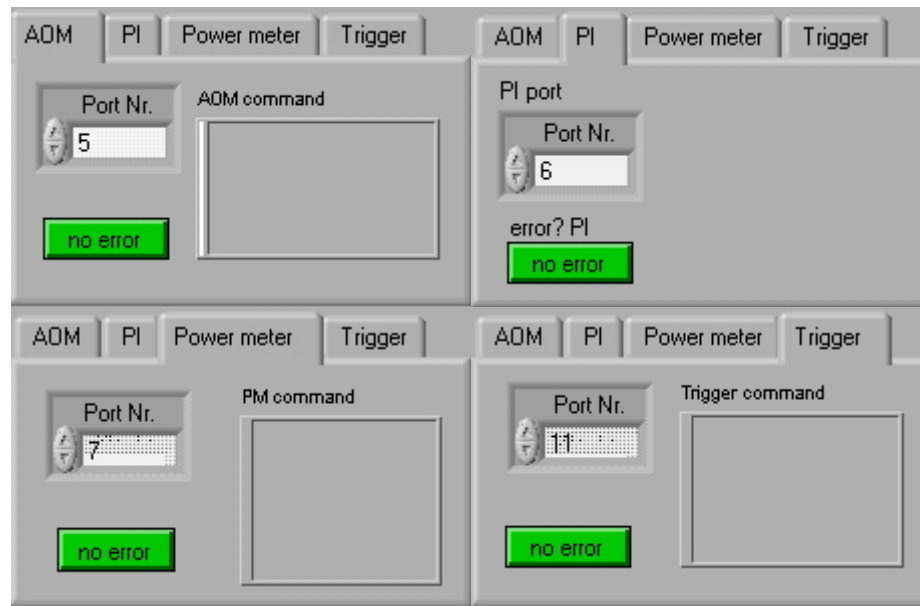


Figure A-4. Computer and hardware communication settings tabs. Different ports represented are for acusto-optical modulator (AOM tab), piezo controller (PI tab), power meter (Power meter tab) and synchronization signal for the SPC card and confocal imaging (Trigger tab).

Modular system of ControlPI program makes it easy to incorporate different communication protocol for different devices. LabView provides a simple basis for other hardware integration (for example a CCD controller).

Imaging control with AFM scripting

Listing of the custom script “TIP fluorescenceSpsSETUP1.vbs”

```

Option Explicit                                     'It's a good idea to use option explicit
                                                    to reduce obscure bugs.

Dim PicoScan                                       'Declare the PicoScan variable
Set PicoScan = CreateObject("PicoScan")           'and place a reference to the
                                                    program in it.

Dim i, N, OffsetBegin, ForceSetPointStep, OffsetValue, msg, PausePeriod,
OffsetValueBegin, PreSweepdelay, theInput, ret
'
'using this script:
'1. one should disconnect "Z-in" input of AFM controller from BIAS output on AFM
break-up box
'2. align cantilever, approach and align optical part
'3. open manually sample to have max piezo range for tip-movement (afmm1251 - apr.-
4200/-3500nm)
'4. find surface again optimizing tip position with reasonably small ServoRange
(500-200nm)
'5. set ServoRange to minimum value and put ServoOffset from SertainValue to "0"
to get the tip "SertainValue" nm away from surface
'6. Put Force Setpoint to "0" and connect "Z-in" input of AFM controller to BIAS
output on AFM break-up box
'7. start the script
'
OffsetValueBegin = PicoScan.ServoOffset           'saving relative position of
                                                    the surface

ret = vbNo
While ret = vbNo
    theInput = InputBox("input PreSweepDelay, (ms)")
    PreSweepdelay = (theInput + 10)/1000          ' + sweepduration time
    theInput = InputBox("input ForceSetpoint step, (V)")
    ForceSetPointStep = theInput
    theInput = InputBox("input number of steps for ForceSetpoint")
    N = theInput
    ReDim ForceSetPointValue(N)
    ReDim OffsetValue(N)
    OffsetValue(1) = OffsetValueBegin
    ForceSetPointValue(1) = 0
    For i = 2 to N
        ForceSetPointValue(i) = ForceSetPointValue(i-1) - ForceSetPointStep
        OffsetValue(i) = OffsetValue(i-1) - 425.6175*ForceSetPointValue(i) + 11.7987
    Next

```

```

msg = msg & "TipFluorescence" & Chr(10)
msg = "      PreSweepDelay: " & PreSweepdelay & " (sec)"& Chr(10)
msg = msg & "ForceSetpoint step: " & ForceSetPointStep & " (V)"& Chr(10)
msg = msg & "      number of steps: " & N & Chr(10)
msg = msg & "" & Chr(10)
msg = msg & "SetPoint and Offset Values" & Chr(10)
For i = 1 to N
    msg = msg & i & "....." & OffsetValue(i) & " : " &
        ForceSetPointValue(i) & Chr(10)
Next
'msg = msg & "" & Chr(10)
'msg = msg & "ScanTime per image (sec):" & Chr(10)
'msg = msg & PicoScan.ScanResolution/PicoScan.ScanLinesPerSecond & Chr(10)
'msg = msg & "Total scanning time (min):" & Chr(10)
'msg = msg & (PicoScan.ScanResolution*N)/(PicoScan.ScanLinesPerSecond*60) &
Chr(10)
ret = MsgBox( "Is it right parameters?" & Chr(10) & msg, vbYesNoCancel, "Tip
fluorescence SPS file generator script" )
if vbCancel then StopScript
WEnd

PicoScan.ServoRange = 0                'preparation for scanning
PicoScan.ServoOffset = 0
PicoScan.ZServoLoop = False
PicoScan.Pause PausePeriod           'wait for equilibrium

PicoScan.StartSPMScan
For i = 1 to N                          'scanning
    PicoScan.ForceSetPoint = ForceSetPointValue(i)
    PicoScan.Pause PicoScan.ScanResolution/PicoScan.ScanLinesPerSecond +
    PicoScan.ScanResolution*PicoScan.ScanResolution*PreSweepdelay
Next
PicoScan.StopSPMScan
PicoScan.ForceSetPoint = 0
PicoScan.ServoOffset = OffsetValueBegin
PicoScan.ZServoLoop = True
MsgBox ("Scan Complit"), vbSystemModal

'ForceSetPointValue = (11,7987 - OffsetValue)/425,6175    'this is true for
AFMM1251 scanner due to calibration. could be changed after recalibration
'OffsetValue = -425,6175*ForceSetPointValue + 11,7987    'this is true for
AFMM1251 scanner due to calibration. could be changed after recalibration

```

Treat AFM data

“Treat AFM data” is the LabView based, custom-written program which allows loading, representation, analysis and saving in various formats (ASCII spreadsheets, jpeg images) of a TCSPC data obtained in confocal scanning mode (Section 2.4) via different SPC cards⁵.

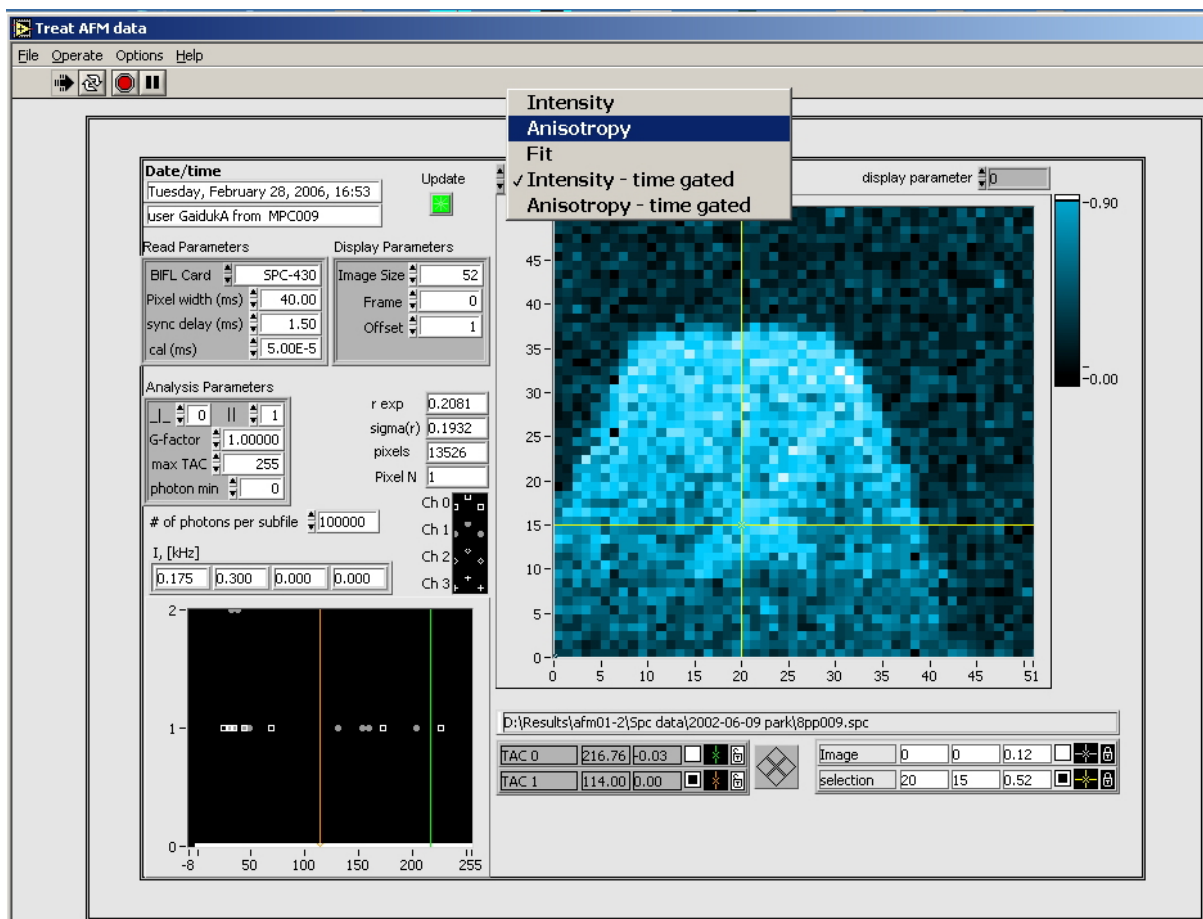


Figure A–5. Control panel of the “Treat AFM data” program developed for Multiparameter Fluorescence Imaging (MFI). The program provides loading, viewing, fast analysis and conversion of TCSPC data. Pop-up menu on the picture shows different dimensions (in terms of MFI) of fluorescence data, available for the presentation as an image.

⁵ Volodymyr Kudryavtsev, Dr. Matthew Antonik and Dr. Suren Felekyan are gratefully acknowledged for the programming work on this program.

WinSpec movies

WinSpec movies is the MatLab based, custom-written program for CCD image data proceeding, post-treatment and further analysis with the help of standard MatLab functions (Figure A–6). It reads standard *.SPE files, saved with the commercial WinSpec software. It allows image sequence custom resizing and rescaling as well as different colour schemes presentation. The program is capable of *.AVI video files creation, combining and displaying. Single frame or the whole image sequence can be addressed and further analyzed in MatLab.

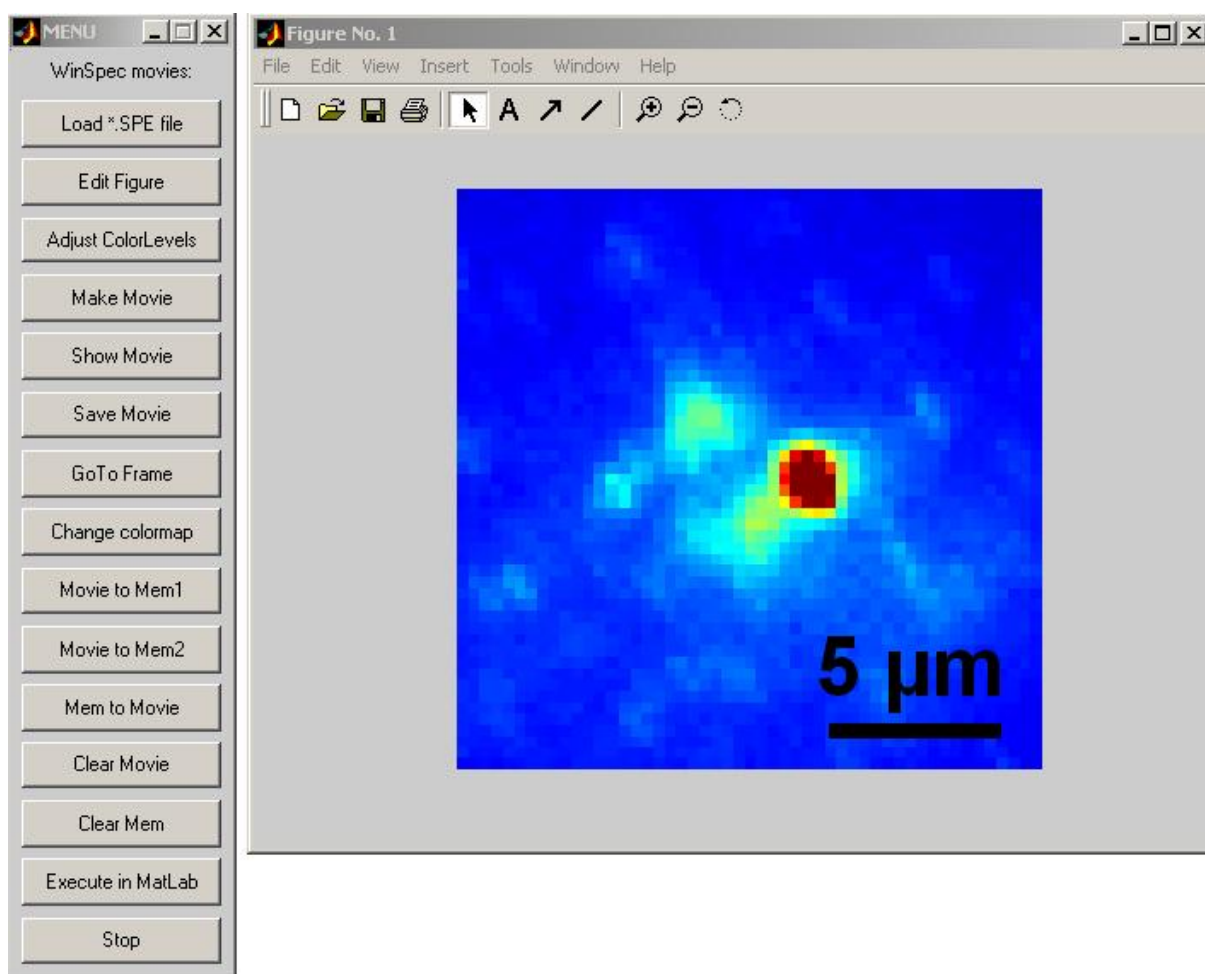


Figure A–6. “WinSpec movies” menu panel with the set of commands and a Figure window with the image sequence loaded.

PicoPull

PicoPull is the LabView based, custom-written program which controls the force spectroscopy mode in the custom-build setup⁶. The interface of force spectroscopy program PicoPull is given on the picture below (Figure A–7). The program controls communication between high-speed acquisition computer board and MI controller. Automatic calibration of the cantilever deflection is possible. Hand control pulling and automatic custom force curve sequences are available. Window (A) - hand control of piezo movement; window (B) - full force curve for automatic pulling; window (C) presents region of interest of the full force curve. For operating PicoPull the standard MI software PicoScan should be running.

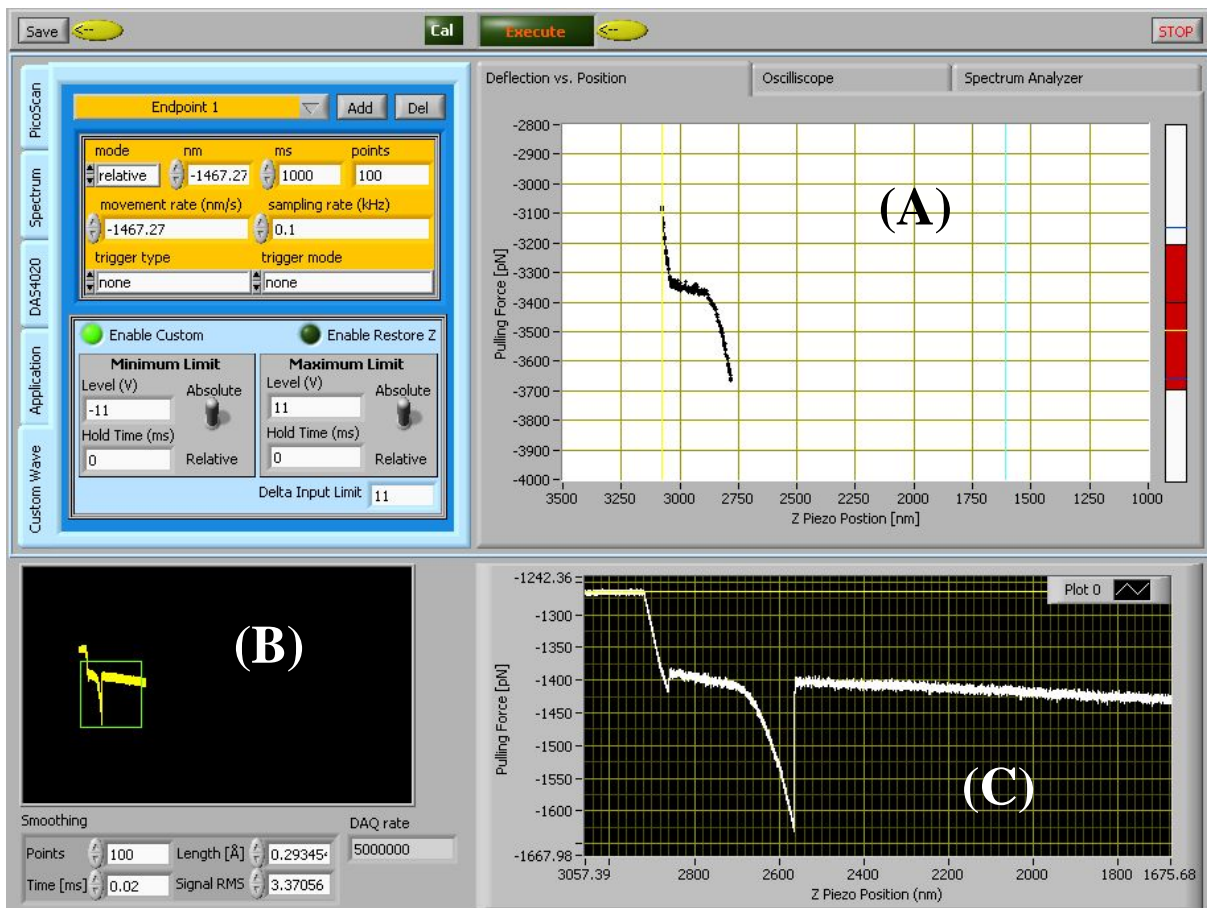


Figure A–7. Control panel of PicoPull custom-written program, which is responsible for the force spectroscopy mode control, data acquisition and data saving.

⁶ Programming and the program title by Dr. Matthew Antonik.

ReadFFTs

ReadFFT files is a custom-written program, allowing reading and reformatting binary files, obtained in PicoPull program in Spectrum Analyzer mode. The binary data contain a big number of data point for the cantilever deflection power spectrum. Here this information can be viewed, and a region selected for ASCII format conversion.

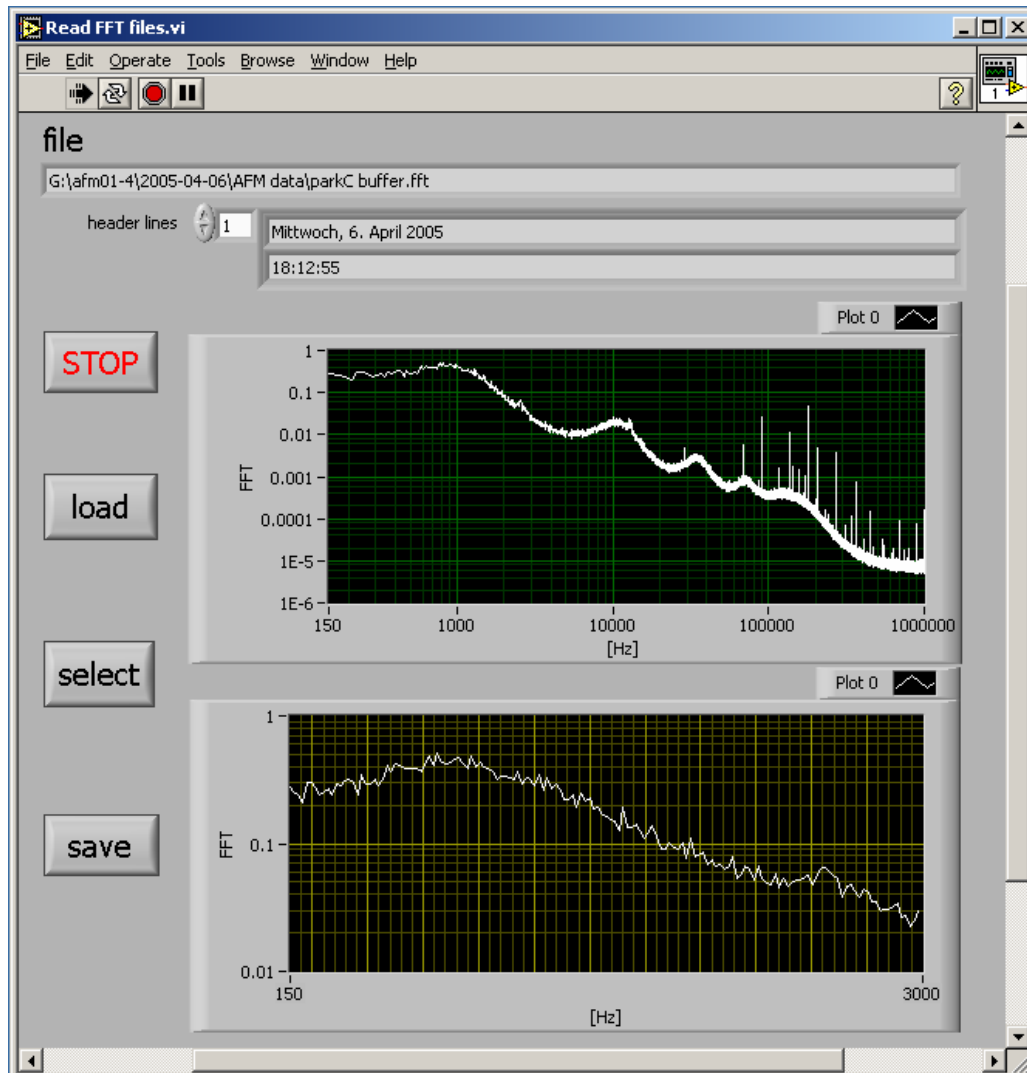


Figure A–8. Control panel of “Read FFT”, a custom-written program, allowing binary data reading and reformatting for the analysis. Binary files are obtained in PicoPull program in Spectrum Analyzer mode.

PicoPeek

PicoPeek is a custom-written program, allowing reading, viewing, post treatment and saving of experimental force spectroscopy data as well as simultaneous force and fluorescence spectroscopy data⁷.

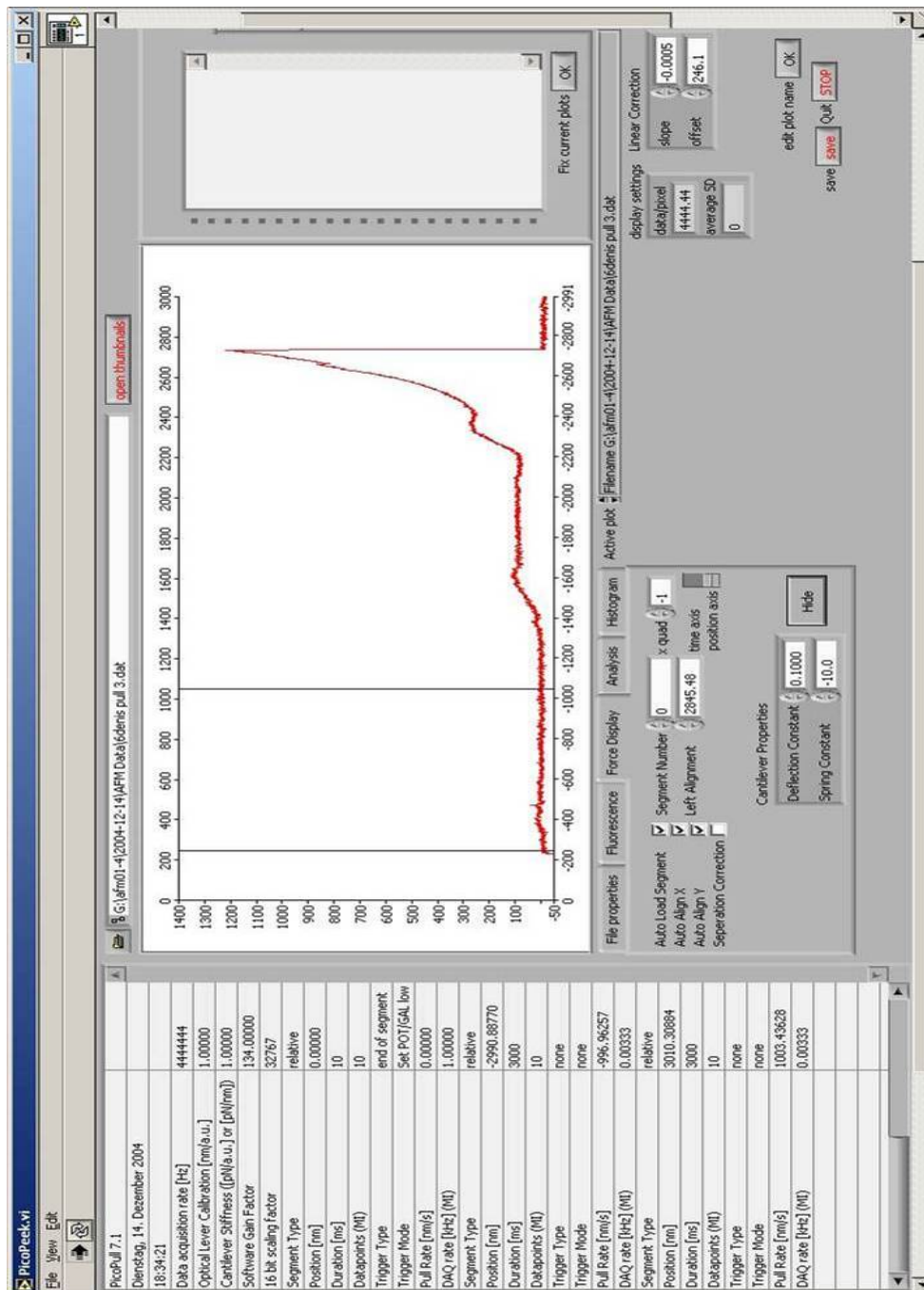


Figure A–9. Control panel of “PicoPeek” home-written program, allowing reading, viewing, post treatment and saving of experimental force spectroscopy data.

⁷ Programming and the program title by Dr. Matthew Antonik.

ViewPicoPeek (FoCuS)

FoCuS is a MatLab-based custom-written procedures package for force spectroscopy data visualization (including offset and tilt corrections and statistical analysis). Either ASCII force curves data saved in PicoPeek or experimental data saved in PicoPull is acceptable for the visualization and analysis.

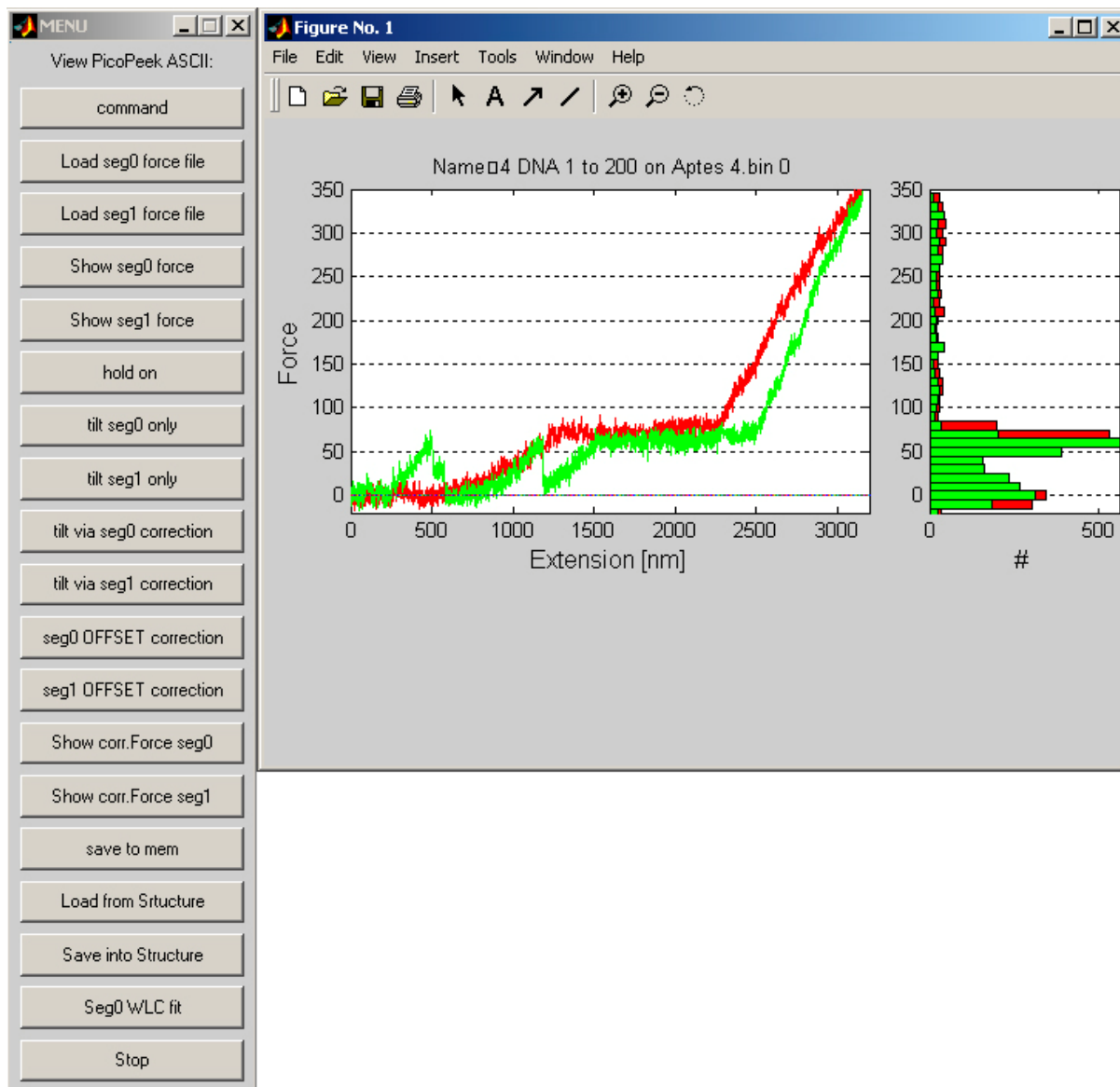


Figure A–10. Menu panel of “ViewPicoPeek” MatLab based program for the force curve correction and statistical analysis. A ‘Figure’ window shows the loaded data of a force spectroscopy experiment. A green line corresponds to a retraction curve force and a red line indicates approach curve force as a function of piezo extension. On the right side of the ‘Figure’ window force histograms for the selected curves are shown.

List of publications

The results of the thesis have been published and presented at international conferences.

Scientific papers:

- I. Gaiduk A., Kühnemuth R., Antonik M., Seidel C.A.M., “Optical characteristics of atomic force microscopy tips for single-molecule fluorescence applications” *Chem.Phys.Chem.* 6 (2005) pp.976.
- II. Antonik M., Felekyan S., Gaiduk A., Seidel C.A.M., “Separating Structural heterogeneities from stochastic variations in fluorescence resonance energy transfer distributions via Photon Distribution Analysis” *J.Phys.Chem.B* 110 (2006) pp.6970.
- III. Gaiduk A., Kühnemuth R., Felekyan S., Antonik M., Becker W., Kudryavtsev V., König M., Oesterhelt F., Sandhagen C. and Seidel C.A.M., “Time-resolved photon counting allows for new temporal and spatial insights into the nanoworld” *Proc. SPIE* 6372 (2006) pp.637203.

Oral presentation:

- “Combining Atomic-force and Fluorescence Spectroscopy for Single Molecule Investigations” 10th International Workshop on Single Molecule Detection and Ultrasensitive Analysis in Life Sciences, 22 – 24 September 2004, Berlin.
- “Time-resolved photon counting allows for new temporal and spatial insights into the nanoworld” Optics EAST, 1-4 October, Boston, USA.

Poster presentations:

- 87th International Bunsen Discussion Meeting: October 3 – 6, 2005, Tutzing / Munich.
- 9th International Conference on Methods and Applications of Fluorescence: Spectroscopy. Imaging and Probes (MAFS), September 4-7, 2005, Lisbon, Portugal.
- VII. Annual Linz Winter Workshop, February 4-7, 2005, Linz, Austria.
- VI. Annual Linz Winter Workshop, January 30 - February 2, 2004, Linz, Austria.
- V. Annual Linz Winter Workshop, January 31 - February 3, 2003, Linz, Austria.
- Life Sciences International Summer School, 15-19 July, 2002, Nottingham, England.

Declaration

I declare that the following thesis has been completed independently, without illegitimate help and has not been submitted previously for a degree.

Alexander Gaiduk

A handwritten signature in blue ink, appearing to read 'A. Gaiduk', with a light blue rectangular stamp or mark behind it.

Düsseldorf, 28.06.2006